UNIVERSITY
OF LATVIA

Kiryl Niherysh

TRANSPORT PROPERTIES OF TOPOLOGICAL INSULATOR BASED HYBRID DEVICES

Doctoral Thesis

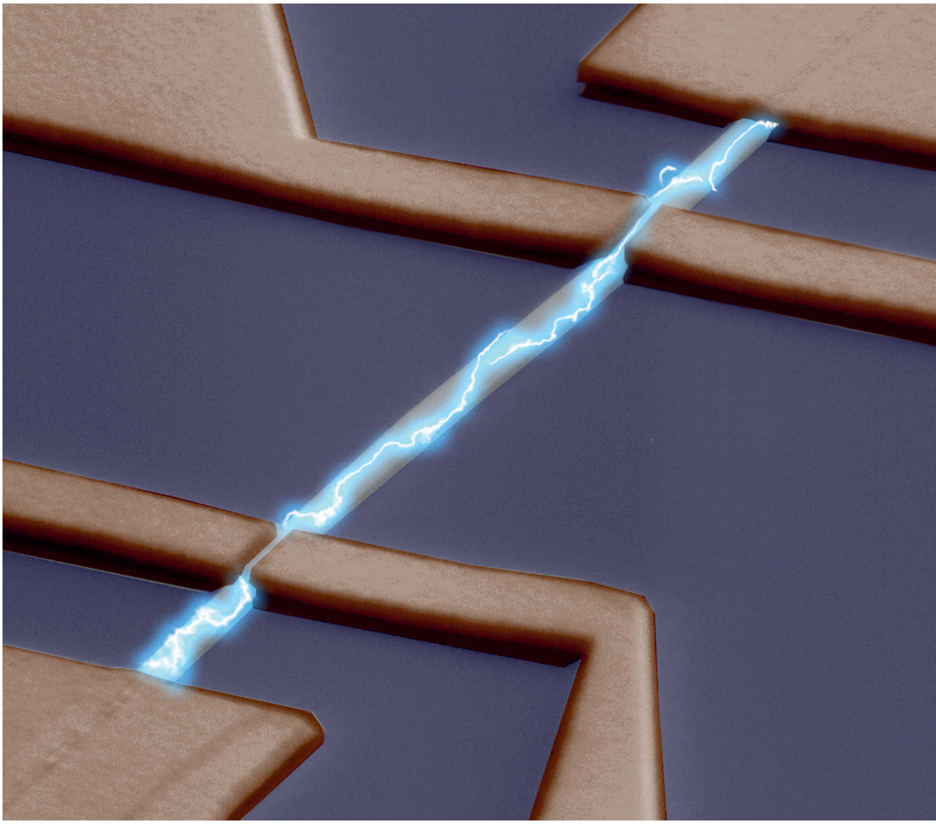

Riga 2024

UNIVERSITY
OF LATVIA

FACULTY OF PHYSICS, MATHEMATICS AND OPTOMETRY
INSTITUTE OF CHEMICAL PHYSICS

Kiryl Niherysh

TRANSPORT PROPERTIES OF TOPOLOGICAL INSULATOR BASED HYBRID DEVICES

DOCTORAL THESIS

Submitted for the Doctoral Degree in Physics
Subfield of Material Physics

Riga 2024

The research for the doctoral thesis was carried out at the Institute of Chemical Physics, University of Latvia and the Department of Microtechnology and Nanoscience MC2, Chalmers University of Technology, Sweden from 2018 to 2024.

This work has been supported by: the European Union's Horizon 2020 research and innovation funding programme (grant agreement 766714/HiTIMe), the Fundamental and Applied Research programme of the Latvian Research Council (lzp−2019/1-0349), the European Social Fund within the project "Strengthening the doctoral capacity of the University of Latvia within the framework of the new doctoral model" (8.2.2.0/20/1/006).

Form of the thesis: dissertation in Physics and Astronomy, subfield of Materials Physics.

Supervisors:

1. Prof., Dr. chem. **Donāts Erts**, University of Latvia, Institute of Chemical Physics;
2. Prof., PhD phys. **Floriana Lombardi**, Chalmers University of Technology, Department of Microtechnology and Nanoscience MC2.

Reviewers:

1. Prof., Dr. phys. **Vjačeslavs Kaščejevs**, University of Latvia;
2. Prof., Dr. habil. phys. **Juris Purāns**, University of Latvia, Institute of Solid State Physics;
3. Prof. PhD phys. **Matteo Salvato**, University of Roma "Tor Vergata".

The thesis will be defended at the public session of the Promotional Committee of Physics and Astronomy, University of Latvia, at 4 pm on the 17th of September 2024, at the University of Latvia, Institute of Solid State Physics, Kengaraga Street 8.

The thesis is available at the Library of the University of Latvia, Raiņa blvd. 19.

Chairman of the Promotional Committee of Physics and Astronomy
Linards Skuja

Secretary of the Promotional Committee of Physics and Astronomy
Sintija Siliņa

ISBN 978-9934-36-272-9
ISBN 978-9934-36-273-6 (PDF)

Cover
A false-coloured SEM image of a nanodevice based on a Bi_2Se_3 nanoribbon.

ABSTRACT

In this thesis the synthesis, structural and electronic transport properties of Bi_2Se_3 and $(Bi_{1-x}Sb_x)_2Te_3$ 3D topological insulators (3D-TIs) incorporated into high-frequency devices with a focus on metrology and charge sensing were studied and exploited. The main driver of the thesis is the prospect of using TI materials to create a quantum single-electron charge pump that can be used as a metrological current standard, or in other words to lay the technological foundations for a TI-based device that can realize the Ampere for the International System of Units *(fr. Systéme international d'unités*, abbrev. SI). The technological developments in this thesis prepare the ground for charge pumping in TI-based devices, as well as for other nanoelectronic devices, such as hybrid devices for quantum information processing, sensing, thermoelectric applications, spintronics, electromechanical switching and so on.

The problem of unavoidable bulk contributions to transport in TI-based devices was explored in-depth. Attempts to solve the problem by employing electrostatic gate tuning, the possibility of using ultrathin TI nanostructures with increased surface-to-volume ratio, strain engineering, as well as compensating doping were discussed. Quantum transport studies have been carried out on nanostructures on a length scale comparable to the electron phase coherence length. The experimentally observed gate conductivity response of ultrathin TI nanostructures shows hints of size-induced quantization of sub-bands. In addition, single-electron transistor devices have been fabricated using TI materials, which is a promising step towards TI-based single-electron charge pumping.

Overall, the results presented in this work demonstrate the variety of enhanced properties of TI materials arising from topological surface states (TSSs), using a huge amount of different transport measurements. Fabricated devices reflect that controlling the size of nanostructures plays an important role in isolating the contributions of TSSs to transport properties.

Keywords: Topological insulator, quantum transport, single-electron transistor (SET), . . .

Contents

ABBREVIATIONS AND SYMBOLS

1D	One-dimensional
2D	Two-dimensional
2DEG	Two-dimensional electron gas
3D	Three-dimensional
AAS	Altshuler-Aronov-Spivak
AB	Aharonov-Bohm
AFM	Atomic force microscopy
ARPES	Angle-resolved photoemission spectroscopy
CVD	Chemical vapour deposition
EBL	Electron-beam lithography
EDX	Energy-dispersive X-ray spectroscopy
FFT	Fast Fourier transform
HRTEM	High-resolution transmission electron microscopy
IQHE	Integer Quantum Hall Effect
PVD	Physical vapour deposition
QD	Quantum dot
RMS	Root mean square
SAED	Selected area (electron) diffraction
SdH	Shubnikov-de Haas
SEM	Scanning electron microscopy
SET	Single-electron transistor
TI	Topological insulator
TSS	Topological surface states
TR	Time-reversal
UCF	Universal conductance fluctuation
WAL	Weak anti-localization
WL	Weak localization
XRD	X-ray diffraction
XRR	X-ray reflectometry

FUNDAMENTAL CONSTANTS

h	Planck constant ($h = 6.626 \times 10^{-34}$) [J·s])
$\hbar$	Reduced Planck constant ($\hbar = 1.055 \times 10^{-34}$) [J·s])
e	Elementary charge ($e = 1.602 \times 10^{-19}$) [C])
m_e	Electron mass ($m_e = 9.109 \times 10^{-31}$) [kg])
k_B	Boltzmann constant ($k_B = 1.381 \times 10^{-23}$) [m^{2}kg/(s^{2}K)])

INTRODUCTION

A globally consistent system of measurement units is a necessary basis for most technological, industrial, and economic activities. In particular, electrical units play a vital role in the modern world, where electrical measurements are ubiquitous.

The system of electrical units is based on the key unit Ampere, which until recently was defined in terms of mechanical units via the laws of classical electromagnetism (Figure 1a) [1]. Already since the 1990s, the classical definition of the ampere led to the adoption of a practical system of units, based on resistance and voltage standards derived from quantum electrical effects. It uses precisely defined conventional values of the von Klitzing constant $R_k = h/e^2$ and the Josephson constant $K_J = 2e/h$, which are not related to the SI. Because of such flaws, the International System of Units proposed on May 20, 2019 to revise the system of units toward a system purely based on constants of nature [2]. For instance, the Ampere can be redefined in terms of the fundamental constant e, the charge of the electron. The proposed redefinition of the Ampere would restore coherence to the SI system. The combination of the Josephson and the quantum Hall effects together with the single-electron transport (SET) electrical quantum effect in one experiment is called “Quantum Metrological Triangle” (Figure 1b). Such a combination can be realized via Ohm's law (voltage = electrical resistance times current). Mathematically this leads to the product of the “phenomenological” constants K_J, R_K, and Q_S, the latter being the charge of the single charge quanta transported in an SET circuit. This product term only contains integer numbers and frequencies, quantities that can be quantified experimentally with very high precision (an uncertainty level of one part in 10^9).

To implement the new definition of the Ampere, an approach to control the number of electrons flowing per unit time and to count the errors occurring in this process is needed. State-of-the-art nanofabrication technology makes it possible to produce SET devices, known as single-electron charge pumps, which generate electric current by moving electrons one at a time in a controlled manner with sufficiently high speed and accuracy [4].

Historically, research into single-electron devices has been motivated by attempts to create a practical charge-pumping device for the realization of a current standard. The basic idea is conceptually very simple: create a device which transports only one electron at a time through some barrier in response to a well-defined periodic stimulus (for example, a voltage applied to a gate electrode with a frequency f). Such a device will generate a current $I = e \cdot f$, where e is the

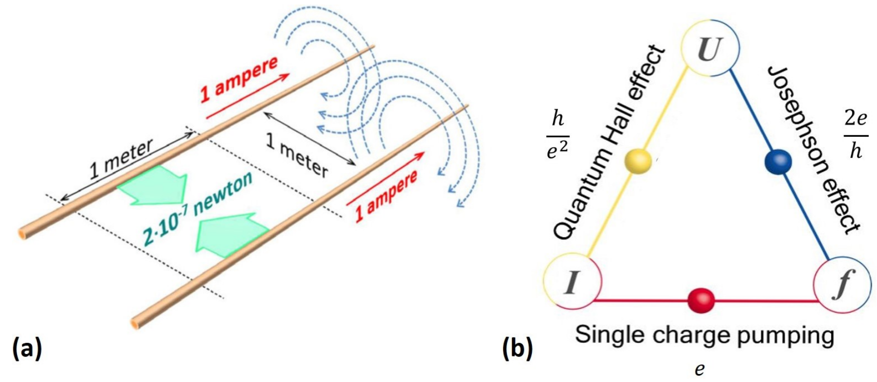

Figure 1: (a) Schematic of the "classical" SI ampere definition, based on the exploitation of Maxwell's equations (The Ampere is that constant current which, if maintained in two straight parallel conductors of infinite length, of negligible circular cross-section, and placed 1 metre apart in vacuum, would produce between these conductors a force equal to 2×10^{-7} Newton per metre of length [3]). The forces depicted by green arrows are caused by the magnetic fields of the conductors (field lines indicated by blue arrows), adapted from [2]. (b) Quantum metrology triangle (QMT) scheme, which shows the relationship between the three quantum electrical effects and the fundamental constants e and h.

fundamental unit of charge. Since frequency can be measured with extremely high accuracy and is easily related to the SI, this leads to an accurate and "natural" realization of the Ampere. The realization of such a quantum standard presents two main challenges: a) it needs to be highly accurate: ideally better than 1 part in 10^8. b) In order to be of practical use for calibration of secondary standards it should generate a current > 1 nA. It has been proven to be especially difficult to fulfil the second requirement, as it implies operation at high ($f = I/e > 6$ GHz) frequencies which severely limits the permissible RC time constant of the device. The ultimate goal is to develop a new concept for the realization of a quantum single-electron charge pump based on a topological insulator (TI) instead of conventional materials (typically GaAs), whose working principle is different from the vast majority of present charge-pumping devices.

Topological insulators belong to a completely new class of quantum materials with properties that are very different from that of ordinary matter. TIs are materials with large band gaps for bulk electrons, like in ordinary insulators, but having gapless Dirac states on surfaces. These states are metallic and due to the spin-momentum locking the back-scattering of Dirac electrons is forbidden. This topological protection from back-scattering makes these states insensitive to disorder and defects. The first experimental observation of TI in 2007 was in a

HgTe/CdTe heterostructure [5], but TI states have been subsequently observed in many other materials. Of particular interest is Bi_2Se_3, since it has a very large bulk bandgap ($\sim$ 300 meV), which means the topological phase can be seen at room temperature [6]. Bi_2Se_3 can be grown in the form of long (many tens of micrometres) nanoribbons which can conveniently be integrated into electronic devices. These ribbons are intrinsically 3D-TIs, and they can also be electrically gated and further patterned to locally create a band gap in the Dirac spectrum. Moreover, the thinning down of such nanoribbons leads to the effective suppression of the parasitic bulk charge carriers and utilization of their peculiar topological surface states due to the high surface-to-volume ratio and high mobility [7, 8]. Thus, TIs have several potential benefits over conventional materials for accurate charge pumping.

The absence of an energy gap at the Dirac surface states in 3D-TIs makes them effectively massless and insensitive to localization or confinement by electrostatic gating due to Klein tunnelling phenomenon. However, a locally reduced size can lead to size-induced quantization of sub-bands [9], which suppresses Klein tunnelling and enables the formation of tunnelling barriers. Two barriers connected in series can then be used to define a TI quantum dot, which has been proposed as a fundamental component for creating novel devices as quantum single-electron pumps for metrology with high precision and current output [10].

This thesis examines the high-frequency properties of devices incorporating topological insulator materials with a focus on metrology and charge sensing. The targeted breakthrough is the demonstration and manipulation of single-charge states in a topological insulator, an important step towards a quantum single-electron charge pump. It is envisioned to operate with high accuracy at higher temperatures and lower magnetic fields than devices based on conventional semiconductor materials. To lay the foundation for this ambitious goal the materials development, theoretical modelling, device fabrication, and electrical transport measurements were combined. The outcomes will also be directly relevant to other nanoelectronic devices utilizing TI materials, such as hybrid devices for quantum information processing, sensing and spintronic applications.

Aim of the thesis

The aim of this thesis is to develop and characterise functioning hybrid devices based on TI materials, which can be used in single-electron transport, quantum information processing, sensing, thermoelectric applications, spintronics, electromechanical switching applications and so on.

Tasks of the thesis

1. To synthesise and characterise 3D-TI materials in the shape of nanoribbons and ultrathin films.
2. To differentiate and examine various approaches to reduce parasitic bulk conductivity in TI nanostructures.
3. To fabricate nanodevices enabling the quantum transport measurements of individual topological insulator nanostructures.
4. To characterize the obtained devices in terms of quantum transport.
5. To fabricate and measure nanodevices based on TI materials, containing quantum dots, to demonstrate the possibility of charge pumping.

Scientific novelty

The work presented in this thesis contributes to experimental research in the field of topological insulators, particularly, in the characterization of quantum transport properties for the potential application as electronic, spintronic and other devices. The following results and findings can be emphasised:

- Systematic optimization of standard growth parameters to achieve the outcome of high-yield ultrathin Bi_2Se_3 nanoribbons with increased surface-to-volume ratio has been performed.
- A change in the growth dynamic of ultrathin TI nanoribbons has been demonstrated, which strongly affects the charge transport properties of topological surface states.
- The size-induced quantization of electronic band structure leading to the formation of discrete Dirac sub-bands in ultrathin TI nanoribbons has been demonstrated.
- The electrostatic field effect was implemented to dynamically manipulate bending deformation in suspended devices based on Bi_2Se_3 nanoribbons.
- An approach based on correlation analysis of Raman modes has been developed, which makes it possible to estimate the type and quantity of strain in Raman active thin films.
- Single-electron transport characteristics of the quantum dots based on TI materials (Bi_2Se_3 and $(Bi_{1-x}Sb_x)_2Te_3$), such as a well-defined Coulomb blockade effect and single-electron tunnelling at sub-Kelvin temperatures have been demonstrated.

Practical significance

Three-dimensional topological insulator materials can be used as an alternative to the conventional materials used in the vast majority of single-electron transport devices. Spin-momentum locking in the surface states reduces unwanted back-scattering, which can lead to an increased signal-to-noise ratio in TI-based devices. A decrease in the geometric size of the TIs causes quantum confinement, which leads to a peculiar gapped Dirac sub-band structure. A locally reduced size can lead to size-induced quantization of sub-bands in the constricted parts, which form effective barriers and allow the formation of a quantum dot. This will enable the creation of some of the most desirable quantum devices for metrology (single-electron devices, charge pumps), spintronics (spin-polarized current source), quantum optics and quantum computing (TI-based Majorana qubits).

The results presented in this thesis in the case of bent nanoribbons may find application in electro-mechanical switches operating in low temperatures, which are suitable for cryogenic mechanics, quantum computing and space applications. In the case of thin films or graphene/Bi_2Se_3 heterostructures, they are excellent for applications where an electrically conductive substrate is required, for example in electronic, spintronic, and even domestic waste heat conversion applications.

Defendable theses

1. The rough-to-smooth transition in the growth dynamic of Bi_2Se_3 nanoribbons with increasing thickness occurs, resulting in a strong correlation between the morphology of the nanoribbons and their transport properties.

2. The increase of the surface-to-volume ratio in ultrathin Bi_2Se_3 nanoribbons leads to size-induced quantum confinement, resulting in a unique gapped Dirac sub-band structure.

3. The possibility of tuning topological surface states in a suspended Bi_2Se_3 nanoribbon due to external bending deformation dynamically introduced by the action of an electrostatic field is demonstrated.

4. Correlation analysis of vibration modes in Bi_2Se_3 thin films probed by the Raman mapping technique is developed to determine the type and amount of strain. This approach can be implemented in various Raman active 2D materials.

5. A functional TI-based single-electron transistors, fabricated using a top-down electron-beam lithography approach are demonstrated, which is a promising step towards a quantum single-electron charge pumping.

List of publications

This thesis is mainly based on the work contained in the following papers:

[I] J. Andzane, A. Felsharuk, A. Sarakovskis, U. Malinovskis, E. Kauranens, M. Bechelany, **K. A. Niherysh**, I. V. Komissarov, and D. Erts, "Thickness-Dependent Properties of Ultrathin Bismuth and Antimony Chalcogenide Films Formed by Physical Vapor Deposition and Their Application in Thermoelectric Generators", *Materials Today Energy* **19** (2020).

[II] **K. A. Niherysh**, J. Andzane, M. M. Mikhalik, S. M. Zavadsky, P. L. Dobrokhotov, F. Lombardi, S. L. Prischepa, I. V. Komissarov, and D. Erts, "Correlation Analysis of Vibration Modes in Physical Vapour Deposited Bi_2Se_3 Thin Films Probed by the Raman Mapping Technique", *Nanoscale Advances* **3** (2021).

[III] G. Kunakova, E. Kauranens, **K. A. Niherysh**, M. Bechelany, K. Smits, G. Mozolevskis, T. Bauch, F. Lombardi, and D. Erts, "Magnetotransport Studies of Encapsulated Topological Insulator Bi_2Se_3 Nanoribbons", *Nanomaterials* **12** (2022).

[IV] J. Andzane, A. Felsharuk, K. Buks, A. Sarakovskis, J. Gabrusenoks, **K. Niherysh**, and D. Erts, "Synthesis and Properties of Bismuth Selenide Based Nanolaminates for Application in Thermoelectrics", *Advanced Materials Interfaces* **9**, 2200385 (2022).

[V] R. Sondors†, **K. Niherysh**†, J. Andzane, X. Palermo, T. Bauch, F. Lombardi, and D. Erts, "Low-Vacuum Catalyst-Free Physical Vapor Deposition and Magnetotransport Properties of Ultrathin Bi_2Se_3 Nanoribbons", *Nanomaterials* **13** (2023).

[VI] **K. Niherysh**, X. Palermo, A. P. Surendran, A. Kalaboukhkov, R. Sondors, J. Andzane, D. Erts, T. Bauch, and F. Lombardi, "Quantum Confinement and Coherent Transport in Ultrathin Bi_2Se_3 Nanoribbons", Submitted to *Physical Review Applied* (2023).

[VII] **K. Niherysh**, L. Jasulaneca, E. Dzene, F. Lombardi, and D. Erts, "Effect of Bending Deformation on Suspended Topological Insulator Nanowires: Towards a Topological Insulator Based NEM Switch", *Sensors and Actuators A*: *Physical* **371**, 115292 (2024).

[VIII] X. Palermo, **K. Niherysh**, A. P. Surendran, Y. Ji, X. Kou, T. Bauch, and F. Lombardi, "Coulomb Blockade and Chaotic Electron Motion in a Topological Insulator Quantum Dot", to be submitted (2024).

† These authors contributed equally.

List of papers that are beyond the scope of this thesis:

[A] N. Kovalchuk, **K. Niherysh**, M. Mikhalik, N. Kargin, I. Komissarov, and S. Prischepa, “Possibility of Determining the Graphene Doping Level Using Raman Spectra”, *Journal of Applied Spectroscopy* **84** (2018).

[B] N. G. Kovalchuk, **K. A. Niherysh**, A. V. Felsharuk, I. A. Svito, T. Tamulevičius, S. Tamulevičius, N. I. Kargin, I. V. Komissarov, and S. L. Prischepa, “Direct Patterning of Nitrogen-Doped Chemical Vapor Deposited Graphene-Based Microstructures for Charge Carrier Measurements Employing Femtosecond Laser Ablation”, *Journal of Physics D: Applied Physics* **52** (2019).

[C] A. P. Surendran, D. Montemurro, G. Kunakova, X. Palermo, **K. Niherysh**, E. Trabaldo, D. S. Golubev, J. Andzane, D. Erts, F. Lombardi, and T. Bauch, “Current-Phase Relation of a Short Multi-mode Bi_2Se_3 Topological Insulator Nanoribbon Josephson Junction with Ballistic Transport Modes”, *Superconductor Science and Technology* **36** (2023).

[D] A. P. Surendran, G. Kunakova, X. Palermo, **K. Niherysh**, D. Montemurro, J. Andzane, D. Erts, D. S. Golubev, S. Lara-Avila, F. Lombardi, and T. Bauch, “Ballistic Transport on Micrometer Scale Revealed by Fabry-Pérot-like Resonances in Bi_2Se_3 Nanoribbon Devices”, Submitted to *Physical Review Applied* (2023).

[E] J. Kosmaca, J. Katkevics, J. Andzane, R. Sondors, L. Jasulaneca, R. Meija, **K. Niherysh**, Y. Rublova, and D. Erts, “Humidity-Dependent Electrical Performance of CuO Nanowire Networks Studied by Electrochemical Impedance Spectroscopy”, *Beilstein Journal of Nanotechnology* **14** (2023).

[F] E. A. Dronina, M. M. Mikhalik, N. G. Kovalchuk, **K. A. Niherysh**, A. V. Felsharuk, S. L. Prischepa, and I. V. Komissarov, “Raman Spectroscopy Study of the Charge Carrier Concentration and Mechanical Stresses in Graphene Transferred Employing Different Frames”, *Journal of Applied Spectroscopy* **90** (2023).

[G] Y. Hu, M. P. Weir, H. J. Pereira, O. J. Amin, J. Pitcairn, M. J. Cliffe, A. W. Rushforth, G. Kunakova, **K. Niherysh**, V. Korolkov, J. Kertfoot, O. Makarovsky, and S. Woodward, “Bi_2Se_3 Interlayer Treatments Affecting the $Y_3Fe_5O_{12}$ (YIG) Platinum Spin Seebeck Effect”, *Applied Physics Letters* **123** (2023).

List of selected international conference presentations:

[a] **K. Niherysh**, X. Palermo, A. P. Surendran, Y. Ji, X. Kou, D. Erts, T. Bauch, and F. Lombardi, "Shaped Topological Insulators: Towards Single-Electron Charge Pump", 82nd *International Scientific Conference of the University of Latvia, "Quantum Sensors and Devices"*, 8 February 2024, Riga, Latvia (oral).

[b] **K. Niherysh**, X. Palermo, A. P. Surendran, J. Andzane, T. Bauch, D. Erts, and F. Lombardi, "Towards Effective Gating of TI-based Devices", 24th *International Conference–School "Advanced Materials and Technologies"*, 22-26 August 2022, Palanga, Lithuania (poster, award for the best poster).

[c] X. Palermo, **K. Niherysh**, A. P. Surendran, Y. Ji, X. Kou, T. Bauch, and F. Lombardi, "Quantum Confinement in Shaped Topological Insulator Nanowires", 29th *International Conference on Low Temperature Physics*, 18-24 August 2022, Sapporo, Japan (poster).

[d] **K. Niherysh**, A. Felsharuk, J. Andzane, A. Kalaboukhov, and D. Erts, "Epitaxial Growth of Topological Insulator Thin Films by Physical Vapour Deposition Technique", 80th *International Scientific Conference of the University of Latvia, "Nanotechnologies and Radiation Processes"*, 3-4 February 2022, Riga, Latvia (oral).

[e] J. Chang, D. Chakraborty, P. Francis, G. Chen, I. Komissarov, **K. Niherysh**, D. Erts, A. Laszcz, F. Lombardi, A. Kalaboukhov, and R. Sobolewski, "Coherent Acoustic Phonons in the Bi_2Se_3 Nanolayer System Explored by Femtosecond, Optical Pump-probe Spectroscopy", 7th *International Scientific Conference "Progress in Applied Surface, Interface, and Thin Film Science. Solar Renewable Energy News"*, 22-24 November 2021, Bratislava, Slovakia (oral).

[f] **K. Niherysh**, X. Palermo, G. Kunakova, J. Andzane, T. Bauch, D. Erts, and F. Lombardi, "Hall Effect Measurements in TI Nanoribbons", 23rd *International Conference–School "Advanced Materials and Technologies"*, 23-27 August 2021, Palanga, Lithuania (poster).

[g] **K. Niherysh**, J. Andzane, M. Mikhalik, S. Prischepa, I. Komissarov, and D. Erts, "Raman Characterization of Quartz/Bi_2Se_3 and Graphene/Bi_2Se_3 Heterostructures", 22nd *International Conference–School "Advanced Materials and Technologies"*,24-28 August 2020, Palanga, Lithuania (poster).

Part I

THEORETICAL OVERVIEW

1 Topology in condensed matter systems

1.1 Topology and topological invariants

Topology is a branch of mathematics which studies objects with geometric properties that are insensitive to smooth continuous deformations (stretching, compression, bending, twisting, etc.). A simple example illustrating the principles of topology is a closed two-dimensional surface in three dimensions (sphere), that can be smoothly deformed into various shapes, such as the surface of a disk or bowl, and these shapes are topologically equivalent. But the sphere cannot be smoothly transformed into the surface of a doughnut. Thus, a sphere and a doughnut are distinguished by an integer topological invariant called the genus of the shape g, which is essentially the number of holes. Since an integer cannot change smoothly, surfaces with a different genus g cannot be deformed into each other and what's why they are considered topologically distinct. In contrast, surfaces that can be transformed into each other are topologically equivalent. According to the Gauss-Bonnet theorem, the integral of the Gaussian curvature over a surface determines an integer topological invariant called the Euler characteristic [11]:

$$\chi = \frac{1}{2\pi} \int\limits_S K dA. \tag{1.1}$$

In the case of a sphere with radius R, $K = 1/R^2$ is the Gaussian curvature, $A = \Omega R^2$, where $\Omega = 4\pi$ is the solid angle and A is the spherical surface area, the Euler characteristic is $\chi = 2$. More generally, the Euler characteristic is quantized and related to the genus by $\chi = 2 - 2g$. Now, for a sphere $g = 0$ and for a doughnut $g = 1$, which makes them topologically distinct.

The idea of topological invariants can be applied to characterise more abstract objects, for example, the band structure of materials.

1.2 Topology and band theory

One of the triumphs of quantum mechanics and condensed matter physics in the 20th century was the development of the band theory of solids, which provides a language for describing the electronic structure of such states. This theory exploits the translational symmetry of the crystal to classify electronic states in terms of their crystal momentum k, defined in a periodic Brillouin zone [12]. The Bloch states $|u_n(k)\rangle$, defined in a single unit cell of the crystal, are eigenstates of the Bloch Hamiltonian $\mathcal{H}(k)$. The eigenvalues $E_n(k)$ define energy bands that collectively form the band structure [13]. According to the band theory, systems can be insulating, semiconducting or metallic, depending on the position of their Fermi energy. The Fermi energy is the highest energy occupied by electrons, with respect to forbidden states, called energy gaps. In a semiconductor or an insulator, the Fermi level is surrounded by a band gap. The closest band above the band gap is called the conduction band, and the closest band beneath the band gap is called the valence band. If the Fermi energy lies in the band gap, there are no low-energy excitations and the system is insulating. On the contrary, if the Fermi energy lies in the energy band (conduction or valence, depending on whether the charge transport is more electron-like or hole-like), low-energy electronic excitation is possible and the system is conducting. In insulators the electrons in the valence band are separated by a large gap from the conduction band, in conductors the valence band overlaps the conduction band, and in semiconductors there is a small enough band gap between the valence band and the conduction band that thermal or other excitations can bridge this gap.

To show how topology can be related to the band structure of materials in condensed matter physics, a brief description of the topological classification of insulators will be provided below. In a conventional insulator, an energy gap separates the occupied valence band states from the empty conduction band states. The slow (adiabatic) change in the Hamiltonian (the system always remains in the ground state (without closing the energy gap)) allows to introduce the concept of topological equivalence between different insulating states. Thus, all conventional insulators are topologically equivalent, if there exists an adiabatic path connecting them, along which the energy gap remains finite. It follows that the connection of topologically inequivalent insulators is necessarily accompanied by a phase transition, in which the energy gap vanishes.

One of the important consequences of topological band theory is the classification of distinct electronic phases (Hamiltonians). For example, if there are two topologically distinct phases in a crystal, the energy gap must tend to zero, otherwise the two phases would be equivalent. Therefore, this indicates the existence of low-energy electronic states associated with the region where the energy gap passes through zero [11, 13].

1.3 Berry phase and Chern numbers

The classification of topological matter is related to topological band theory and can be understood in terms of the Berry phase [14]. Due to the translation symmetry of crystalline materials, each eigenstate of the Hamiltonian $\mathcal{H}$ for single-particle states in a periodic potential can be labelled by their crystal momentum k belonging to the first Brillouin zone. Consider a quantum system changing slowly (adiabatically) as a function of time along path C in the parameter space. The Bloch wave functions $|\psi_n(k)\rangle$ must satisfy the time-dependent Schrödinger equation [11, 14–16]:

$$i\hbar\frac{\partial}{\partial t}\left|\psi_n\left(k\right),t\right\rangle = \mathcal{H}(k\left(t\right)\left|\psi_n\left(k\right),t\right\rangle \tag{1.2}$$

The wave function is given by:

$$\left|\psi_n\left(k\right),t\right\rangle = \exp\left[-\frac{i}{\hbar}\int\limits_0^t E_n\left(k\left(t'\right)\right)dt'\right]e^{i\gamma_n(t)}\left|u_n\left(k\left(t\right)\right)\right\rangle \tag{1.3}$$

where two terms on the right side of the Eq. (1.3) correspond to dynamical and geometric phase factors, respectively.

After substituting Eq.(1.3) into the time-dependent Schrödinger equation (1.2) and multiplying it from the left by $\langle u_n(k(t))|$, one finds geometric phase γ_n, which can be expressed as a path integral in the parameter space:

$$\gamma_n = \int\limits_C dk\cdot A_n(k), \tag{1.4}$$

where $A_n(k) = \left\langle u_n(k(t))\middle|\frac{\partial}{\partial k}u_n(k(t))\right\rangle$ is a vector potential, called the Berry connection or Berry vector potential, $u_n(k)$ - the cell periodic eigenstates of the Bloch Hamiltonian in k-space. For a closed path C, γ_n is known as the Berry phase [15].

In analogy to the magnetic field electrodynamics, by using the Stokes' theorem the Berry phase can be written as a surface integral:

$$\gamma_n = \int\limits_S \mathcal{F}d^2k, \tag{1.5}$$

where $\mathcal{F} = \frac{\partial}{\partial k}\times A_n\left(k\right) = \frac{\partial}{\partial k}\left\langle u_n\left(k\left(t\right)\right)\middle|\frac{\partial}{\partial k}u_n\left(k\left(t\right)\right)\right\rangle$ defines the Berry curvature, S is the surface of k-space connected to contour C.

The Berry phase and curvature depend only on the Hamiltonian $\mathcal{H}$ and directly reflect its properties. The Berry curvature integrated over a closed 2D space (such as a Brillouin zone) is a multiple of 2π. This defines a topological invariant called the Chern number.

In two-dimensional electron gas (2DEG) systems, at low temperatures and strong perpendicular magnetic field, the electrical conductivity takes quantized values that are fundamentally different from the predictions of classical physics [17]. This precise quantization in terms of fundamental constants (such as Planck's constant h and the charge of an electron e) was measured with very high precision and determined to be an integer:

$$\sigma_{xy} = n\frac{e^2}{h}, \tag{1.6}$$

where the value n is an integer (Chern number). The quantization of the σ_{xy} conductivity occurred for many-particle mesoscopic systems and was universal because it did not depend on microscopic details, such as the exact value of the magnetic field, the purity of the sample, the electron mobility etc. For the discovery of this phenomenon called the integer quantum Hall effect (IQHE), Klaus von Klitzing won the Nobel Prize in 1985. This exact quantization was later theoretically explained based on ideas from topology, related to a topological invariance of the energy bands by Thouless, Kohomoto, Nightingale and den Nijs (TKNN) [18]. The topological invariant defined for the IQHE system is the TKNN number, also known as the Chern number, closely related to the Berry phase, which can be written in terms of Berry curvatures as [13]:

$$n = \frac{1}{2\pi}\int\limits_{BZ} \mathcal{F} d^2k, \tag{1.7}$$

where the Chern number n corresponds to the total Berry flux or phase in the whole Brillouin zone [11], taking integer values.

Similar considerations about the genus g of the shapes from Section 1.1 are valid for systems with different Chern numbers belonging to topologically distinct classes. It is not possible to smoothly transform one Hamiltonian (band structure) into another. Thus, at the interface of topologically distinct materials, the band gap must close, and this leads to the origin of edge states. This topological understanding of the IQHE is a remarkable leap of progress, opening up the field of topological electronic states in condensed matter physics.

1.4 Topological insulators

For a material where TR symmetry is not broken, the Chern number is vanishing to zero. However, this does not mean that the electronic state carries no topological property in this case. Similarly to the Chern number, other relevant topological invariants can be defined to describe the topological classes. Thus, a new type of topological invariant $\mathbb{Z}_2$ for systems with spin-orbit coupling was introduced [19]. With the help of $\mathbb{Z}_2$, a time-reversal invariant insulator can be further classified as a trivial insulator with $\nu = 0$ or a non-trivial topological insulator (TI) with $\nu = 1$, respectively. In 2D case, a $\mathbb{Z}_2$ topological insulator (also called a quantum spin Hall insulator (QSHI)) was experimentally observed in mercury telluride quantum well devices [20]. TI is different from a trivial insulator in the sense that it has gapped insulating states in the bulk but gapless states on the edge due to its topological property. The band structure of a 2D-TI can be understood from the viewpoint of “band-inversion” in momentum space (Figure 1.1).

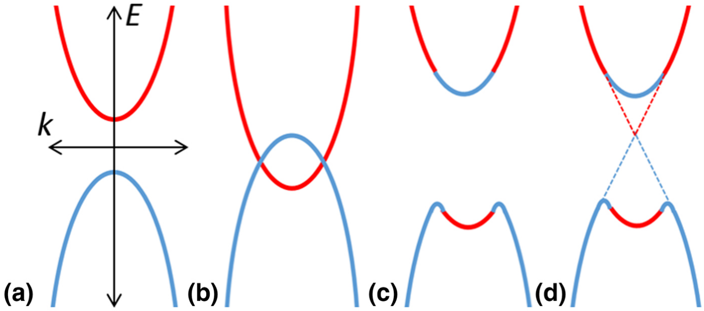

Figure 1.1: Schematic of the band structure evolution resulting in the formation of a topological insulator. (a) Normal band structure, (b) band inversion due to strong spin-orbit coupling, (c) band renormalization, and (d) formation of the topological surface states along with bulk valence and conduction bands. Adapted from [21].

In the case of a band insulator, the valence band comprises states with s-type (blue) symmetry and whose conduction band comprises states with p-type (red) symmetry, as shown schematically in Figure 1.1a. If the material has a substantial spin-orbit coupling, a band inversion can occur at high-symmetry points in the Brillouin zone as shown in Figure 1.1b. This leads to a band structure renormalization, as shown in Figure 1.1c. At the Γ point, the conduction band will now have s-type symmetry, while the valence band will have p-type symmetry. At an interface between this inverted material and a topologically trivial material (like vacuum), topological surface states (TSSs) will form a Dirac cone, since the transition from $\nu = 1$ to $\nu = 0$ occurs (dashed lines in Figure 1.1d). These surface states exhibit spin-momentum locking, meaning that the momentum of the electron determines the spin. This leads to topological protection of the electrons occupying the TSSs since the electrons cannot backscatter into other TSSs without undergoing a spin flip. The linear dispersion of these TSSs results in small electron masses and large Fermi velocities, similar to electrons found in graphene [21, 22].

Using the 2D topological invariant $\mathbb{Z}_2$ as a building block, a 3D crystal can be characterized by a triplet of 2D topological numbers for the three crystal orientations, respectively. In such a way, one can extend the topological classes from 2D to 3D [23]. In three dimensions, the topological insulators are characterized by four independent $\mathbb{Z}_2$ invariants $\nu_0(\nu_x \nu_y \nu_Z)$ [13, 24]. Here ν_0 is the total $\mathbb{Z}_2$ number and the $\nu_{x,y,z}$ are the 2D $\mathbb{Z}_2$ numbers along the x, y, z directions. The last three weak indices are related to the parity of the band structure at the high symmetry points of the Brillouin zone. They account for which surfaces of a topological system will host surface states. The main invariant is ν_0, a strong index which lets one classify materials into strong ($\nu_0 = 1$) and weak ($\nu_0 = 0$) topological insulators. In weak topological insulators (for example vacuum ($\nu_0 = 0$)), the Fermi circle encloses an even number of Dirac cones in their Fermi surface and they are not topologically protected. However, strong 3D-TIs ($\nu_0 = 1$) are characterized by an odd number of Dirac cones enclosed by the Fermi circle, so at least one Dirac cone will be uncoupled from others, allowing for protected TSSs with special spin texture against disorder by TR symmetry.

In this thesis, two strong 3D-TI materials such as bismuth selenide (Bi_2Se_3) and bismuth antimony telluride ($(Bi_{1-x}Sb_x)_2Te_3$) with invariants (1;0,0,0) were used. Bismuth selenide is a layered van der Waals material belonging to the bismuth dichalcogenides group. The layers are arranged along the *c*-axis direction in a sequence of five covalently bonded atomic layers (Se-Bi-Se-Bi-Se), which form a quintuple layer (QL). One unit cell consists of three QLs, where van der Waals forces bond adjoining QLs (Figure 1.2a). Bi_2Se_3 has a rhombohedral crystal structure, with lattice parameters a and c of 4.143 and 26.636 Å, respectively [6]. A material very similar to Bi_2Se_3 is $(Bi_{1-x}Sb_x)_2Te_3$ (BST) (Figure 1.2b). BST is an alloy of Sb_2Te_3 and Bi_2Te_3 and is described as Bi-doped Sb_2Te_3. Sb_2Te_3 and Bi_2Te_3 have the same crystal structure and close lattice parameters [25]. It opens up the possibility of making a mixed compound without any added difficulties due to strain [25].

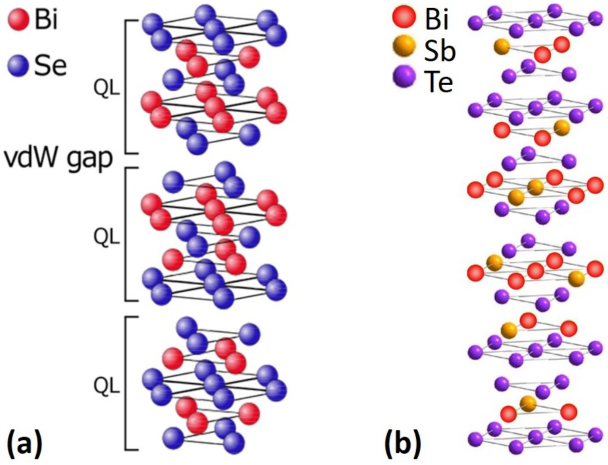

Figure 1.2: Crystal structure of (a) Bi_2Se_3 and (b) $(Bi_{1-x}Sb_x)_2Te_3$, where the Bi atoms are partially substituted by Sb. Adapted from [25, 26].

The non-trivial topology of these TIs manifested in the existence of gapless metallic surface states. These topological states are protected against strong localization by time-reversal symmetry and host Dirac-like fermions, whose spin and momentum are locked to each other. These compounds have a relatively large bulk band gap ($\sim$ 300 meV) and a single TSS per surface, making them an excellent platform for the experimental study of topological phases. With the spin-orbit coupling effect considered, the band structure of Bi_2Se_3 exhibits an inversion at the Γ point with the Dirac point well separated from the bulk valence band (BVB) and bulk conduction band (BCB), as shown in Figure 1.3a [27]. The band structure of BST can be engineered by changing the stoichiometry of the material. By increasing the ratio of bismuth to antimony, the Fermi level is shifted up while the Dirac cone shifts down towards the valence band. For pure Bi_2Te_3 it is predicted that the Fermi level is positioned in the conduction band (due to the electron-type bulk carriers induced by Te vacancies), while the Dirac point (DP) is in the valence band (Figure 1.3b). On the other side, for Sb_2Te_3 it is predicted that the DP lies within the bulk gap, while the Fermi level is in the BVB (due to the hole-type bulk carriers induced by Sb-Te anti-site defects) (Figure 1.3c) [28]. Ideally, by mixing the two compounds one can simultaneously achieve charge compensation and tune the position of the DP. For $(Bi_{1-x}Sb_x)_2Te_3$ with a Sb content of $x = 0.88$, both the Dirac point and the Fermi level are predicted to be in the bulk energy gap [25].

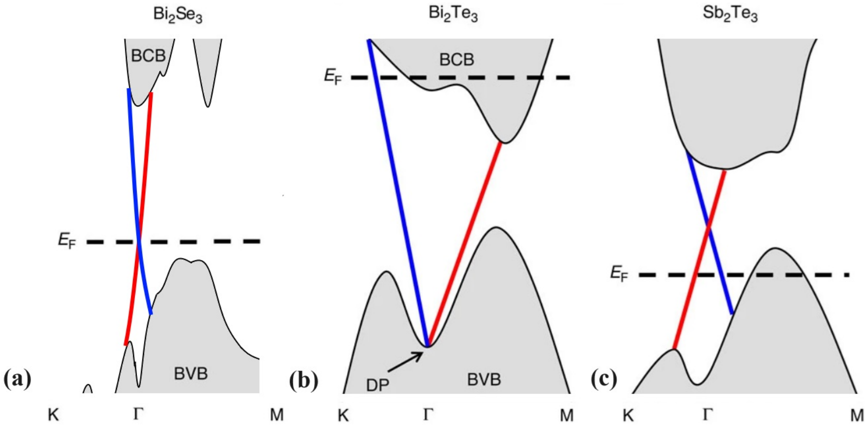

Figure 1.3: Schematic of the band structure of Bi_2Se_3 (a), Bi_2Te_3 (b) and Sb_2Te_3 (c) based on theoretical calculations and ARPES experiments. Adapted from [25, 27, 28]. The BVB and BCB are the bulk valence band and bulk conduction band, respectively. The Dirac Point (indicated DP) appears at the high symmetry Γ-point; two other high symmetry points K and M are indicated. E_F denotes the position of the Fermi level, and the two colours in the Dirac cone indicate the spin coupling to the momentum.

2 Quantum transport

Quantum transport measurements are a powerful method for studying the physics of TSSs of 3D-TIs, despite the presence of a bulk conductivity. For example, Shubnikov-de Haas, Aharonov-Bohm and Altshuler-Aronov-Spivak oscillations, universal conductance fluctuation and weak anti-localization phenomena allow the investigation of the unique properties of spin-helical Dirac fermions.

The basics of quantum transport focused on the different types of quantum interferences and energy quantization effects are introduced in this chapter.

2.1 Magnetotransport

For the actual transport measurements, samples of two geometric shapes are usually used: narrow Hall bars geometry or nearly square/circular van der Pauw configuration (Figure 2.1). In both types of samples, the Hall voltage is developed perpendicular to the current and the applied magnetic field. Using these sample geometries, the longitudinal (parallel to the current direction) and transverse (perpendicular to the current direction) resistances R_{xx} and R_{xy} can be determined. These two quantities allow to analyse the characteristics of the material from which the sample is made.

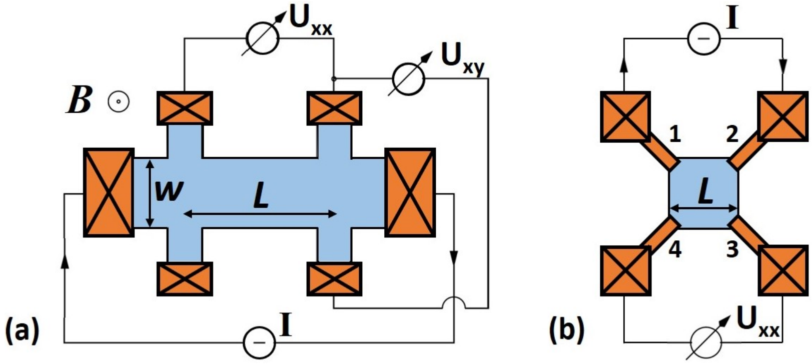

Figure 2.1: Schematic depiction of a four-probe measurement of the longitudinal R_{xx} and transverse R_{xy} resistances.

In the absence of a magnetic field, an electric field $\vec{E}$ accelerates the charges, resulting in a current in the direction of $\vec{E}$. A well-known equation that describes how current flows under the influence of an electric field is called Ohm's law [29]:

$$\vec{j} = \sigma\vec{E} \text{ or } \vec{E} = \rho\vec{j}, \tag{2.1}$$

where vector $\vec{j}$ is the current density, parallel to the flow of charges, and the proportionality constants σ and ρ are the conductivity and resistivity, respectively. If a uniform current I flows through a sample of length L and cross-sectional area S (Figure 2.1a), the current density is equal to $j = I/S$. Since the potential drop along the sample is $U = EL$, then Eq. (2.1) can be re-written as $U = \dfrac{I\rho L}{S}$, and hence $R = \dfrac{\rho L}{S}$.

In the presence of a magnetic field, in addition to current j_x flowing in the sample due to the electric field E_x (x-direction), the Lorenz force acts on the electrons leading to their deflection in the y-direction. Thus, the electrons accumulate on the side of the sample, and consequently, an electric field E_y builds up in the y-direction. At the equilibrium state, the Coulomb (electrostatic) forces of this transverse field E_y (also called the Hall field) are balanced by the Lorenz force, and current flows only in the x-direction. As mentioned above, two quantities such as the ratio of the field along the sample E_x to the current density j_x (called magnetoresistance $\rho_{xx} = E_x/j_x$) and the transverse field E_y can be extracted by performing measurements in a magnetic field. Since E_y is balanced by the Lorenz force, it is also proportional both to the applied magnetic field B and to the current along the sample j_x. Thus, the ratio E_y/j_xB is known as the Hall coefficient ρ_{xy} or R_H.

To calculate the magnetoresistance and Hall coefficient, the current densities j_x and j_y in the presence of electric (with components E_x and E_y) and magnetic (applied perpendicularly to the sample) fields need to be found. So, the equation of electron motion under an external Lorentz force $\vec{F} = -e\left(\vec{E} + \vec{v} \times \vec{B}\right)$ acting on each electron, can be expressed as [29]:

$$\frac{d\vec{p}}{dt} = \vec{F} - \frac{\vec{p}}{\tau}, \tag{2.2}$$

where $\vec{p}$ is the momentum of the electron and τ is the relaxation time. The Lorentz force is not the same for each electron, because it depends on the electron velocity $\vec{v}$. Therefore, the force in Eq. (2.2) can be replaced by the average force $\langle F\rangle$ per electron. Considering $\langle p\rangle = m\langle v\rangle$, with $\langle p\rangle$ and $\langle v\rangle$ are averaged momentum and velocity per electron, Eq. (2.2) can be written:

$$\frac{d}{dt}\langle p(t)\rangle = -e\left(E + \frac{\langle p(t)\rangle}{m} \times B\right) - \frac{\langle p(t)\rangle}{\tau}. \tag{2.3}$$

In the equilibrium state the current is independent of time $\left(\frac{d}{dt}\langle p(t)\rangle = 0\right)$, and Eq. (2.3) for p_x and p_y components will take the form:

$$\begin{aligned} 0 &= -eE_x - \omega_c p_y - \frac{p_x}{\tau} \\ 0 &= -eE_y + \omega_c p_x - \frac{p_y}{\tau}, \end{aligned} \tag{2.4}$$

where $\omega_c = \frac{eB}{m}$ is cyclotron frequency. Multiplying the Eqs. (2.4) by $-n_e e\tau/m$ and introducing the current carrier density as $j = -en_e v$ one can obtain:

$$\begin{aligned} \sigma_0 E_x &= \omega_c \tau j_y + j_x \\ \sigma_0 E_y &= -\omega_c \tau j_x + j_y, \end{aligned} \tag{2.5}$$

where $\sigma_0 = \frac{n_e e^2 \tau}{m}$ is the Drude conductivity. Since the Hall field E_y requires that there be no transverse current, by setting j_y to zero in the second Eq. of (2.5) one can find:

$$E_y = -\left(\frac{\omega_c \tau}{\sigma_0}\right) j_x = -\left(\frac{B}{n_e e}\right) j_x. \tag{2.6}$$

Thus, the Hall coefficient is

$$R_H = \frac{E_y}{j_x B} = -\frac{1}{n_e e}. \tag{2.7}$$

It can be found that the Hall coefficient depends only on the properties of the material such as charge (electrons/holes) and concentration of the conducting carriers. The Hall coefficient does not depend on the scattering time τ and is insensitive to scattering processes occurring in the material.

Considering that $j_y = 0$, from the first Eq. of (2.5) one can recognise the formula of Ohm's law (Eq. (2.1)), where the conductivity is independent of an applied magnetic field. However, in strong magnetic fields, electrons under the influence of the Lorentz force form closed orbits (cyclotron radius r_c becomes smaller than the electron mean free path l_e, in order to prevent its scattering inside the cyclotron orbit). As a result, a large number of closed loops are formed between the scattering centres interfering with each other, which leads to a quantization of the electronic states when a strong perpendicular magnetic field is applied.

The dynamics of electrons in a trivial 2DEG at low temperature can be described by the Schrödinger equation (called the single-band effective mass equation, due to the fact that only the lowest sub-band ($n = 1$) is occupied and the higher sub-bands do not play a significant role) [30]:

$$\left[E_n + \frac{(i\hbar\nabla + eA)^2}{2m^*} + U(x,y)\right]\Psi(x,y) = E\Psi(x,y)\,, \tag{2.8}$$

where $U(x,y)$ is the potential energy due to space-charge, A is the vector potential and m^* is the effective electron mass. In the absence of a magnetic field, the energy eigenstates can be obtained from the eigenstates of wave function $\Psi(x,y)$, setting $U(x,y) = 0$ and $A = 0$:

$$E = E_n + \frac{\hbar^2}{2m^*}\left({k_x}^2 + {k_y}^2\right). \tag{2.9}$$

In a 2D system with dimensions L_x and L_y, the electrons have the wave numbers $k_x = n\frac{2\pi}{L_x}$ and $k_y = n\frac{2\pi}{L_y}$. Every state in 2D $k(k_x, k_y)$-space is attributed to area S:

$$\frac{2\pi}{L_x} \times \frac{2\pi}{L_y} = \frac{4\pi^2}{S}. \tag{2.10}$$

All states with energy $E_F = \frac{\hbar^2 k^2}{2m^*}$ are enclosed by a circle with radius $k = \left|\vec{k}\right|$ in k-space and area πk^2. Thus, the total number of states Z belonging to the energy E_F is:

$$Z = \frac{\pi k^2}{4\pi^2/S} = \frac{Sk^2}{2\pi} = \frac{m^* S E_F}{2\hbar^2} \cdot g_s g_v, \tag{2.11}$$

where g_s and g_v are the spin and valley degeneracy factors, respectively. Here $g_s = 2$ according to Pauli's principle, which describes the possibility of occupying every state with two electrons of opposite spin $s = \pm\frac{1}{2}$. The number of electrons that are allowed to occupy a certain area is $Z_s = Z/S$. Thus, the density of states $D_n(E)$ at energy E_n in sub-band n can be calculated by taking a derivative:

$$D_n(E) = \frac{dZ_s}{dE_n} = g_s g_v \frac{m^*}{2\pi\hbar^2} = const. \tag{2.12}$$

If the number of electrons is large enough to start filling an additional sub-band, a jump in the density of states occurs (Figure 2.2a). Since it was assumed that only the first sub-band is occupied, the obtained constant density of states $D_n(E)$ will be used for all considered energies. Thus, the charge carrier density per unit area reads as:

$$n_e = \int_0^{E_F} D_n(E)dE = g_s g_v \frac{m^*}{2\pi\hbar^2} E_F. \tag{2.13}$$

However, in high magnetic fields, due to quantum interference of the wave functions of electrons moving along closed cyclotron loops, the step-like density of states (Figure 2.2a) breaks down into a sequence of quantized energy eigenvalues (spaced by $\hbar\omega_c$) called Landau levels (LLs) (Figure 2.2b). The total energy of electrons can be written as:

$$E = E_n + \hbar\omega_c \left(n + \frac{1}{2}\right), \tag{2.14}$$

where n is a new quantum number called the LL index.

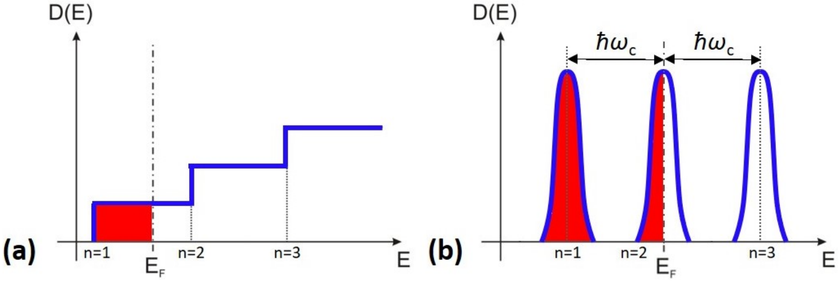

Figure 2.2: (a) Density of states (DOS) of a 2DEG without a magnetic field. The step-like increase in the onset of different sub-bands is shown by the blue line. The red area indicates occupied states at a given Fermi energy. (b) Conversion of DOS to Landau levels with energy difference $\hbar\omega_c$ in strong magnetic fields.

In the ideal case, the density of states peaks are δ-functions, however in practice, scattering processes and potential fluctuations in the sample broaden them in energy. Since the LLs are spaced homogeneously with energetic difference $\hbar\omega_c$ one may calculate the number of states in every LL, also called degeneracy:

$$N_L = D_n\left(E\right)\hbar\omega_c = g_s g_v \frac{m^*\hbar\omega_c}{2\pi\hbar^2} = g_s g_v \frac{m^*\hbar e B}{2\pi\hbar^2 m^*} = g_s g_v \frac{eB}{h} = g_s g_v \frac{B}{\phi_0}, \tag{2.15}$$

where $\phi_0 = h/e$ is the fundamental flux quantum. The Eq. (2.15) results in the fact that for each flux quantum there is one state available in each LL. One can say that the electrons perform their cyclotron motion around a flux quantum. The assumption that the flux quanta are distributed homogeneously over the sample leads to a uniform charge carrier distribution for a completely filled LL. For an arbitrary number of charge carriers n_e, a certain number of LLs will be filled:

$$\nu = \frac{n_e}{N_L} = \frac{1}{g_s g_v} \cdot \frac{n_e h}{eB}. \tag{2.16}$$

Since the energies of Landau levels depend on changes in a magnetic field, the resistivity ρ_{xx} undergoes one oscillation cycle when the Fermi energy moves from the centre of one Landau level to the next LL. An increase in a magnetic field leads to two effects: a linear increase in the energy states separation $\hbar\omega_c$ between two LLs and a linear increase in the degeneracy of the LLs according to Eq. (2.15). Consequently, this results in a redistribution of electrons between LLs in order to occupy the most energetically favourable states. The evolution of the DOS from a constant (at $B = 0$) to the spectrum of Landau levels with increasing magnetic field is shown in Figure 2.3.

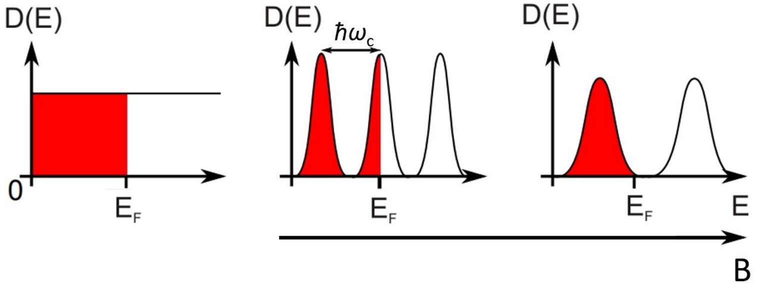

Figure 2.3: Evolution of the DOS of a 2DEG in an increasing magnetic field.

Since the charge carrier density and the number of occupied states below the Fermi energy are constant, further increasing B will cause LL to exceed Fermi energy. Thus, as B increases, E_F will quickly move from an almost empty LL to the next filled LL, since the DOS at the edges of the LL is very small compared to the centre. Once this LL is empty, E_F will move to the highest occupied state of the next underlying LL and move upwards again, until that LL is also depleted. This idealized mechanism (Figure 2.3) is valid for a δ-shaped LL. However, in real samples LLs broadening smears out the highly variable DOS at E_F, as LLs cross E_F. Therefore, whenever LL is full and E_F is between two LLs, a minimum of ρ_{xx} will be observed. Thus, ρ_{xx} will oscillate as a magnetic field changes. These oscillations in longitudinal resistivity are called Shubnikov-de Haas (SdH) oscillations.

The distance between i and i+1 resistivity minima can be found from Eq. (2.15), assuming that the given n_e is constant:

$$\begin{aligned} n_e = i \cdot N_L = i \cdot g_s g_v \cdot \frac{eB_i}{h} &\Longrightarrow \frac{1}{B_i} = \frac{i g_s g_v e}{h n_e} \\ n_e = (i+1) \cdot N_L = (i+1) \cdot g_s g_v \cdot \frac{eB_{i+1}}{h} &\Longrightarrow \frac{1}{B_{i+1}} = \frac{(i{+}1) g_s g_v e}{h n_e}. \end{aligned} \tag{2.17}$$

Then,

$$\Delta\left(\frac{1}{B}\right) = \frac{1}{B_{i+1}} - \frac{1}{B_i} = g_s g_v \cdot \frac{e}{hn_e}. \tag{2.18}$$

It can be concluded that the Shubnikov-de Haas oscillations are periodic in the $1/B$ field. The SdH frequency is then defined by:

$$f_{SdH} = \frac{1}{\frac{1}{B_{i+1}} - \frac{1}{B_i}} = n_e \cdot \frac{h}{g_s g_v \cdot e}. \tag{2.19}$$

Previously, 2D-like SdH oscillations accompanied by a quantized Hall effect were observed in magnetotransport measurements performed in highly doped $n-$type Bi_2Se_3 samples [31]. It was shown, that observed 2D magnetotransport and QHE are attributed not to the topological surface states, but to the bulk of the sample behaving as many parallel 2D electron systems (Figure 2.4).

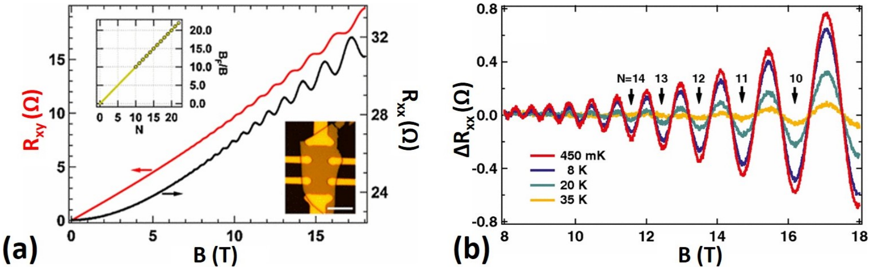

Figure 2.4: (a) Magnetotransport measurements of high-quality exfoliated single-crystalline Bi_2Se_3 flake (in the bottom inset), performed at $T = 450$ mK. The black and red lines correspond to four-terminal longitudinal resistance R_{xx} and Hall resistance R_{xy} as functions of a perpendicular magnetic field, respectively. The top inset shows the positions of the observed minima in $R_{xx}(B)$, plotted against the assigned LL indices N. (b) Shubnikov-de Haas oscillations $\Delta Rxx(B)$, extracted from $R_{xx}(B)$ by subtracting a polynomial background at different temperatures. Arrows label selected LL indices. Adapted from [31].

The observed results have important implications for 3D-TI transport studies, because they provide a general caution that observing 2D transport behaviour does not necessarily indicate the TI surface states. The main challenge is associated with extracting 2D surface states transport from measurements of 3D samples, whose bulk is often conductive. It is important to know other (non-TI surface states) sources of carriers in the TI materials that could also demonstrate 2D transport characteristics. Thus, in addition to magnetoresistance and Hall measurements, the key task of distinguishing and separating surface state transport from bulk carriers can be solved by performing a full set of analyses, including Aharonov-Bohm and Altshuler-Aronov-Spivak effects, electrostatic Fermi energy tuning by gating, as well as weak anti-localization phenomenon investigation.

2.2 Transport regimes

Transport in electronic systems can be classified by relating its size to some specific characteristic length scales (l_e and L_φ) that determine how carriers propagate through the sample. The electron mean free path l_e is a measure of the distance between subsequent scattering events. The phase-coherence length L_φ is the relevant length scale, which determines if phase-coherent transport can be observed in electronic systems. It is a measure of the distance where an electron propagates coherently before its phase becomes randomized. At low temperatures, the phase-coherence length can be larger than the elastic mean free path ($L_\varphi > l_e$) [32]. By comparing l_e and L_φ with the dimensions L and w of the sample, different transport regimes can be classified (Figure 2.5).

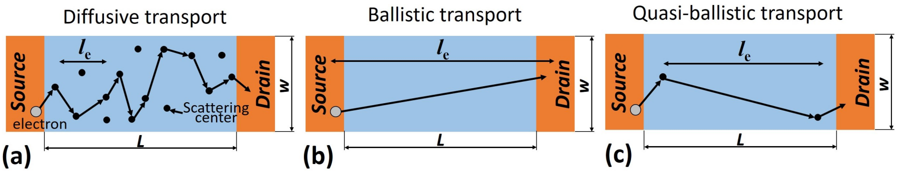

Figure 2.5: Schematic illustration of the different transport regimes: (a) a diffusive conductor ($l_e < L, w$), (b) a ballistic conductor ($L, w < l_e$), (c) a quasi-ballistic conductor ($w < l_e < L$). In the diffusive transport regime, many scattering events occur while the electron crosses the sample. In the ballistic regime, the electron crosses the sample without any elastic scattering event. Boundary scattering and internal impurity scattering (black dots) are equally important and can be present in the quasi-ballistic regime.

For the case where the mean free path is smaller than the dimensions of the sample ($l_e < L, w$), many scattering events occur, while the electrons propagate through the structure. The carriers are moving randomly (diffusively) through the sample (Figure 2.5a) [33]. If the phase-coherence length L_φ is shorter than the mean free path l_e, the transport is considered classical. In contrast, if $L_\varphi > l_e$, then quantum effects due to the wave nature of electrons can be expected. This diffusive regime is called the quantum regime [32]. In case if l_e is larger than the dimensions of the sample ($L, w < l_e$), the movement of electrons throughout the system occurs without any scattering; this regime is called ballistic (Figure 2.5b). One can distinguish an intermediate quasi-ballistic regime, where one of the system's dimension is shorter than l_e, while the other is still longer than l_e and diffusive ($w < l_e < L$) (Figure 2.5c).

2.3 Phase-coherent transport

Interference effects of electron waves due to phase-coherent transport can be seen even in large samples, where the phase coherence length is much smaller than the dimensions of the sample. These quantum phenomena can provide a lot of information on the fundamental properties of the quasiparticles.

According to the classical approach to charge transport in a disordered conductor, electrons must diffuse from point r to point r' along an extremely complex diffusion path (called the Feynman path). Some of these electron trajectories may contain closed loops (Figure 2.6). Each Feynman path can be expressed by its own wave function, and the total conductance of the conductor is determined by the wave functions superposition of all paths [34]. If the sample size is large enough, the averaging of all the quantum interferences caused by the Feynman paths will be zero. At low temperatures and small length scales, electrons interfere coherently with each other, slightly changing the probability of an electron to cross the sample (the interference can no longer be eliminated by the Feynman path averaging). As a result, the conductance of the sample is affected by interference effects, and quantum corrections to the classical transport model must be taken into account. The typical length scale at which these interference effects are significant is the phase coherence length L_φ, which is the typical length over which the electronic phase remains deterministic.

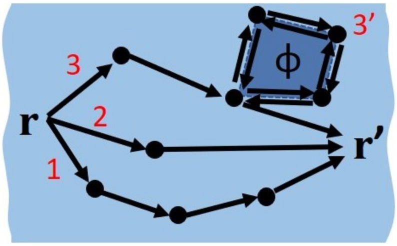

Figure 2.6: Schematic view of a classical approach to diffusive transport of electrons, propagating from point r to r'. The red numbers indicate possible electron propagation trajectories. The trajectory $3'$ represents a closed loop. In the presence of a magnetic field, the closed trajectory $3'$ owns magnetic flux ϕ penetrating this loop.

According to the Feynman path description of electron diffusion, the probability $P(r, r', t)$ for motion from point r to point r' in a time t consists of the squared absolute value of the sum of probability amplitudes ($A_i = |A_i| e^{i\varphi_i}$) for each trajectory [33, 34]:

$$P\left(r,r',t\right)=\left|\sum_{i}A_i\right|^2=\sum_{i}\left|A_i\right|^2+\sum_{i\neq j}A_iA_j^*, \tag{2.20}$$

where the first term on the right-hand side of Eq. (2.20) corresponds to the classical diffusion probability, while the second term accounts for quantum interference. If the beginning and end points of path r and r' are different, then the interference term averages out (in the diffusive transport regime), because different trajectories have uncorrelated phases. In case r and r' coincide (closed loop), the amplitudes A^+ (for clockwise propagation around the closed loop) and A^- (counterclockwise propagation) of two time-reversed returning trajectories are equal ($A^+=A^-\equiv A$). Since $\varphi^+=\varphi^-$:

$$\begin{gathered}P\left(r,r',t\right)=\left|\sum_{i}A_i\right|^2=\\=\left|A^++A^-\right|^2=\left|A^+\right|^2+\left|A^-\right|^2+2Re\left(A^+A^{-*}\right)=4\left|A\right|^2,\end{gathered} \tag{2.21}$$

which is then twice higher than for the non-phase-coherent (classical) transport, where the probability is $\left|A_1\right|^2+\left|A_2\right|^2=2\left|A\right|^2$. The enhanced probability of return to the point of departure (origin point) implies that the net current through the sample is reduced. Hence, the carriers are localized within the loop. Such localization does not depend on the size of the loop as long as its length is smaller than the phase coherence length L_φ. This effect is called weak localization (WL) and "it is one of those unique cases where the superposition principle of quantum mechanics leads to observable consequences at the macroscopic level" [33, 35].

2.4 Weak localization and weak anti-localization

The enhanced propagation probability of coherently back-scattered (returning to the starting point) electrons leads to a drop in conductivity (increase in resistivity) due to coherence effects. A larger number of scattering centres increase the probability of back-scattering of the electrons. The magnitude of the weak localization correction $\Delta\sigma$ to the classical (Drude) conductivity σ_0 can be obtained quantitatively, and it is proportional to the probability of return to the point of departure. Since $\Delta\sigma$ is assumed to be a small correction, the probability can be estimated by solving the classical diffusion equation. The probability density of returning to the origin $r'=r=0$:

$$P\left(r,r',t\right)=\frac{1}{\left(4\pi Dt\right)^{d/2}}, \tag{2.22}$$

where d denotes a d-dimensional space, $D = \frac{1}{d}{v_F}^2\tau$ is the diffusion constant, v_F is the Fermi velocity and τ is the elastic scattering time. The weak localization correction is given by the time integral of the return probability:

$$\Delta\sigma = -\frac{2\hbar}{m^*}\sigma_0 \int\limits_0^\infty dt P\left(r, r', t\right)\left(1 - e^{-t/\tau}\right)e^{-t/\tau_\varphi}. \tag{2.23}$$

The correction is negative because the conductivity is reduced due to coherent back-scattering. Since the electron can be considered as a wave packet with a linear extension determined by Fermi wavelength $\lambda_F = 1/k_F$, in d-dimensional space this electron will sweep out the volume $\lambda_F^{d-1} v_F dt$ over the time interval $[t, t + dt]$. Thus, the factor $(\hbar/m^*) \propto \lambda_F^{d-1} v_F$ follows in the path integral formalism from the area covered by a wave packet of width λ_F^{d-1} and length $v_F dt$. The factor $\left(1 - e^{-t/\tau}\right)$ indicates that the electron is elastically scattered (at least once), and the factor e^{-t/τ_φ} reveals that the phase of the electrons is preserved up to the phase breaking time τ_φ (after which the electrons lose the phase coherence as a result of inelastic scattering).

In total, the correction to the conductance in d-dimensional space for $d = 1, 2, 3$ can be expressed as [33, 36]:

$$\Delta\sigma = \begin{cases} -\frac{2\hbar}{m^*}\sigma_0 \int\limits_0^\infty dt w^{-1} \left(4\pi D t\right)^{-1/2}\left(1 - e^{-t/\tau}\right)e^{-t/\tau_\varphi} = -\frac{e^2}{2\pi\hbar}\frac{L_\varphi}{w}\left[1 - \left(1 + \frac{\tau_\varphi}{\tau}\right)^{-1/2}\right] \\ -\frac{2\hbar}{m^*}\sigma_0 \int\limits_0^\infty dt \left(4\pi D t\right)^{-1}\left(1 - e^{-t/\tau}\right)e^{-t/\tau_\varphi} = -\frac{e^2}{2\pi^2\hbar}\ln\left(1 + \frac{\tau_\varphi}{\tau}\right) \\ -\frac{2\hbar}{m^*}\sigma_0 \int\limits_0^\infty dt \left(4\pi D t\right)^{-3/2}\left(1 - e^{-t/\tau}\right)e^{-t/\tau_\varphi} = -\frac{e^2}{2\pi^2\hbar}\frac{1}{L_\varphi}\left[\left(1 + \frac{\tau_\varphi}{\tau}\right)^{-1/2} - 1\right]. \end{cases} \tag{2.24}$$

Since the return probability depends on the dimensionality d, the functions $\Delta\sigma$ for various d are different. The characteristic length which is compared with the size of a particular sample is the phase coherence length L_φ. Depending on whether the return probability $P\left(\tau_\varphi\right)$ on the time scale τ_φ is determined by 3D, 2D or 1D diffusion, one can define 3D, 2D or 1D weak localization, respectively. In terms of the phase coherence length $L_\varphi = \sqrt{D\tau_\varphi}$, the criterion for the dimensionality is that 2D weak localization occurs for $L_\varphi \ll w$ and 1D weak localization for $L_\varphi \gg w$. In the 1D-case, diffusion is effectively reduced to one dimension, so an additional factor of $1/w$ must be added to the return probability [33]. The conditions for implementing dimensionality reduction are rather mild, since the determination of space configuration operates with scale L_φ, while the diffusion takes place in scale l_e. For example, for nanoribbons/nanowires or thin films with thickness larger than l_e but smaller than L_φ, the diffusion process remains 3D-dimensional. An electron in the wire/film can move between two elastic scattering events along an arbitrary direction, including the direction along the wire/film normal. However, the quantum correction for such nanostructures is determined assuming that d =2 [37].

The lower the dimensions, the more the interference effect is pronounced. A comparison of the 1D and 2D cases reveals that the weak localization correction to the conductance is much larger for the 1D case. For instance, for the typical 2D electron gas (2DEG) with $\mu_e = 10^6$ cm^2/V·s at $n_e = 3 \times 10^{11}$ cm^{-2}, a conductance correction of less than 0.1% would be expected, while for the 1D nanowire based on this 2DEG with parameters w = 200 nm and a phase-breaking time $\tau_\varphi = 10^{-10}$ s the correction is $\approx$ 6% [32]. The maximum conductance correction in a narrow channel is thus of order e^2/h, independent of the properties of the sample. This "universality" is at the origin of the phenomenon of universal conductance fluctuation (UCF), which is discussed in the next section.

In the presence of a magnetic field, time-reversal invariance breaks, which leads to the development of the phase difference φ between A^+ and A^- probability amplitudes. This phase (called the Aharonov-Bohm phase) results from the fact that the canonical momentum $\vec{p} = m\vec{v} - e\vec{A}$ of an electron in a magnetic field contains the vector potential $\vec{A}$. Thus, during propagation around a closed loop in clockwise (+) and counterclockwise (−) directions, a phase difference occurs [33]:

$$\varphi = \frac{1}{\hbar}\oint_{+} \vec{p^{+}} d\vec{l} - \frac{1}{\hbar}\oint_{-} \vec{p^{-}} d\vec{l} = \frac{2e}{\hbar}\int \left(\nabla \times \vec{A}\right) dS = \frac{2eBS}{\hbar} = \frac{2S}{{L_m}^2} = 4\pi\frac{\phi}{\phi_0}. \quad (2.25)$$

Here, $\vec{A}$ is the vector potential of the magnetic field, S is the enclosed cross-surface of the loop, $\phi = B \cdot\ S$ is the total magnetic flux through the loop, $L_m = \sqrt{\hbar/eB}$ is the magnetic length, and $\phi_0 = h/e$ is the fundamental magnetic flux quantum.

Since many enclosed trajectories with a wide distribution of loop areas contribute to the weak localization effect, depending on the size of these loops, different phase shifts $\Delta\varphi$ develop when a magnetic field is applied. If a magnetic field is increased starting from zero, the constructive interference is destroyed first for the largest loops ($S \gtrsim {L_m}^2$). Finally, if a magnetic field is sufficiently large, the phase difference will be randomly distributed between the ensemble of loops. On average, the degree of localization decreases with the increase of a magnetic field, resulting in a continuous decrease of the resistance [32].

In analogy to the phase coherence length $L_\varphi = \sqrt{D\tau_\varphi}$ with phase-breaking time τ_φ, the characteristic magnetic relaxation time τ_B related to L_m can be estimated via the relationship $L_m \sim \sqrt{D\tau_B}$. With a sufficiently strong magnetic field B_φ, the magnetic effect replaced the intrinsic scattering ($\tau_B \gtrsim \tau_\varphi$) and became the limiting factor of WL. The weak localization effect can be studied experimentally by measuring the positive magnetoconductance peak associated with its suppression by a magnetic field (Figure 2.7). The significance of such experiments relies on the possibility of direct determination of the electron phase coherence length L_φ using a famous Hikami-Larkin-Nagaoka (HLN) equation quantitatively describes this process [38]:

$$\sigma\left(B\right)-\sigma\left(0\right)=\alpha\frac{e^2}{2\pi^2\hbar}\left[\psi\left(\frac{1}{2}+\frac{B_\varphi}{B}\right)-\ln\left(\frac{B_\varphi}{B}\right)\right], \tag{2.26}$$

where α is a pre-factor (for the case when neither spin-orbit interaction nor magnetic scattering occurs $\alpha = 1$), $\psi\left(x\right) \approx \ln\left(x\right) - 1/x$ is the digamma function, and $B_\varphi = \dfrac{\hbar}{4e{L_\varphi}^2} = \dfrac{\hbar}{4eD\tau_\varphi}$ is the inelastic scattering strength expressed via the dimension of a magnetic field.

So far, the WL mechanism has been observed for systems with electrons in which the spin orientation is conserved. However, for a material with strong spin-orbit coupling, where spin is fully locked with momentum, the situation is completely opposite. The time-reversed scattering loops are equivalent to moving an electron on the Fermi surface by one cycle. As a result, at zero-field the electron picks up the Berry phase $\gamma_n = \pi$ instead of 0, which leads to a destructive quantum interference that suppresses the back-scattering and enhances the conductivity. This phenomenon is called weak anti-localization (WAL). In contrast to the WL effect, an enhanced conductivity is found at $B = 0$. However, if a magnetic field is applied then the WAL effect is gradually suppressed (Figure 2.7a,b).

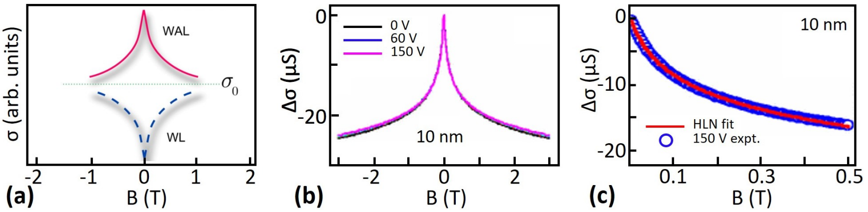

Figure 2.7: (a) Schematic view of the conductance changes in a magnetic field. A weak localization (WL) downward cusp is presented by the blue dashed line. A weak anti-localization (WAL) curve shows the upward cusp (the pink line). The green line represents the Drude σ_0 (classical) conductivity. Adapted from [39]. (b) Magneto-conductivity, defined as $\Delta\sigma\left(B\right) = \sigma\left(B\right) - \sigma(0)$ of a Bi_2Se_3 single-crystalline thin film with thickness 10 nm, measured with applied gate voltages of 0, 60, and 150 V at $T = 1.8$ K. (c) Experimental data from (b) for the gate voltage of 150 V with the Hikami-Larkin-Nagaoka (HLN) fit. Adapted from [40].

The topological surface states can also be treated with the HLN theory as traditional 2D electron systems with strong spin-orbit interaction. Strong spin-orbit coupling always results in dominant WAL with a pre-factor $\alpha \approx -0.5$. If both surfaces contribute equally to the transport, this would lead to $\alpha \approx -1$ [40].

WL and WAL analysis is a very useful tool for characterizing transport properties in mesoscopic devices because it does not require a specific geometry to observe it. Since WL and WAL are not sensitive to ensemble averaging, it is very convenient to extract a quantitative value of L_φ and its temperature and magnetic field dependences, especially in large systems where all other coherence effects are averaged out.

2.5 Universal conductance fluctuations

As discussed in previous sections, quantum mechanical correlations persist over a phase coherence length L_φ, which can be much larger than the elastic mean free path l_e. Quantum interference effects lead to significant sample-to-sample fluctuations in conductance if the sample size is not much larger than L_φ. An electron is able to propagate along a certain number of paths in order to cross a fully coherent mesoscopic conductor. As mentioned above, it is possible to define different trajectories (Feynman paths) that will interfere (Figure 2.8). Among these trajectories, a limited number of paths may be found that meet again after a certain distance. The important fact is that it is necessary to take into account the absence of a specific well-defined loop geometry. If a magnetic field is applied, the paths become penetrated by a magnetic flux ϕ, and all electronic loops will contribute to the interference term with a random magnetic frequency. Since only a limited number of trajectories exist, an effective averaging out of the oscillations is prevented. Thus, the fluctuation pattern should be aperiodic (without any specific frequency). Even different samples with the same geometry and made of the same material demonstrate that each sample has a different fluctuation pattern. This is why this individual pattern of a sample is called a fingerprint.

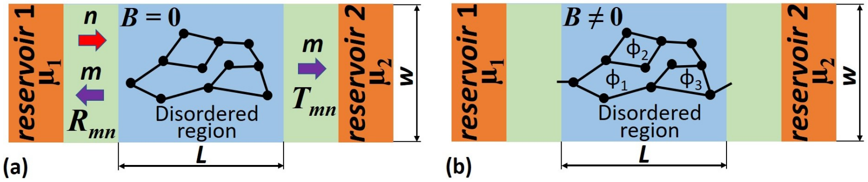

Figure 2.8: Electron trajectories in an idealized conductor connecting a disordered region (blue) to two reservoirs having electrochemical potentials μ_1 and μ_2 (orange), through ideal one-dimensional ballistic areas (green). Here, n denotes the incoming channel, while m is the outgoing channel (transmitted or reflected). In the case of applying a magnetic field (b), the loops are penetrated by magnetic flux ϕ_1, ϕ_2, ϕ_3.

The most convenient way to study the effect of fluctuation is to use the Landauer-Büttiker formalism, to relate the conductance and conductance fluctuations to the transmission probabilities of the different quantum channels.

As shown in Figure 2.8a, the conductor is connected to the reservoirs (with corresponding chemical potentials) through ideal one-dimensional (1D) ballistic areas. Assume that reservoir 1 can supply electrons to the conductor up to a maximum energy of μ_1 at zero temperature. Since inelastic scattering is prohibited within ballistic areas, electrons once injected into the conductor maintain their energy until they reach one of the reservoirs. Thus, each carrier from the ballistic area that reaches the reservoir is absorbed by the reservoir, regardless of the phase and energy of the carriers. The current injected from reservoir 1 can be expressed as:

$$I_{inj} = e\int\limits_{0}^{\mu_1} D_{1D}\left(E\right)v(E)dE = \frac{2e}{h}\mu_1, \tag{2.27}$$

where $D_{1D}\left(E\right) = 2/hv\left(E\right)$ is the density of states of a 1D system, $v(E)$ is the velocity of the electrons, and μ_1 is the electrochemical potential of reservoir 1. Part of the current supplied by reservoir 1 can be reflected back. R_{11} is defined as the reflection probability for a reflection of carriers from the ballistic area back into reservoir 1. Then, the current reflected into reservoir 1 can be written as:

$$I_R = -\frac{2e}{h}R_{11}\mu_1. \tag{2.28}$$

Moreover, electrons from reservoir 2 can be transmitted into reservoir 1. The transmission probability from reservoir 2 into reservoir 1 ($1 \leftarrow 2$) is defined as T_{12}, then the equation for the current transmitted into reservoir 1 has the form:

$$I_T = -\frac{2e}{h}T_{12}\mu_2. \tag{2.29}$$

It can be seen that the net current passing by reservoir 1 is given by Landauer-Büttiker formula [41]:

$$I = I_{inj} + I_R + I_T = \frac{2e}{h}\left[\left(1 - R_{11}\right)\mu_1 - T_{12}\mu_2\right]. \tag{2.30}$$

Since the conductor is connected on both terminals to reservoirs with the electrochemical potentials μ_1 and μ_2, the following expressions are obtained according to the Landauer-Büttiker formalism described above:

$$\begin{cases} \left(h/2e\right)I = \left(1 - R_{11}\right)\mu_1 - T_{12}\mu_2, \\ -\left(h/2e\right)I = \left(1 - R_{22}\right)\mu_2 - T_{21}\mu_1. \end{cases} \tag{2.31}$$

In absence of a magnetic field ($B = 0$), time-reversal invariance holds, so $T_{12} = T_{21} = T = 1 - R_{11} = 1 - R_{22}$. Thus, the expression for the conductance can be presented as follows:

$$G = \frac{I}{U} = \frac{Ie}{\mu_1 - \mu_2} = \frac{2e^2}{h}T, \tag{2.32}$$

here the voltage drop U is given by the difference between the electrochemical potentials divided by e: $U = (\mu_1 - \mu_2)/e$. If back-scattering is neglected ($T = 1$), the conduction through the sample is given by:

$$G = \frac{2e^2}{h}. \tag{2.33}$$

The constant value of G is a fact of the assumption that the channels are 1D$-$dimensional (the density of states and velocity in Eq. (2.27) were used for the 1D case). However, in the case of 2D or 3D systems, the total transmission probability from reservoir j to reservoir i ($i \leftarrow j$) $T_{ij} \neq 0$ and can be expressed as:

$$T_{ij} = \sum_{m,n}^{N} T_{ij,mn}, \tag{2.34}$$

where $T_{ij,mn}$ the transmission probability from n-th channel of reservoir j to m-th channel of reservoir i, and N is the total number of channels. Thus, according to the Landauer-Büttiker formalism, the total conductance with N channels is determined by the expression (the indices i, j for the reservoirs are omitted here):

$$G = \frac{2e^2}{h}\sum_{m,n}^{N} T_{mn}. \tag{2.35}$$

The Drude (classical) conductance of a diffusive conductor for a single spin and a single valley direction ($g_s = g_v = 1$) can be expressed as [33]:

$$\sigma_0 = \frac{w}{L}\frac{n_e e^2 \tau}{m^*} = g_s g_v \frac{w}{L}\frac{e^2}{h}\frac{k_F l_e}{2} = \frac{e^2}{h}\frac{\pi l_e}{2L}N, \tag{2.36}$$

where N equals to the number of transverse channels in a conductor of width w. For the case when $l_e < L$, each channel N has on average the same transmission probability given by $\frac{\pi l_e}{2L}$ according to Eqs. (2.35) and (2.36). The ensemble-averaged transmission probability does not depend on channel n or m, so the correspondence between Eqs. (2.35) and (2.36) requires [33]:

$$\langle T_{mn} \rangle = \frac{\pi l_e}{2LN}. \tag{2.37}$$

Since transmission processes in the diffusive transport regime occur via many collisions of impurities (Figure 2.8), the sequence of scattering events can be common for different channels of the conductor. However, if reflection processes are considered, it can be assumed that only a few scattering events are responsible for back-reflection, so reflections in different channels are considered uncorrelated [42]. Taking this concept for granted, reflection and transmission probabilities can be related by the current conservation law:

$$\sum_{m,n}^{N} T_{mn} = N - \sum_{m,n}^{N} R_{mn}, \tag{2.38}$$

here T_{mn} and R_{mn} denote transmission and reflection probabilities from channel n into channel m, respectively.

As mentioned above, each sample has different impurity configurations corresponding to a different Feynman path, and the interference is also different, so, the conductance G of each sample varies from each other. However, the conductance fluctuations can be averaged via some statistical distribution $\delta G = G - \langle G \rangle$, where the mean value $\langle G \rangle$ represents the ensemble averaging. The magnitude of the conductance fluctuations is characterized by its variance:

$$var\,(G) = \langle \delta G^2 \rangle = \langle (G - \langle G \rangle)^2 \rangle. \tag{2.39}$$

Taking Eqs. (2.35), (2.38) and (2.39) into account, the variance of conductance is equal to:

$$\begin{aligned} var\,(G) &= \left(\frac{e^2}{h}\right)^2 var\left(N - \sum_{m,n}^{N} R_{mn}\right) = \\ = \left(\frac{e^2}{h}\right)^2 var\left(\sum_{m,n}^{N} R_{mn}\right) &= \left(\frac{e^2}{h}\right)^2 N^2 var\,(R_{mn}) \end{aligned} \tag{2.40}$$

and it is assumed that reflections are uncorrelated and $var\,(R_{mn})$ is independent of m and n. According to the Eq. (2.40), in order to obtain the variance of G, the variance of reflection probability must be calculated first:

$$\begin{aligned} var\,(R_{mn}) &= \langle\ (R_{mn} - \langle R_{mn} \rangle)^2 \rangle = \langle {R_{mn}}^2 - 2R_{mn}\langle R_{mn} \rangle + {\langle R_{mn} \rangle}^2 \rangle = \\ &= \langle {R_{mn}}^2 \rangle - 2\langle R_{mn} \rangle \langle R_{mn} \rangle + {\langle R_{mn} \rangle}^2 = \langle {R_{mn}}^2 \rangle - {\langle R_{mn} \rangle}^2. \end{aligned} \tag{2.41}$$

By analogy to the Feynman concept for describing the probability of propagation between points r and r', as already expressed by Eq. (2.21), the probability of reflection from channel n to m for all possible paths $i (i = 1, 2, \ldots, M)$ can be expressed as the square of the total amplitude of all possible paths:

$$P_{mn} = \left| \sum_{i} A_i \right|^2, \tag{2.21}$$

where A_i denotes independent complex random variables representing the probability amplitude due to the i-th Feynman path that connects channel n to m. Assuming that the reflections are uncorrelated and neglecting terms of order unity compared with M (assuming $M \gg 1$), to calculate $var\,(R_{mn}) = \langle {R_{mn}}^2 \rangle - \langle R_{mn} \rangle^2$ one may write [43]:

$$\langle {R_{mn}}^2 \rangle = 2 \langle \sum_i |A_i|^2 \rangle^2 = 2 \langle R_{mn} \rangle^2. \tag{2.42}$$

Thus, the variance of the reflection probability is equal to the square of its average:

$$var\,(R_{mn}) = \langle {R_{mn}}^2 \rangle - \langle R_{mn} \rangle^2 = 2\langle R_{mn} \rangle^2 - \langle R_{mn} \rangle^2 = \langle R_{mn} \rangle^2. \tag{2.43}$$

Based on Eq. (2.37) and averaging of (2.38), it follows that:

$$\langle R_{mn} \rangle = \frac{1}{N}\left(1 - order\left(\frac{l_e}{L}\right)\right) \approx \frac{1}{N}, \tag{2.44}$$

where the term of order $\left(\frac{l_e}{L}\right)$ expresses the fact that as long as $l_e \ll L$ (the case for a sufficient number of scattering centres in the conductor), most of the incoming electrons are reflected into N reflecting channels (the transmission probability is small ($T_{mn} \to 0$)). So, finally one can conclude that the variance of conductance is equal to:

$$var\,(G) = \left(\frac{e^2}{h}\right)^2 N^2 var\,(R_{mn}) \approx \left(\frac{e^2}{h}\right)^2, \tag{2.45}$$

independently of l_e and L in the diffusive limit ($l_e \ll L$). This is why it is called universal conductance fluctuation (UCF). The general formula reads as:

$$\delta G = \sqrt{var\,(G)} = \frac{g_s g_v}{2\sqrt{\beta}} C \frac{e^2}{h}, \tag{2.46}$$

where g_s, g_v are spin and valley degeneracy factors, C depends on the sample geometry (actually, of its effective dimensionality), while $\beta = 1$ in a zero magnetic field and $\beta = 2$ when the magnetic field breaks time-reversal symmetry [32, 33, 42, 43].

2.6 Altshuler-Aronov-Spivak oscillations

As was shown in Section 2.4, the presence of closed loops in the conductor is responsible for reducing the resistance when a magnetic field is applied (WL effect, Figure 2.8b). However, if the shape of these enclosed loops is restricted by a fixed, well-defined geometry, the resistance may oscillate due to interference effects.

If the conductor has the shape of a ring and a magnetic flux penetrates through this ring, then observed oscillations are called Altshuler-Aronov-Spivak (AAS) oscillations.

Assuming that the conductor has a series of interconnected ring-shaped loops of approximately the same geometry, then the phase shift between time-reversed paths can be written as shown above in Eq. (2.25):

$$\varphi = 4\pi \frac{\phi}{\phi_0}, \tag{2.25}$$

and following the Eq. (2.21), the total propagation probability in a loop is given by:

$$\begin{aligned} P = \left|\sum_i A_i\right|^2 &= \left|A_1 exp\left(i2\pi\frac{\phi}{\phi_0}\right) + A_2 exp\left(-i2\pi\frac{\phi}{\phi_0}\right)\right|^2 = \\ &= 2\left|A_1\right|^2\left[(1 + cos\left(4\pi\frac{\phi}{\phi_0}\right)\right]. \end{aligned} \tag{2.47}$$

From the equation described above, one can conclude that the resistance in this type of structure should oscillate with a period of $\phi_0/2$ [32, 44].

In order to observe AAS oscillations, the phase-coherence length L_φ must be larger than the circumference of a ring. Since all time-reversed trajectories have the same phase, as long as the phase coherence length remains longer than the ring circumference, the amplitude of the AAS should not vanish, because these oscillations are insensitive to ensemble averaging. Depending on the type of material, each ring produces either a maximum or minimum at $B = 0$, depending on the absence or presence of spin-scattering. This ensures that after the summation of the contribution of each element (in the case of a series of interconnected loops), the Altshuler-Aronov-Spivak oscillations are not averaged out.

The AAS effect can be used to measure the phase coherence length L_φ, which provides information about decoherence in the system. Moreover, due to its insensitivity to ensemble averaging, AAS can be approximated very well by theoretical models. Such approximations quantify the fundamental parameter L_φ with good accuracy, similar to another type of quantum correction (also insensitive to ensemble averaging), such as weak localization.

2.7 Aharonov-Bohm oscillations

The Altshuler-Aronov-Spivak oscillations arise as a result of electron propagation along time-reversed trajectories and interference at the point of departure. In contrast to it the Aharonov-Bohm (AB) effect is based on electron waves propagating along two different branches of a ring structure and interfering on the opposite side of the ring (Figure 2.9).

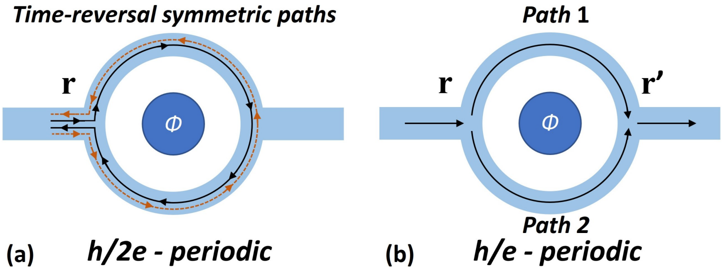

Figure 2.9: Schematic picture of a ring-shaped conductor. The ring is penetrated by a magnetic flux $\phi = BS$, where S is the surface of the ring. The interference of two time-reversed symmetrical trajectories leads to Altshuler-Aronov-Spivak oscillations ($h/2e$-periodic) as a function of a magnetic field (a). The interference of two electron waves propagating on the opposite side of the ring results in Aharonov-Bohm oscillations (h/e-periodic) as a function of a magnetic field (b).

Considering the geometry in which electrons are confined on the ring (Figure 2.9b), they will propagate along either one or the other arm of the ring. If half the circumference of the ring is smaller than the phase coherence length ($C/2 < L_\varphi$), then the electrons will propagate coherently along both arms of the ring and interfere on the other side (at point r'). Assuming a fully coherent ring ($C < L_\varphi$), then interference must be taken into account when calculating the total conductance. By analogy to the Eq. (2.25), the phase difference $\Delta\varphi$ of two electron waves propagating along the upper and the lower branches of the ring (paths 1 and 2 in Figure 2.9b) and interfering at the endpoint r' of the ring is given by:

$$\begin{aligned}\Delta\varphi = \chi_1 - \chi_2 - \frac{e}{\hbar}\int\limits_{path1} \vec{A}d\vec{l} + \frac{e}{\hbar}\int\limits_{path2} \vec{A}d\vec{l} = \\ = \Delta\chi + \frac{e}{\hbar}\oint \vec{A}d\vec{l} = \Delta\chi + \frac{e}{\hbar}\int \left(\nabla \times \vec{A}\right) dS = \Delta\chi + 2\pi\frac{\phi}{\phi_0},\end{aligned} \tag{2.48}$$

where χ_1 and χ_2 are the phases that acquire electron waves when propagating along path 1 and path 2. In contrast to the weak localization effect, the propagating paths are different and therefore not time-reversed. Since the impurity configurations on both branches are different, the accumulated phases in these branches are also different.

It can be seen from Eq. (2.48), that a phase shift of 2π is achieved if the magnetic flux is changed by the magnetic flux quantum ϕ_0. Thus, the period of Aharonov-Bohm oscillations is twice as large as the period of Altshuler-Aronov-Spivak oscillations.

In contrast to AAS, the AB effect is sensitive to ensemble averaging. Even within the same ring, the distribution of scattering centres in different arms is different, which leads to the phase difference $\Delta\chi$. Therefore, in the case of a series of rings even with the same geometry (operating as an ensemble of N incoherent rings), a different phase shift $\Delta\chi$ will be accumulated. As a result, no clear maximum or minimum (as for the AAS oscillations) is expected at $B = 0$. In addition, the amplitude of the Aharonov-Bohm oscillations decreases if the signal of many rings is averaged, since the contributions of the interferences of different rings with the same oscillation period, but with statistically distributed phase shifts $\Delta\chi$ are averaged out [32, 33, 44].

Additional information about the Aharonov-Bohm effect can be obtained by studying the temperature evolution of oscillations. In the diffusive regime, the amplitude of AB oscillations is a function of the phase coherence length and roughly scales with $T^{-1/2}$ [45]:

$$\Delta G(L_\varphi) \sim T^{-1/2}. \tag{2.49}$$

Since L_φ increases with decreasing temperature, at a certain temperature, the sample becomes fully coherent ($L_\varphi \geq C$, where C is the circumference). As a result, the AB amplitude reaches a maximum and saturates. The observation of the plateau at $L_\varphi = C$ is a way to roughly estimate L_φ. In addition, due to the relationship between L_φ and τ_φ ($L_\varphi = \sqrt{D\tau_\varphi}$), the transport regime (ballistic or diffusive) and the system dimensionality can be determined. For instance, in the absence of inelastic scattering with weak electron-electron interaction, the phase-breaking time can be estimated as $\tau_\varphi \sim \hbar/k_B T$, where k_B is Boltzmann constant, and then the diffusion constant D can be found in accordance with the experimental data [33, 45].

The observation of Aharonov-Bohm oscillations in Bi_2Se_3 nanoribbons provides important information about topological surface states. Despite the influence of bulk carriers on the overall conductance, the interaction between bulk and surface electrons does not destroy the phase coherence of surface states. Since the interference effect requires a full revolution around the perimeter of the ribbon, the robust surface states not only exist on the top and bottom surfaces, but also propagate coherently through the side walls of the nanoribbon (Figure 2.10a). The primary oscillation period corresponds to Aharonov-Bohm (h/e) quantization, while Altshuler-Aronov-Spivak oscillations (with $h/2e$ period) are suppressed in the low-magnetic-field region. The absence of the AAS effect is due to a special property of topological surface states. Electrons with opposite momentum have opposite spin polarization. For these states, back-scattering events are forbidden at $B = 0$, but are present at finite field strengths, even if the flux is an integer multiple of the flux quanta $h/2e$. Consequently, the anti-localization behaviour observed at $B = 0$ is absent for other integer multiples of flux $h/2e$, resulting in a suppression of the AAS effect (Figure 2.10b and c) [46].

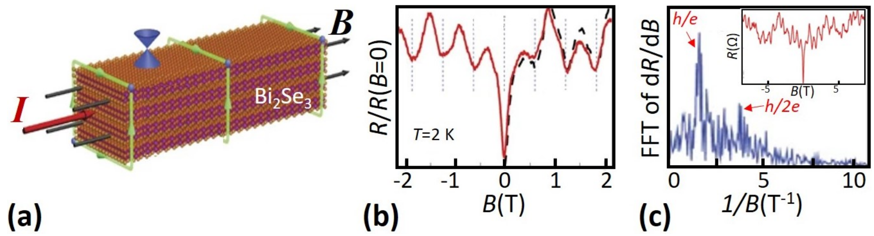

Figure 2.10: (a) Schematic picture of 2D topological surface states of a layered Bi_2Se_3 nanoribbon under a magnetic field applied along the length of the ribbon. (b) Normalized magnetoresistance of the nanoribbon as a function of a magnetic field at 2 K. Modulation of the resistance with a period $\Delta B = \phi_0 S$ is depicted by the black dotted lines corresponding to one flux quantum ($\phi_0 = h/e$) threaded through the cross-section of the nanoribbon S. (c) Fast Fourier transform of the derivative dR/dB over the entire range of magnetic field (±9 T). The locations of h/e and $h/2e$ flux quantization are labelled by the red arrows. The inset shows the magnetoresistance curve measured over the entire magnetic field range at 2 K. Adapted from [46].

Along with AB and AAS oscillations, observed in longitudinal (parallel to the length of TI nanoribbons) magnetotransport, signatures of periodic conductance fluctuation (magneto-fingerprints), associated with Aharonov-Bohm orbits, were observed in diffusive devices based on epitaxial Bi_2Se_3 thin film, which was not explicitly patterned into loops. The periodic magneto-fingerprint arises from the coherent scattering of electron waves at the step-edges of triangular terraces found on the surface of these thin film devices. This magneto-fingerprint has the characteristics expected from the conventional theory of UCF in 2D systems (Figure 2.11) [47].

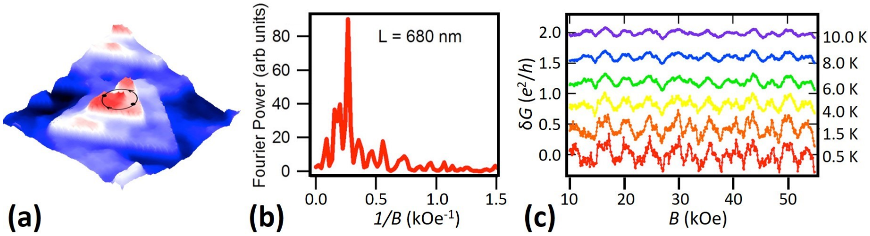

Figure 2.11: (a) Atomic force microscopy (AFM) image of a 1×1 μm^2 surface area of Bi_2Se_3 thin film, with a simplistic circular Aharonov-Bohm orbit, arising from step-edge scattering at the triangular terrace. (b) Fourier power spectrum of the magneto-fingerprint from a device with a channel length $L = 680$ nm, measured at $T = 0.5$ K. The power spectrum reveals a dominant peak associated with periodic fluctuations. (c) The magneto-fingerprint in the temperature range from 0.5 to 10 K demonstrates the reproducibility of conductance fluctuations and depicts their amplitude reducing with increasing temperature, which is consistent with standard UCF theory in a 2D system, where $L < L_\varphi$. Adapted from [47].

2.8 Quantum confinement in TI nanoribbons

In this thesis, TI nanoribbons of various geometric sizes were studied. In general, their length can reach several tens of micrometres, and the transverse dimensions (thickness and width) in some cases reach values below 10 and 80 nm, respectively. In the weak-disorder regime (when the electron phase coherence length is comparable to the circumference C of the thin/narrow nanoribbon with a rectangular cross-section (Figure 2.12)), those transverse dimensions are small enough to induce the quantum confinement of transverse-momenta k_l (schematically shown in Figure 2.12b). This effect modifies the band structure of the TSSs.

The energy dispersion of TSSs within the confined nanoribbon structure is expressed by [48, 49]:

$$E\left(k_x, k_l\right) = \pm\hbar v_F\sqrt{k_x^2 + k_l^2}, \tag{2.50}$$

where k_x is the coaxial momentum and $k_l = \dfrac{2\pi\left(l + 1/2 - \phi/\phi_0\right)}{C}$ is the confined transverse momentum. The $\hbar$ is a reduced Planck constant, v_F is Fermi velocity, and $\phi_0 = h/e$ being the fundamental magnetic flux quantum, the 1/2 term is present here due to the Berry phase in the TI. The nanoribbon dispersion is characterized by quantized transverse momentum sub-bands of quantum number $l = 0, \pm1, \pm2, \ldots$ (Figure 2.12b).

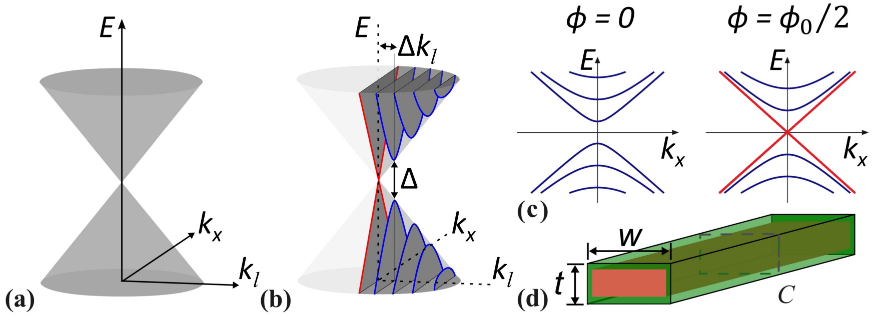

Figure 2.12: Energy dispersion relation in TI nanoribbons. The dispersion $E\left(k_x, k_l\right)$ for an ordinary nanoribbon (a) represents a Dirac cone. (b) Schematic view of the confined nanoribbon: transverse energy modes cutting the Dirac cone into sub-bands that are parallel to k_x and separated by $\Delta k_l = 2\pi/C$, where $C = 2(w + t)$, where w and t are the width and the thickness of the nanoribbon, respectively (panel (d)). (c) Schematic projection of the transverse levels in the $E\left(k_x\right)$ plane. Left: for $\phi = 0$, (π-Berry phase), all transverse sub-bands are shifted by $\Delta k_l/2$, and no transverse mode intersects the Dirac point. Right: for $\phi = \phi_0/2$, (the additional Aharonov-Bohm π phase compensates the Berry phase), linear zero-energy states crossing the Dirac point are recovered. Adapted from [48, 49].

Due to quantum confinement, the quantized transverse momentum k_l must verify periodic boundary conditions around the nanoribbon, as the wave function of the TSSs propagates around the nanoribbon. Thus, $k_l = n \times \frac{2\pi}{C}$, with C the circumference of the nanoribbon with a rectangular cross-section $C = 2(w + t)$ and $n \in \mathbb{Z}$.

The transverse modes quantization has a direct effect on their transmissions, due to the spin texture of the Dirac cone. Only for an applied magnetic flux $\phi/\phi_0 = l + 1/2$, there is a state at zero energy, because of the π-Berry phase picked up by Dirac fermions while circulating around the nanoribbon, so that no transverse mode at $k_l = 0$ exists under zero field. In order to compensate the Berry phase and recover the perfectly transmitted mode, a half quantum flux $\phi_0/2 = h/2e$ must be applied along the nanoribbon [48]. In this case, a pair of gapless linear Dirac surface sub-bands is established (Figure 2.12c). When the magnetic flux further increases, the surface state spectrum will again be gapped. The topological phase transition can be observed with a period of one full integer flux quantum.

Without applied magnetic flux or at other values of the magnetic flux applied ($\phi \neq \phi_0/2$), the surface states dispersion has a finite energy gap around zero. The size of this energy gap in the surface state spectrum of quantized transverse modes is given by [49]:

$$\Delta = \frac{2\pi v_F \hbar}{C} = \frac{h v_F}{C}. \tag{2.51}$$

Recently, direct evidence of the quantized Dirac sub-bands in TI thin bulk-insulating $(Bi_{1-x}Sb_x)_2Te_3$ nanowires has been observed using gate tuning of the chemical potential across the Dirac point [9]. When the back-gate voltage was applied to the devices, semi-oscillatory features in the $R(V_G)$ traces were observed (Figure 2.13). These features were identified as the signature of sub-band crossings.

Crossing a sub-band by the Fermi energy (due to an applied back-gate potential) implements two contrasting effects on the system. Opening a new conduction channel reduces the resistivity (since more charge can be transported) and simultaneously increases the resistivity due to effective scattering from other bands into a new channel (the contribution to the conductivity from each channel decreases). The latter effect is dominant and leads to pronounced R peaks even when only a few channels are present [9].

Since these sub-bands can be manipulated by a magnetic flux, they are an ideal platform for the realization of single-electron transistors and charge pumps, as well as for the generation of stable Majorana zero-energy modes, playing a key role in topological quantum computing.

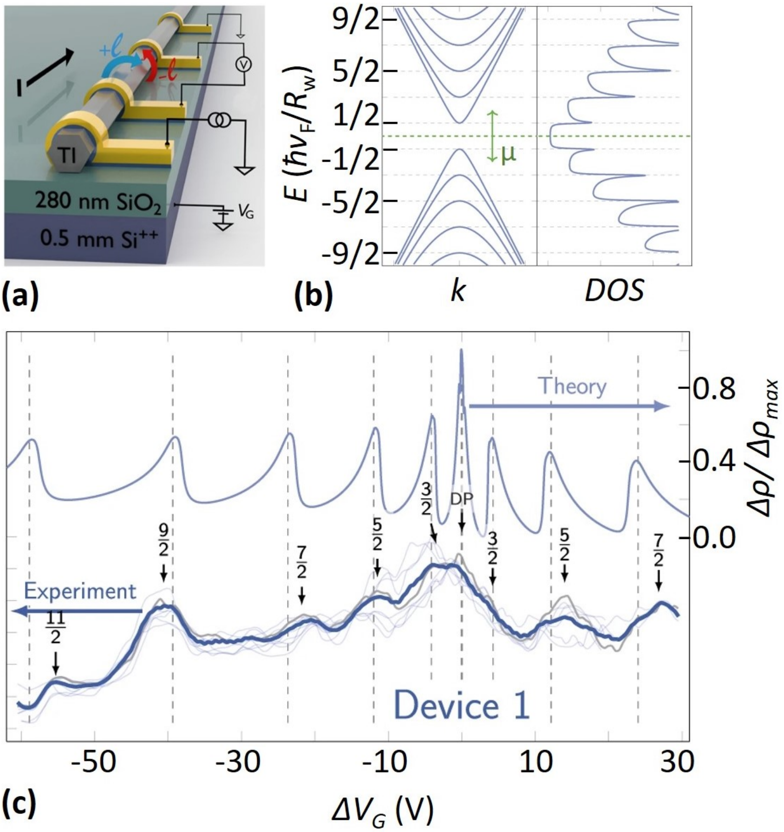

Figure 2.13: (a) Schematic of the device based on $(\mathrm{Bi}_{1-x}\mathrm{Sb}_x)_2\mathrm{Te}_3$ thin nanowire. (b) The sub-band structure of quantum-confined TI surface states described by Eq. (2.50) (left panel) and the corresponding density of states (right panel). (c) Experimental $R(V_G)$ dependence (lower curves), measured at $T = 2$ K. The large oscillations arising from the sub-band structure and the corresponding maxima are labelled by arrows. The upper curve is the theoretically calculated resistivity with a small density of impurities. Pronounced maxima arise at sub-band crossings (dashed lines). Adapted from [9].

3 Single-electron transport through quantum dots

As device sizes are reduced to nanoscale, the emergence of quantum mechanical effects can lead to a different way for devices to operate, opening up new horizons for applications. In the present chapter the aspects of charge transport, with emphasis on devices, in which the level spacing and the charging energy play an essential role, will be observed.

3.1 Single-electron transistor

A single-electron transistor (SET) is a nanodevice that can control the transport of single elementary charges onto and into a quantum dot. It can also function as a classic field-effect transistor (FET). The SET can also be used as an ultrasensitive electrometer. The SETs are promising ultrasensitive devices, that can be used to study charged nanoscale systems.

A single-electron transistor consists of a quantum dot (a small conductive island) placed between two tunnelling junctions (barriers), connected to the source and drain electrodes. It also has a gate electrode, as in a conventional FET (Figure 3.1). To achieve a transport regime of single elementary charges through the SET, two requirements should be borne in mind. First, the resistance of the tunnelling junctions must be larger than the quantum resistance $R_q = h/e^2 \simeq 25.8$ kΩ. Otherwise, the number of electrons in the quantum dot (QD) fluctuates because of the Heisenberg uncertainty principle. Second, the energy for adding one electron to the QD must be larger than the thermal energy $E_{add} \gg k_B T$. Otherwise, the heated electrons will continuously tunnel through the barriers, and the one-by-one electron transfer will not occur. The equivalent electrical circuit of the SET is shown in Figure 3.1c. Each tunnelling junction in the SET has intrinsic tunnelling capacitance and resistance (parallel to each other, for example, C_S and R_S). The equivalent circuit also has a gate electrode, which is used to adjust the background charge and as the SET input [50, 51].

Even if the SET quantum dot is very small (nanometre scale), it still contains a large number of electrons ($N \sim 10^9$). However, if relatively high-potential barriers are created between the QD and the source/drain, tunnelling to and from the dot will be weak, and the number of electrons on the dot N will be a well-defined integer. In this case, current can only flow when electrons tunnel one by one from

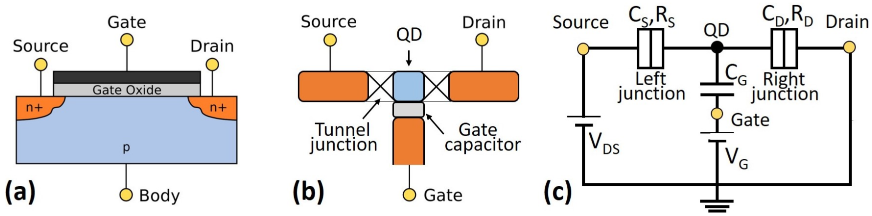

Figure 3.1: Schematic representations of a conventional FET (a) and SET (b). The SET consists of a quantum dot (QD) connected to the source and drain electrodes by tunnelling junctions, and the gate electrode to shift the electrostatic potential of the dot. (c) Equivalent circuit for the SET.

source to drain. The Coulomb repulsion between electrons on the dot results in considerable energy required for adding an extra electron. The electron cannot obtain this additional amount of energy until an increase in bias voltage provides this energy. This principle is called the Coulomb blockade and is responsible for the electrons tunnelling one by one [52].

According to the equivalent circuit (Figure 3.1c), electrostatic calculation shows the relation between different potentials as a function of the number of electrons in the QD, which can be expressed as:

$$V_{QD}\left(N\right) = \frac{\left(-eN + C_S V_S + C_D V_D + C_G V_G\right)}{C_\Sigma}, \tag{3.1}$$

where $C_\Sigma = C_S + C_D + C_G$ is the total capacitance of the QD. The expression (3.1) can be written in the form:

$$V_{QD} = V_{ext} + \frac{Q}{C_\Sigma}, \tag{3.2}$$

where $V_{ext} = (C_S V_S + C_D V_D + C_G V_G)/C_\Sigma$, $Q = -eN$, and e is the elementary charge. It can be seen, that the potential on the dot is determined by the charge residing in it and by the induced potential V_{ext} of the source, drain and gate.

The configuration for which all voltages and charges are equal to zero is taken as the reference configuration. The total electrostatic energy of the system, with respect to the reference configuration, after changing the source, drain and gate potentials and putting N electrons to the dot is identified as the work required to place an extra charge on the dot, when the charge Q is already present there:

$$U_{ES}\left(N\right) = \int\limits_{Q=0,\ V_{ext}=0}^{-Ne,\ V_{ext}} \left(V_{QD} dQ + Q dV_{ext}\right) = \frac{\left(Ne\right)^2}{2C_\Sigma} - NeV_{ext}. \tag{3.3}$$

Then total energy, including the “quantum energy” due to the orbital energies is:

$$U\left(N\right)=\frac{\left(Ne\right)^{2}}{2C_{\Sigma}}-NeV_{ext}+\sum_{n=1}^{N}E_{n}, \tag{3.4}$$

where the energy levels E_n correspond to states which can be occupied by the electrons in the device, provided that their total number does not change, since a change in this number will lead to a change in the Coulomb energy, which is accounted by the first term. This expression for the total energy is called the constant interaction model [32].

The second term in Eq. (3.4) arises due to the quantum nature of the dot, containing a set of quantum states with discrete energies (levels). The density of states of the device consists of a series of δ-functions, corresponding to the bound-state energies. If the number of electrons within the QD is fixed, the freedom of electron distribution over the energy spectrum is still preserved. The only limitation is the fact that, in accordance with the Pauli principle, a quantum state can contain no more than one electron. The change in the total energy of the device is mainly determined by the splitting of levels, which is characterized by the energy scale $\Delta = E_{N+1} - E_N$. According to statistical mechanics, a particle current is caused by a chemical potential difference, so the chemical potential of the QD is the relevant quantity driving the current from source to drain. In the independent particle picture, the energy of an individual particle is identical to the chemical potential (which is defined as the difference in total energy between a system with $N+1$ and N particles). Therefore, the single-particle energy of the dot can be considered as a “chemical potential”.

To see if the current is flowing through the device, one should compare the chemical potentials on the source and drain:

$$\mu\left(N\right)=U\left(N\right)-U\left(N-1\right)=\left(N-1/2\right)\frac{e^{2}}{C_{\Sigma}}-eV_{ext}+E_{N}. \tag{3.5}$$

From the definition of V_{ext} it follows that, while maintaining a constant source and drain voltage, an effective change in the chemical potential occurs due to a change in the gate voltage. So, the addition of electrons to the QD will be either favourable or unfavourable depending on the gate charge, which in its turn depends on the gate voltage. The factor $\alpha = C_G/C_\Sigma$ indicates the capacitive coupling of the SET QD to the gate electrode.

The distance between the different chemical potential levels can be written as:

$$\mu\left(N+1\right)-\mu\left(N\right)=\frac{e^{2}}{C_{\Sigma}}+E_{N+1}-E_{N}=\frac{e^{2}}{C_{\Sigma}}+\Delta. \tag{3.6}$$

For typical metallic and semiconductor quantum dots Δ is significantly smaller than the charging energy, so:

$$\mu\left(N+1\right)-\mu\left(N\right)\approx\frac{e^{2}}{C_{\Sigma}}. \tag{3.7}$$

This quantity is called the addition energy E_{add}, which is required to add or remove an electron to or from the dot.

The schematic energy diagrams of the SET device are illustrated in Figure 3.2, which show that the gate effect shifts the QD levels up and down, leaving the source and drain chemical potentials unchanged.

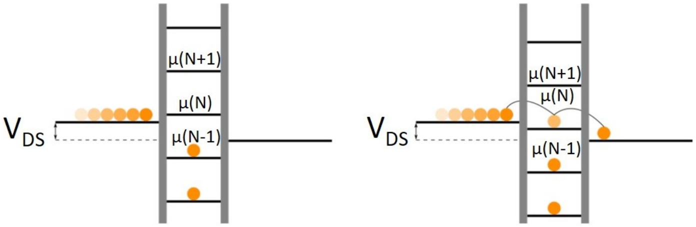

Figure 3.2: Schematic energy diagrams of the electrochemical potentials of QD, connected to the source and drain terminals, across which a small bias voltage V_{DS} is applied. The gate voltage is used to shift the electrostatic potential of the energy levels and achieve a single-electron tunnelling regime. Left: there is no energy level in the QD between the left and right terminals, and no current flows through the dot. Right: one energy level is between two terminals, and via tunnelling through the barriers current is allowed to flow.

The process of carrier transport through the SET device, corresponding to energy diagrams (Figure 3.2) is shown in Figure 3.3a. When a small positive voltage V_G is applied to the gate electrode, positive charges are induced there, the number of which is determined by $C_G V_G/e$, where C_G is the gate capacitance. To minimize the free energy of the system, the same number of electrons must be induced in the QD from the source through the tunnelling junction. In the case of $C_G V_G/e = N$, where N is some integer, the QD receives N electrons. After that, the movement of electrons no longer occurs and the system goes into the Coulomb blockade state (the left equivalent circuit in Figure 3.3a). If $C_G V_G/e$ is not an integer (for example, $N+1/2$), the number of electrons in the QD changes with time and on average becomes $N+1/2$. At first, one electron reaches the dot from the source, and the number of electrons in the QD becomes $N+1$, and consequently, one electron tunnels to the drain from the QD, resulting in N electrons remaining on the QD. Thus, the system enters the state of single-electron tunnelling and the transfer of electrons one after another is repeated. As a result, a net current arises between the source and drain electrodes (right equivalent circuit in Figure 3.3a). So, when the gate voltage is swept, the Coulomb blockade and the single-electron tunnelling states alternately occur, and the source-drain current versus gate voltage characteristics show repeating sharp peaks, as shown in the bottom panel of Figure 3.3a. This phenomenon is called the Coulomb-blockade oscillations.

A chart with a complete description of the SET operation, in which two voltages (V_{DS} and V_G) are swept independently from each other and source-drain current is recorded, is called a stability diagram (Figure 3.3b). The rhombic-shaped areas coloured in pink represent the region of the Coulomb blockade state (no current through the SET) and are known as Coulomb diamonds. Outside of Coulomb diamonds, the number of electrons in a QD fluctuates between certain numbers. The rate of these fluctuations is determined by how far the V_{DS} voltage conditions are from Coulomb (pink) diamonds. In the blue diamonds, the fluctuation is minimal (the number of electrons only changes between two adjacent integers). These regions belong to states of single-electron tunnelling. The shape and size of Coulomb diamonds are determined only by the gate and tunnelling junction capacitances. So, the maximum V_{DS} voltage for a Coulomb blockade is given by e/C_Σ, where C_Σ is the total QD capacitance. Each slope of the diamond is determined by $-C_G/C_D$ and $C_G/(C_G + C_S)$ (Figure 3.3b) [32].

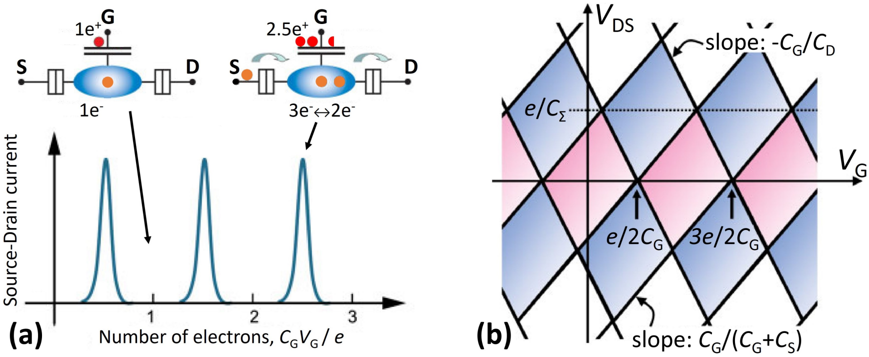

Figure 3.3: (a) Schematic of transport through the SET device. The top panel represents the equivalent circuits explaining the Coulomb blockade state (left) and single-electron tunnelling state (right). The bottom panel is source-drain current dependency as a function of a number of charges $C_G V_G/e$ induced by the gate. (b) Stability diagram of the SET, in which two voltages (V_{DS} and V_G) are swept independently from each other. Adapted from [32].

Similar to Figure 3.3b, a plot representing the current or differential conductance of a device as a function of the bias and gate voltage is called a charge-stability diagram (Figure 3.4a). The lines in the V_{DS}, V_G–plane separating the region of suppressed current from the region with a finite current (determined by the condition that the chemical potential of the source/drain is aligned with the level potential on the QD (Figure 3.2b)) can be calculated. Assuming that the drain is grounded (Figure 3.1c) and using the Eq. (3.5), the chemical potential aligned to the source (while maintaining a constant charge on the QD) can be expressed:

$$V = \beta \left(V_G - V_C\right), \tag{3.8}$$

where $\beta = C_G/(C_G + C_D)$ and $V_C = (N - 1/2)\dfrac{e}{C_G} + \dfrac{C_\Sigma}{C_G} \cdot \dfrac{E_N}{e}$ is the voltage corresponding to the chemical potential on the dot in the absence of an external potential. If the chemical potential is aligned with the drain:

$$V = \gamma \left(V_C - V_G\right), \tag{3.9}$$

where $\gamma = C_G/C_S$. And, irrespective of the grounding, one can conclude:

$$\frac{C_\Sigma}{C_G} = \frac{1}{\alpha} = \frac{1}{\beta} + \frac{1}{\gamma}. \tag{3.10}$$

Thus, the schematic arrangement of the Coulomb diamonds due to the difference in chemical potentials of the levels is shown in Figure 3.4a. No current flows inside these diamonds, and the quantum dot is in a Coulomb blockade state. Current can flow along the edges of the diamond (here the electrochemical potentials of the source/drain and quantum dot are equal). From this charge-stability diagram, a lot of information on the quantum dot can be extracted. For instance, the addition energy can be derived by measuring the width of the diamond. Considering two successive states of the QD with chemical potentials $\Delta\mu_N$ and $\Delta\mu_{(N+1)}$, and the fact that both states have the same gate-coupling parameter α, it can be seen that the upper and lower vertices of the diamond are both at a distance ΔV_{DS} from the zero-bias line:

$$\Delta V_{DS} = \frac{\left|\mu_N - \mu_{(N+1)}\right|}{e} = \frac{E_{add}}{e}, \tag{3.11}$$

where the difference in chemical potentials is the electron addition energy E_{add} (Eq. (3.7)). Combining this with the slopes of the sides of the diamond, which provide the relative values of C_G, C_S and C_D, all of these capacitances can be determined explicitly (Figure 3.4a).

Figure 3.4b shows the differential conductance dI/dV_{DS} versus (V_G, V_{DS}) for a Bi_2Te_3 single-electron transistor device, measured at a temperature of 40 mK [53]. Such a data set is assembled by taking a trace of dI/dV_{DS} versus V_{DS} at a fixed value of V_G. For the next trace, V_G is slightly changed and this is repeated many times. The recorded dI/dV_{DS} is then displayed in colour as a function of two variables. The blue diamond-shaped areas correspond to regions of the Coulomb blockade (ground states), where $dI/dV_{DS} \approx 0$. The gate voltage fills the quantum dot with electrons, moving the energy levels, while the bias voltage shifts the chemical potential of the source and drain electron baths. Pronounced Coulomb current oscillations as a function of the gate voltage, showing a sequential tunnelling regime (in which transport is only allowed if the chemical potential of the source (or drain) crosses one empty level of the quantum dot) are presented in Figure 3.4c.

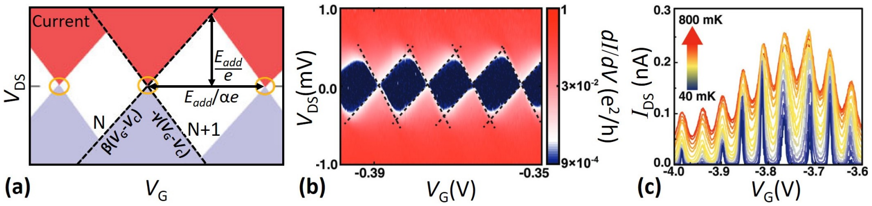

Figure 3.4: (a) Schematic two-dimensional plot of current as a function of bias and gate voltages (charge-stability diagram). For a small bias, current flows at only three points (indicated by orange circles), which corresponds to the situation shown in Figure 3.2 (right panel). The red areas represent a positive current, the purple - a negative current, and the white areas represent the Coulomb blockade (no current) state. Adapted from [32]. (b) Charge-stability diagram of a Bi_2Te_3 single-electron transistor device, exhibiting Coulomb diamonds. (c) Coulomb current oscillations as a function of the gate voltage at different temperatures. Multiple resonances are clearly visible. Adapted from [53].

3.2 Single-charge transfer devices

Due to the inability to control the time interval of each individual electron transfer in a SET due to the stochastic nature of electron tunnelling, more sophisticated devices synchronized with the gate clock are required for ultimate single-electronics applications. These devices include single-electron pumps and single-electron turnstiles with both fixed and tunable barriers. While turnstiles require a bias voltage to operate, pumps can deliver current even at zero bias. The operational principle of both types of devices is based on conveying an electron from the source to the drain in one cycle of the gate clock. Thus, the generated current is equal to $e \cdot f$, where e is the elementary charge and f is the clock frequency [54].

3.2.1 Turnstile device for single electrons

The quantized current generation was successfully achieved using the scheme based on a single semiconducting quantum dot, defined by metal gates in a two-dimensional electron gas (2DEG), where turnstile operation was performed using barrier modulation by applying radio frequency (RF) signals to the gates. Such devices were realised on top of GaAs/AlGaAs heterostructures containing a 2DEG below the surface [55, 56]. The current in these turnstile devices is driven by an external DC bias V_{DS}, while the clocked "On" and "Off" switching of the barriers ensures the desired order of electron transfer events (Figure 3.5a). In order to obtain quantized current, the number of tunnelling events has to be controlled each time, which is achieved by employing the Coulomb blockade of tunnelling [57].

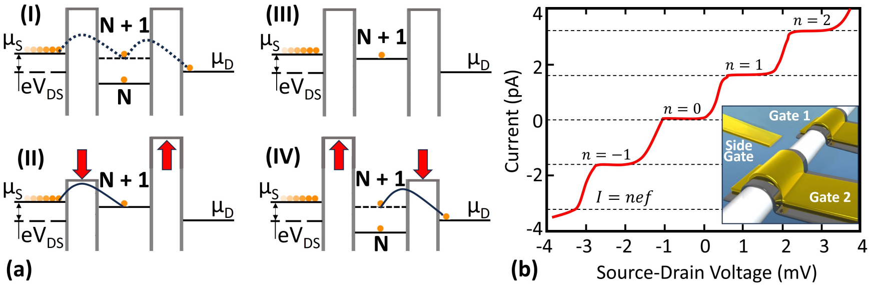

Figure 3.5: (a) Schematic energy diagrams for turnstile operation. The electrochemical potentials of the source and drain reservoirs are denoted by μ_S and μ_D, respectively. $V_{DS} = (\mu_S - \mu_D)/e$ is the bias voltage. The level N between the potential barriers denotes the electrochemical potential $\mu(N)$ of the QD with N electrons in it. (I-IV) are four stages of a RF cycle, where the probability for electron tunnelling is large when the barrier is low (solid lines), and small when the barrier is high (dashed lines). Adapted from [55, 57]. (b) Turnstile IV characteristic measured at 10 mK with RF signals of $f = 10$ MHz, where DC gate voltages on Gate 1 and Gate 2 are set at -120 and -195 mV, respectively (see inset). A series of clear steps of quantized current corresponding to $I = nef$ (n-integer, which is indicated by dotted lines) was observed. Adapted from [56].

Figure 3.5a (stage I) represent the schematic potential landscape of the QD connected to the leads in the case of static tunnel barriers. The electron states in the source and drain reservoirs are occupied up to the electrochemical potentials μ_S and μ_D, respectively, which differ due to the bias voltage $V_{DS} = (\mu_S - \mu_D)/e$. The line labelled N denotes the electrochemical potential $\mu(N)$ of the QD when it contains N electrons. The addition of an extra electron to the QD into the lowest available energy state would increase the electrochemical potential to $\mu(N + 1)$, indicated by line $N + 1$ in the Figure 3.5a ($\mu(N + 1) - \mu(N) = e^2/C$, Eq. 3.7). Further electron tunnelling into the QD will be suppressed if μ_S, $\mu_D < \mu(N + 2)$

(Coulomb blockade). Tunnelling out of the dot reduces the number of electrons and the electrochemical potential again, and a new electron can repeat this process. By varying the voltage on the centre (side) gate (Figure 3.5b inset), the conductance of the dot is expected to oscillate between zero (Coulomb blockade) and nonzero (no Coulomb blockade). This operation regime (SET behaviour) is described in the previous section (Figure 3.2).

The turnstile sequence of operation for a Coulomb blockaded QD is shown in Figure 3.5a (stages II–IV). For a turnstile operation, the tunnelling probability (stage I) must be small because it produces an unwanted leakage current. When the left barrier is reduced, the probability for the $N+1$ electron to tunnel into the dot is strongly enhanced, as illustrated by the solid line. Simultaneously, the increase of the right barrier suppresses the probability of tunnelling out of the dot. Tunnelling into the dot of a second electron is prevented by the Coulomb blockade. At half the cycle time (stage III), the barriers are in their equilibrium position again, but compared with stage I, one extra electron is confined in the dot. The $N+1$ electron tunnels out when the right barrier is reduced, and simultaneously, the left barrier is increased, which is illustrated in stage IV. Completing the cycle yields the situation shown in stage I, and exactly one electron has passed through the quantum dot. Repeating this process with a frequency f results in a current $I = ef$. Increasing the bias voltage, thereby increasing the number n of charge states contained in the energy interval between μ_S and μ_D produces a quantized current $I = nef$, corresponding to frequency-determined current steps in the Coulomb staircase (Figure 3.5b) [55–57].

3.2.2 Single-electron charge pump

Another device with single-electron charge manipulation capability, which allows the transfer of electrons one by one at a rate fixed by an externally controlled frequency, is called a single-electron charge pump. The main working principle of a charge pump is similar to that of an SET, however, the design of the pump is slightly different. As for the SET, the device consists of a QD connected to the source and drain electrodes by tunnelling barriers. However, instead of only one QD with barriers, the charge pump consists of two dots connected in series. In other words, the charge pump is a system of two coupled SETs that can be controlled by gates independently. The equivalent circuit of the single-electron pump is shown in Figure 3.6a.

Since a single-electron pump consists of two coupled SETs, the operation of the device is based on the same principles as for SET. The charge quantization occurs in QDs isolated by tunnelling barriers of capacitance C_i and resistance R_i. The charging energy e^2/C_Σ, which prohibits the addition of a second electron, is larger than the thermal energy k_BT. The resistance of the tunnelling junctions must be larger than the quantum resistance $R_q = h/e^2 \simeq 25.8\ \mathrm{k\Omega}$.

Figure 3.6b shows a stability diagram of the pump, consisting of two series-connected QDs isolated by tunnelling junctions. Each dot is capacitively coupled to gates (synchronized with frequency f), which are used to control its charge state. The QD_1 and QD_2 consist of n_1 and n_2 number of electrons, respectively, while n_0 is the number of electrons that pass through the pump.

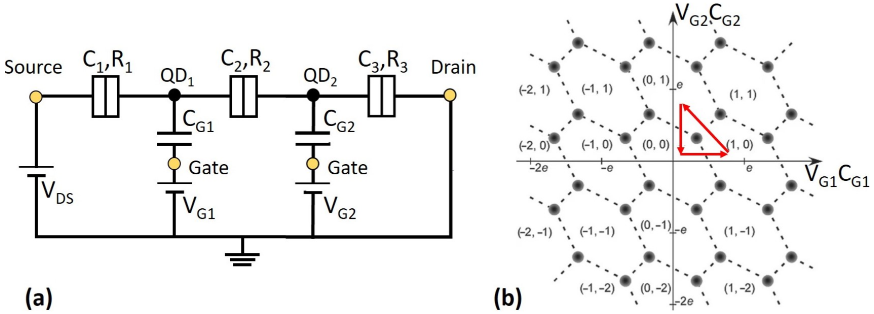

Figure 3.6: (a) Equivalent circuit of the single-electron charge pump. (b) Stability diagram of the single-electron charge pump at zero bias voltage. The number of electrons in the left and right QDs is represented by $(n_1,\, n_2)$. The red arrows indicate the gate-voltage trajectory for the pump operation. Adapted from [54].

At zero bias voltage V_{DS}, the local stability domain in the diagram is associated with each $(n_1,\, n_2)$ pair located in the $(Q_1 = C_{G1}V_{G1},\, Q_2 = C_{G2}V_{G2})$-plane. Although each domain consists of an elongated hexagon. The translational symmetry of this pattern corresponds to a square lattice, as shown in Figure 3.6b. Three neighbouring domains share a common triple point (for example, the point surrounded by the red arrows is common for domains (0, 0), (1, 0) and (0, 1)). The corresponding configurations have the same energy at this point. The pump cycle can be described as follows: first, a small bias voltage (much less than the Coulomb gap voltage e/C, where $C = C_1 = C_2 = C_3$ is the capacitance of the tunnelling junctions) and gate voltages are applied, which place the circuit in parameter space in the vicinity of the triple point. Then, two periodic signals with the same frequency f, but shifted in phase by $\sim \pi/2$ are superimposed on the gate voltages. Thus, the circuit adiabatically follows the closed trajectory indicated by the red arrows in Figure 3.6b. Assuming that the initial configuration of the pump is (0, 0), and that the trajectory follows counterclockwise, the circuit first moves from (0, 0) to (1, 0), allowing one electron to tunnel through the leftmost junction. Then the device configuration changes to (0, 1) as one electron passes through the central junction. Finally, the system returns to its initial configuration (0, 0), releasing one electron through the rightmost junction. During a complete cycle, one electron is transferred from the source to the drain. Thus, two gate voltages induce a current $I = e \cdot f$ to flow through the circuit, while the direction of the current is determined by the phase shift [54, 58–60].

The operating principle of the pump can also be illustrated using schematic energy diagrams (Figure 3.7). The two gates change the energy levels of the electrons on both QDs individually. To pump an electron through the device, a sinusoidal signal with a phase shift of $\sim \pi/2$ must be applied to the gates.

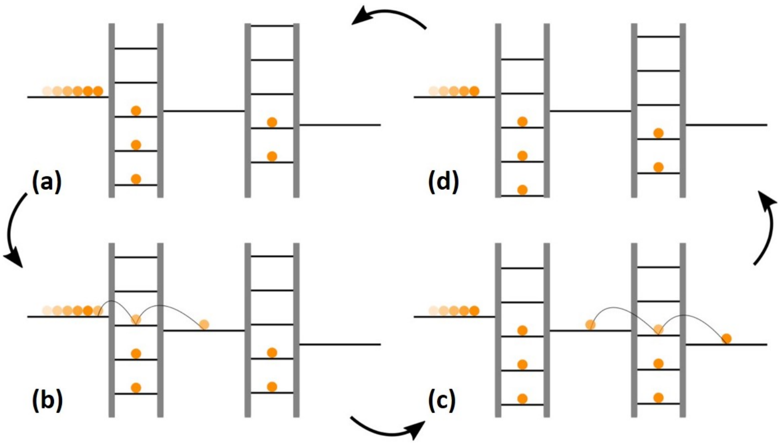

Figure 3.7: Schematic energy diagrams of the charge pump cycle. (a) None of the QDs allows transport, (0, 0) state. (b) QD_1 is open and QD_2 is closed. The electron tunnels from the source to the central island, (1, 0) state. (c) QD_1 is closed and QD_2 is open. The electron tunnels through QD_2 to the drain, (0, 1) state. (d) None of the QDs allows transport again, (0, 0) state.

The double-barrier single-electron pumps have been realized with silicon-based MOSFETs technology [61–63]. The gates were designed to efficiently control both the barriers and the electrostatic potential of the QD (Figure 3.8a). A map of drain-source current I_{DS} as a function of barrier voltages reveals the Coulomb resonances which correspond to a match in energy between $\mu_S = \mu_D$ and the electrochemical potential $\mu(N)$ for electron addition or removal between $N-1$ and N electron states on the QD (Figure 3.8b).

The working principle of pumping is illustrated in Figure 3.8c. First, the relative RF amplitudes on the two gates are tuned to obtain a trajectory parallel to the Coulomb lines (elliptic contours in the V_{g_1}-V_{g_2} plane). These contours can be set to turn around a Coulomb peak without ever crossing a black segment (where current flows). If the contour can be extended to turn around several Coulomb lines (as illustrated by the blue ellipse in Figure 3.8c), instead of a net current $I = ef$ for the green ellipse, one can expect $I = Nef$, where N is the number of Coulomb lines enclosed by the contour ($N = 4$ for the blue ellipse). The sign of the current can be simply changed by turning in the other direction [62, 63].

An important feature of the pumping cycle is that it consists of a sequence of equilibrium states, and the desired operation relies on the device following this sequence of states sufficiently closely, i.e. adiabatically. The average charge per cycle transferred between the source and the drain by an adiabatic pump is determined solely by the equilibrium charge diagram and the pumping contour, but not the rate at which the contour is traversed. Under strict adiabaticity conditions, an adiabatic pump requires at least two parameters to produce a non-zero DC current. In the above example of parametric modulation of V_{g_1} and V_{g_2}, the adiabaticity condition requires the pumping contour to enclose a finite area in order to yield a finite pumped charge per period in the low-frequency limit [57].

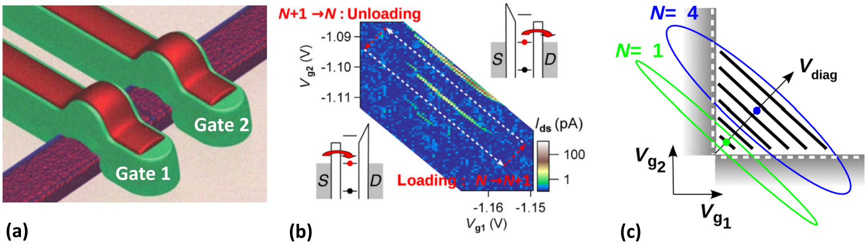

Figure 3.8: (a) Schematic view of the double-barrier single-electron pump layout. The single metallic island is controlled by two gate voltages V_{g_1} and V_{g_2} on which DC and RF signals are applied. Adapted from [63]. (b) 2D plot of drain-source current versus both gate voltages at 500 mK. The dashed lines indicate the four sequences of electron pumping. For the white lines, the potential of the island is kept constant, hence its population as well. The two red lines cross the Coulomb line and, therefore, require a population change $N \longleftrightarrow N + 1$. Such transitions involving a population change happen when one of the two barriers is very high, forcing electron transfer to occur through the other one. (c) Schematics of pumping contours realized with phase-shifted RF signals on the gates. The Coulomb lines are drawn in black. Increasing the phase shift results in wider ellipses enclosing several lines: one for the green ellipse, and four with the blue one. Adapted from [62].

3.2.3 Realisation of a quantum charge pump based on TIs

So far, most charge pumps have been manufactured using conventional semiconducting materials such as GaAs or silicon [4, 56, 57, 61, 62]. Here, a new concept of a quantum single-electron charge pump based on a topological insulating material instead of a conventional semiconductor is proposed. The experimental observation of sub-band signatures in TI nanowires (Section 2.8) makes such structures a promising platform for the realization of charge pumps. It has been theoretically predicted that quantum confinement within a defined section of a long TI nanowire or nanoribbon makes it possible to create a quantum dot, the transport through which is uniquely based on the nature of the topological surface states.

By constricting the radius of a TI nanowire, confinement effects open a gap in the surface states of the material, creating a tunnelling barrier, that can be controlled either with the gate or by threading half a magnetic flux quantum ($\phi = \phi_0/2 = h/2e$) along the wire. Two constrictions in series can then be used to create a quantum dot in the middle, and two radio frequency (RF) gate voltages can be used to trigger single-electron emission. The geometrical structure of the constricted TI nanowire is depicted in Figure 3.9a. The different sections of the nanowire are denoted as "N" and "C", where "N" is a region of normal radius and "C" is a region of constricted radius [10].

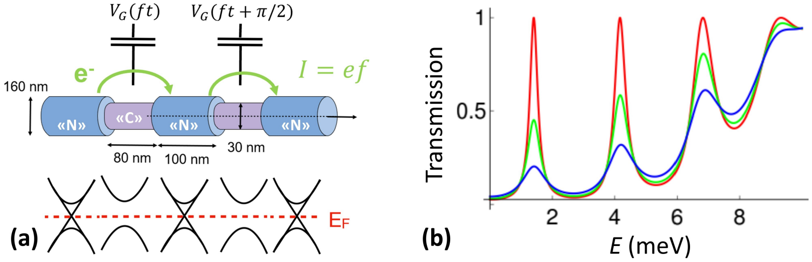

Figure 3.9: (a) Geometrical model of the TI charge pump (top panel). Schematic band structure experienced by an incident electron (bottom panel). (b) Sub-gap resonances positions as a function of external parameters (gates or flux). Different colours indicate three different levels of dephasing of the quasi-bound states in the "NCNCN" structure. Adapted from [10].

The larger band gap (smaller radius) of the constricted region "C" plays a vital role in achieving strong bound-states inside the confined region. The electrostatic potential induced by gates or the external flux threaded along the nanowire axes can be used to change the band gap profile along the axes of the "NCNCN" system, which in turn changes the resonant condition and leads to a shift in energy levels of the quantum dot.

The computed resonances in the transmission probability function of the surface states in response to applied magnetic flux or gate voltages at the constrictions "C" of the "NCNCN" TI nanowire are shown in Figure 3.9b. They are a typical signature of bound-state formation within the middle region. Different line colours correspond to different levels of dephasing of the quasi-bound states in the "NCNCN" structure. As can be seen, partial loss of coherence attenuates and broadens the transmission peak at resonance, however, the quantum dot level structure is not significantly impacted by dephasing.

In conclusion, electron transport through discrete TI quantum dot states can be modulated by external magnetic flux and/or gate voltages. This facilitates the creation of some of the most desirable quantum devices for metrology (single-electron devices), spintronics, and quantum computing [10].

4 Bulk conduction problem in TIs

An ideal TI has a fully insulating bulk so only the TSSs contribute to electrical conductivity. However, in practice, TI materials have a highly conducting bulk due to crystal defects. The conducting bulk masks TSSs conductivity and prevents the exploration of new physics and applications specifically attributed to TSSs. Thus, the main challenge in TI research has been to suppress parasitic bulk conduction and implement TSS-dominated transport.

4.1 Se vacancies in Bi_2Se_3 crystal

Bi_2Se_3 is known to be naturally heavily doped due to crystal defects, such as chalcogen (Se) vacancies or anti-sites. This native doping effect pushes the Fermi level E_F into the bulk conduction band, making its bulk states conducting ($n-$type). If the dopant atom is embedded in the crystal, it forms the Coulomb potential, resulting in the formation of hydrogen-like bound-states with an effective Bohr radius $a_B = \varepsilon(m_e/m^*) \times 0.5$ Å, where ε is the dielectric constant, m_e is the electron mass, m^* is the effective mass and 0.5 Å is the free space Bohr radius [64, 65]. For the case of Se vacancy in Bi_2Se_3, $\varepsilon \approx 110$ and $m^* = 0.15m_e$, thus $a_B \approx 37$ nm. As dopant density increases, the average distance between the dopant atoms decreases and eventually becomes comparable to the effective Bohr radius. When this happens, electrons that were bound to the dopant sites can delocalize and move freely to neighbouring sites, causing the insulator to become a metal. According to the Mott criterion, this critical value was quantified as ${N_c}^{-1/3} \approx 4a_B$, and in the case of Bi_2Se_3 $N_c \approx 3 \times 10^{14}$ cm^{-3}. Based on this calculation, it is clearly seen that any Bi_2Se_3 crystals will have conducting bulk states. Even the lowest ever reported 3D carrier density for Bi_2Se_3 single crystals of $\sim 10^{16}$ cm^{-3} [66] is already two orders of magnitude higher than N_c and has a conducting bulk [65].

4.2 Two-dimensional accumulation layer/ band-bending effect

In addition, extra interfacial defects tend to form bulk-derived two-dimensional electron gas near the surfaces [64, 67]. This 2DEG and the bulk conduction channel compete with TSSs and make it difficult to detect TSSs through transport measurements.

As shown in Section 2.1, the analysis of Shubnikov-de Haas oscillations showed that these oscillations can originate not only from the TSSs, but also from the bulk [31]. This effect is explained by the manifestation of the bending of the bulk bands near the surface, which is due to the fact that E_F lies in the bulk conduction band, although near the surface it lies in the band gap (Figure 4.1a).

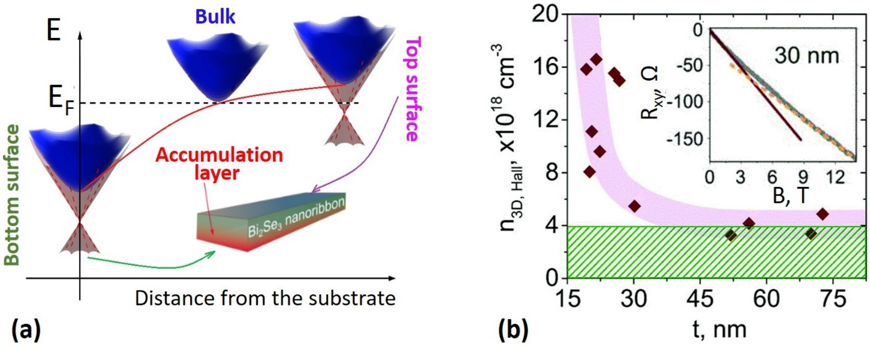

Figure 4.1: (a) Schematic illustration of a band-bending effect in a Bi_2Se_3 nanoribbon. At the interface between the bottom surface of the nanoribbon and the substrate, a 2DEG accumulation layer with carrier density of $\sim 2 \times 10^{13}$ cm^{-2} is formed. It leads to downward band-bending at this interface and strongly affects the total charge carrier density of the nanoribbon. (b) 3D carrier density extracted from the Hall effect in the magnetic field range of $0 - 2$ T and $T = 2$ K (inset) as a function of the nanoribbon thickness. The pink-shaded region is an eye guide, and the green-striped region indicates the upper bound for the bulk carrier concentration. Adapted from [7].

Figure 4.1b shows the 3D carrier density obtained from Hall effect measurements as a function of the nanoribbon thickness synthesised by our group [7, 68]. It is clearly seen that the carrier density increases with decreasing nanoribbon thickness (marked with a pink guide). Qualitatively the same behaviour was observed by another group [69] for thin films of Bi_2Se_3. The increase in carrier density for the thinnest nanoribbons/films indicates a stronger contribution from surface carriers. In the case where surface states with an electron density larger than the bulk are formed, the thickness reduction increases the effective carrier density, since the bulk contribution becomes less dominant [7]. For nanoribbons with the thickness of $\gtrsim 40$ nm, the three-dimensional carrier density reaches the value of $\approx 4 \times 10^{18}$ cm^{-3} (green-striped region), which is a hypothetical upper limit for the concentration of bulk carriers in thin nanoribbons.

The linear fit of the Hall resistance (Figure 4.1b inset) in the low magnetic field range depicts the deviation from the linearity in higher magnetic fields. This non-linearity indicates the contributions of different conducting channels with different carrier concentrations and mobility to the total Hall conductance. The trivial 2DEG formed at the nanoribbon-substrate interface extends well inside the bulk [70] and has low carrier mobility because of increased electron-electron scattering (since the carrier concentration here is larger compared to the top surface according to the band-bending effect). Due to this fact, it overlaps with the bottom surface states and dominates in conductance. The carrier concentration and mobility of the two channels (2DEG/bulk and surface states) can be extracted from the two-carrier analysis of the longitudinal and transverse magneto-conductance measurements. The transition from the R_{xx} and R_{xy} resistances to longitudinal and transverse conductance is:

$$\sigma_{xx} = \frac{R_{xx}}{{R_{xx}}^2 + {R_{xy}}^2} \text{ and } \sigma_{xy} = -\frac{R_{xy}}{{R_{xx}}^2 + {R_{xy}}^2}. \tag{4.1}$$

The conductance tensor in the perpendicular magnetic field is equal to:

$$\sigma_{xx} = e\left(\frac{n_1\mu_1}{1+{\mu_1}^2B^2} + \frac{n_2\mu_2}{1+{\mu_2}^2B^2}\right);\ \sigma_{xy} = eB\left(\frac{n_1{\mu_1}^2}{1+{\mu_1}^2B^2} + \frac{n_2{\mu_2}^2}{1+{\mu_2}^2B^2}\right), \tag{4.2}$$

where n_1 and μ_1 are the carrier density and the mobility of the first channel, and n_2 and μ_2 – of the second, respectively.

Thus, according to the two-carrier analysis, for nanoribbons with thickness in range from 21 to 63 nm, the averaged 2D carrier density corresponding to the top surface states is about $\sim 2.4 \times 10^{12}$ cm^{-2}, while the averaged mobility is ~ 5850 cm^2/V·s. The two-dimensional carrier density corresponding to 2DEG/bulk is about $\sim 2.7 \times 10^{13}$ cm^{-2}, with the averaged mobility $\sim$ 1000 cm^2/V·s. While the Hall two-dimensional carrier density (which includes all existing types of carriers) is around $\sim 1.1 \times 10^{13}$ cm^{-2}, and Hall mobility is ~ 1820 cm^2/V·s, respectively.

In the case of Bi_2Se_3 thin films with thickness in a range from 8 to 30 nm the Hall two-dimensional carrier density is $\sim 2.0 \times 10^{13}$ cm^{-2}, with Hall mobility of ~ 210 cm^2/V·s, respectively.

Despite the high mobility (for nanoribbons), the presence of a contribution of 2DEG/bulk in order of $\sim 2 - 3 \times 10^{13}$ cm^{-2} for both Bi_2Se_3 nanoribbons and films tends to degrade the transport properties. To take advantage of the peculiar properties of TI nanodevices, it is necessary to reduce the contribution of the bulk carriers and/or tune the Fermi energy level close to the Dirac point.

Part II

EXPERIMENTAL

5 Materials and methods

In this chapter, material growth, device fabrication process and transport measurement techniques used in this thesis will be discussed. The first section will examine the growth of Bi_2Se_3 nanostructures in the form of nanoribbons and thin films using physical vapour deposition (PVD). In the second section, the nanofabrication process of the devices prepared for quantum transport measurements will be shortly reviewed. And in the third section, the setups for transport measurements will be described.

5.1 Bi_2Se_3 growth

The physical vapour deposition (PVD) technique refers to a wide range of technologies, in which material is released from a source and deposited onto a substrate using mechanical, electromechanical or thermodynamic processes. Bi_2Se_3 nanostructures grown in the form of nanowires, nanoribbons or thin films were synthesised by the most common PVD method - thermal evaporation, using a single-zone quartz tube furnace (Figure 5.1).

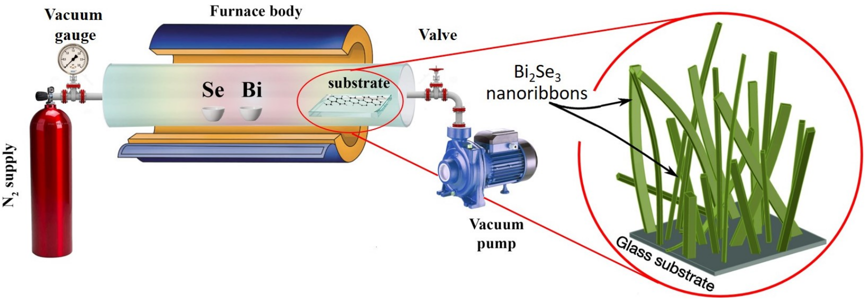

Figure 5.1: Scheme of the experimental setup for deposition of Bi_2Se_3 nanostructures.

The synthesis process of Bi_2Se_3 nanoribbons and thin films is similar, but there is one significant difference: to form long crystalline nanoribbons, a flow of N_2 gas is introduced during the cooling process, which leads to much faster growth in the flow direction. So, the whole process can be described as follows: first,

Bi_2Se_3 powder (for nanoribbons growth) or two separate Bi and Se powders (for films growth) were used as source materials. The target substrate (can be glass, quartz, graphene, Si/SiO_2 chips, mica, etc.) was placed downstream from the source materials, located in the central part of the furnace tube (Figure 5.1). The tube was then flushed with N_2 gas for 5 min to create an inert atmosphere before synthesis. After this, the furnace was heated from room temperature at a rate of 13 °C/min for 45 and 10 min at a starting pressure of $2-4$ and 0.1 Torr until the temperature in the centre of the furnace reached 585 and 500 °C for the growth of nanoribbons and films, respectively. The furnace was kept at 585 °C for 15 min for nanoribbons growth and 1 min at 500 °C for thin films growth, and afterwards was turned off to cool down naturally. The time at which the furnace is at maximum temperature can be varied to control the thickness of nanoribbons/films, and the parameters presented here correspond to standard growth [68]. When the temperature in the centre of the furnace decreased to 540 °C, an N_2 gas flow was introduced in the tube with a dynamic pressure of 25 Torr, initiating the growth of the nanoribbons. The flow was terminated once the temperature reached 475 °C. For the growth of nanoribbons and films, the tube was filled with N_2 to atmospheric pressure at 475 °C to stop the deposition process [68, 71](Papers I, II, III, IV).

5.2 Nanofabrication

5.2.1 Hall bars for individual nanoribbons

Most of Bi_2Se_3 nanoribbon-based devices have been fabricated on pre-patterned Si/SiO_2 (300 nm) chips. To make such chips, first, a 4-inch Si wafer (with high-quality thermal SiO_2 (300 nm)) was coated with S-1813 photoresist on the top side to protect the top oxide layer during subsequent wet chemical etching (using buffered oxide etchant (BOE)) of the oxide from the back side. Immediately after etching, a Ti/Au (5/195 nm) metal bilayer was deposited on the etched back side using an electron-beam thin film evaporator Lesker PVD 225 to create back-gate contact. The wafer was then cleaned in acetone and coated with $\approx$ 160 nm of MMA EL6 copolymer with a top layer of $\approx$ 180 nm of ARP 6200.13 (1:2) resist for electron-beam lithography (EBL, JEOL JBX 9300FS) patterning of chip marks. This recipe uses the lower dose-to-clear property of the bottom layer with respect to the top layer, thereby creating an “undercut” in the two layers of resist. The undercut prevents evaporated metals from sticking to the resist during lift-off. After resist development followed by EBL exposure the Ti/Au (5/45 nm) chip marks were evaporated. The subsequent lift-off process was carried out in hot acetone (Figure 5.2). After patterning, the wafer was diced into 5×5 or 7×7 mm^2 sized chips.

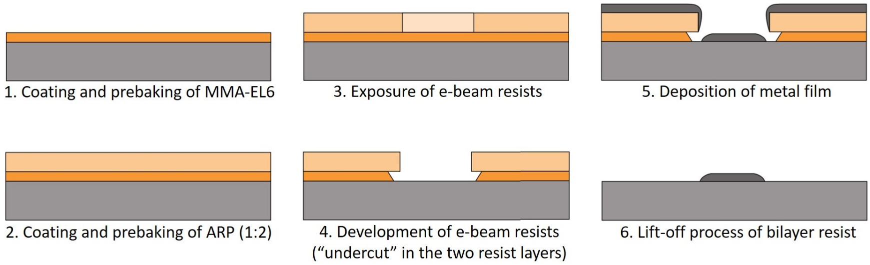

Figure 5.2: Schematic of the EBL process. On top of the substrate (grey), two layers of resist with different dose-to-clear are coated. After development, "undercuts" are formed in two layers of resist. This technology prevents evaporated metals from sticking to the resist during lift-off.

As described in the previous section, the growth of free-standing stoichiometric Bi_2Se_3 nanoribbons is made on a glass substrate and nanostructures are randomly distributed on the surface (Figure 5.3a). Thus, the nanoribbons were transferred to the pre-patterned chip by slightly pressing this chip (a flip-chip method) to the glass with nanoribbons. The transferred nanoribbons were analysed using optical (Figure 5.3b) and atomic force microscopes to distinguish the suitable ones. The selected nanoribbons were patterned using EBL to create electrical contacts (the same process as in Figure 5.2) in the Hall bars configuration (Figure 2.1a). Since the surfaces of Bi_2Se_3 nanoribbons oxidize in the air, the samples were stored in an inert atmosphere after the synthesis to reduce the thickness of the formed native oxide layer. To remove the oxide layer and provide a robust ohmic contact, the surface of the nanoribbon was etched off (approximately $3 - 4$ nm) with Ar-ion milling (Oxford Ionfab 300 Plus) prior to the deposition of the metal electrodes. After etching, the sample was immediately loaded into a vacuum chamber of a metal evaporator. To enhance adhesion, an extremely thin adhesion layer of Ti (5 nm) was deposited before the gold evaporation (80 nm). False-coloured SEM image of a device with Hall bar electrodes' geometry based on a single ultrathin (15 nm) nanoribbon is shown in Figure 5.3c. The six-contacts geometry (two large electrodes at the ends of a nanoribbon for passing current and two pairs of Hall bars) allows measurements of the longitudinal V_{xx} and transverse V_{xy} voltages in a four-probe configuration, thus eliminating the contact resistance effects (Papers III, V, VI).

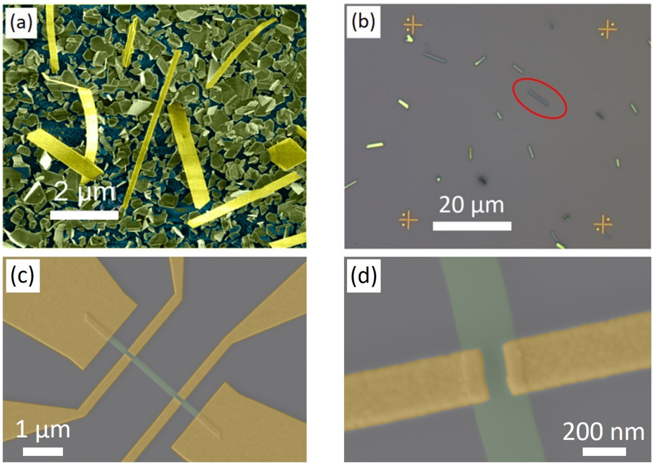

Figure 5.3: (a) False-coloured SEM image of as grown free-standing Bi_2Se_3 nanoribbons on a glass substrate. (b) Optical image of transferred nanoribbons to Si/SiO_2 chip. The red circle highlights the nanoribbon (15 nm thick) selected for further fabrication. (c) False-coloured SEM image of a fabricated device based on the nanoribbon from panel (b). (d) Zoom-in SEM image of the Hall bars overlapping the nanoribbon.

5.2.2 h-BN encapsulated devices

To fabricate the device encapsulated with h-BN flakes on a Si/SiO_2 substrate, local back-gate electrodes Ti/Au (5/25 nm) were patterned via EBL as mentioned above. Then, using a polydimethylsiloxane (PDMS)-assisted transfer technique (Figure 5.4), the stamping process of the first exfoliated h-BN flake was carried out using an alignment microscope with a custom-made attachment.

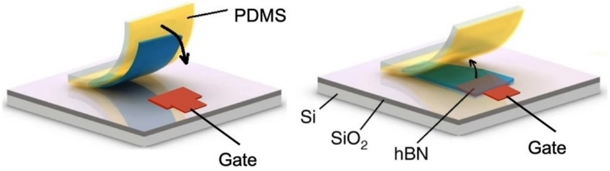

Figure 5.4: The scheme of transferring an exfoliated h-BN flake onto a pre-patterned gate electrode using a PDMS-polymer stamp. A Bi_2Se_3 nanoribbon can be placed on the top of the transferred h-BN using the same method. Then the device can be encapsulated with another flake to enable gating from both top and bottom surfaces.

Next, using the same method, the Bi_2Se_3 nanoribbon was selectively placed (stamped) onto the gate/h-BN stack. Electrical contacts to the nanoribbon were then defined using EBL followed by Ti(5 nm)/Au(50 nm) evaporation. The h-BN for the top gate dielectric was placed with the help of another stamping process, which is followed by patterning of the top gate electrode (Figure 5.5) [72].

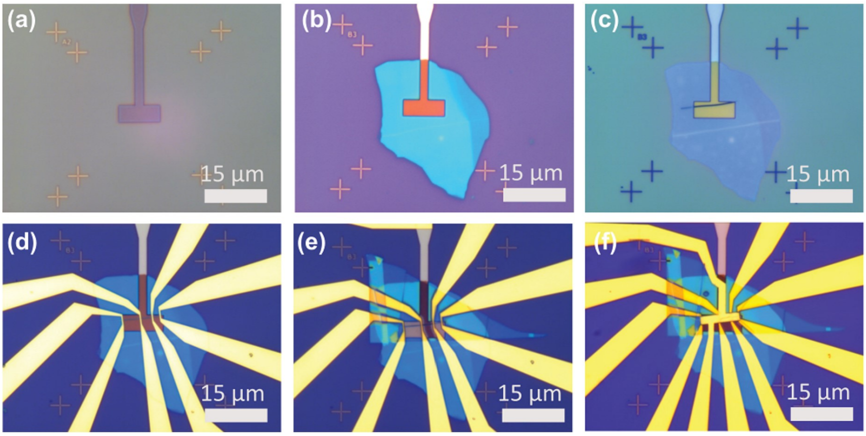

Figure 5.5: Optical images of various steps involved in the fabrication of the h-BN encapsulated TI device. (a) A local back-gate electrode deposited onto a Si/SiO_2 substrate. (b) The first stamped layer of h-BN for the bottom gate. (c) A Bi_2Se_3 nanoribbon transferred to the gate/h-BN stack. (d) Electrical contacts to the nanoribbon are deposited. (e) The second stamped layer of h-BN for the top gate. (f) The top gate electrode is deposited. Adapted from [72].

5.2.3 Devices for mechanical bending

To investigate the change in transport properties caused by the bending deformation, devices for measurements of the suspended (and further bended) and supported parts within the same Bi_2Se_3 nanoribbon were fabricated (Figure 5.6). First, Si/SiO_2 (300 nm) chips with marks were patterned via EBL to define the shape of the trenches. After that, the pre-patterned chips were etched by reactive-ion etching (Oxford Instruments PlasmaPro Cobra) in a mixture of CHF_3 (20 sccm) and O_2 (5 sccm) at 10 °C and 200 W power for 8 min (using Cr mask) to fully etch a SiO_2 layer. Next, Ti/Au (5/95 nm) back-gate contacts were evaporated by an e-beam evaporator. Then free-standing Bi_2Se_3 nanoribbons were transferred to the chip with the trenches using a flip-chip method. The nanoribbons transferred across the trenches were patterned using EBL to create electrical contacts. To remove the native oxide the surface of the nanoribbons was etched off with Ar-ion milling prior to the deposition of the metal electrodes (Paper VII).

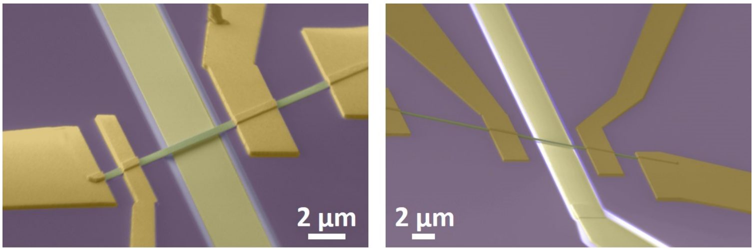

Figure 5.6: Tilted false-colour SEM images of the fabricated devices based on Bi_2Se_3 nanoribbons (green) transferred onto Si/SiO_2 substrates (violet), containing an etched trenches with gold back-gate electrodes (light-yellow) inside. The metal electrodes are shown in yellow. The devices consist of the suspended and supported parts.

5.2.4 SET devices

To fabricate a topological SET device, that consists of two consecutive constrictions forming tunnelling barriers, between which a quantum dot could be formed, thin and wide Bi_2Se_3 nanoribbons were patterned by defining an etching mask in an ARP 6200.13 (1:1) resist using EBL. The pattern was then transferred to TI by Ar-ion milling, during which the sample was cooled down to liquid nitrogen temperature to avoid thermal damage. There are two possible ways to create constrictions in the nanoribbon using etching: thinning the nanostructure from the top or, alternatively, from the sides. The former leads to significant damage of residual materials in the etching area, as well as to an increase in the concentration of charge carriers (Figure 5.7).

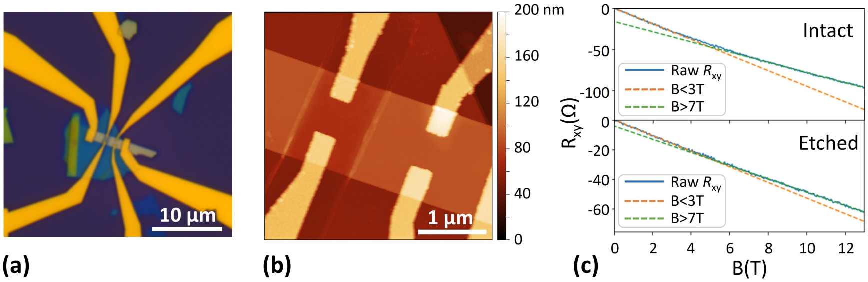

Figure 5.7: (a) Optical image of the device based on a Bi_2Se_3 nanoribbon (transferred to h-BN), containing a constriction fabricated by etching from the top. Two pairs of the Hall bars were patterned to compare the properties of the etched and intact parts. (b) AFM image of the device. The thickness of the h-BN is 58 nm, and the Bi_2Se_3 nanoribbon is 31 nm (intact) and 18 nm (etched). (c) The Hall effect measurements revealing $n_{2D} = -1.3 \times 10^{13}$ and -2.6×10^{13} cm^{-2} for the intact and etched parts.

Since only ultrathin nanoribbons (with reduced bulk conductivity) are suitable for the fabrication of SET devices due to the ability to effectively tune the Fermi energy, top etching of such thin material results in complete destruction and makes the device non-conducting. Thus, for Bi_2Se_3-based SET fabrication the nanoribbons are constricted only along their width, as shown in Figures 5.8a and b.

To fabricate SET devices, a 13 nm thick $(Bi_{1-x}Sb_x)_2Te_3$ film grown by MBE on a sapphire substrate was also used. The electrodes were first patterned on the film by EBL, followed by evaporation of a 3/50 nm thick Ti/Au layer, and lift-off. Single-electron transistors were then carved in the films by another EBL and Ar-ion milling, using the resist as an etching mask. A plunger (side) gate is also patterned in the film during the same EBL step to tune the charge state inside the dot. False-coloured SEM image of the typical device is shown in Figure 5.8c (Paper VIII).

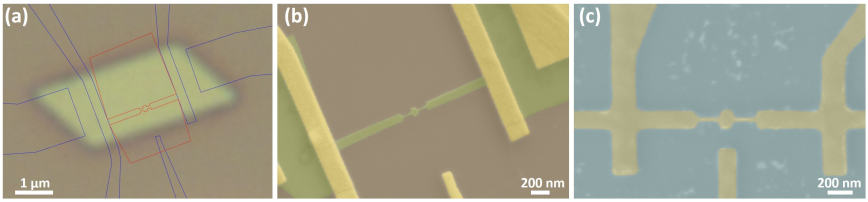

Figure 5.8: (a) Optical image of a Bi_2Se_3 nanoflake (transferred to Si/SiO_2) with an EBL-mask pattern (the blue contours are the metal contact designs, the red contour is the etching mask). (b) False-coloured SEM image of the fabricated device from panel (a). (c) False-coloured SEM image of an SET device based on a $(Bi_{1-x}Sb_x)_2Te_3$ film with a thickness of 13 nm.

5.3 Low-temperature electrical measurements

After nanofabrication, the patterned devices were contacted to study transport properties. Magnetotransport measurements were performed either in the physical property measurement system PPMS (Quantum Design DynaCool) equipped with external electronics, or in a ^{3}He Oxford Heliox dipstick with a base temperature of $\approx$ 300 mK, or in Oxoford Trition closed cycle ^{3}He/^{4}He dilution refrigerator with a base temperature of 20 mK. Devices with the Hall bars geometry were measured in DC bias mode at the temperatures of $300 - 2$ K. The biasing circuit consists of a voltage source V_b (Keithley 2400), a bias resistor R_b (for current biasing), and a sampling resistor R_s that is used for probing the current supplied to the device (Figure 5.9a). Both the voltage drops across the longitudinal V_{xx} and transverse V_{xy} contacts of the device as well as I_bR_s are measured using a setup consisting of three low-noise differential amplifiers (Stanford Instruments) connected to the digital multimeters (Keithley 2000), to get voltages and current across the device, respectively (Figure 5.9b). The gate electrode was connected to another source meter V_G (Keithley 2400) through a bias resistor with nominal 1MΩ to reduce the noise.

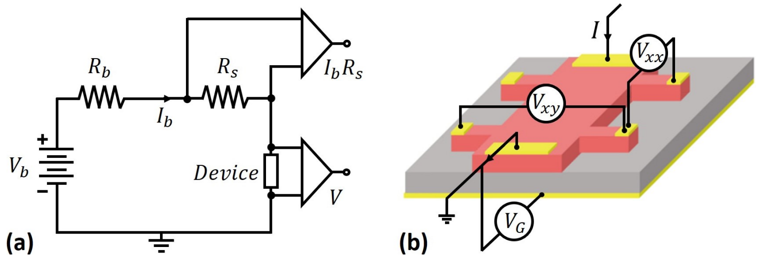

Figure 5.9: (a) Schematic of the current bias circuit and a sample configuration (b), showing a back-gated Hall bar device used in the electron transport measurements.

The transport in the single-electron transistor devices was measured at a base temperature of 22 mK. The samples were biased by applying an AC voltage of 1 Hz to a 1 MΩ bias resistor in series with the device, and measuring the voltage and current along with a National Instruments DAQ and Stanford Instruments voltage pre-amplifiers. The conductance is then obtained by numerical differentiation.

Part III

RESULTS AND DISCUSSION

6 Structural characterization of Bi_2Se_3 nanostructures

Size, crystalline structure, growth direction, surface morphology and chemical composition of the synthesised nanoribbons and thin films are determined using scanning electron microscopy (SEM), atomic-force microscopy (AFM), high-resolution transmission electron microscopy (HRTEM), X-ray diffraction and reflectometry (XRD and XRR), Raman spectroscopy, selected area (electron) diffraction (SAED) and energy-dispersive X-ray spectroscopy (EDX) techniques.

6.1 Characterization of Bi_2Se_3 thin films

Figure 6.1a illustrates a typical SEM image of a thin Bi_2Se_3 film deposited on a fused silica substrate. In general, all synthesised Bi_2Se_3 thin films have a uniform distribution of Bi and Se chemical elements over an area of 100×100 μm^2 with a chemical composition of 40 ± 5 at% for Bi and 60 ± 5 at% for Se, which corresponds to the stoichiometry of Bi_2Se_3. Figure 6.1b shows an example EDX spectrum and the corresponding EDX map of the elements Bi and Se. As can be seen, Bi and Se have uniform contrasts, which means these elements are distributed uniformly in the film. A typical Raman spectrum of Bi_2Se_3, consisting of both Stokes and anti-Stokes contributions, is shown in Figure 6.1c. According to Group theory, four Raman active modes (E_g^1, A_{1g}^1, E_g^2, A_{1g}^2, where E modes represent in-plane atomic vibrations, while A modes are vibrations along the c-axis perpendicular to the layers) were observed, which indicates the formation of thin Bi_2Se_3 films of good quality. Thin films grow with the c-axis perpendicular to the substrate surfaces, which appears to be the most energetically favourable growth direction. The XRD spectrum analysis (Figure 6.1d) revealed the presence of diffraction peaks related only to the $(003n)$ family group, thereby confirming the growth of the Bi_2Se_3 thin film with the crystallographic c-axis. The pronounced XRR intensity oscillations confirm the presence of smooth interfaces and surfaces of the synthesised films. The thicknesses of films were obtained from XRR measurements fits, as well as from AFM measurements. The representative AFM image and height profiles are presented in Figure 6.1e and f, respectively. An artificial scratch was introduced to determine the thickness (Papers I, II, IV).

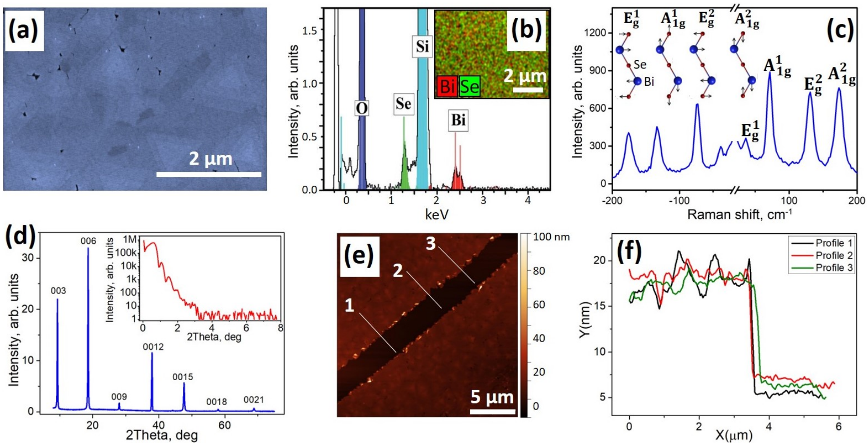

Figure 6.1: (a) False-coloured SEM image of a Bi_2Se_3 thin film on a fused silica substrate. (b) EDX spectrum, revealing a chemical composition of 40±5 at% for Bi and 60±5 at% for Se. The inset is an EDX map, illustrating a uniform distribution of the elements Bi and Se. (c) Raman spectrum of a Bi_2Se_3 film. The inset is the displacement patterns of phonon modes in the Bi_2Se_3 structure. (d) X-ray diffraction pattern of a Bi_2Se_3 thin film, in which only the peaks of the (003*n*) family group are visible. The inset is X-ray reflectivity (XRR) measurements. (e) AFM image of a thin Bi_2Se_3 film grown on a fused silica. (f) Height profiles shown in panel (e).

6.2 Characterization of Bi_2Se_3 nanoribbons

The synthesised nanoribbons are stoichiometric (Bi (35±5) : Se (65±5) at%), single-crystalline with lengths up to 40 – 50 μm and thicknesses starting from $8-10$ nm. The widths can vary from 50 nm up to $1-2$ μm and more (Figure 6.2). Normally, due to the rapid oxidation under ambient conditions, the synthesised nanostructures are covered with a few nm native oxide layer, which can be either amorphous or poly-crystalline. Figures 6.2b and c represent false-colour HRTEM images of a nanoribbon. The bulk area demonstrates a single-crystalline structure, while the surface of the nanoribbon is covered with a few nm thick native oxide layer of Bi_2Se_3 - BiO_x. SAED pattern of the nanoribbon along the [001]-zone axis is shown in Figure 6.2d. The growth direction of the synthesised nanoribbons is [110]. As for the thin films, the thicknesses of nanoribbons transferred to Si/SiO_2 substrate were obtained from AFM measurements. The representative AFM image and height profiles are presented in Figures 6.2e and f, respectively (Papers III, V, VI).

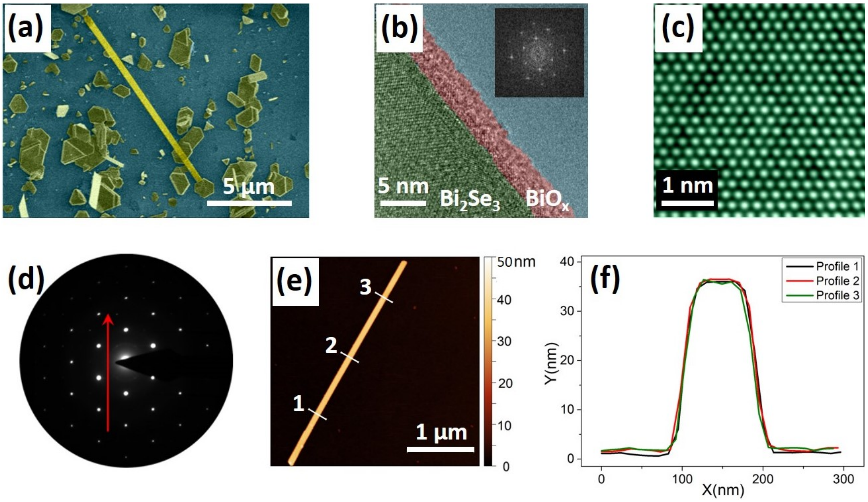

Figure 6.2: (a) False-coloured SEM image of a Bi_2Se_3 nanoribbon and the nanoplate seeds. (b) False-coloured HRTEM image of a nanoribbon. The bulk area demonstrates a single-crystalline structure (green colour). The inset is FFT image illustrating a single-crystalline structure of the nanoribbon. The surface of the nanoribbon is covered with a few nm thick native oxide layer of Bi_2Se_3 - BiO_x (pink). (c) HRTEM micrograph of Bi_2Se_3 nanoribbon structure illustrating its crystallinity. (d) SAED pattern of the nanoribbon along the [001]-zone axis. The red arrow marks the nanoribbon growth direction [110]. (e) AFM image of Bi_2Se_3 nanoribbon transferred to a Si/SiO_2 substrate. (f) Height profiles of the nanoribbon shown in panel (e).

7 Reduction of bulk contribution to transport in Bi_2Se_3 nanostructures

The main problem encountered when fabricating devices using 3D-topological insulators is the unavoidable presence of bulk conductivity. These bulk states often mask the effects of unconventional topological surface states or complicate transport analysis on these devices. As seen in Chapter 4, PVD-grown Bi_2Se_3 nanostructures have a significant contribution to the transport arising from conducting bulk states, and in the current chapter, the attempts to solve this issue will be discussed. In the first section, attempts to reduce bulk carriers with electrostatic gate effect using various dielectric substrates will be explored. In the following sections, changes in the growth process leading to increased surface-to-volume ratio and strain engineering in nanoribbons and films will be examined.

7.1 Electrostatic gating effect

To take advantage of the peculiar properties of TI nanodevices, it is necessary to reduce the contribution of the bulk carriers and/or tune the Fermi energy level close to the Dirac point. The possibility to continuously drive the Fermi level from the conduction to the valence band can be achieved by the electrostatic gating effect. On the other hand, when an electrostatic field is applied through the gate electrode to a TI-based device, additional carriers dope the nanostructure, forming an accumulation layer (2DEG) at the dielectric-topological insulator interface, again leading to the energy band-bending effect (Section 4.2).

As was demonstrated in Chapter 4, when Bi_2Se_3 nanoribbons transferred onto a Si/SiO_2 substrate, a trivial two-dimensional accumulation layer with a high charge carrier density up to $\sim 2 \times 10^{13}$ cm^{-2} is formed at the substrate-nanoribbon interface. This makes it difficult to tune the Fermi level close to the Dirac point due to the relatively low dielectric constant of the substrate ($\varepsilon_{SiO2} \approx 4$). For instance, for 65 and 70 nm thick nanoribbons, the 2D carrier concentrations obtained from the Hall effect measurements changed from 6.25×10^{12} and 2.44×10^{13} cm^{-2} to 6.18×10^{12} and 2.38×10^{13} cm^{-2} with an applied back-gate voltage of -40 V, respectively. Then, 22 and 28 nm thick nanoribbons were transferred to a $SrTiO_3$ substrate with an extremely high dielectric constant ($\varepsilon_{SrTiO3} \approx 20000$), and the tunability of the devices increased from 1.40×10^{12} and 1.65×10^{13} cm^{-2} to 1.15×10^{12} and 1.40×10^{13} cm^{-2} with an applied back-gate voltage of -20 V, respectively. However, for nanoribbons with a thickness of 22 nm or more, the interface accumulation layer was not completely depleted by back-gating through the substrate. Also, the results of studying Bi_2Se_3 nanoribbons on various oxide substrates demonstrate that the formation of an accumulation layer is a common feature characterizing the interface with Bi_2Se_3. This effect can be explained by the different densities of oxygen atoms at the interface between the native oxide of Bi_2Se_3 nanoribbon (Figure 6.2b) and oxygen from the dielectric layer, which leads to the formation of dipoles. The sign of the dipole can determine the formation of depletion or accumulation layers at the interface between these two oxides [8].

Alternatively, oxygen-free, high-quality 2D material hexagonal boron nitride (h-BN) can be used as the gate dielectric to minimize the influence of 2DEG between the substrate and Bi_2Se_3. An h-BN flake exfoliated from h-BN powder can withstand an electric field with a strength of $\simeq 0.7$ V/nm, which allows to apply sufficient gate voltages, without field screening or leakage.

In this experiment, the Bi_2Se_3 nanoribbon with a width and a thickness of 480 and 70 nm, respectively, encapsulated with h-BN flakes (Figure 5.5) was used. Measurements were performed in a four-probe configuration (the voltage probes are spaced by 3 μm) in a 300 mK dipstick at base temperature (Figure 7.1). During the measurements, the gates were controlled by individual voltage sources. The thicknesses of the bottom and top h-BN flakes are ≈ 25 and ≈ 15 nm, respectively.

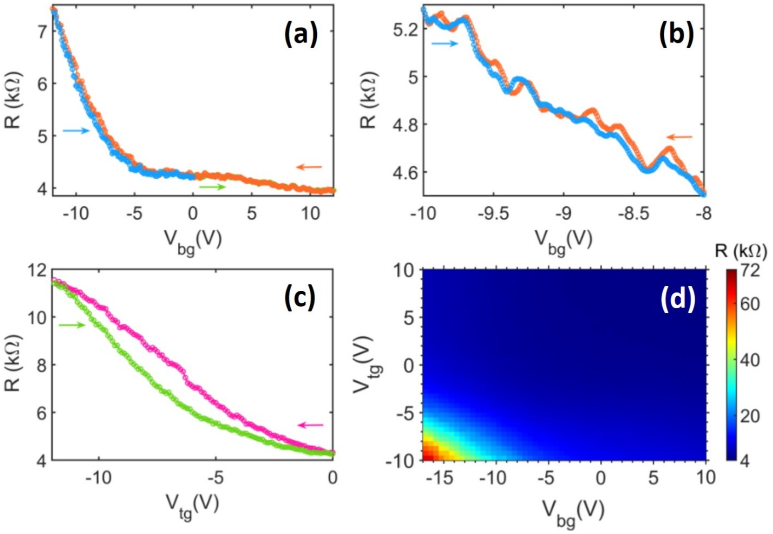

Figure 7.1: (a) Device resistance R_{xx} as a function of the back-gate voltage V_{bg}, with $V_{tg} = 0$ V. The arrows indicate the sweep direction. (b) Reproducible resistance oscillations in the range from -8 to -10 V of V_{bg} voltage in both sweep directions ($V_{tg} = 0$ V). (c) R_{xx} as a function of the top-gate voltage V_{tg}, with $V_{bg} = 0$ V. (d) 2D resistance map of the device with both V_{bg} and V_{tg} applied. Adapted from [72].

First, the device resistance $R_{xx} = 4.2$ kΩ was measured at zero back and top-gate voltages. Then, R_{xx} as a function of the back-gate voltage was measured, while the top-gate voltage was maintained at zero (Figure 7.1a). At $V_{bg} = -12$ V, the resistance of the device almost doubles compared to the zero-voltage case. The resistance oscillations, which are reproducible in both forward and backward sweeps, were observed at high values of the back-gate voltage (Figure 7.1b). These oscillations might indicate the transverse quantization in our device, as it was observed in similar TI devices (Section 2.8) [9]. An analogous behaviour of R_{xx} as a function of the top-gate voltage with zero V_{bg} is shown in Figure 7.1c. However, since the top h-BN flake is thinner, with $V_{tg} = -12$ V the resistance of the device has increased by approximately ≈ 2.8 times (due to increased electrostatic field strength). Also, the hysteresis in the top gate response of the device has been observed. This might be explained by accumulated charges in the thinner h-BN or in the interface between the nanoribbon and top h-BN flake. In Figure 7.1d, the 2D plot represents the resistance map of the device in terms of V_{bg} and V_{tg}. It is clearly seen that the device resistance increases sharply in the region of high negative gate voltages and reaches a peak value of 72 kΩ at $V_{bg} = -17$ V and $V_{tg} = -10$ V, which is approximately 17 times higher in comparison with the initial resistance. Such a sharp increase in the device resistance and high sheet resistance (on the order of 11.5 kΩ/□ compared to the initial value of 0.67 kΩ/□) may indicate that the Fermi energy position is indeed close to the Dirac point. Unfortunately, due to the increase in leakage current through the dielectric at high applied voltages, it was not possible to apply even larger negative gate voltages to show a decrease in resistance after the Dirac point, when the carrier types switch from electrons to holes. However, a double-gate TI device with h-BN dielectrics could be a way to study transport around the Dirac point in our devices [72].

7.2 An increase of surface-to-volume ratio

The depth of the accumulation layer D at the dielectric-topological insulator interface can be estimated by solving the Poisson equation in the full depletion approximation to yield $D = \left(2k\varepsilon_0 \Delta E/(e^2 n)\right)^{-1/2}$, where k is the dielectric permittivity of Bi_2Se_3, ΔE is the shift of Fermi energy across the band-bending region due to the applied gate voltage ($\Delta E \leq 300$ meV, Bi_2Se_3 bandgap), and n is the carrier density. The values of the accumulation layer depth ranging from 10 to 35 nm for TI samples with carrier density $n \sim 10^{19}$ cm^{-3} usually reported in the literature [70]. To suppress bulk conduction, the sample thickness should be smaller than D, so that the gate can effectively modulate the charge carrier density through the entire sample. Thus, in addition to the electrostatic gating effect, a reduction of the contribution from bulk can be achieved by thinning the samples (Paper II).

7.2.1 Synthesis of ultrathin nanoribbons

The advantage of PVD growth is its simplicity and easily adjustable synthesis parameters, such as the partial pressure of vaporized source material, the heating and deposition time and rate, and the substrate temperature. The use of ultrathin nanoribbons (less than 20 nm thick) obtained by the deposition described in Section 5.1 is complicated due to their extremely small quantity. Thus, optimisation of the synthesis process is necessary to achieve an increased yield of ultrathin nanoribbons.

Here, the basic synthesis parameters (temperature, time and vapour pressure) of the standard catalyst-free physical vapour deposition method for obtaining free-standing Bi_2Se_3 nanoribbons (described in Section 5.1) were systematically optimised to achieve the outcome of the nanoribbons with thicknesses below 15 nm. This value was chosen as an upper limit for optimizing growth parameters, according to the depth of the accumulation layer D for TI samples with carrier density $n \sim 10^{19}$ cm^{-3}, which is close to our nanoribbons (Chapter 4).

The growth of the Bi_2Se_3 nanoribbons during the deposition process is initiated by the temporary N_2 gas flow, which is introduced in the furnace tube during the cooling stage (Figure 7.2a). During the standard growth process, nanoplates are deposited on the substrate for a time $t_1 + t_2$. They serve as seeds for the subsequent formation of nanoribbons during the N_2 streaming. As the top surface of the nanoplate is chemically saturated by selenium atoms, adatoms adsorbed there from the gas phase cannot form covalent bonds. Thus, they diffuse in the direction of the gas flow and bond to the nanoplate crystal at the edges, which leads to a much faster growth rate in the N_2 flow direction, forming long crystalline nanoribbons. Since the cross-section of the nanoribbons is correlated to that of the seed nanoplates from which they grow (Figure 7.2b), it can be influenced by changing the conditions in which the nanoplates are grown.

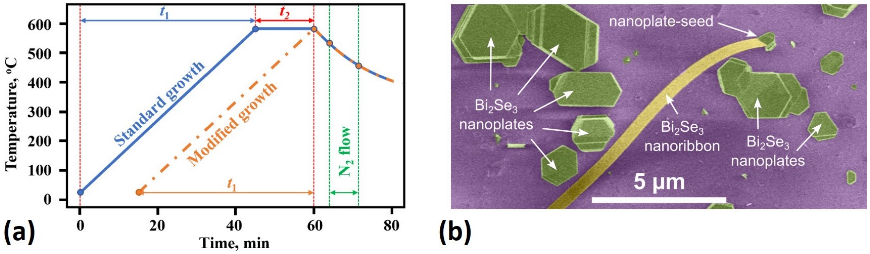

Figure 7.2: (a) Schematic of the synthesis process. The solid blue line corresponds to the standard growth described in Section 5.1, and the orange dot-dashed line corresponds to a modified growth with $t_2 = 0$ min. (b) False-colour SEM image of a Bi_2Se_3 nanoribbon and the nanoplate seed.

The thickness of the nanoribbons is most likely determined by the thickness of the nanoplates or, in the case of a step-like structure of the nanoplates - by the thickness of the step. In turn, the growth rate and, consequently, the thickness of the nanoplates/steps depend on the diffusion rate of the vaporized source material. The rate of evaporation can be approximated by the Hertz-Knudsen equation:

$$\frac{dN}{dt} = \frac{\alpha_e N_A \left(p_e - p_h\right)}{\sqrt{2\pi MRT}}, \tag{7.1}$$

where N is a number of evaporated atoms per surface area, t is time, α_e is the coefficient of evaporation, N_A is Avogadro number, p_e is equilibrium pressure, p_h is hydrostatic pressure, M is molecular weight of the evaporated species, R is the universal gas constant, T is absolute temperature. Considering the constant initial mass of the source material and its heating rate in all syntheses, the amount and diffusion rate of the vaporised source Bi_2Se_3 is governed by the three variable parameters: maximal heating temperature of the source material T_m, the initial pressure in the furnace tube p_1, and time t_2 during which the source material is kept at maximum temperature T_m (Figure 7.2a). Thus, the nanoribbon thickness can be changed by adjusting only these parameters.

To determine the optimal growth conditions for the nanoribbons with thicknesses below 15 nm, the parameters T_m, p_1 and t_2 were varied in the ranges $575 - 590$ °C, $0.1 - 18$ Torr and $0 - 30$ min, respectively. Variation of T_m did not result in the increased outcome of the ultrathin nanoribbons compared to the standard parameter $T_m = 585$ °C. Thus, this value was selected as the constant parameter. Furthermore, only parameters t_2 and p_1 were varied (Figure 7.3).

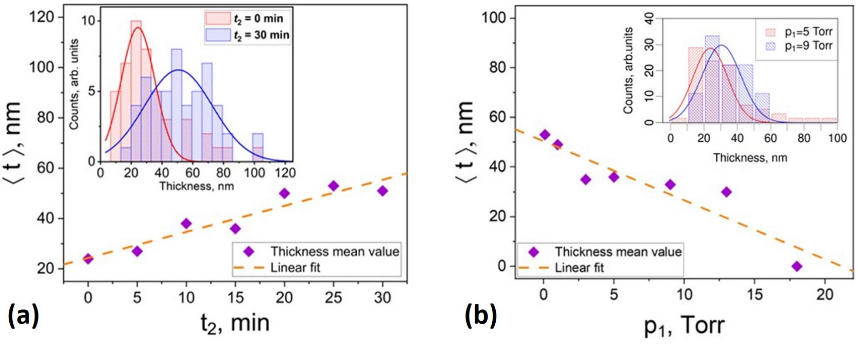

Figure 7.3: A Bi_2Se_3 nanoribbon mean thickness $\langle t \rangle$ as a function of time t_2 at constant initial pressure $p_1 = 5$ Torr (a), and as a function of the initial pressure p_1 at constant time $t_2 = 0$ min (b). The orange dashed lines correspond to a linear fit of the experimental data. Insets: Bi_2Se_3 nanoribbon thickness distribution histograms for $t_2 = 0$ min and 30 min at constant $p_1 = 5$ Torr (left), and for $p_1 = 5$ Torr and 9 Torr at constant $t_2 = 0$ min (right). Solid lines correspond to the Gaussian distribution of experimental data, from which the mean thickness $\langle t \rangle$ was calculated.

Generally, the mean thickness of the nanoribbons linearly decreased with the decrease in the source material heating time t_2 while the pressure p_1 was kept constant (Figure 7.3a). It is most likely related to the decreased amount of the evaporated source material and, consequently, the thickness of the nanoplate seeds. In contrast, an increase in the initial pressure p_1 (while t_2 was constant) resulted in a slight decrease in the mean thickness $\langle t \rangle$ of the nanoribbons from $\approx$ 50 nm down to $\approx$ 30 nm when the p_1 increased from 0.1 to 13 Torr, while further increasing p_1 results in the absence of nanoribbons (Figure 7.3b).

According to all statistical calculations of the nanoribbons thickness distribution as a function of synthesis parameters, the initial pressure $p_1 = 5$ Torr and time $t_2 = 0$ min were found to be optimal for obtaining the highest yield (up to 18%) of the nanoribbons in $10 - 15$ nm range (Paper V).

7.2.2 Transport properties of ultrathin nanoribbons

The synthesis parameters not only influence the geometry of the nanoribbons but also determine their growth mechanism, affecting their transport properties. Bi_2Se_3 nanoribbons synthesised using parameters $p_1 = 5$ Torr and $t_2 = 0$ min were transferred to a Si/SiO_2 (300 nm) substrate for transport measurements.

For all measured devices, the sheet resistance linearly decreased with the decrease in temperature (a metallic transition, due to bulk defects), reaching saturation at about 30 K (Figure 7.4a).

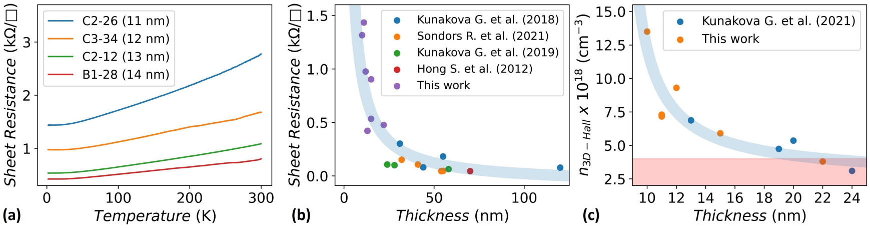

Figure 7.4: (a) Sheet resistance of different nanoribbons as a function of temperature. (b) Sheet resistance as a function of nanoribbon thickness measured at 2 K. Purple marks are data from this work, and the coloured marks (blue, orange, green and red) are data from Kunakova G., et al. (2018) [7], Sondors R. et al. (2021) [71], Kunakova G., et al. (2019) [73] and Hong S. et al. (2012) [74], respectively. The light-blue-shaded region is a guide to the eye, indicating a dramatic increase in sheet resistance as thickness decreases. (c) The three-dimensional concentration of charge carriers $n_{3D-Hall}$ as a function of nanoribbons thickness. Orange marks are data from this work, the blue marks are data from Kunakova G., et al. (2021) [8], respectively. The light-blue-shaded region is a guide to the eye, and the pink-shaded region indicates the upper bound for the bulk carrier concentration [7].

Reduction of the nanoribbons' thickness increases their surface-to-volume ratio, which in turn reduces the metallic bulk conduction of Bi_2Se_3 nanostructures. This is evidenced by the increase in the sheet resistance of the nanoribbons with the decrease in their thickness (Figure 7.4b). The value of the three-dimensional charge carrier concentration (extracted from the Hall effect measurements) increases as the thickness of the nanoribbons decreases, indicating a stronger contribution from TI surface carriers, since the bulk contribution becomes less dominant. The dependence of $n_{3D-Hall}$ as a function of the nanoribbon thickness is presented in Figure 7.4c.

Transport properties of the obtained Bi_2Se_3 nanoribbons with thicknesses below 15 nm showed that the values of the sheet resistance for these nanoribbons are approximately an order of magnitude higher in comparison with the values reported previously for the thicker Bi_2Se_3 nanoribbons synthesised using catalyst-free PVD. However, an increase in carrier concentration and sheet resistance is not the only effect observed after nanoribbon thinning. Further, coherent transport in ultra-thin nanoribbons, observed due to the peculiar morphology as a result of changes in the growth mechanism, will be considered.

Figure 7.5 shows AFM images and surface profiles for 12 and 22 nm thick nanoribbons, grown during the same process ($p_1 = 5$ Torr and $t_2 = 0$ min). The thin nanoribbon (Figure 7.5a) shows the presence of small grains on the surface, while the thicker one (Figure 7.5b) has an atomically flat surface. These images indicate that the growth kinetics of thin nanoribbons differ from that of thick ones.

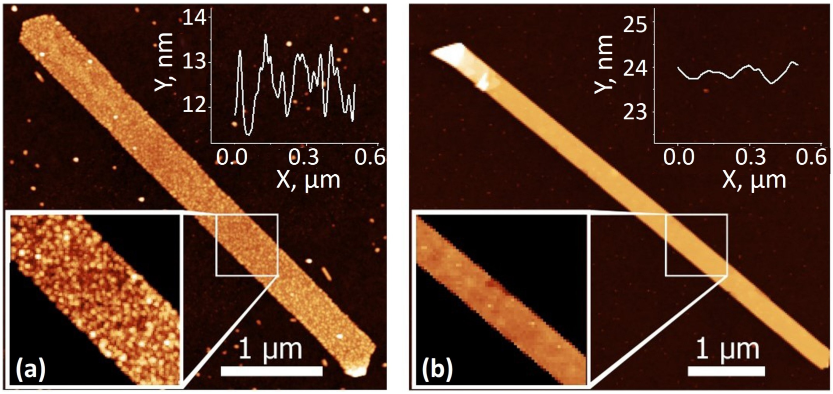

Figure 7.5: (a) AFM image of a 12 nm thick nanoribbon grown with the rough mechanism. The inset is the surface profile with RMS roughness around $\sim$ 670 pm. (b) AFM image of a 22 nm thick nanoribbon in which the rough-to-smooth growth transition mechanism occurred. The inset is the surface profile with RMS roughness around $\sim$ 130 pm. The y-axis range is identical to the one of the inset on the panel (a) to emphasize the significant difference.

Now a possible growth scenario that can occur when time t_2 is changed from 15 to 0 min will be proposed. During the vapour-solid deposition process, the formation of nanoribbon-like nanostructures is determined by growth kinetics. As mentioned earlier, the top surface of the nanoplates (seeds) is chemically saturated. As a result, newly arriving growth species (adatoms) will diffuse to side edges with atomic steps, ledges, and kinks. The two-dimensional nucleation probability on the surface of nanoribbons can be described as [75]:

$$P_N = Aexp\left(\frac{\pi\sigma^2}{{k_B}^2T^2\ln\left(p/p_0\right)}\right), \tag{7.2}$$

where P_N is the nucleation probability, A is a constant, σ is the surface energy, k_B is the Boltzmann constant, T is the absolute temperature, p is the actual vapour pressure, and p_0 is the equilibrium vapour pressure corresponding to the temperature T. If the vapour pressure $p < p_0$, the chemical potential of the crystal is larger than that of the vapour and the crystal should sublimate. However, if $p > p_0$ the vapour should crystallise. In our experiment, the deposition of nanostructures proceeds in the supersaturated state $(p/p_0) > 1$. Therefore, the supersaturation ratio (p/p_0) and temperature are two dominant factors in controlling the morphology of the products in the vapour-solid growth process [76].

The amount of evaporated material at the start of nanoribbon growth in the case of $t_2 = 0$ min is much less than in the case of the standard growth, where $t_2 = 15$ min. Nanoplates (seeds) deposited only over time t_1 have smaller thicknesses in comparison with flakes deposited during time $t_1 + t_2$. However, their side edges with atomically rough steps, regardless of the plate thickness, act as effective "catalyst" that initiates the growth of nanoribbons in the lateral direction. As in the case of the vapour-liquid-solid growth mechanism, the edge side area of the "catalyst" plate, from which the nanoribbon growth occurs, can be saturated with adatoms more easily for thinner seeds compared to thicker ones [77]. The value of supersaturation at the edge surface tends to decrease for plates with higher thicknesses. A decrease in supersaturation may lead to the rough-to-smooth transition of the crystal growth mechanism [78]. In our case, during the same deposition process, nanoribbons less than 15 nm thick have a rough surface, while ribbons more than 15 nm thick have a smooth morphology, indicating a 2D growth mechanism. This suggests that a transition from rough to smooth growth takes place in our experiment. Moreover, this growth scenario is consistent with the appearance of a high yield of thin nanoribbons. At some point, the growth particles from the vapour cannot saturate the side edge of very thick seeds, and the chemical potential of the crystal itself becomes larger than that of the vapour $(p_0 > p)$. In this case, the growth of the thickest nanoribbons may stop, while the growth rate of crystals from saturated seeds increases with a decrease in their thickness. The difference in morphology between thicker and thinner nanoribbons strongly affects the charge transport properties of the topological surface states.

The magnetoresistance R_{xx} as a function of the magnetic field (up to 12 T) applied perpendicularly to the surface of the nanoribbons at low temperatures (2 K) was measured. Thin Bi_2Se_3 nanoribbons with thicknesses below 15 nm show well-pronounced magnetoresistance oscillations in the entire range of the magnetic fields, while for thicker nanoribbons they are only visible at high fields ($B > 5$ T) (Figure 7.6a). This difference can be explained by the coherent scattering of electron waves from surface irregularities associated with the peculiar morphology of the thin nanoribbons (due to different growth mechanisms compared to the thicker ones), which leads to the appearance of Altshuler-Aronov-Spivak (AAS)-like orbits. The Hall resistance R_{xy} was also measured to estimate the sheet carrier density n_{2D} of individual nanoribbons (Figure 7.6b). The values of n_{2D} extracted from the data are respectively 1.2×10^{13} cm^{-2} for Device I (thickness $t = 12$ nm, and width $w = 360$ nm), and 8.8×10^{12} cm^{-2} for Device II ($t = 22$ nm, and $w = 310$ nm), while the negative slope indicates n-type carriers for both devices.

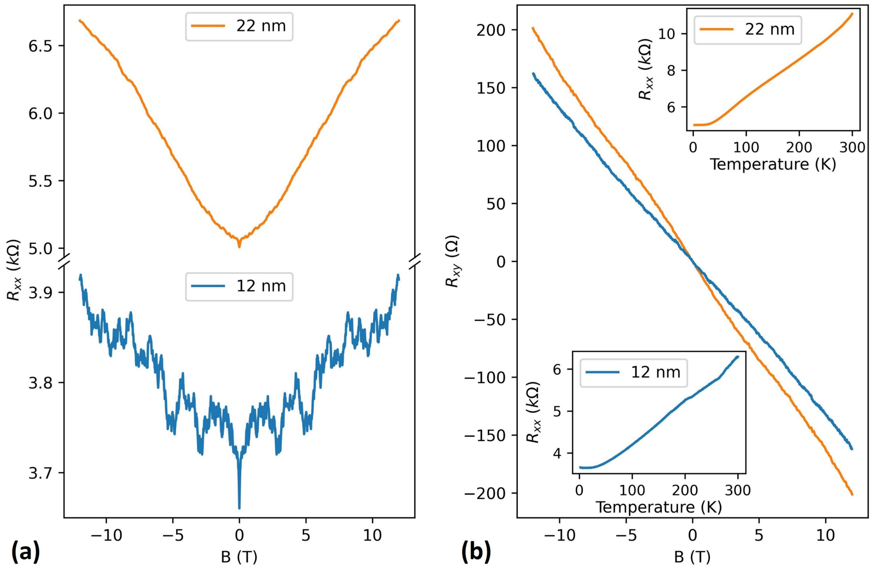

Figure 7.6: The magnetic field dependence of the longitudinal R_{xx} (a) and transverse R_{xy} (b) resistances for 12 nm (blue, Device I) and 22 nm (orange, Device II) thick ribbons measured at 2 K, respectively. The insets in (b) represent the metallic temperature dependence of R_{xx} for the two devices.

For the thick nanoribbon ($t = 22$ nm, Device II), pronounced oscillations were found by subtracting a polynomial background from the magnetoresistance data and plotting the obtained results in $1/B$ (inset of Figure 7.7a). The observed oscillations are associated with a quantum phenomenon known as Shubnikov-de Haas oscillations. Fourier transform (FT) analysis on the SdH oscillations was carried out to determine the oscillation frequencies. However, due to the small number of oscillation periods observed in the field range of the measurements, the resolution of the FT power spectrum is low. So, the experimental FT data-points were fitted with a Gaussian approximation to determine the frequency more accurately. One standard deviation of the fitting parameter defines the error bars when determining the frequency. Thus, the FT data fit of the oscillations reveals a dominant frequency $F_1^{II} = 17.5 \pm 4.3$ T and an additional (second) frequency $F_2^{II} = 35.1 \pm 4.0$ T, corresponding to $n_{2D\_1}^{II} = 4.23 \pm 1.04 \times 10^{11}$ cm^{-2} and $n_{2D\_2}^{II} = 8.49 \pm 0.97 \times 10^{11}$ cm^{-2} according to the Onsager relationship [7, 79], respectively.

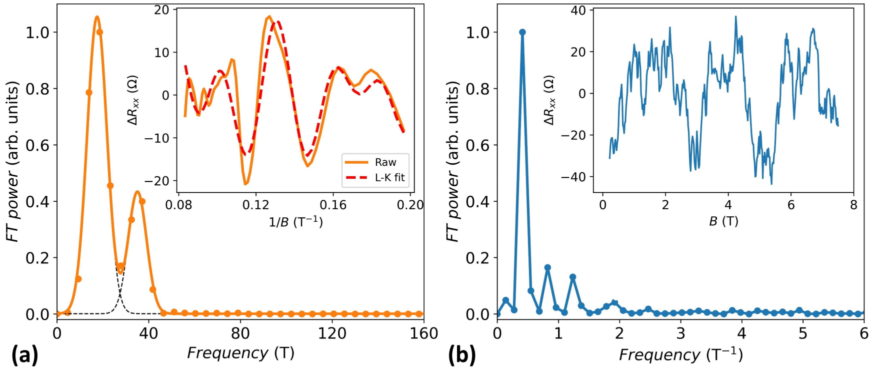

Figure 7.7: FT power spectra of (a) $\Delta R_{xx}\,(1/B)$ (shown in the inset) for a 22 nm thick (Device II) nanoribbon and (b) $\Delta R_{xx}\,(B)$ (in the inset) for a 12 nm thick ribbon (Device I) measured at 2 K, respectively. A 5^{th}-order polynomial was subtracted to remove the magnetoresistance background from the data. The dot marks correspond to the experimental data extracted from the FT power spectra. The black dashed lines represent the Gaussian fits of the experimental points for two observed peaks (panel (a)). The solid line represents the sum of Gaussian fits. The red dashed line in the inset of panel (a) represents the multi-frequency Lifshitz-Kosevich fit of experimental data.

The oscillatory component of ΔR_{xx} was also fitted by the Lifshitz-Kosevich expression with a Berry phase included to take into account the topological character of the system [79–85]:

$$\Delta R_{xx} \simeq \Delta R_0 \sqrt{\frac{B}{2F}} R_T R_D \cos\left[2\pi(\frac{F}{B} + \frac{1}{2} + \varphi)\right], \tag{7.3}$$

where the first pre-factor ΔR_0 is the amplitude of the oscillation in the high-field limit $1/B \to 0$. The second pre-factor is the temperature reduction factor $R_T = \frac{\lambda m^* T/B}{\sinh(\lambda m^* T/B)}$, with $\lambda = \frac{2\pi^2 k_B T}{\hbar\omega_c} = \frac{2\pi^2 k_B T m^*}{\hbar e B}$, where m^* is the cyclotron mass, T is the temperature, k_B is Boltzmann's constant. The third pre-factor is the Dingle reduction factor representing the exponential decrease of ΔR_{xx} with decreasing field B: $R_D = e^{-\lambda_D}$, with $\lambda_D = \frac{2\pi^2 k_B T_D}{\hbar\omega_c} = \frac{2\pi^2 k_B T_D m^*}{\hbar e B} = \frac{\pi m^*}{\tau_D e B}$, where T_D is the Dingle temperature, τ_D is the Dingle scattering time, which is related to the quantum mobility by $\mu = e\tau_D/m^*$. The oscillation of ΔR_{xx} is described by the cosine term with a frequency F and phase factor $\varphi = \beta - \delta$. The value of the phase offset $\beta = 1/2$ should correspond to Dirac fermions with a π Berry phase, and $\beta = 0$ (or equivalently 1) should correspond to trivial fermions. In turn, the phase shift correction δ is associated with the Fermi-surface dimension ($\delta = 0$ for the 2D Fermi surface and $\delta = -1/8$ or $+1/8$ for the 3D system ($-$ for electrons and $+$ for holes), respectively) [84].

The matching of the fit and the raw data is remarkable (inset of Figure 7.7a). Moreover, two fitted frequencies ($F^{II}_{1-LK} = 23.6 \pm 0.7$ and $F^{II}_{2-LK} = 35.9 \pm 0.6$ T) converged to the values obtained from the FT analysis. In conclusion, the presence of two frequency peaks in a high magnetic field leads to the beating pattern of SdH oscillations caused by two different electron densities, originating from the top surface states and the bulk.

As shown in Figure 7.6a, thin nanoribbons (less than 15 nm) exhibit instead a strong oscillatory pattern in the entire range of a magnetic field. The phenomenology of these oscillations is compatible with that of universal conductance fluctuation. However, the FT calculated from $\Delta R_{xx}(B)$ below 7 T (to exclude the possible impact of SdH on the magnetoresistance) shows instead a single (dominant) peak at $F^{I}_{UCF} = 0.41 \pm 0.07$ T^{-1} (Figure 7.7b). A well-defined periodicity is unusual for conventional UCF. However, it can be explained if the fluctuations originate from AAS-type orbits, with similar characteristic areas that become accessible because of the specific surface morphology of the thin nanoribbons [47].

The characteristic AAS area of these orbits can be calculated as $S = \phi \times F^{I}_{UCF}$, where $\phi = h/2e$ is the magnetic flux quantum relevant for AAS oscillations. From the extracted orbit area $S = 0.0008$ μm^2 one can estimate a characteristic path length for the electrons as $L \sim 2\sqrt{\pi S} = 100$ nm. The calculated value $2R_{AAS} = 32$ nm (for circular orbits $L = 2\pi R_{AAS}$ is in good agreement with the characteristic size of the surface irregularities of about 29.4±1.6 nm, which was extracted using the two-dimensional fast Fourier transform (2D-FFT) of AFM image presented in the inset of Figure 7.5a (Figure 7.8).

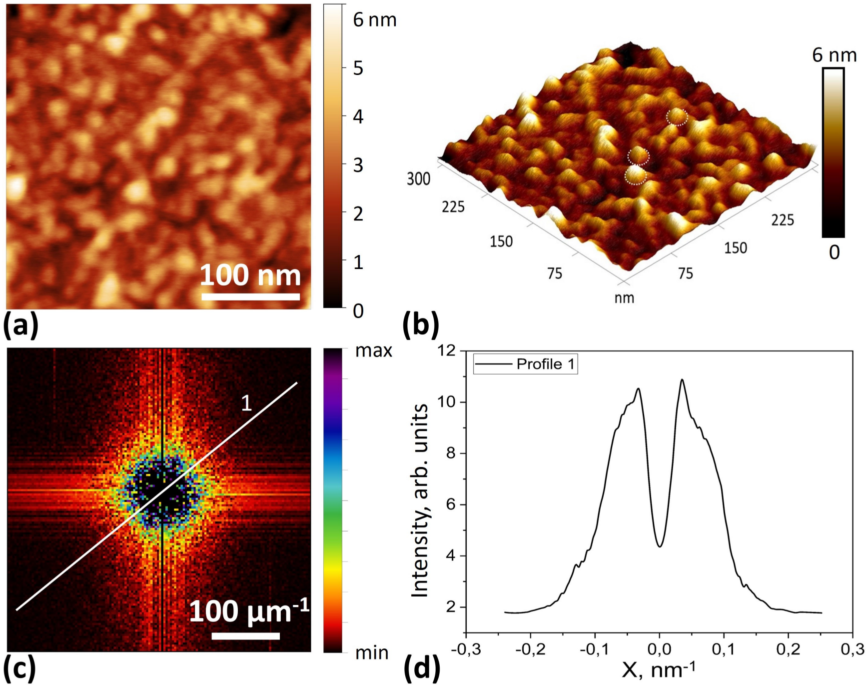

Figure 7.8: AFM measurements of a nanoribbon surface (Device I). (a) Scan size of 310×310 nm^2. (b) 3D AFM plot of the image presented in panel (a). White dashed circles delimitate possible AAS orbits. (c) The frequency spectrum image of the data from panel (a). (d) Profile 1 taken from 2D FFT-map from panel (c): the frequency value at the peak corresponds to 0.034 ± 0.002 nm^{-1}.

The transport properties of Device III based on a Bi_2Se_3 nanoribbon with a maximized surface-to-volume ratio (thickness $t = 12$ nm, and width $w = 85$ nm) will be reviewed further. The $R_{xx}(B)$ pattern changed after warming up to room temperature (typical behaviour for UCF phenomenon), which excludes that the magnetoresistance oscillations can be only attributed to SdH oscillations (Figure 7.9a). The onset of SdH oscillations requires the condition $\mu B \gg 1$, where μ is the electron mobility. This condition is not usually satisfied below 5 - 6 T considering the typical Hall mobility values in our nanoribbons are between 1200 - 2100 cm^2/V·s as shown in Chapter 4. Indeed, the estimated values of Hall mobility for Device I and Device II are $\mu_1 = 1075$ and $\mu_2 = 1210$ cm^2/V·s, respectively.

To determine whether the UCF come from interference effects in the bulk or the 2D topological surface, the angular dependence of R_{xx} with respect to the out-of-plane magnetic field was studied. In an ideal 2D electron system, the interference pattern depends only on the normal component of the magnetic field $B_\perp = B\cos\theta$, where θ is the angle between the direction normal to the nanoribbon plane and the orientation of a magnetic field. After subtracting a 5^{th}-order polynomial background the resulting oscillation patterns $\Delta R_{xx}(B)$ (measured at various angles θ) superimpose if plotted against $1/B_\perp$ below 5 T, which confirms the 2D origin of UCF (Figure 7.9b). However, the analysis becomes more complicated at higher fields due to the coexistence of UCF and SdH oscillations.

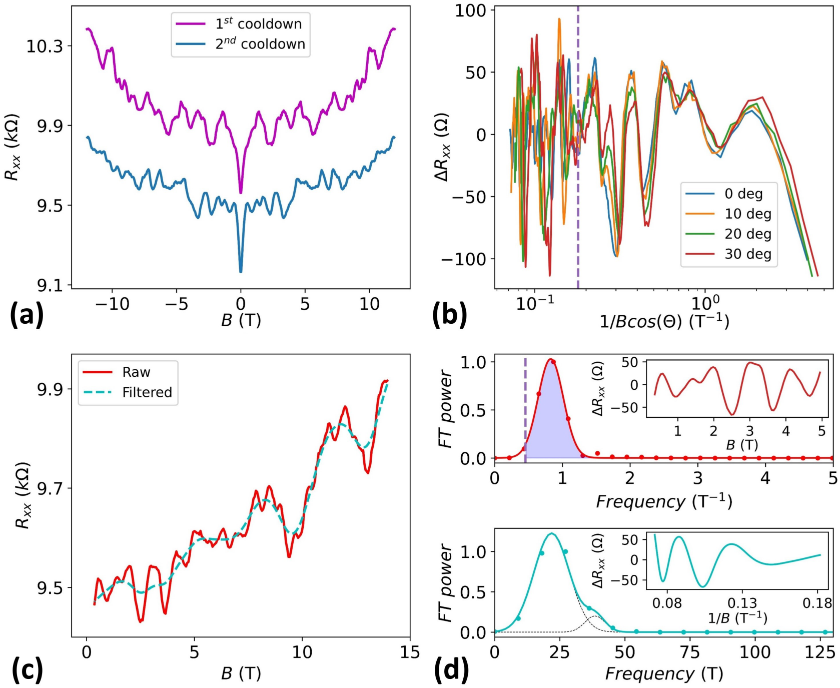

Figure 7.9: (a) The magnetoresistance of Device III (thickness $t = 12$ nm, and width $w = 85$ nm) as a function of a magnetic field after the first and second cooldowns, measured at 2 K. (b) Background-removed resistance ΔR_{xx} as a function of $1/B\cos\theta$. The x-axis is plotted on a logarithmic scale to show a clear data superimposition at low magnetic fields. The vertical dashed line denotes a magnetic field of 5.5 T. (c) Filtering data to exclude UCF (Device III, $\theta = 30$ deg): the red curve is the original data, and the cyan dashed curve is low-pass filtered data (using as cut-off frequency F_c^{III} from the top panel in (d)). (d) Fourier analyses of $\Delta R_{xx}(B)$ (top panel) from the low magnetic field region (in the inset) and the obtained oscillations after filtering $\Delta R_{xx}(1/B)$ (bottom panel (inset)).

In general, the coherence of the AAS-like orbits associated with the specific morphology of the samples is also observable at higher magnetic fields. To remove the contributions of UCF from the magnetoresistance, a low-pass Butterworth filter with a cut-off frequency $F_c^{III} = F_{UCF}^{III} - 2\delta_G$ was applied (Figure 7.9c). Here $F_{UCF}^{III} = 0.83 \pm \delta_G$ T^{-1} is FT frequency extracted from UCF oscillations in a low magnetic field (below 5.5 T, upper panel of Figure 7.9d) and $\delta_G = 0.19$ T^{-1} is the standard deviation of the Gaussian distribution.

The filtered curve was subtracted by a 5^{th}-order polynomial background in the $1/B$ field. Since the interference between UCF and SdH oscillations is observed above $5-6$ T, the subtracted curve was considered at magnetic fields above 5.5 T. As in Figure 7.7a, the power spectrum data points obtained from the FT of the filtered curve were fitted by the Gaussian approximation. The resulting data fit gives one dominating frequency $F_{1-FT}^{III} = 21.9 \pm 6.8$ T and a second frequency $F_{2-FT}^{III} = 38.6 \pm 3.9$ T, with the corresponding 2D carrier concentrations about $n_{2D-1}^{III} = 5.3 \pm 1.64 \times 10^{11}$ cm^{-2} and $n_{2D-2}^{III} = 9.3 \pm 0.94 \times 10^{11}$ cm^{-2}, respectively (Figure 7.9d). The presence of two peaks with different frequencies results in a beating pattern of SdH oscillations.

The same filtering procedure of magnetoresistance oscillations was applied to $R_{xx}(B)$ measured at different θ angles. It should be noted here that due to the different periodicity of the observed phenomena (B-periodic UCF, associated with AAS-orbits [47], and $1/B$-periodic SdH [86]) the low-pass filter can cut off the high-frequency component of SdH oscillations when filtering UCF. However, the Fourier spectrum after filtering shows a similar pattern as compared to a thicker nanoribbon (Device II, Figure 7.7a) in which the UCF is not so pronounced, and no filtering was applied for this analysis. This legitimates our procedure.

Finally, to show that the SdH oscillations extracted using the UCF filtering procedure can be attributed to the 2D quantum phenomena, the dependence of R_{xx} at high magnetic fields ($B \geq 5$ T) as a function of the angle θ was studied. The plots of ΔR_{xx} in $1/B$ (measured at 2 K) for several angles after applying the filtering procedure are presented in Figure 7.10a. Since the resolution of the FT spectrum is low, the filtered ΔR_{xx} curves for different angles of the magnetic field were fitted by the multi-frequency Lifshitz-Kosevich function (Eq. 7.3) using the least-squares method. The fitted curves are presented by red dashed lines in Figure 7.10a. The frequencies $F_{1-LK}^{III} = 25.02 \pm 0.09$ T and $F_{2-LK}^{III} = 46.4 \pm 0.11$ T are very similar to the frequency values obtained using FT ($F_{1-FT}^{III} = 21.9 \pm 6.8$ T and $F_{2-FT}^{III} = 38.6 \pm 3.9$ T, Figure 7.9d bottom panel). The carrier mobility: $\mu_1^{III} = 8980$ and $\mu_2^{III} = 1830$ $\mathrm{cm}^2/\mathrm{V{\cdot}s}$ was obtained from the Dingle scattering time ($\mu = e\tau_D/m^*$). Such a high quantum mobility (up to 10000 $\mathrm{cm}^2/\mathrm{V{\cdot}s}$) was previously observed in Bi_2Se_3 nanoribbons with a thickness below 30 nm [7]. The angular dependence of the obtained frequencies is presented in Figure 7.10b. It is clearly visible that F_{1-LK}^{III} follows the $1/\cos\theta$ trend (typical for 2D electron systems), while F_{2-LK}^{III} exhibits a weak angular dependence, which is typical for bulk electrons [7, 82]. Thus, the high mobility, angular dependence $1/\cos\theta$ together with the phase factor $\varphi \approx 0.5$ allow to conclude that the frequency F^{III}_{1-LK} corresponds to carriers from surface states, and the frequency F^{III}_{2-LK} represents bulk carriers. This assumption is further confirmed by measurements with an applied back-gate voltage.

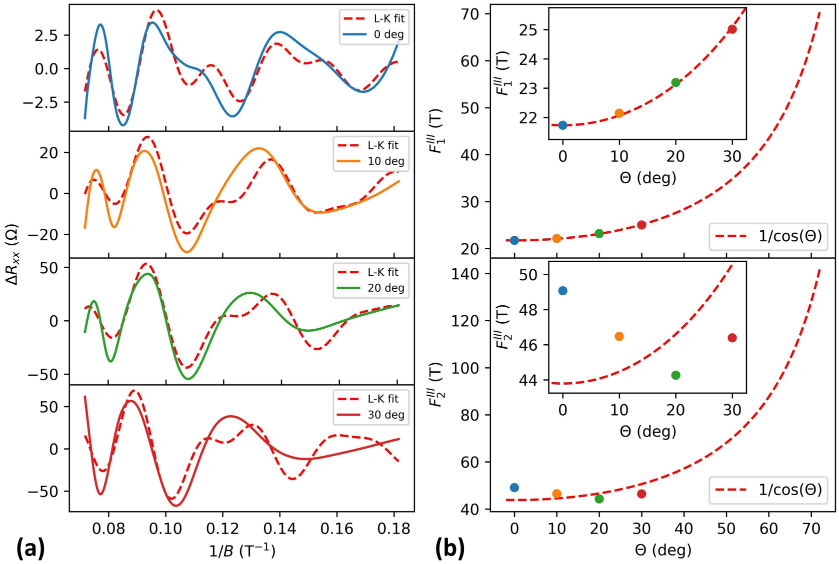

Figure 7.10: (a) Shubnikov-de Haas oscillations of a Bi_2Se_3 nanoribbon (Device III) after subtracting the background and UCF. The curves are fitted by the multi-frequency Lifshitz-Kosevich function (Eq. 7.3, red dashed lines). (b) SdH oscillation frequencies obtained from the Lifshitz-Kosevich fit as a function of the applied magnetic field angle (the colour of the dots corresponds to the colour in panel (a)). The measurements were carried out at a temperature of 2 K. The red dashed lines represent the $1/\cos\theta$ fit. Insets are the zoom-in region to show a clear dependence of F^{III}_{1-LK} as a function of angle and a weak angular dependence for F^{III}_{2-LK}.

The R_{xx} as a function of the gate voltage has been studied for Device III. When the back-gate voltage $V_g = -8$ V is applied to the nanoribbon, frequency $F^{III}_{1\_0V\_LK} = 21.7\pm0.01$ T changed slightly to $F^{III}_{1\_-8V\_LK} = 21.3\pm0.02$ T, while the second frequency $F^{III}_{2\_0V\_LK} = 49.1\pm0.01$ T shifted to $F^{III}_{2\_-8V\_LK} = 38.8 \pm 0.03$ T. Due to screening effects, the gate voltage should first be able to deplete the layers closest to the interface. Indeed, it has been recently reported that for Bi_2Se_3 nanoribbons as thin as 9 nm [8] the effect of the back-gate on the top surface electrons becomes visible only after full depletion of the bottom surface states and the accumulation layer. This fact confirms that the SdH oscillations with frequency F^{III}_1 observed in the measurements belong to the top surface states, while the second frequency F^{III}_2 is attributed to the bulk states.

In addition to the expected increase of the resistance due to the depletion of the nanoribbon carriers by the gate, the reproducible oscillations of R_{xx} as a function of back-gate voltage V_g were observed (Figure 7.11a). Further, it will be shown that size quantization effects are essential in the fabricated devices.

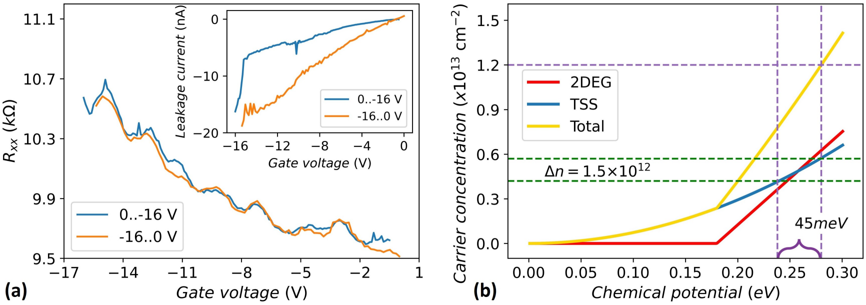

Figure 7.11: (a) R_{xx} as a function of back-gate voltage. The blue (0.. − 16 V) and orange (−16..0 V) curves represent two scan sweeps with different directions. During the measurements, the leakage current was monitored and kept below 3% of the measured current (the inset). The measurements were carried out at a temperature of 2 K. (b) The charge carrier concentration as a function of the Fermi energy. The red line is the energy dependence in the case of regular 2DEG, the blue line is the energy dependence in the case of Dirac states, and the yellow one is the energy dependence at the substrate/nanoribbon interface, where both types of carriers exist.

The band structure of surface carriers in TI nanoribbons is described by the momentum vector k along the nanoribbon axis and the angular momentum l (Section 2.8):

$$E_l(k) = \pm \hbar v_F \sqrt{k^2 + \frac{\pi (l)^2}{S}}, \tag{7.4}$$

where l is half-integer $\pm\frac{1}{2}, \pm\frac{3}{2}, \ldots$, $\hbar$ is the reduced Planck constant, v_F is Fermi velocity (for Bi$_2$Se$_3$ is 5×10^5 m·s^{-1}), S is the cross-sectional area of the nanoribbon. The oscillations observed in $R_{xx}(V_g)$ could be a sign of the sub-band formation (Eq. (7.4)): when the chemical potential crosses one sub-band, a new conduction channel becomes accessible, leading to pronounced resistance dips.

The charge carrier concentration of a trivial 2DEG is given by $n_{2DEG} = k_F^2/2\pi$. The corresponding Fermi energy can be calculated as:

$$E_{F(2DEG)} = \frac{\hbar^2 k_F^2}{2m^*} = \frac{\hbar^2 \pi}{m^*} n_{2DEG}, \tag{7.5}$$

where k_F is Fermi wavevector, m^* is effective mass, for the Bi$_2$Se$_3$ case $m^* = 0.15 m_e$. For Dirac fermions the carrier concentration is $n_{SS} = k_F^2/4\pi$, and the Fermi energy can be written as:

$$E_{F(SS)} = \hbar k_F v_F = \hbar v_F \sqrt{4\pi n_{SS}}. \tag{7.6}$$

Considering that the bottom of the conduction band is located 180 meV above the Dirac point [87], one can estimate the position of the Fermi level from the total charge carrier concentration at the substrate/nanoribbon interface using Eqs. (7.5) and (7.6). Thus, for a typical carrier concentration in our nanoribbons on a Si/SiO$_2$ substrate of $n \simeq 1.2 \times 10^{13}$ cm^{-2}, the calculated E_F is ≈ 270 meV. The contributions to the total carrier concentration as a function of the chemical potential measured from the Dirac point are shown in Figure 7.11b, where the blue line represents the bottom TSSs, the red line is the trivial 2DEG, and the yellow one is the sum of the two.

To estimate the carrier concentration change induced by the applied gate voltage, the capacitance between the back-gate electrode and the bottom surface of the 3D-TI nanoribbon was numerically computed using COMSOL Multiphysics. So, considering a simple asymmetric metallic parallel plate geometry, where one electrode is given by the doped silicon and the other is the nanoribbon, the static surface charge carrier density per applied gate voltage $\sigma \simeq 1.5\ \times 10^{-4}$ C/m^{2}V was numerically calculated. Considering this σ, one can estimate the change of the carrier concentration at the bottom interface as $\Delta n = \sigma V_g/e = 1.5 \times 10^{12}$ cm^{-2} for the maximum applied voltage ($V_g = -16$ V). It can be assumed that the change of carrier concentration occurs mainly in the bottom TSSs, which is justified by the fact that the trivial 2DEG at the bottom extends well inside the bulk, and therefore is screened by the TSS [87]. In this case, the Δn corresponds to a change in the chemical potential of ≈ 45 meV (Figure 7.11b). For the dimensions of the nanoribbon in this study (Device III), the distance between the sub-band minima $\Delta = hv_F/C \approx 9$ meV, where h is the Planck constant and $C = 2(w+t)$ is the circumference of the nanoribbon with a rectangular cross-section (Section 2.8) was found. The change in the chemical potential would therefore correspond to the crossing of approximately 5 sub-bands which is very close to the 5 to 6 $R_{xx}(V_g)$ oscillations observed in Figure 7.11a.

In the presence of a magnetic field applied along the topological insulator nanoribbon, Eq. (7.4) can be re-written as (Section 2.8):

$$E_l(k) = \pm \hbar v_F \sqrt{k^2 + \frac{\pi(l - \phi/\phi_0)^2}{S}}, \tag{7.7}$$

where $\phi = BS$ is a magnetic flux threading the cross-section area S of the nanoribbon, and $\phi_0 = h/e$ is the fundamental flux quantum. According to Eq. (7.7), the energy-momentum relation is periodic in ϕ/ϕ_0, which leads to the appearance of Aharonov-Bohm oscillations of G_{xx} [88]. In the quasi-ballistic regime, h/e AB oscillations are predicted to dominate over $h/2e$ AAS oscillations. AAS oscillations originate from interference between time-reversed paths, due to weak anti-localization and, thus, differ from AB oscillations in their physical origin. In the quasi-ballistic regime, the circumference of the nanoribbon should not be much longer than the mean free path l_e. The pattern of these oscillations also depends on the carrier density, which can be changed by applying a gate voltage. At the Dirac point, magnetoconductance minimum at $\phi/\phi_0 = 0$ and maximum at $\phi/\phi_0 = 0.5$ should be observed. However, even away from the Dirac point, the AB phase can alternate with applied gate voltage, when E_F is crossing the sub-bands [88]. Figure 7.12a presents the magnetoconductance as a function of two different back-gate voltages (0 and −8 V), demonstrating that maxima and minima at finite magnetic flux alternate with an applied gate and the oscillations period at $V_g = 0$ V is close to ϕ_0, as shown by the FT of $\partial G_{xx}/\partial(\phi/\phi_0)$ (Figure 7.12b). However, there is also a component in the FT at approximately twice the frequency, that can be attributed to AAS. This can be explained by the presence of a strong WAL peak (Figure 7.9a), which indicates that a fraction of the modes has a more diffusive character. Since the gate voltage was not high enough to tune the chemical potential to the Dirac point, the alternating maxima and minima of G_{xx} as a function of gate voltage indicate the crossing of sub-bands by the Fermi level. This behaviour has not previously been observed in non-topological systems. The fact that by decreasing the gate voltage the ratio between the AB and AAS inverts (Figure 7.12b) can be explained by more diffusive modes contributing at $V_g = -8$ V.

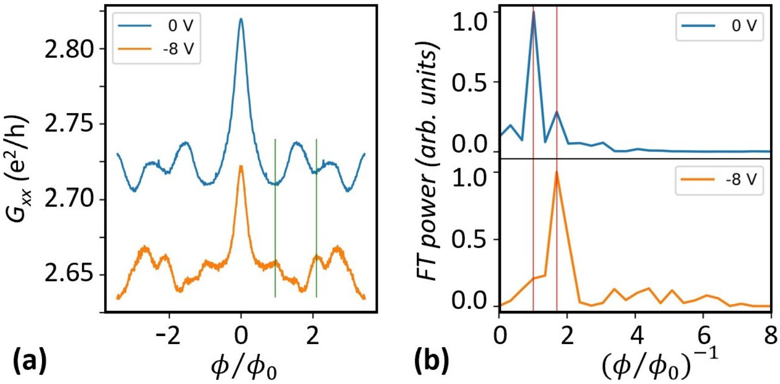

Figure 7.12: (a) The magnetoconductance as a function of ϕ/ϕ_0 for two different back-gate voltages 0 and −8 V. The measurements were carried out at a temperature of 2 K. (b) Fourier transforms of $\partial G_{xx}/\partial(\phi/\phi_0)$ from panel (a).

In summary, the observed phenomena originate from the TSSs and dominate the ultrathin ($t < 15$ nm) nanoribbon transport. Ultrathin nanoribbons show pronounced conductance oscillations as a function of gate voltage, which can be attributed to the ballistic transport and quantized sub-bands. The results highlight the importance of material growth and quantum confinement to exploit the unique properties of TSSs, establishing 3D-TI nanoribbons as a promising platform for a variety of novel applications (Paper VI).

7.3 Strain engineering in Bi_2Se_3 nanostructures

Another effective approach to continuously tune the energy spectrum of TI is strain engineering. Applying strain to a crystal will cause lattice stretching or compressing in different directions, resulting in the change of lattice constants. This results in the change of overlapping and hybridisation of electron orbitals and may be responsible for the modified electronic properties. In experiments, mechanical strain can be applied through the bending of samples or via lattice mismatch between substrates and epitaxy layers. Since the crystal structure of Bi_2Se_3 consists of covalently bonded quintuple layers, which are weakly bonded via van der Waals forces (Figure 1.2), their band structure and especially the Dirac states at the surface are considered to be very sensitive to uniform uniaxial strain. The opportunity to externally tune the Dirac states by applying strain could lead to further improvement in future TI devices [89].

While the synthesis of reduced-size nanostructures or the compensating doping approaches allow optimization of TI material properties before device fabrication and are irreversible, strain engineering provides a reversible route for modifying the electronic structure in TI-based devices. Thus, strain is a particularly exciting way to manipulate and control the Fermi level in TIs, since different types of deformations can lead to different properties [90]. For example, strain may lead to phase transitions from topological to trivial states and vice-versa [91]. It has been theoretically calculated that the electronic band gap of Bi_2Se_3 decreases with tensile in-plane strain and increases with compressive in-plane strain [92].

7.3.1 Applying strain via mechanical bending

Taking into consideration the sensitivity of TSSs to external strain, the magnetotransport measurements of the suspended and supported parts within the same Bi_2Se_3 nanoribbon were performed to investigate the change in transport properties caused by the bending deformation effect. To implement this experiment, devices based on a Bi_2Se_3 nanoribbon, containing the supported and suspended (over a trench with a gate electrode) parts were fabricated (Figures 5.6 and 7.13).

To study the electronic properties and distinguish the difference in source-drain transport between the suspended and supported parts of the device, the magnetotransport measurements with a magnetic field applied perpendicularly to the nanoribbon were performed at 2 K. Figure 7.14a represents the longitudinal sheet resistance, calculated as $R_{xx}(\Omega/\square) = R_{xx}(\Omega) \times w/L$, where w is the actual nanoribbon width and L is the distance between the longitudinal contacts, as a function of a magnetic field. The value $R_{xx}(\Omega/\square)$ is slightly different for the suspended and supported parts. This difference can be attributed to the influence of contact resistance in the case of supported part measurements (three-probe configuration, Figure 7.13a).

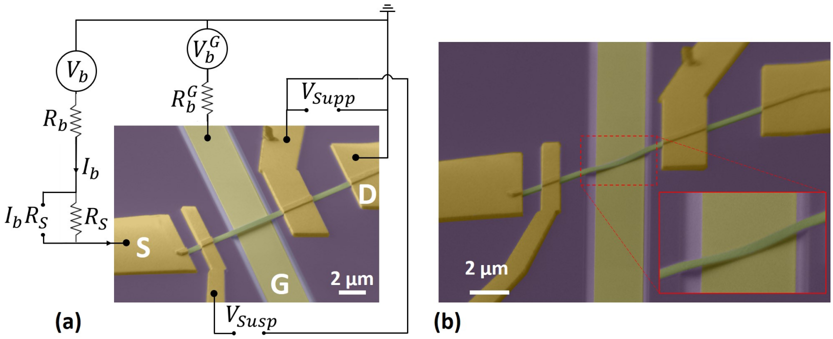

Figure 7.13: Tilted false-colour SEM images of the device, containing the suspended and supported parts. (a) The device (with the measurements scheme) in the "OFF" configuration (the unstrained suspended ribbon above the back-gate electrode). (b) The device in the "ON" configuration (the ribbon is touching the gate).

For both suspended and supported parts of the device, the ΔR_{xx} oscillations were found by subtracting a polynomial background. This effect is associated with the SdH oscillations. The FT of the $d^2\Delta R_{xx}/dB^2$ for the supported part reveals only two frequencies at $F^1_{supp} = 42.3$ T and $F^2_{supp} = 70.6$ T. Following the Onsager relation [79, 93], these frequencies correspond to $n^1_{2D-supp} = 1.02 \times 10^{12}$ cm^{-2} and $n^2_{2D-supp} = 1.71 \times 10^{12}$ cm^{-2}, respectively (Figure 7.14b). A similar multi-frequency pattern (with two dominating frequencies) was previously observed for Bi_2Se_3 nanoribbons with thickness above 30 nm by our group [7]. Since the surface states (at the substrate-nanoribbon interface) are overlapped with the charge accumulation layer having lower charge carrier mobility, the bottom surface SdH oscillations do not usually appear in the magnetoresistance. Moreover, these frequencies (previously observed in [7]) were unaffected by the applied gate voltage (up to -75 V), indicating that they correspond to either bulk or surface state carriers at the top surface (at the nanoribbon-vacuum interface). Thus, observed F^1_{supp} and F^2_{supp} can be attributed to the top surface states at the interface with vacuum and to the bulk, respectively.

For the suspended part, the FT of the $d^2\Delta R_{xx}/dB^2$ oscillations demonstrates three frequencies: $F^1_{susp} = 13.1$ T, $F^2_{susp} = 45.8$ T, and $F^3_{susp} = 70.5$ T, which correspond to $n^1_{2D-susp} = 3.16 \times 10^{11}$ cm^{-2}, $n^2_{2D-susp} = 1.11 \times 10^{12}$ cm^{-2}, and $n^3_{2D-susp} = 1.70 \times 10^{12}$ cm^{-2}, respectively (Figure 7.14c). The appearance of the third (lowest) frequency is attributed to the states from the bottom surface, which are no longer masked by the accumulation layer. Since the SdH frequencies of TI are sensitive to external strain [89], the fact that the frequencies corresponding to the top surface states for the suspended and supported parts remain almost the same is in good agreement with the absence of deformation at the suspended part, as shown in Figure 7.13a.

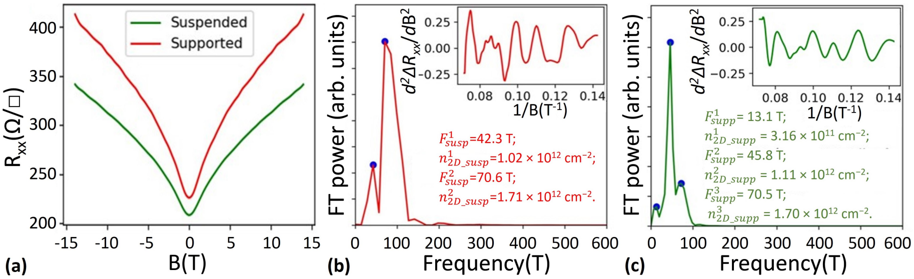

Figure 7.14: Magnetotransport measurements of the device presented in Figure 7.13a. (a) The longitudinal sheet resistance $R_{xx}(\Omega/\square)$ as a function of a magnetic field for the suspended and supported parts. Shubnikov-de Haas oscillations analysis: the Fourier transform power spectra of $d^2\Delta R_{xx}/dB^2$ (presented in the insets) for the supported part shown in (b), and for the suspended part shown in (c), respectively.

After examination of the suspended and supported parts in a relaxed state, the R_{xx} as a function of the gate voltage has been studied. According to existing analytical models of bending [94, 95], the strain of a bent nanoribbon in the thickness direction can be divided into three types: pure elastic, elastoplastic, and pure plastic deformations (Figure 7.15). In the case of pure elastic deformation, the top surface (inner side) of the nanoribbon experiences compressive stress, while the bottom surface (outer side) is under tensile stress, and there is no stress in the middle (neutral layer (NL)). After removing the bending moment M, the elastic deformation will be restored. As shown in [96], if the radius of bending curvature R is much larger than the substrate thickness t and the dominant deformation occurs in the longitudinal direction, the bending strain can be calculated using the formula of the continuum mechanics model for elastic beams: $\varepsilon = t/2R$. In the case of elastoplastic deformation, the NL is displaced from the centroid of the cross-section due to mass conservation effects, which induces a transition of tensile/compressive stresses across the thickness of the nanoribbon. The direction of NL displacement is related to the material properties and the bending curvature. In most cases (for materials with similar behaviour under compressive/tensile stresses), the neutral layer is shifting towards the centre of curvature. After releasing the bending moment M, the elastic deformation is restored, but the plastic deformation remains, which leads to deviations in the dimensions of the nanoribbon. If large enough stretching is applied during the bending process, NL can extend beyond the cross-section, thus the stress gradient across the thickness of the nanoribbon will be reduced and elasticity will decrease sharply (plastic deformation) compared to the pure bending effect [95].

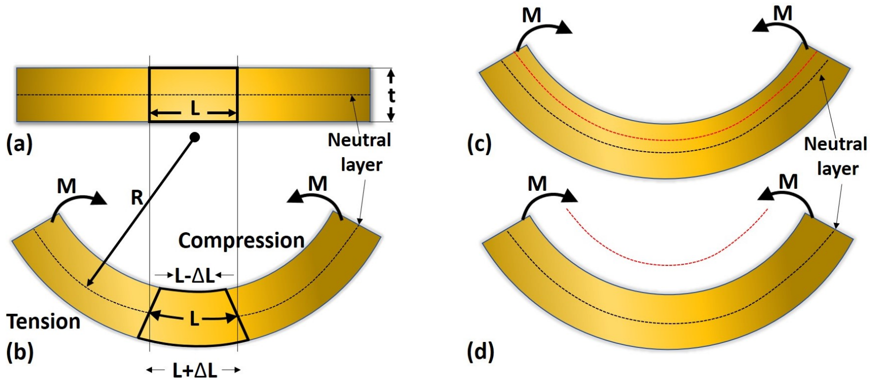

Figure 7.15: Scheme of the distribution of various types of deformation along the thickness of the nanoribbon. (a) A nanoribbon before bending (relaxed state). (b) A nanoribbon under elastic deformation. The predominant deformation occurs in the longitudinal direction. (c) A nanoribbon in elastoplastic deformation regime. (d) Shift of NL beyond the nanoribbon cross-section (the entire cross-section is under tensile strain) (plastic deformation).

Applying a negative voltage to the gate electrode first of all leads to the formation of oppositely charged carriers (depletion layer) at the bottom surface of the nanoribbon. As far as a depletion layer is formed, electrostatic attractive forces (between a negatively charged gate electrode and positively charged bottom surface of the nanoribbon) uniaxially bend the nanoribbon towards the gate. During such bending, the top surface of the nanoribbon experiences compressive stress, while the bottom surface is under tensile stress (Figure 7.15b). When a negative voltage is applied to the device, there is a clear increase in the resistance of the suspended part (Figure 7.16a bottom panel), while the resistance of the supported part remains unchanged (Figure 7.16a top panel (inset)). As the dielectric constant of SiO_2 ($\varepsilon_{SiO2} \approx 4$) is higher than that of vacuum ($\varepsilon_{vac} = 1$), the effect of changing Fermi energy via the gating effect (at the initial moment when the distance to the ribbon is the same) should be more effective in the case of the supported ribbon, even in the presence of the accumulation layer. Thus, the change in resistance when the nanoribbon is suspended is attributed to the mechanical deformation (bending towards the gate).

During the gate voltage sweep, the current between the gate electrode and the nanoribbon I_{GD} (leakage current) also was monitored (Figure 7.16a top panel). At a certain point (−1.45 V) the I_{GD} starts increasing because the distance (separation) between the nanoribbon and the gate becomes small and a tunnelling effect appears. A further increase in the potential at the back gate leads to the emersion of pronounced peaks in the gate-drain current and resistance curves.

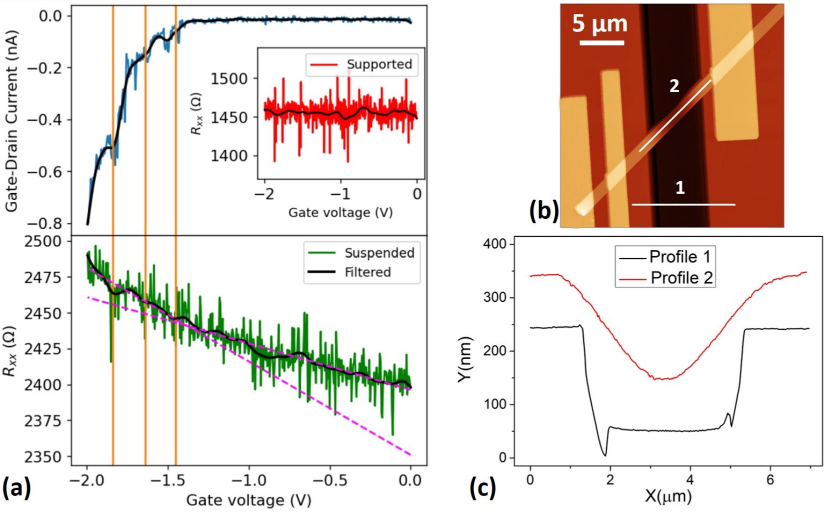

Figure 7.16: (a) I_{GD} and R_{xx} of the suspended and supported (in the inset) parts of the nanoribbon as a function of back-gate voltage. The blue, red, and green lines represent experimental data. The black lines depict filtered data. The vertical orange lines indicate rapid changes due to mechanical deformation. The change in the slope of R_{xx} as a function of gate voltage, depicted by two purple dashed lines, indicates the point of the initial action of additional van der Waals forces to the electrostatic attractive force, resulting in faster deformation of the nanoribbon. (b) AFM image of the device in "ON" mode. (c) Height profile of the bent nanoribbon, presented in (b).

This may be due to the logarithmically increasing tunnelling current with decreasing distance [97], as well as the action of additional attractive van der Waals forces that come into play when the distance between the nanosized objects is several nanometres [98]. The change in the resistance slopes (purple dashed lines in Figure 7.16a bottom panel) indicates the point of initial action of additional van der Waals forces. At −1.84 V (left orange line in Figure 7.16a), I_{GD} starts to increase sharply, which is a sign of the device switching to the "ON" mode. To prove the fact that the increase in source-drain resistance (with gate range from 0 to −1.84 V) is a result of mechanical deformation and not of the tuning of the Fermi energy due to the field effect, the back-gate voltage was further increased to −2 V. After this the gate-drain current value increased linearly from ≈ -0.6 nA to -1.7 μA, which means the device is in stable "ON" mode. Even after that, the increased resistance of the suspended part remains at the same value (does not decrease to the initial value before gating/bending). It is a sign of the deformation effect, since the influence of the electric field does not affect the nanoribbon anymore. AFM image and height profile of the bent nanoribbon in "ON" mode are presented in Figures 7.16b and c, respectively.

To investigate the strain-induced rearrangement of the electronic properties after bending the nanoribbon to the gate contact, magnetotransport was remeasured in "ON" mode at a fixed voltage on the back gate of −2 V. The longitudinal sheet resistance as a function of a magnetic field is presented in Figure 7.17. It is clearly seen, that $R_{xx}(\Omega/\square)$ value of the supported part remains unaffected by the gate voltage, while the suspended part reveals an increase in resistance (3.84%) in comparison with the data presented in Figure 7.14a. Following the analysis of SdH oscillations described above, no difference was found for the supported part before and after applying gate voltage, as expected. However, the suspended part exhibits a slight shift of $F^{2\_-2V}_{susp} = 41.5$ T ($n^{2\_-2V}_{2D-susp} = 1.00 \times 10^{12}$ cm^{-2}) towards lower frequency in comparison with $F^{2}_{susp} = 45.8$ T ($n^{2}_{2D_{susp}} = 1.11 \times 10^{12}$ cm^{-2}), as well as $F^{1\_-2V}_{susp} = 22.4$ T ($n^{1\_-2V}_{2D_susp} = 5.38 \times 10^{11}$ cm^{-2}) towards higher value comparing to $F^{1}_{susp} = 13.1$ T ($n^{1}_{2D_susp} = 3.16 \times 10^{11}$ cm^{-2}), while the third frequency remains the same $F^{3\_-2V}_{susp} \approx F^{3}_{susp}$. All values of the SdH frequencies and 2D carrier concentrations in relaxed and deformed states are summarized in Table 7.1.

Table 7.1: Results of the SdH analysis.

State	Design	Channel	F_{SdH}, T	n_{2D}, cm^{-2}	Deformation
"OFF" (0 V)	Suspended	Top surface	45.8	1.11×10^{12}	relaxed
		Bottom surface	13.1	3.16×10^{11}	relaxed
		Bulk	70.5	1.70×10^{12}	relaxed
	Supported	Top surface	42.3	1.02×10^{12}	relaxed
		Bottom surface	-	-	relaxed
		Bulk	70.6	1.70×10^{12}	relaxed
"ON" (−2 V)	Suspended	Top surface	41.5	1.00×10^{12}	compression
		Bottom surface	22.4	5.38×10^{11}	tension
		Bulk	70.4	1.70×10^{12}	relaxed
	Supported	Top surface	42.3	1.02×10^{12}	relaxed
		Bottom surface	-	-	relaxed
		Bulk	70.6	1.70×10^{12}	relaxed

The observed results are consistent with [89, 99], where the tensile strain shifts the Dirac point towards lower energies, while compressive strain causes a shift to higher energies. So, the SdH frequencies experience upshift/downshift with tension/compression of the nanoribbon on the bottom/top surface. The downshift of $F^{2\_-2V}_{susp}$ frequency (top surface states) is attributed to the induced compressive deformation on the top surface of the nanoribbon. The upshift of $F^{1\_-2V}_{susp}$ (bottom surface states) frequency is attributed to the induced tensile deformation on the bottom surface of the nanoribbon. The fact that the SdH frequency representing bulk charge carriers remains unchanged after the performed measurements and is identical to the value of the relaxed (supported) part, indicates that the NL is not displaced from the centroid of the nanoribbon cross-section, and there is a balance of stresses on the top and bottom surfaces, which is a clear sign of elastic deformation regime. Taking into consideration an elastic deformation regime, the formula $\varepsilon = t/2R$ can be used to estimate the amount of nanoribbon deformation. For a given device, the radius of curvature $R = 21.5$ μm (calculated based on AFM measurements (Figure 7.16c)), and therefore the strain $\varepsilon = 0.22\%$.

After completing the magnetoresistance measurements, the gate swept from -2 to 0.25 V. The gate-drain current as well as the gate dependence of resistance for the suspended part are shown in Figure 7.17c. The linear behaviour of the current-voltage characteristic (IVC), as well as the absence of a change in resistance during the sweep, indicate that the balance between attractive van der Waals (F_{vdW}) + electrostatic (F_{elec}) and repulsive elastic F_{elas} forces is violated ($F_{vdW} + F_{elec} > F_{elas}$), which results in strong attachment of the nanoribbon to the gate electrode (Figures 7.13b and 7.17c bottom inset) [100].

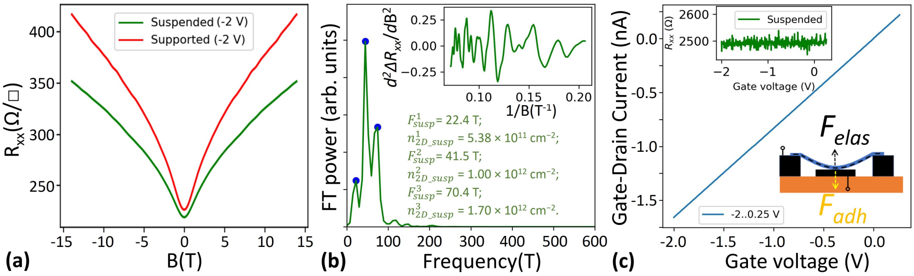

Figure 7.17: Magnetotransport measurements of the device in “ON” mode (with a fixed gate voltage of -2 V). (a) The longitudinal sheet resistance $R_{xx}(\Omega/\square)$ as a function of a magnetic field for the suspended and supported parts. (b) Fourier transform power spectra of $d^2\Delta R_{xx}/dB^2$ (presented in the insets) for the suspended part. (c) The gate-drain current of the suspended part as a function of back-gate voltage after magnetotransport measurements. The top inset is R_{xx} as a function of gate voltage. The bottom inset is the schematic of “ON” mode, when $F_{vdW} + F_{elec} > F_{elas}$.

In summary, uniaxial electrostatic bending of the nanoribbon towards the gate results in compressive strain on the top surface and tensile strain on the bottom surface, as evidenced by a shift in the SdH oscillations frequencies corresponding to these surfaces. The bulk frequency remains the same for the supported part, suspended and suspended deformed parts, which is a sign of the elastic deformation regime. During the bending process, an increase in the source-drain resistance of 3.84% was observed. It is associated with the effect of deformation, since after the switching to “ON” mode the resistance value remained unchanged (Paper VII).

7.3.2 Applying strain via lattice mismatch

Now mechanical strain applied to Bi_2Se_3 thin films via lattice mismatch between graphene substrates and Bi_2Se_3 layers will be observed. Although the physical properties of 2D materials are rather well understood, their wide practical applications are still challenging due to the extreme sensitivity of these materials to the substrates they are supported by. Strain is one of the most prominent phenomena occurring at the interface of the contacting materials, which can change their band structure. Therefore, strain can be considered not only as a problem that must be taken into account when designing a device, but also as an opportunity to tune the properties of the material. As mentioned above, in the case of topological insulators, theoretical studies indicate that the bulk band gap and the spin-polarized Dirac surface states can be tailored by strain.

Strain, defined as the lattice parameter deviation of a material from its bulk value, is quantitatively expressed as $\varepsilon = (a - a_0)/a_0$, where a is the lattice parameter of the strained material and a_0 is the value of the bulk. It is most commonly caused by the lattice mismatch between the deposited material and the substrate.

Since Bi_2Se_3 is a Raman-active material, Raman spectroscopy can be used as a powerful and non-destructive tool for the determination of mechanical strain in this material with micrometric spatial resolution. The correlation analysis of Raman modes positions can be used not only to separate the impact of strain and charge carrier density on the phonon spectrum, but also to calculate the absolute values of these parameters [101]. This fact makes the correlation analysis of Raman modes a unique tool for studying the properties of materials. In this work, a systematic study of mechanical strain in single-layer graphene/Bi_2Se_3 (SLG/Bi_2Se_3) heterostructures with different Bi_2Se_3 layer thicknesses, and in Bi_2Se_3 films of the same thicknesses deposited on quartz substrates (Q/Bi_2Se_3) was performed.

Bi_2Se_3 films of various thicknesses ($3-400$ nm) were synthesised by the physical vapour deposition technique (Section 5.1). SLG was synthesised using a First Nano Easy tube 101 CVD reactor and transferred from copper foil onto quartz (fused silica) slides by the methyl methacrylate (PMMA) polymer-assisted method. Raman spectra of SLG, SLG/Bi_2Se_3 and Q/Bi_2Se_3 structures were obtained at room temperature, by scanning sample areas of 20×20 μm^2 with 785 nm (for Bi_2Se_3 films) and 473 nm (for graphene) excitation wavelengths and 100× objective. Throughout these measurements the edge filter cutting at ≈ 85 cm^{-1} was used, so only two of the four Raman active modes were observed.

To perform the correlation analysis of Bi_2Se_3 films deposited on quartz and graphene the experimental Raman datapoints of Bi_2Se_3 were plotted in the coordinates of a higher frequency mode vs lower frequency mode (A^2_{1g} vs E^2_g). Figure 7.18a indicates the pronounced scattering of datapoints of the Bi_2Se_3 ultra-thin films deposited on quartz along the straight lines with the slope ~ 0.85 (this value was obtained from a linear fitting of datapoints for Bi_2Se_3 films deposited on quartz, Figure 7.18a, inset). The deviation of experimental data from their linear fit is less than 0.5 cm^{-1}, which is comparable with the spectral resolution of the Raman measurements and reveals strong reliability of the claimed dependency.

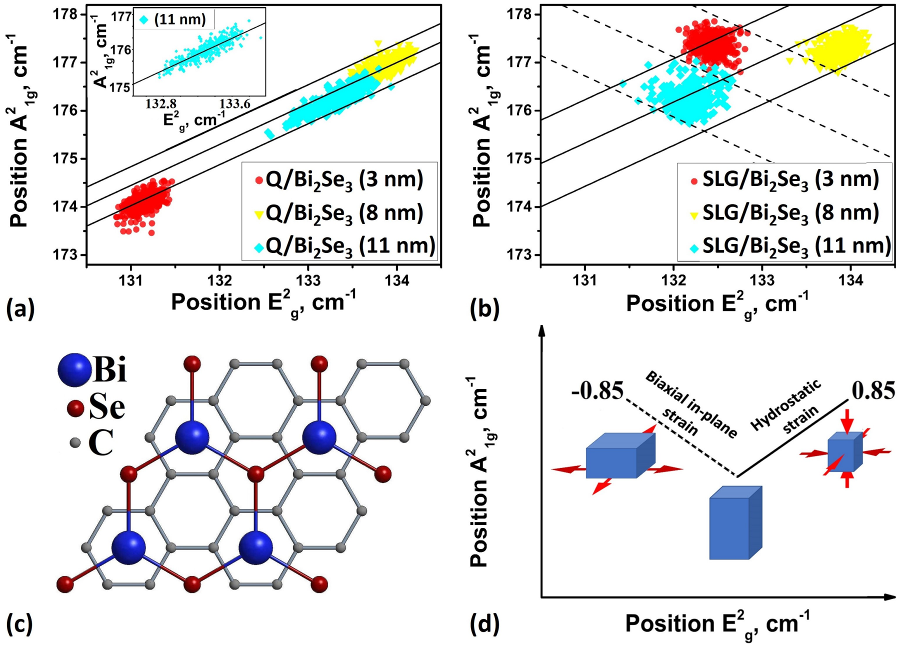

Figure 7.18: The positions of A^2_{1g} band as a function of E^2_g band positions for Bi_2Se_3 ultrathin films deposited on quartz (a) and graphene (b). The inset in panel (a) is a linear fit of A^2_{1g} vs E^2_g dependency for 11 nm Bi_2Se_3. (c) The top view of the SLG/Bi_2Se_3 interlayer stacking pattern. (d) Bi_2Se_3 strain distribution scheme based on A^2_{1g} band as a function of E^2_g Raman band positions scattered along different slopes. The solid line with the slope of $\sim$ 0.85 corresponds to the hydrostatic strain of Bi_2Se_3. The dashed line with the slope of ~ -0.85 corresponds to the biaxial in-plane tensile strain of Bi_2Se_3.

The Raman frequency vibrations in topological insulators such as Bi_2Se_3 are governed by various thickness-dependent factors, including spin-orbit coupling, charge carrier concentration, and strain. The linear scattering of A^2_{1g} on E^2_g experimental points is most probably related to the distribution of strain value in the films. Indeed, for the experimental values of Raman hydrostatic pressure coefficients $\left(\frac{d\omega_{A^2_{1g}}}{dP}\right)_T = 2.68$ cm^{-1}/GPa and $\left(\frac{d\omega_{E^2_g}}{dP}\right)_T = 3.13$ cm^{-1}/GPa [102], their ratio is $\left(\frac{d\omega_{A^2_{1g}}}{dP}\right)_T / \left(\frac{d\omega_{E^2_g}}{dP}\right)_T = 0.856$, which is in good agreement with the experimental data presented above. That scatter of the experimental datapoints along solid lines with a slope of ~ 0.85 (Figure 7.18a) indicates that Bi_2Se_3 films deposited on quartz experience strain distributed hydrostatically throughout the film (i.e. crystal lattices are strained or expanded both in-plane and out-of-plane simultaneously as it is illustrated in Figure 7.18d). Presumably, this distribution of the strain may be related to the growth process specifics as different thermal expansion coefficients of the quartz substrate and PVD-grown Bi_2Se_3, and Volmer-Weber thin films growth mode, where growth occurs not layer-by-layer, but by the formation of separate islands, which subsequently coalesce. Indeed, the Volmer-Weber growth mechanism of Bi_2Se_3 films leads to the appearance of strain which is mainly concentrated in the grooves between the grains. In case of strong interaction of the deposited material with the substrate, this type of strain is considered to be hydrostatic [103].

In contrast to the scatter of the A_{1g}^2 vs E_g^2 datapoints of Q/Bi_2Se_3 samples, the scatter of these datapoints for Bi_2Se_3 thin films deposited on SLG does not show a pronounced linear shape (Figure 7.18b), but rather the rhomb-shaped spots with an additional scatter of experimental datapoints along the dashed line with a negative slope (~ -0.85) are observed. This could be explained by the red-shift of the in-plane E_g^2 Raman mode positions and the simultaneous blue-shift of the out-of-plane A_{1g}^2 mode positions, which are related to the in-plane tensile strain, originating from the lattice mismatch between the SLG and Bi_2Se_3. Assuming the same absolute values of Raman pressure coefficients for both compressive and tensile strains, in the case of biaxial strain a scatter of the experimental datapoints along the line with the slope ~ -0.85 should be obtained, in contrast with the hydrostatic strain (Figure 7.18a). As the hexagonal lattice constant of the SLG is smaller than Bi_2Se_3 lattice constant (Figure 7.18c), the Bi_2Se_3 epitaxial film should experience in-plane tensile strain and compressive strain parallel to the c-axis. Indeed, due to the hexagonal honeycomb lattice of graphene (the lattice constant $a_{Gr} = 2.46$ Å), the stacking pattern between single-layer graphene and Bi_2Se_3 with surface Se atoms in the hollow centres of carbon hexahedral rings (Figure 7.18c) has the lowest binding energy and thus is a stable structure [104]. The relation between Bi_2Se_3 and graphene lattice parameters reads $a_{Bi_2Se_3} = a_{Gr} \cdot \sqrt{3}$. For this stacking order, the lattice mismatch for Bi_2Se_3 (tensile strain) is 2.9%. Thus, the approach to the separation of the origin of strain in PVD-deposited ultrathin Bi_2Se_3 films on quartz and SLG substrates based on the correlation analysis of Raman mode behaviour is as follows (Figure 7.18d): a scatter of the experimental A_{1g}^2 vs E_g^2 datapoints along the solid line with a positive slope (~ 0.85) is associated with simultaneous compression or extension both in-plane and along the c-axis (hydrostatic strain), in turn, the scatter of these datapoints along the dashed line with a negative slope (~ -0.85) is associated with the biaxial in-plane strain caused by the lattice mismatch of the heterostructure layers.

As was appointed above, the Raman technique has an advantage as non-contact probing of physical properties and provides access to simultaneous measurements of materials in heterostructures. Therefore, the developed theory of Raman scattering in SLG allows to calculate the lattice parameter of graphene in studied heterostructures based on the correlation analysis of $2D$ and G graphene bands positions [101]. In its turn, the $\mathrm{Bi_2Se_3}$ in-plane lattice parameter can be calculated according to the atomic arrangement presented in Figure 7.18c. Thus, the in-plane strain in $\mathrm{Bi_2Se_3}$ film deposited on graphene can be evaluated.

Using the proposed strain separation method (Figure 7.18d), the phonon deformation potential (PDP), which quantitively connects strain and Raman shift can be calculated. For the thinnest $\mathrm{Bi_2Se_3}$ (3 nm) film deposited on graphene, where the film is fully strained by the substrate and strain considered to be coherent across the thickness, the PDP will be estimated. This calculation is based on a simple idea. The in-plane tensile strain in 3 nm thin $\mathrm{Bi_2Se_3}$ associated with the negative ~ -0.85 slope originates only from the lattice mismatch between the graphene and $\mathrm{Bi_2Se_3}$. Therefore, the change in the $\mathrm{Bi_2Se_3}$ lattice parameter is directly related to the change in the graphene lattice parameter (Figure 7.18c). Thus, the variation of the graphene lattice parameter can be easily transformed into variations of the $\mathrm{Bi_2Se_3}$ plane lattice parameters. In combination with the variations of the A_{1g}^2 and E_g^2 shifts, the PDP values of these modes for the $\mathrm{Bi_2Se_3}$ in-plane strain can be obtained.

For the strain evaluation of the graphene layer in SLG/$\mathrm{Bi_2Se_3}$ heterostructure with 3 nm thick $\mathrm{Bi_2Se_3}$ layer, $\Delta\omega_{2D}/\Delta\omega_G$ Raman data differences were plotted in Figure 7.19a. Two dashed lines with a slope of ~ 0.7 were drawn through the upper and lower points of the $2D$ vs G plot to the intersection with the bold solid line (with a slope of ~ 2.2), representing a fixed biaxial strain in the ideal graphene [101]), as shown in Figure 7.19a. The strain range variation of the graphene layer can be calculated by determining the difference $\Delta\omega_G$ between the intersection points of thin dashed lines (with a slope of ~ 0.7) with the bold solid line and the G band position for the ideal SLG (Figure 7.19a, purple star mark), and then dividing the calculated $\Delta\omega_G$ values by the averaged sensitivity factor for the G band (-69.1 ± 3.4 cm^{-1}/%) [101]. Following the strain calculation procedure for the graphene layer in the SLG/$\mathrm{Bi_2Se_3}$ heterostructure described above, the graphene strain range from -0.165% to -0.078% for the SLG/$\mathrm{Bi_2Se_3}$ heterostructure with 3 nm thin $\mathrm{Bi_2Se_3}$ layer was determined. The lattice parameter of the strained graphene a_{Gr}^{3nm} was found to be varying from 2.456 to 2.458 Å. Using these values, the lattice parameter for the $\mathrm{Bi_2Se_3}$ layer in the SLG/$\mathrm{Bi_2Se_3}$ heterostructure $a_{Bi_2Se_3}^{3nm} = a_{Gr}^{3nm} \cdot \sqrt{3}$ was found to vary from 4.254 to 4.258 Å, which equals to the $2.80 - 2.89\%$ tensile strain in a 3 nm thick $\mathrm{Bi_2Se_3}$ film ($a_{Bi_2Se_3}^{Bulk} = 4.138$Å). A_{1g}^2 vs E_g^2 plot for a 3 nm thick $\mathrm{Bi_2Se_3}$ film deposited on SLG is shown in Figure 7.19b. The dashed line with a slope of ~ -0.85 indicates the in-plane tensile strain introduced by the $\mathrm{Bi_2Se_3}$ and graphene lattice mismatch and is associated with the blue and red shift of A^2_{1g} and E^2_g modes, respectively. Raman shifts ΔE^2_g and ΔA^2_{1g} estimated from Figure 7.19b are equal to 0.68 and 0.62 cm^{-1}, respectively. This results in PDP values for biaxial in-plane strain for 3 nm thin Bi_2Se_3 film deposited on graphene of -7.64 cm^{-1}/% for the in-plane mode and -6.97 cm^{-1}/% for the out-of-plane mode. The obtained results are in good agreement with values reported in the literature [105, 106], but obtained by different methods (Paper II).

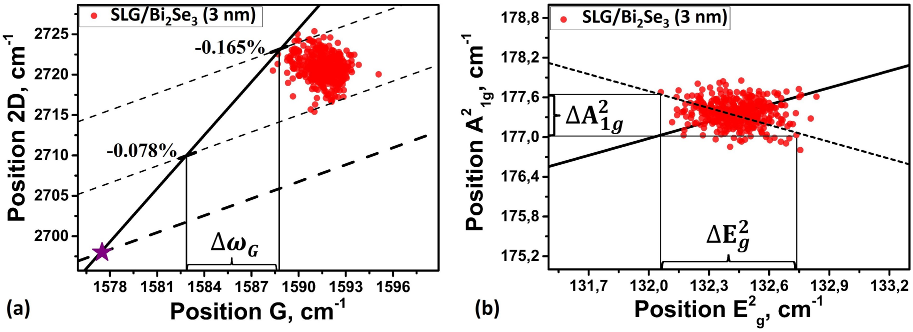

Figure 7.19: (a) $2D$ vs G dependency of the graphene layer in SLG/Bi_2Se_3 (3 nm) heterostructure. The purple star mark is the position for unstrained and undoped graphene. The bold solid line (with a slope of ~ 2.2) passing through the purple star mark is responsible for the biaxial strain in the ideal graphene. The bold dashed line (with a slope of ~ 0.7) passing through the purple star mark is responsible for the charge carrier concentration in the ideal graphene [101]. The dashed lines (with a slope of ~ 0.7) parallel to the bold dashed line are responsible for the charge carrier concentration with fixed biaxial strain. (b) A^2_{1g} vs E^2_g dependency for 3 nm Bi_2Se_3 film deposited on graphene. The solid line (slope ~ 0.85) is related to the hydrostatic strain distribution. The dashed line (slope ~ -0.85) is related to the strain caused by graphene (lattice mismatch).

In summary, despite the improved charge transport properties of strained nanoribbons and thin films, their use in single-electron devices is still challenging and requires sophisticated designs and complex fabrication processes. However, the results presented above in the case of bent nanoribbons may find application, for example, in nanoelectromechanical switches operating in low temperatures, which is suitable for cryogenic mechanics [107], quantum computing [108] and space applications [109]. In the case of thin films, graphene/Bi_2Se_3 heterostructures are excellent for applications, where an electrically conductive substrate is required (for example electronic [110], spintronic [111], and even domestic waste heat conversion [112] applications can be realised based on graphene/TI heterostructures).

8 Suppression of bulk conductivity in TIs via compensation doping

The bulk conductivity of TIs can be successfully suppressed by introducing chemical compensating dopants into nanostructures. One of the ways to suppress bulk defects in TIs is to compensate doping by growing ternary or quaternary components like $(Bi_{1-x}Sb_x)_2Te_3$ or $Bi_{2-x}Sb_xTe_{3-y}Se_y$. Such alloys based on Bi_2Se_3, Sb_2Te_3 and Bi_2Te_3 lead to a significant improvement in the quality of topological materials, especially in bulk crystals. These compounds are useful for tuning the bulk defects chemistry of the material, resulting in a decrease in charge carrier density and suppression of bulk conductivity. In addition, the use of electrostatic gating helps to further deplete carriers and lower E_F towards the Dirac point.

In this thesis, 13 nm thick $(Bi_{1-x}Sb_x)_2Te_3$ films grown by molecular-beam epitaxy (MBE) on a sapphire substrate, provided by the group of Prof. Xufeng Kou (ShanghaiTech University, China) were used.

8.1 Structural characterization of $(Bi_{1-x}Sb_x)_2Te_3$ thin films

Despite the ultra-high claimed quality of MBE-grown films, some basic characterisations were performed before the device fabrication process began.

Figure 8.1a shows a representative SEM image of a $(Bi_{1-x}Sb_x)_2Te_3$ thin film. The thin film exhibits a crack-free, continuous and uniform area over 5×5 mm^2. Figure 8.1b illustrates an example of the Raman spectrum of $(Bi_{1-x}Sb_x)_2Te_3$. During these measurements, the edge filter cutting at ≈ 85 cm^{-1} was used. So, only two of the four (E_g^2 and A_{1g}^2) Raman active modes were observed because the E_g^1 and A_{1g}^1 modes have energies below this limit. However, observed in-plane E_g^2 and out-of-plane A_{1g}^2 modes (the inset shows the displacement patterns of these modes) designate the high quality of thin films. The thickness (13 nm) and morphology of the film were obtained using AFM measurements. The representative AFM image and height profiles are presented in Figures 8.1c and d, respectively. An artificial scratch was introduced to determine the thickness.

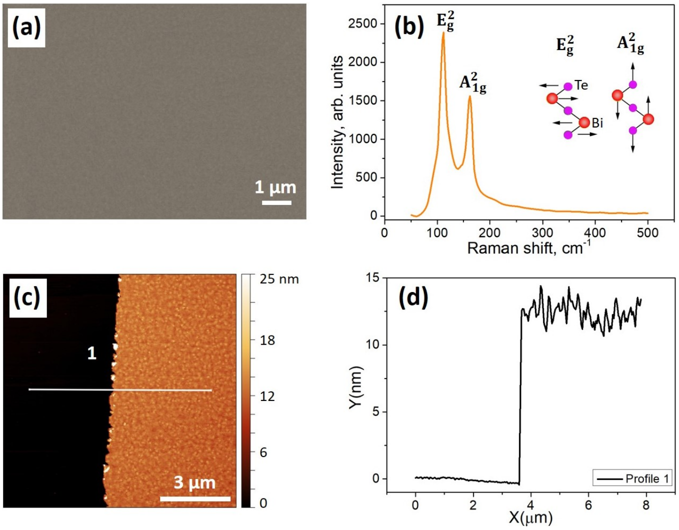

Figure 8.1: (a) False-coloured SEM image of a $(Bi_{1-x}Sb_x)_2Te_3$ thin film on a sapphire substrate. The thin film exhibits a crack-free, continuous and uniform area over 5×5 mm^2. (b) Raman spectrum of a $(Bi_{1-x}Sb_x)_2Te_3$ film. The inset shows the displacement patterns of E_g^2 and A_{1g}^2 phonon modes, which were observed. (c) AFM image of a thin (13 nm) $(Bi_{1-x}Sb_x)_2Te_3$ film. An artificial scratch was introduced to determine the thickness. (d) Height profile shown in panel (c).

8.2 Electrical characterization of $(Bi_{1-x}Sb_x)_2Te_3$ thin films

In the case of $(Bi_{1-x}Sb_x)_2Te_3$, the substituting of Bi with Sb pulls the Dirac point of Bi_2Te_3 from beneath the bulk valence band into the bulk band gap (Figures 1.3b and c). Since Bi_2Te_3 is n-type and Sb_2Te_3 is intrinsically p-type, the E_F in the solid solution of $(Bi_{1-x}Sb_x)_2Te_3$ with x in the range $0.75 < x < 0.96$ is tuned into the bulk bandgap with the sheet carrier density in the order of $\sim 1 \times 10^{12}$ cm^{-2} [65].

Before the fabrication, the sheet resistance of the film $R_\square = 4$ kΩ per square area, its sheet carrier density $n_{2D} = 5.3 \times 10^{12}$ cm^{-2} with n-type carriers, and its Hall mobility $\mu \approx 200 - 250$ cm^2(V·s)$^{-1}$ were measured in the Van der Pauw configuration at 2 K (Figure 8.2). The longitudinal resistance shows the expected weak anti-localisation dip, but no visible Shubnikov-de Haas oscillations. This is due to the low carrier mobility, for which the onset of oscillations would be beyond the available magnetic field range (± 14 T). The 3D carrier concentration extracted from the Hall effect data is $\sim 3.9 \times 10^{18}$ cm^{-3}, which is lower than in Bi_2Se_3 nanoribbons of the same thickness ($\sim 9 \times 10^{18}$ cm^{-3}) (Figure 7.4c). Like

Bi_2Se_3, this material is easily damaged by heating or etching processes. Figure 8.2c shows the carrier density at 300 K measured by the Hall effect on the film between successive 3-min annealings at increasingly higher temperatures. The annealing time was chosen to be the same as what one can use to bake the resist layers for lithography. Figure 8.2c demonstrates that the carrier density remains stable until at least 90 °C. It starts to increase at 110 and 130 °C, but the relative change is only a few percent. This means that while one should not bake the sample repeatedly, annealing it a few times in order to lift off contacts and cure the etching mask, resist does not significantly degrade the quality of the material.

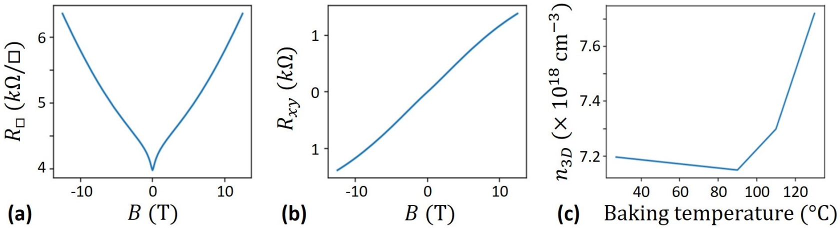

Figure 8.2: (a) Magnetoresistance and (b) Hall effect of the $(Bi_{1-x}Sb_x)_2Te_3$ film measured before patterning. Measurements were performed at 2 K. The low-field (± 2 T) carrier concentration is 3.9×10^{18} cm^{-3}. (c) The carrier concentration in the same film at 300 K after successive annealings of 3 min on a hotplate.

The two-carrier analysis (for carriers corresponding to TSSs and bulk states) of longitudinal G_{xx} and transverse G_{xy} magnetoconductance was also carried out (Figure 8.3a and b). The parameters $n_1 = 1.8{\times}10^{12}$ cm^{-2} and $\mu_1 = 711$ cm^2(V·s)$^{-1}$ correspond to charge carrier density and mobility of surface states, and $n_2 = 3.2 \times 10^{12}$ cm^{-2} and $\mu_2 = 467$ cm^2(V·s)$^{-1}$ correspond to the bulk. The obtained carrier concentrations in good agreement with results reported in the literature ($n \simeq 2 \times 10^{12}$ cm^{-2} and $\mu \simeq 500$ cm^2(V·s)$^{-1}$) [28]. WAL cusp was fitted with the Hikami-Larkin-Nagaoka (HLN) curve (Figure 8.3c). In the result, a pre-factor $\alpha = -0.97$ was obtained, indicating two conducting channels (TSSs and bulk). The value of electron coherence length $L_\varphi = 76$ nm at 2 K was extracted.

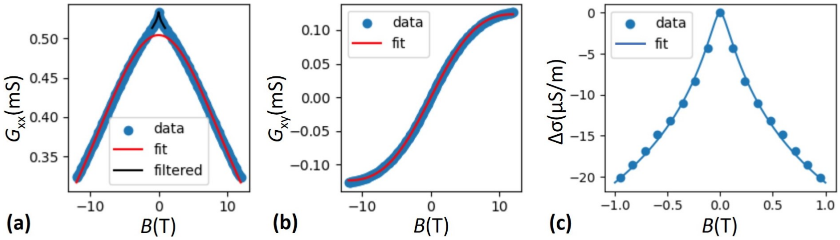

Figure 8.3: The two-carrier analysis of G_{xx} (a) and G_{xy} (b) magnetoconductance for a 13 nm thick $(Bi_{1-x}Sb_x)_2Te_3$ film, respectively. (c) WAL cusp with HLN fit, revealing a pre-factor $\alpha = -0.97$, indicating two conducting channels, and $L_\varphi = 76$ nm.

9 Single-electron transport: towards TI single-electron charge pump

9.1 Bi_2Se_3 SET

Nanoribbons with a thickness of $10-15$ nm are most favourable for device fabrication due to the ability of efficient tuning of the Fermi energy, however, top etching of such a thin material leads to complete destruction and makes the device non-conducting. Thus, to create tunnelling barriers, between which a quantum dot could be formed, the Bi_2Se_3 nanoribbons are constricted only along their width were used for the fabrication of SET devices. The typical constriction sizes that were achieved using this method were $40-50$ nm in width and $80-100$ nm in length (Figure 9.1a).

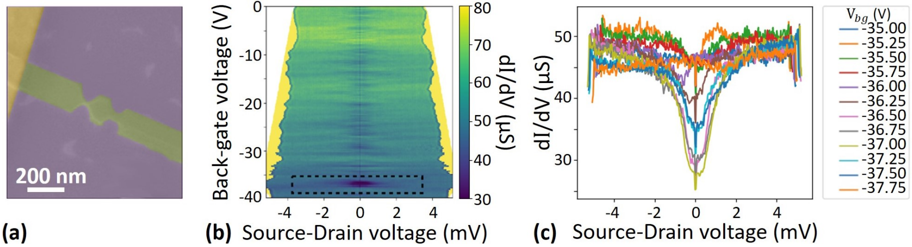

Figure 9.1: (a) False-colour SEM image of a quantum dot device patterned in a Bi_2Se_3 nanoribbon. The left barrier is 40 nm wide and 80 nm long. (b) The differential conductance map of the device taken at 300 mK. (c) The conductance curves reveal a kink (non-linearity) feature that becomes pronounced at higher gate voltages and indicates the onset of a quantum dot behaviour.

Figures 9.1b and c show the differential conductance map measured at 300 mK in the ^{3}He cryostat of the device shown in panel a. In this experiment, the gate voltage was applied through the back of a Si/SiO_2 substrate. For two similar devices with a constriction width of 50 nm or less, the appearance of non-linearity in the IV curves/differential conductance was observed at low bias voltage. For the sample with the narrowest barriers, shown in Figure 9.1a, an enhancement of these non-linearity features was noted near -37 V. This indicates the onset of the Coulomb blockade in the device. However, the resistance of the devices was typically in the $10-20$ kΩ range (at zero back-gate voltage), which is still below the $R_q \approx 25.8$ kΩ per barrier, required to observe a single-electron transistor behaviour. Other devices with constrictions wider than 50 nm showed fully linear

IV curves. This suggests that if the non-linearity feature is observed due to the Coulomb blockade, the constrictions need to be made longer than 80 nm and/or narrower than 50 nm to achieve a fully developed Coulomb blockade regime.

9.2 $(Bi_{1-x}Sb_x)_2Te_3$ SET

Single-electron transistors based on a 13 nm thick $(Bi_{1-x}Sb_x)_2Te_3$ film grown by MBE on a sapphire substrate were also fabricated. SEM image of the device is shown in Figure 9.2a. It is a 150 nm wide by 1.3 μm long nanoribbon, in which two constrictions (170 nm in length and 22 nm in width) were made. These constrictions serve as tunnelling barriers to define a central island of 100 nm in length, where a quantum dot should form. To tune the charge state inside the quantum dot, a plunger (side) gate electrode was also fabricated from the film material during the same fabrication (lithography) step (Figure 9.2a).

The electron transport properties of the devices were measured in a ^{3}He/^{4}He dilution refrigerator with a base temperature of 20 mK. Figure 9.2b presents a colour plot of the differential conductance dI/dV of the device pictured in panel a, plotted against source-drain voltage V (measured in the 4-points configuration) and the applied gate voltage V_G. It exhibits small diamond-like regions near zero bias, in which the conductance of the device is strongly attenuated. The diamonds have a regular periodicity $\Delta V_G = 15.2$ mV in gate voltage, but have a width in source-drain voltage that varies smoothly from diamond to diamond. Outside of these regions, the conductance background is mostly constant in this range and has a value around one-half of the quantum conductance $G_0 = e^2/h$, where e and h are respectively the electron charge and the Planck constant.

These diamond features are typical manifestations of the Coulomb blockade, which indicates charging effects occurring in a region of the device that behaves as a quantum dot (Section 3.1). The size of the dot can be estimated from the diamond periodicity in gate voltage as follows. First, the gate capacitance can be calculated from the diamond periodicity as $C_G = e/\Delta V_G = 11$ aF. Then, the effective size of the dot can be roughly approximated to an isolated disk of radius R, for which the capacitance is given by $C_G = 8\varepsilon_0\varepsilon_r R$, where ε_0 is the permittivity of vacuum and $\varepsilon_r \approx 5.5$ is the relative permittivity of the gate dielectric. The latter value is taken as the average permittivity of vacuum ($\varepsilon_r = 1$) and the sapphire substrate ($\varepsilon_r \approx 10$). This yields a radius of $R = 27$ nm, which is consistent with a dot being formed in the central island. The obtained effective size of the quantum dot is smaller than the actual size of the island, but significantly exceeds the actual size of the constricted region. This discrepancy can be explained by the approximation of the rectangular shape of the island to the disk, as well as by the native oxidation of the TI material and possible damage to the side edges of the film during etching. Also, the value is likely underestimated though, as the formula does not take into account the screening effects of the leads nearby, which also contribute to the measured value.

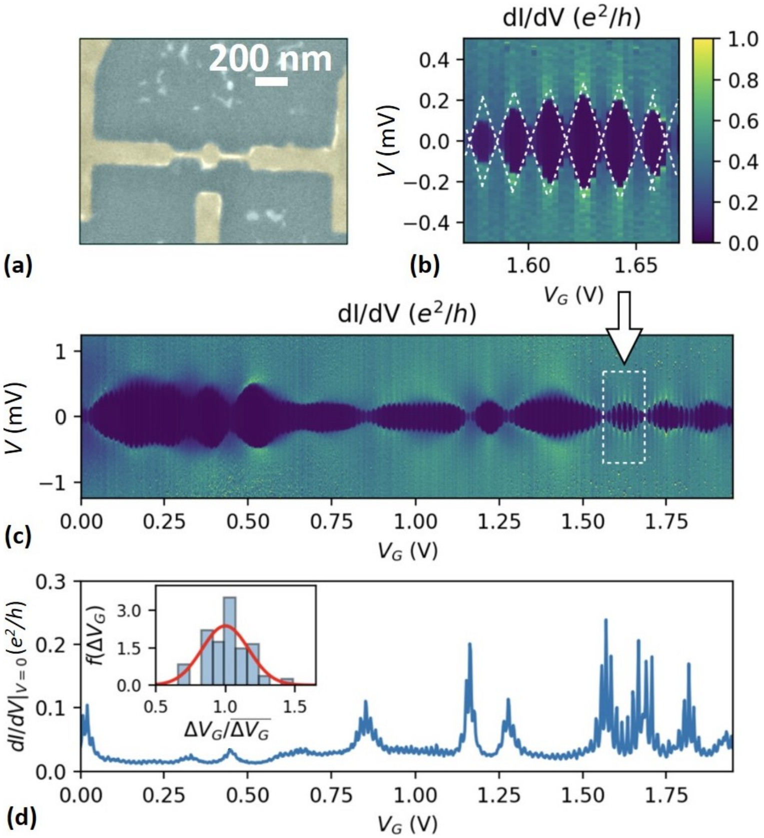

Figure 9.2: (a) False-coloured SEM image of the BST single-electron transistor on sapphire. (b) A small-scale differential conductance map of the same device at 20 mK, showing the Coulomb diamonds. The dotted white lines indicate the slopes used for estimating the capacitance of the barriers. (c) The same conductance map on a larger gate and voltage scale, the dotted square indicates the diagram region shown in panel (b). The colour scale is shared for both plots. (d) Zero-bias conductance curve as a function of gate voltage from the same data set as (c), with the normalized peak spacing distribution of the small diamonds in the inset. The red curve is a Gaussian fit with a mean value of $\Delta V_G = 15.2$ mV, and a standard deviation $\sigma = 2.6$ mV.

The tunnelling capacitance of the barriers C_T can also be obtained from the slopes of the diamond using $C_T = C_G(dV_G/dV + 1/2)$, where dV_G/dV is the slope of the diamond boundaries (white lines in Figure 9.2b). This yields $C_T \approx 310$ aF for both constrictions because the diamond pattern is symmetrical around $V = 0$ V. Lastly, the charging energy of the QD $E_c = e^2/2C_\Sigma = 0.13$ meV was calculated, where $C_\Sigma = 2C_T + C_G = 631$ aF is the total capacitance of the island.

As mentioned earlier, the width of the diamonds is modulated in source-drain voltage, which becomes more visible when scanning over a wider range of gate voltages, as shown in the map presented in Figure 9.2c. The measurement reveals that the diamond width varies in a smooth but aperiodic manner that is very reminiscent of a beating pattern. The corresponding zero-bias conductance curve as a function of gate voltage is plotted in Figure 9.2d and exhibits a series of broad peaks with irregular spacing. These peaks correspond to the points where the large modulation patterns close in the map (Figures 9.2c and d). Additionally, a small 15 mV Coulomb oscillation from the island dot is superimposed.

The observed beating pattern can be explained by considering multiple quantum dots in series. The typical size of these features in gate voltage is $150 - 250$ mV, which suggests that these dots should be small, about $3 - 5$ nm in radius using the same formula as for the island capacitance. This is consistent with additional dots being formed in the barriers. For a Coulomb peak to be visible, all the dots must be in or near the tunnelling state at a given value of V_G. This also results in the extinction of all the other peaks, as the current cannot flow if one or more dots are in the blockade regime. Lastly, as the Coulomb oscillation from the central island seemingly has a much shorter periodicity than the width of these peaks, it does not lead to extinction but strongly modulates the pattern. In earlier studies, this phenomenon was called "stochastic Coulomb blockade" and was attributed to the different capacitances C_1 and C_2 for quantum dots. Unless the ratio C_1/C_2 is negligible, this results in both the peak-to-peak spacing and the activation energies of the conductance at the peaks that persist are random [113].

How the dots themselves are formed, can be understood by considering the band structure of the TI. In the leads and the island, the linear dispersion of the surface states makes the Dirac electrons effectively massless, thus insensitive to localization by defects or local electric fields thanks to Klein tunnelling (the absence of normal backscattering of electrons even under the case of potential barriers). However, in the constrictions, the size-induced quantization opens a gap (Δ) at the Dirac point (Section 2.8). In the absence of magnetic fields and for a cylindrical nanowire of equivalent radius $R \approx 10 - 15$ nm, value Δ is given by $2\hbar v_F l/R \approx 20 - 25$ meV, where $v_F \approx 4.3 \times 10^5$ ms^{-1} is the Fermi velocity in BST, and $l = 1/2$ is the angular momentum of the lowest-lying sub-band. It is not negligible, and results in a band curvature that makes the Dirac electrons massive again in the constrictions. As a consequence, these regions can act as tunnel barriers due to the suppression of Klein tunnelling, and be used to define a dot in the central island. This comes with a trade-off though, as it also enables again trapping by charge puddles or conductance-limiting segments, which can cause the formation of quantum dots in narrow semiconductor nanowires [114].

As the different possible mechanisms have different sensitivities to magnetic fields, the effect of an out-of-plane field B on the Coulomb blockade features was also investigated (Figure 9.3).

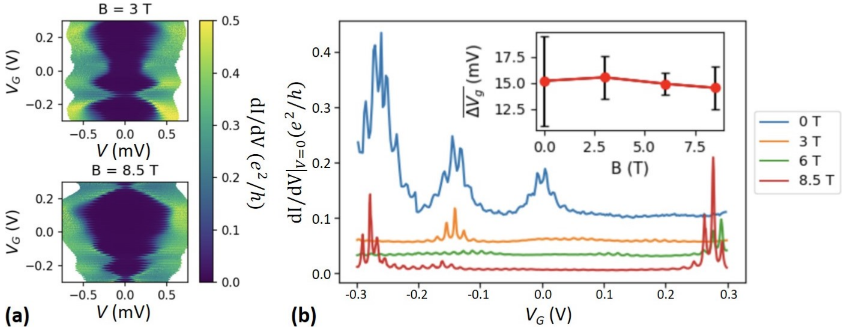

Figure 9.3: (a) Small conductance maps for a perpendicular field of 3 and 8.5 T, respectively. (b) Zero-bias conductance of the device for several values of the out-of-plane magnetic field. The curves are offset from the lowest to the highest field for clarity. The inset shows the mean peak spacing for the island dot (15 mV oscillation) as a function of a magnetic field. Error bars represent one standard deviation.

To see whether the Coulomb diamond patterns are affected by the field, smaller conductance maps for several values of the field were measured, two of which are shown in Figure 9.3a. In these maps, the larger patterns change drastically in shape and periodicity upon applying the field. The zero-bias traces of these maps, plotted in Figure 9.3b, reveal that the amplitude of individual peaks is erratically affected by the field. The series arrangement of the dots makes it difficult to disentangle effects. The presence of quantized dot levels is known to be affected by magnetic fields either through orbital or Zeeman shifts [115], which could lead to attenuation if the peaks from both barriers become out of tune. Another possibility is that the dot formation mechanism is interference-based, such as a mesoscopic Coulomb blockade, in which the conductance of the peaks can be attenuated through weak-(anti)localization [116]. In contrast, the oscillations related to the central dot are still visible at all fields in the maps and in the zero-bias curves. Their periodicity and regularity seem to be preserved, which is also seen when plotting the evolution of mean peak spacing ΔV_G with a magnetic field, in the inset of Figure 9.3b. This suggests that the central dot behaves in a more conventional way.

The evolution of the zero-bias conductance at $V_G = 0$, which is presented in Figure 9.4a for several values of the temperature was also investigated. For these parameters, the conductance is almost equal to that at $V \gg e/C_\Sigma$, meaning that the three dots are simultaneously in the tunnelling state. At 20 mK, a broad zero-field peak was observed, that seems to reduce upon increasing the temperature, as well as conductance fluctuations for $|B| \geq 2$ T. These are not exactly periodic, but reproducible for consecutive magnetic field sweeps, and weakly affected by increasing the temperature from 20 to 400 mK. The patterns do change if the charge inside the dot is changed either by the gate voltage or by the electrostatic background though. Lastly, all these features vanish as the voltage is increased further away from e/C_Σ, meaning that they are related to the occurrence of the Coulomb blockade and do from the magnetoresistance in the portion of the TI nanowire that is measured in series. On top of these, one can observe a small weak anti-localization peak in the range where $|B| < 250$ mT, which is also observed in the film before patterning (Figure 8.2a). A possible cause for this, is universal conductance fluctuation (UCF) inside the dot, in a similar fashion to what has been observed in gate-defined dots in 2D electron gases [117] and graphene billiards [118]. As sketched in Figure 9.4b, when an electron enters a dot, it can scatter elastically at the boundaries or on impurities multiple times before exiting, which results in a chaotic motion. If there is an out-of-plane magnetic field, a magnetic flux is threaded through the area A enclosed by these scattering paths, along which the electron acquires a finite Aharonov-Bohm phase. This leads to an oscillation of the conductance with a periodicity $\Delta B = \phi_0/A$, where $\phi_0 = h/e$ is the fundamental flux quantum. All of these paths contribute to the conductance with a different periodicity, the sum of which leads to aperiodic but reproducible fluctuations with the magnetic field.

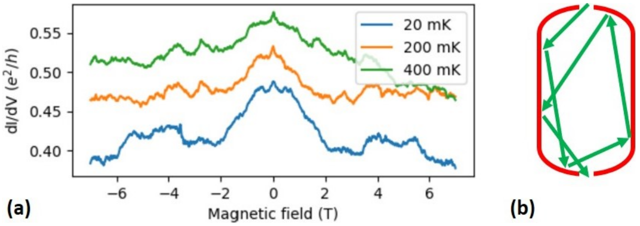

Figure 9.4: (a) dI/dV of the device at $V_G = 0$ and $T = 20$ mK, showing UCF superimposed on a decreasing magnetoconductance background. (b) Schematic picture of electron trajectories inside the dot, in which electrons are scattered against edges and impurities and can enclose a finite area.

To summarise, functional TI-based single-electron transistors were fabricated using a top-down electron-beam lithography approach. The Coulomb diamonds measured at 20 mK indicate the formation of a QD inside the central island as intended. However, the opening of the gap in the constrictions that enables to lift Klein tunnelling and confine electrons also re-introduces trapping mechanisms by local potential barriers. This leads to the formation of additional small QDs in the barriers, which strongly influence the transport properties of the device. This is an intrinsic limitation of the presented approach, but may be mitigated by patterning shorter or slightly wider constrictions to minimize the chances of forming dots there. The fluctuations in the conductance of the device with a magnetic field were also observed, which can be qualitatively explained by a chaotic motion of the electrons inside the dot. While these results are a promising first step towards TI-based single-electron sources, the challenges highlighted in the present work are still to be overcome before successfully realizing such a device (Paper VIII).

10 Conclusions

1. The rough-to-smooth transition in the growth dynamic of Bi_2Se_3 nanoribbons with increasing thickness is demonstrated. The rough growth regime of ultrathin nanoribbons (less than 15 nm thick) leads to a peculiar surface morphology, which strongly affects the transport properties of topological surface states. Magnetotransport measurements of ultrathin nanoribbons show that the transport features are affected by Altshuler-Aronhov-Spivak-like coherent orbits at low magnetic fields, while Shubnikov-de Haas oscillations take over at high fields.

2. Ultrathin nanoribbons (with thicknesses close to 10 nm) exhibit pronounced conductance oscillations as a function of gate voltage, that can be attributed to ballistic transport and quantized sub-bands.

3. The tunability effect of Dirac surface states in a suspended Bi_2Se_3 nanoribbon due to external bending deformation (dynamically introduced by an electrostatic field) is demonstrated. With a dynamic increase in bending, the Shubnikov-de Haas oscillation frequencies, representing the carriers of the top and bottom surface states, experience downshift/upshift with compressive/tensile strain, while the bulk frequency remains unchanged.

4. Correlation analysis of vibration modes in physical vapour deposited Bi_2Se_3 thin films probed by the Raman mapping technique is developed to determine the type and amount of strain. A Bi_2Se_3 film grown on a quartz substrate, experiences hydrostatic strain, while the same film deposited on quartz/graphene experiences additional in-plane tensile strain, originating from the lattice mismatch between graphene and Bi_2Se_3, accompanied by compression in the *c*-axis.

5. Functional topological insulator (Bi_2Se_3 and $(Bi_{1-x}Sb_x)_2Te_3$)-based single-electron transistors are fabricated using a top-down electron-beam lithography approach. The Coulomb diamonds measured at 20 mK indicate the formation of a quantum dot and single-electron transport through the devices.

ACKNOWLEDGEMENTS

I would like to thank my supervisor Donāts Erts for providing me motivation and necessary assistance over the years of my PhD studies. I am incredibly grateful for the opportunity to be a part of an exceptional research institute. Besides, I am highly indebted to my supervisor Floriana Lombardi. The experience and knowledge you shared with me have contributed to my professional growth a lot. You set a great example through your professionalism, dedication to science and brilliant personal qualities. Moreover, despite all the challenges I faced, you have always been supportive, understanding and kind to me. Next, I want to thank Thilo Bauch for his outstanding ability to explain sophisticated things easily and to find creative ways out of every situation, no matter how complicated it is.

I express gratitude to Gunta Kunakova, my colleague who guided me during the initial period of my work in the cleanrooms. Alongside with numerous experimental techniques, you shared endless optimism and support with me.

I would like to make acknowledgment to my colleague and friend Xavier Palermo. I consider it to be a huge luck to meet and to work with such a great person. I learned a lot from you, and that is something I will always be grateful for! Thank you for supporting me in any, sometimes even silly, ideas, and accompanying me in all activities that took place outside the lab. I will keep it as pleasant memories for many years.

To my friend and neighbour Andrei Felsharuk, who always gives me a helping hand in any life situation. I'm grateful for all the fun we had during this period. Maybe one day you'll be lucky enough to beat me at snooker. Be patient and keep practising.

In addition, thanks also go to my co-workers from the Institute of Chemical Physics. First of all, to Jana Andžāne and Margarita Volkova, who taught me the basics of material growth. Then, to Raimonds Popļausks who is the most helpful assistant in all the technical issues. It has always been a great pleasure to have a conversation with you. To Alexandrs Dutovs, who was not only a good colleague for me but also a personal fishing coach. I would like to thank Jeļena Kosmača for her contagious smile and good mood. Also, I send my appreciation to Vanda Voikiva, Raimonds Meija, Raitis Sondors, Līga Jasulaņeca and many other people I interacted with. I can't but mention Signe Laimiņa-Koka, Elīna Kerre and Linda Ungure, who had been providing documentary management that was an essential part of the working process.

My appreciation extends to people from Chalmers University of Technology. First and foremost, I would like to thank my prior and current officemates - Alessia Garibaldi, Federico Chianese and of course, legendary Edoardo Trabaldo. You will always be my buddies. You taught me that being a graduate student is not only about solving academic problems, but also about arranging your free time. To a greater extent, this is Edo's merit. He has a particular superpower to unite people around him and to organise various events. Federico and Alessia were always ready to keep fruitful conversations and they were constantly reminding me there is a way out of the lab.

I would also like to acknowledge wonderful people from the QManD group who were always ready to help: Alexei Kalaboukhov, who never rejected to assist or to advise me on various issues; Riccardo Arpaia, the soul of our company, for creating the best-ever travel guide over Italy that made the trip unforgettable; Ananthu Surendran, a member of the TI-squad, with whom we fought shoulder to shoulder against TI nanostructures. Thank you for sharing the beauty of the world through your photographs and for exciting badminton games. I can't but mention Eric Wahlberg. His industriousness deserves admiration. Eric is not only a well-organised person but also a sunny soul. I'd like to thank Núria Alcalde-Herraiz for keeping all the organisational issues under control. It has always been a pleasure for me to interact with you. Also, I express my gratitude to Karn Rongrueangkul, Andrea d'Alessio, Marco Biagi and Feike van Veen, who brought a fresh breath of passion, vision and energy to the routine. It is an honour to work with you all.

I am privileged to have close Indian mafia friends: Richa Mirta, Naveen Shetty, Aditya Jayaraman and of course Arpita Shady-Mukherjee (the best of the Bengalis). I will never forget our journeys, table tennis matches, picnics, dinners at legendary Indian BBQ and many other memories that will always be a part of me. Your friendship and presence in my life made these years unforgettable.

I'd like to acknowledge my teammates Lars Sjöström, Roselle Ngaloy, Bing Zhao and his wife Liu Na and Ivo Cools, who helped me to dilute sedentary work with ping-pong and tennis battling.

I want to thank all members of the QDP group: Dag Winkler, Avgust Yurgens, Samuel Lara-Avila, Andrey Danilov, Sergey Kubatkin, Vittorio Buccheri, Nermin Trnjanin, Anamul Md Hoque, Munis Khan, Maha Khademi, Johanna Huhtasaari and her cat Percy, who showed up uncontrollably on my Facebook, Awse Salha, Oleg Shvetsov, and others I forgot to mention for making my presence at Chalmers full of joy and pleasure.

I am grateful to my first supervisor Ivan Komissarov, who introduced me to the world of science and still has been participating in my scientific research.

I'm obliged to Jan and Agneta Carlsson, my closest people in Sweden, for constant support, encouragement and belief in my success. You did and still do everything possible to make me feel as happy and comfortable as in my own home.

I would like to thank my beloved lady Anastasia. Your patience and calmness during the ups and downs of my research always brought me back on track. Thank you for your constant love and support.

Above all, I would like to thank my family. You taught me many important life lessons and gave me everything needed to succeed in life. Although we are miles apart, I always feel your unconditional love and support. Thank you for cheering me up, motivating and making me believe there is nothing I can't handle. Without you this journey would not have been possible.

References

[1] H. Scherer, S. P. Giblin, X. Jehl, A. Manninen, F. Piquemal, and D. A. Ritchie, “Introducing Joint Research Project “Quantum Ampere” for the realisation of the new SI ampere”, EPJ Web of Conferences **77** (2014).

[2] H. Scherer and H. W. Schumacher, “Single-Electron Pumps and Quantum Current Metrology in the Revised SI”, Annalen der Physik **531** (2019).

[3] BIPM, *Le Système international d’unités / The International System of Units (“The SI Brochure”)*, 9th ed. (Bureau international des poids et mesures, 2019).

[4] S. P. Giblin, A. Fujiwara, G. Yamahata, M. H. Bae, N. Kim, A. Rossi, M. Möttönen, and M. Kataoka, “Evidence for universality of tunable-barrier electron pumps”, Metrologia **56**, 044004 (2019).

[5] M. König, S. Wiedmann, C. Brüne, A. Roth, H. Buhmann, L. W. Molenkamp, X.-L. Qi, and S.-C. Zhang, “Quantum Spin Hall Insulator State in HgTe Quantum Wells”, Science **318**, 766–770 (2007).

[6] K. Mazumder and P. M. Shirage, “A brief review of Bi_2Se_3 based topological insulator: From fundamentals to applications”, Journal of Alloys and Compounds **888**, 161492 (2021).

[7] G. Kunakova, L. Galletti, S. Charpentier, J. Andzane, D. Erts, F. Léonard, C. Spataru, T. Bauch, and F. Lombardi, “Bulk-free topological insulator Bi_2Se_3 nanoribbons with magnetotransport signatures of Dirac surface states”, Nanoscale **10**, 19595–19602 (2018).

[8] G. Kunakova, T. Bauch, X. Palermo, M. Salvato, J. Andzane, D. Erts, and F. Lombardi, “High-Mobility Ambipolar Magnetotransport in Topological Insulator Bi_2Se_3 Nanoribbons”, Physical Review Applied **16**, 1 (2021).

[9] F. Münning, O. Breunig, H. F. Legg, S. Roitsch, D. Fan, M. Rößler, A. Rosch, and Y. Ando, “Quantum confinement of the Dirac surface states in topological-insulator nanowires”, Nature Communications **12** (2021).

[10] R. Saxena, E. Grosfeld, S. E de Graaf, T. Lindstrom, F. Lombardi, O. Deb, and E. Ginossar, “Electronic confinement of surface states in a topological insulator nanowire”, Physical Review B **106**, 035407 (2022).

[11] C. L. Kane, “Chapter 1 - Topological Band Theory and the Z_2 Invariant”, in *Topological Insulators*, edited by M. Franz and L. Molenkamp, Contemporary Concepts of Condensed Matter Science (Elsevier, 2013), pp. 3–34.

[12] F. Bloch, “Über die Quantenmechanik der Elektronen in Kristallgittern”, Zeitschrift für Physik **52** (1929).

[13] M. Z. Hasan and C. L. Kane, “Colloquium: Topological insulators”, Reviews of Modern Physics **82**, 3045–3067 (2010).

[14] M. Nakahara, *Geometry, Topology and Physics* (CRC press, Boca Raton, 2018).

[15] D. Xiao, M.-C. Chang, and Q. Niu, “Berry phase effects on electronic properties”, Reviews of Modern Physics **82**, 1959–2007 (2010).

[16] S.-Q. Shen, “Topological Invariants”, in *Topological Insulators: Dirac Equation in Condensed Matter* (Springer Singapore, Singapore, 2017), pp. 125–152.

[17] K. v. Klitzing, G. Dorda, and M. Pepper, “New Method for High-Accuracy Determination of the Fine-Structure Constant Based on Quantized Hall Resistance”, Physical Review Letters **45**, 494–497 (1980).

[18] D. J. Thouless, M. Kohmoto, M. P. Nightingale, and M. den Nijs, “Quantized Hall Conductance in a Two-Dimensional Periodic Potential”, Physical Review Letters **49**, 405–408 (1982).

[19] C. L. Kane and E. J. Mele, “Z_2 Topological Order and the Quantum Spin Hall Effect”, Physical Review Letters **95**, 146802 (2005).

[20] B. A. Bernevig, T. L. Hughes, and S.-C. Zhang, “Quantum Spin Hall Effect and Topological Phase Transition in HgTe Quantum Wells”, Science **314**, 1757 (2006).

[21] T. Ginley, Y. Wang, Z. Wang, and S. Law, “Dirac plasmons and beyond: the past, present, and future of plasmonics in 3D topological insulators”, MRS Communications **8** (2018).

[22] S.-T. Pi, H. Wang, J. Kim, R. Wu, Y.-K. Wang, and C.-K. Lu, “New Class of 3D Topological Insulator in Double Perovskite”, The Journal of Physical Chemistry Letters **8** (2017).

[23] H. Weng, R. Yu, X. Hu, X. Dai, and Z. Fang, “Quantum anomalous Hall effect and related topological electronic states”, Advances in Physics **64**, 227–282 (2015).

[24] L. Fu, C. L. Kane, and E. J. Mele, “Topological Insulators in Three Dimensions”, Physical Review Letters **98**, 106803 (2007).

[25] H. Zhang, C.-X. Liu, X.-L. Qi, X. Dai, Z. Fang, and S.-C. Zhang, “Topological insulators in Bi_2Se_3, Bi_2Te_3 and Sb_2Te_3 with a single Dirac cone on the surface”, Nature Physics **5**, 438–442 (2009).

[26] M. Ye, K. Kuroda, M. M. Otrokov, A. G. Ryabishchenkova, Q. Jiang, A. Ernst, E. V. Chulkov, M. Nakatake, M. Arita, T. Okuda, T. Matsushita, L. Toth, H. Daimon, K. Shimada, Y. Ueda, and A. Kimura, “Persistence of the topological surface states in Bi_2Se_3 against Ag intercalation at room temperature”, The Journal of Physical Chemistry C **125**, 1784–1792 (2021).

[27] Y. L. Chen, J.-H. Chu, J. G. Analytis, Z. K. Liu, K. Igarashi, H.-H. Kuo, X. L. Qi, S. K. Mo, R. G. Moore, D. H. Lu, M. Hashimoto, T. Sasagawa, S. C. Zhang, I. R. Fisher, Z. Hussain, and Z. X. Shen, “Massive Dirac Fermion on the Surface of a Magnetically Doped Topological Insulator”, Science **329**, 659–662 (2010).

[28] J. Zhang, C.-Z. Chang, Z. Zhang, J. Wen, X. Feng, K. Li, M. Liu, K. He, L. Wang, X. Chen, Q. K. Xue, X. Ma, and Y. Wang, “Band structure engineering in $(Bi_{1-x}Sb_x)_2Te_3$ ternary topological insulator”, Nature Communications **574** (2011).

[29] N. W. Ashcroft and N. D. Mermin, *Solid State Physics* (Holt-Saunders, 1976).

[30] S. Datta, *Quantum Transport: Atom to Transistor* (Cambridge University Press Cambridge, 2006).

[31] H. Cao, J. Tian, I. Miotkowski, T. Shen, J. Hu, S. Qiao, and Y. P. Chen, "Quantized Hall Effect and Shubnikov de Haas Oscillations in Highly Doped Bi_2Se_3: Evidence for Layered Transport of Bulk Carriers", Physical Review Letters **108** (2012).

[32] G. Schmid, *Nanotechnology: Principles and Fundamentals*, Nanotechnology (Wiley−VCH, Weinheim, 2008).

[33] C. Beenakker and H. van Houten, "Quantum Transport in Semiconductor Nanostructures", in *Semiconductor Heterostructures and Nanostructures*, Vol. 44, Solid State Physics (Academic Press, 1991), pp. 1–228.

[34] R. Feynman, A. Hibbs, and D. Styer, *Quantum Mechanics and Path Integrals*, Dover Books on Physics (Dover Publications, 2010).

[35] S. Chakravarty and A. Schmid, "Weak localization: The quasiclassical theory of electrons in a random potential", Physics Reports **140**, 193–236 (1986).

[36] C. W. J. Beenakker and H. van Houten, "Boundary scattering and weak localization of electrons in a magnetic field", Physical Review B **38**, 3232–3240 (1988).

[37] V. F. Gantmakher and L. I. Man, *Electrons and Disorder in Solids* (Oxford University Press, 2005).

[38] S. Hikami, A. I. Larkin, and Y. Nagaoka, "Spin-Orbit Interaction and Magnetoresistance in the Two Dimensional Random System", Progress of Theoretical Physics **63**, 707–710 (1980).

[39] H.-Z. Lu and S. Q. Shen, "Finite-Temperature Conductivity and Magnetoconductivity of Topological Insulators", Physical Review Letters **112** (2014).

[40] J. Chen, H. J. Qin, F. Yang, J. Liu, T. Guan, F. M. Qu, G. H. Zhang, J. R. Shi, X. C. Xie, C. L. Yang, K. H. Wu, Y. Q. Li, and L. Lu, "Gate-Voltage Control of Chemical Potential and Weak Antilocalization in Bi_2Se_3", Physical Review Letters **105**, 176602 (2010).

[41] M. Büttiker, Y. Imry, R. Landauer, and S. Pinhas, "Generalized many-channel conductance formula with application to small rings", Physical Review B **31**, 6207–6215 (1985).

[42] B. Altshuler, "Fluctuations in the extrinsic conductivity of disordered conductors", JETP Letters **41**, 648–651 (1985).

[43] P. A. Lee, "Universal conductance fluctuations in disordered metals", Physica A: Statistical Mechanics and its Applications **140**, 169–174 (1986).

[44] A. G. Aronov and Y. V. Sharvin, "Magnetic flux effects in disordered conductors", Reviews of Modern Physics **59**, 755–779 (1987).

[45] S. Washburn, C. P. Umbach, R. B. Laibowitz, and R. A. Webb, "Temperature dependence of the normal-metal Aharonov-Bohm effect", Physical Review B **32**, 4789–4792 (1985).

[46] H. Peng, K. Lai, D. Kong, S. Meister, Y. Chen, X.-L. Qi, S.-C. Zhang, Z.-X. Shen, and Y. Cui, "Aharonov-Bohm interference in topological insulator nanoribbons", Nature Materials **9** (2010).

[47] A. Kandala, A. Richardella, D. Zhang, T. C. Flanagan, and N. Samarth, “Surface-sensitive two-dimensional magneto-fingerprint in mesoscopic Bi_2Se_3 channels”, Nano Letters **13**, 2471–2476 (2013).

[48] J. H. Bardarson, P. W. Brouwer, and J. E. Moore, “Aharonov-Bohm Oscillations in Disordered Topological Insulator Nanowires”, Physical Review Letters **105** (2010).

[49] D. Rosenbach, K. Moors, A. R. Jalil, J. Kolzer, E. Zimmermann, J. Schubert, S. Karimzadah, G. Mussler, P. Schuffelgen, D. Grutzmacher, H. Luth, and T. Schapers, “Gate-induced decoupling of surface and bulk state properties in selectively-deposited Bi_2Te_3 nanoribbons”, SciPost Physics Core **5**, 017 (2022).

[50] M. A. Kastner, “The single-electron transistor”, Reviews of Modern Physics **64**, 849–858 (1992).

[51] H. Ahmed, “Single electron electronics: Challenge for nanofabrication”, Journal of Vacuum Science Technology B: Microelectronics and Nanometer Structures Processing, Measurement, and Phenomena **15**, 2101–2108 (1997).

[52] L. P. Kouwenhoven, D. G. Austing, and S Tarucha, “Few-electron quantum dots”, Reports on Progress in Physics **64**, 701 (2001).

[53] Y. Jing, S. Huang, J. Wu, M. Meng, X. Li, Y. Zhou, H. Peng, and H. Xu, “A Single-Electron Transistor Made of a 3D Topological Insulator Nanoplate”, Advanced Materials **31**, 1903686 (2019).

[54] Y. Takahashi, Y. Ono, A. Fujiwara, K. Nishiguchi, and H. Inokawa, “Silicon Single-Electron Devices”, in *Device Applications of Silicon Nanocrystals and Nanostructures*, edited by N. Koshida (Springer US, 2009), pp. 125–172.

[55] L. P. Kouwenhoven, A. T. Johnson, N. C. van der Vaart, C. J. P. M. Harmans, and C. T. Foxon, “Quantized current in a quantum-dot turnstile using oscillating tunnel barriers”, Physical Review Letters **67**, 1626–1629 (1991).

[56] Y. Nagamune, H. Sakaki, L. P. Kouwenhoven, L. C. Mur, C. J. P. M. Harmans, J. Motohisa, and H. Noge, “Single electron transport and current quantization in a novel quantum dot structure”, Applied Physics Letters **64**, 2379–2381 (1994).

[57] B. Kaestner and V. Kashcheyevs, “Non-adiabatic quantized charge pumping with tunable-barrier quantum dots: a review of current progress”, Reports on Progress in Physics **78**, 103901 (2015).

[58] H. Grabert and M. H. Devoret, *Single charge tunneling: Coulomb blockade phenomena in nanostructures*, Vol. 294 (Springer Science & Business Media, 2013).

[59] H. Pothier, P. Lafarge, C. Urbina, D. Esteve, and M. H. Devoret, “Single-Electron Pump Based on Charging Effects”, Europhysics Letters **17**, 249 (1992).

[60] W. Poirier, S. Djordjevic, F. Schopfer, and O. Thévenot, “The ampere and the electrical units in the quantum era”, Comptes Rendus Physique **20**, 92–128 (2019).

[61] Y. Ono and Y. Takahashi, “Electron pump by a combined single-electron/field-effect-transistor structure”, Applied Physics Letters **82**, 1221–1223 (2003).

[62] X. Jehl, B. Voisin, T. Charron, P. Clapera, S. Ray, B. Roche, M. Sanquer, S. Djordjevic, L. Devoille, and R. Wacquez and M. Vinet, “Hybrid Metal-Semiconductor Electron Pump for Quantum Metrology”, Physical Review X **3**, 021012 (2013).

[63] X. Jehl, B. Roche, M. Sanquer, R. Wacquez, M. Vinet, T. Charron, S. Djordjevic, and L. Devoille, “Multi-charge pumping at 1GHz with a hybrid metal/semiconductor device”, in Conference on Precision Electromagnetic Measurements (2012), pp. 250–251.

[64] M. Brahlek, N. Koirala, N. Bansal, and S. Oh, “Transport properties of topological insulators: Band bending, bulk metal-to-insulator transition, and weak anti-localization”, Solid State Communications, 54–62 (2015).

[65] M. Salehi, X. Yao, and S. Oh, “From classical to quantum regime of topological surface states via defect engineering”, SciPost Physics Lecture Notes, 58 (2022).

[66] N. P. Butch, K. Kirshenbaum, P. Syers, A. B. Sushkov, G. S. Jenkins, H. D. Drew, and J. Paglione, “Strong surface scattering in ultrahigh-mobility Bi_2Se_3 topological insulator crystals”, Physical Review B **81**, 241301 (2010).

[67] M. Brahlek, Y. S. Kim, N. Bansal, E. Edrey, and S. Oh, “Surface versus bulk state in topological insulator Bi_2Se_3 under environmental disorder”, Applied Physics Letters **99**, 012109 (2011).

[68] J. Andzane, G. Kunakova, S. Charpentier, V. Hrkac, L. Kienle, M. Baitimirova, T. Bauch, F. Lombardi, and D. Erts, “Catalyst-free vapour-solid technique for deposition of Bi_2Te_3 and Bi_2Se_3 nanowires/nanobelts with topological insulator properties”, Nanoscale **7**, 15935–15944 (2015).

[69] Y. S. Kim, M. Brahlek, N. Bansal, E. Edrey, G. A. Kapilevich, K. Iida, M. Tanimura, Y. Horibe, S.-W. Cheong, and S. Oh, “Thickness-dependent bulk properties and weak antilocalization effect in topological insulator Bi_2Se_3”, Physical Review B **84**, 073109 (2011).

[70] M. Bianchi, D. Guan, S. Bao, J. Mi, B. B. Iversen, P. D. King, and P. Hofmann, “Coexistence of the topological state and a two-dimensional electron gas on the surface of Bi_2Se_3”, Nature Communications **1**, 128 (2010).

[71] R. Sondors, G. Kunakova, L. Jasulaneca, J. Andzane, E. Kauranens, M. Bechelany, and D. Erts, “High-yield growth and tunable morphology of Bi_2Se_3 nanoribbons synthesized on thermally dewetted Au”, Nanomaterials **11**, 2020 (2021).

[72] A. P. Surendran, “Transport properties of Bi_2Se_3 Topological Insulator Nanoribbon-Superconductor hybrid junctions”, PhD thesis (Chalmers University of Technology, Dec. 2023).

[73] G. Kunakova, T. Bauch, E. Trabaldo, J. Andzane, D. Erts, and F. Lombardi, “High transparency Bi_2Se_3 topological insulator nanoribbon Josephson junctions with low resistive noise properties”, Applied Physics Letters **115** (2019).

[74] S. S. Hong, J. J. Cha, D. Kong, and Y. Cui, “Ultra-low carrier concentration and surface-dominant transport in antimony-doped Bi_2Se_3 topological insulator nanoribbons”, Nature Communications **3**, 757 (2012).

[75] Z. Dai, Z. Pan, and Z. Wang, “Novel Nanostructures of Functional Oxides Synthesized by Thermal Evaporation”, Advanced Functional Materials **13**, 9–24 (2003).

[76] C. Yan, N. Singh, and P. S. Lee, “Morphology Control of Indium Germanate Nanowires, Nanoribbons, and Hierarchical Nanostructures”, Crystal Growth and Design **9**, 3697–3701 (2009).

[77] V. A. Nebol'sin, E. V. Levchenko, V. Yuryev, and N. Swaikat, "About the Shape of the Crystallization Front of the Semiconductor Nanowires", ACS Omega **8** (2023).

[78] X.-Y. Liu, P Bennema, and J. Van der Eerden, "Rough-flat-rough transition of crystal surfaces", Nature **356**, 778–780 (1992).

[79] D. Shoenberg, *Magnetic oscillations in metals* (Cambridge university press, 2009).

[80] M. Brahlek, N. Koirala, M. Salehi, N. Bansal, and S. Oh, "Emergence of Decoupled Surface Transport Channels in Bulk Insulating Bi_2Se_3 Thin Films", Physical Review Letters **113**, 026801 (2014).

[81] W. Zhao, C. X. Trang, Q. Li, L. Chen, Z. Yue, A. Bake, C. Tan, L. Wang, M. Nancarrow, M. Edmonds, D. Cortie, and X. Wang, "Massive Dirac fermions and strong Shubnikov–de Haas oscillations in single crystals of the topological insulator Bi_2Se_3 doped with Sm and Fe", Physical Review B **104**, 085153 (2021).

[82] K. Shrestha, D. E. Graf, V. Marinova, B. Lorenz, and P. C. W. Chu, "Simultaneous detection of quantum oscillations from bulk and topological surface states in metallic $Bi_2Se_{2.1}Te_{0.9}$", Philosophical Magazine **97**, 1740–1754 (2017).

[83] J. Xiong, Y. Luo, Y. Khoo, S. Jia, and R. J. Cava and N. P. Ong, "High-field Shubnikov-de Haas oscillations in the topological insulator Bi_2Te_2Se", Physical Review B **86**, 045314 (2012).

[84] A. K. Okazaki, S. Wiedmann, S. Pezzini, M. L. Peres, P. H. O. Rappl, and E. Abramof, "Shubnikov–de Haas oscillations in topological crystalline insulator SnTe(111) epitaxial films", Physical Review B **98**, 195136 (2018).

[85] O. Pavlosiuk, P. Swatek, and P. Wisniewski, "Giant magnetoresistance, three-dimensional Fermi surface and origin of resistivity plateau in YSb semimetal", Scientific Reports **6**, 38691 (2016).

[86] L. Schubnikow and W. J. de Haas, "Magnetische Widerstandvergrößerung in Einkristallen von Wismut bei tiefen Temperaturen", Leiden Communications **207**, 3 (1930).

[87] L. Veyrat, F. Iacovella, J. Dufouleur, C. Nowka, H. Funke, M. Yang, W. Escoffier, M. Goiran, B. Eichler, O. G. Schmidt, B. Buchner, S. Hampel, and R. Giraud, "Band bending inversion in Bi_2Se_3 nanostructures", Nano Letters **15**, 7503 (2015).

[88] S. Cho, B. Dellabetta, R. Zhong, J. Schneeloch, T. Liu, G. Gu, M. J. Gilbert, and N. Mason, "Aharonov-Bohm oscillations in a quasi-ballistic three-dimensional topological insulator nanowire", Nature Communications **6**, 6–10 (2015).

[89] C. Schindler, C. Wiegand, J. Sichau, L. Tiemann, K. Nielsch, R. Zierold, and R. H. Blick, "Strain-induced Dirac state shift in topological insulator Bi_2Se_3 nanowires", Applied Physics Letters **111** (2017).

[90] E. Tang and L. Fu, "Strain-induced partially flat band, helical snake states and interface superconductivity in topological crystalline insulators", Nature Physics **10**, 964–969 (2014).

[91] C. Lin et al., "Visualization of the strain-induced topological phase transition in a quasi-one-dimensional superconductor $TaSe_3$", Nature Materials **20**, 1093 (2021).

[92] X. Luo, M. B. Sullivan, and S. Y. Quek, “First-principles investigations of the atomic, electronic, and thermoelectric properties of equilibrium and strained Bi_2Se_3 and Bi_2Te_3 including van der Waals interactions”, Physical Review B **86** (2012).

[93] Z. Ren, A. A. Taskin, S. Sasaki, K. Segawa, and Y. Ando, “Large bulk resistivity and surface quantum oscillations in the topological insulator Bi_2Te_2Se”, Physical Review B **82**, 241306 (2010).

[94] J. Zhou, X. Yang, B. Wang, and W. Xiao, “Springback prediction of 7075 aluminum alloy V-shaped parts in cold and hot stamping”, The International Journal of Advanced Manufacturing Technology, 1–14 (2021).

[95] J. Ma and T. Welo, “Analytical springback assessment in flexible stretch bending of complex shapes”, International Journal of Machine Tools and Manufacture **160**, 103653 (2021).

[96] R. Roldán, A. Castellanos Gomez, and E. Cappelluti and F. Guinea, “Strain engineering in semiconducting two-dimensional crystals”, Journal of Physics: Condensed Matter **27**, 313201 (2015).

[97] G. Binnig, N. Garcia, H. Rohrer, J. M. Soler, and F. Flores, “Electron-metal-surface interaction potential with vacuum tunneling: Observation of the image force”, Physical Review B **30**, 4816–4818 (1984).

[98] D. Erts, A. Lõhmus, R. Lõhmus, H. Olin, A. Pokropivny, L. Ryen, and K. Svensson, “Force interactions and adhesion of gold contacts using a combined atomic force microscope and transmission electron microscope”, Applied Surface Science **188**, 460–466 (2002).

[99] W. Liu, X. Peng, C. Tang, L. Sun, and K. Zhang and J. Zhong, “Anisotropic interactions and strain-induced topological phase transition in Sb_2Se_3 and Bi_2Se_3”, Physical Review B **84**, 245105 (2011).

[100] L. Jasulaneca, J. Kosmaca, R. Meija, and J. Andzane and D. Erts, “Review: Electrostatically actuated nanobeam-based nanoelectromechanical switches - materials solutions and operational conditions”, Beilstein Journal of Nanotechnology **9**, 271–300 (2018).

[101] J. E. Lee, G. Ahn, J. Shim, Y. S. Lee, and S. Ryu, “Optical separation of mechanical strain from charge doping in graphene”, Nature Communications **3**, 1024 (2012).

[102] R. Vilaplana, D. Santamaría-Pérez, O. Gomis, F. J. Manjón, J. González, A. Segura, A. Muñoz, P. Rodríguez-Hernández, E. Pérez-González, V. Marín-Borrás, V. Muñoz Sanjose, C. Drasar, and V. Kucek, “Structural and vibrational study of Bi_2Se_3 under high pressure”, Physical Review B **84**, 184110 (2011).

[103] S. G. Mayr and K. Samwer, “Model for Intrinsic Stress Formation in Amorphous Thin Films”, Physical Review Letters **87**, 036105 (2001).

[104] L. Kou, B. Yan, F. Hu, S. C. Wu, T. O. Wehling, C. Felser, C. Chen, and T. Frauenheim, “Graphene-based topological insulator with an intrinsic bulk band gap above room temperature”, Nano Letters **13**, 6251–6255 (2013).

[105] Y. Yan, X. Zhou, H. Jin, C.-Z. Li, X. Ke, G. Van Tendeloo, K. Liu, D. Yu, and M. Dressel and Z. M. Liao, “Surface-Facet-Dependent Phonon Deformation Potential in Individual Strained Topological Insulator Bi_2Se_3 Nanoribbons”, ACS Nano **9** (2015).

[106] Q. Li, Y. Wang, T. Li, W. Li, F. Wang, A. Janotti, S. Law, and T. Gu, “Localized Strain Measurement in Molecular Beam Epitaxially Grown Chalcogenide Thin Films by Micro-Raman Spectroscopy”, ACS Omega **5**, 8090–8096 (2020).

[107] L. Jasulaneca, R. Meija, E. Kauranens, R. Sondors, J. Andzane, R. Rimsa, G. Mozolevskis, and D. Erts, “Cryogenic nanoelectromechanical switch enabled by Bi_2Se_3 nanoribbons”, Materials Science and Engineering: B **275**, 115510 (2022).

[108] E. Lee and J. W. Kang, “Molecular Dynamics Analysis of Graphene-Based Nanoelectromechanical Switch”, ECS Transactions **72**, 1 (2016).

[109] R. Benoit and N. Barker, “Reliability of RF MEMS switches at cryogenic (liquid He) temperatures”, Microelectronics Reliability **111**, 113706 (2020).

[110] J. Chae, S.-H. Kang, S. H. Park, H. Park, K. Jeong, T. H. Kim, S.-B. Hong, K. S. Kim, Y.-K. Kwon, J. W. Kim, et al., “Closing the surface bandgap in thin Bi_2Se_3/graphene heterostructures”, ACS Nano **13**, 3931–3939 (2019).

[111] K. Zollner and J. Fabian, “Single and bilayer graphene on the topological insulator Bi_2Se_3: Electronic and spin-orbit properties from first principles”, Physical Review B **100**, 165141 (2019).

[112] J. Andzane, A. Felsharuk, A. Sarakovskis, U. Malinovskis, E. Kauranens, M. Bechelany, K. A. Niherysh, and I. V. Komissarov and D. Erts, “Thickness-Dependent Properties of Ultrathin Bismuth and Antimony chalcogenide Films Formed by Physical Vapor Deposition and Their Application in Thermoelectric Generators”, Materials Today Energy **19** (2020).

[113] I. M. Ruzin, V. Chandrasekhar, E. I. Levin, and L. I. Glazman, “Stochastic Coulomb blockade in a double-dot system”, Physical Review B **45**, 13469 (1992).

[114] H. Van Houten, C. W. J. Beenakker, and A. A. M. Staring, “Coulomb-Blockade Oscillations in Semiconductor Nanostructures”, in *Single Charge Tunneling: Coulomb Blockade Phenomena In Nanostructures*, edited by H. Grabert and M. H. Devoret (Springer US, 1992), pp. 167–216.

[115] J. Güttinger, T. Frey, C. Stampfer, T. Ihn, and K. Ensslin, “Spin States in Graphene Quantum Dots”, Physical Review Letters **105**, 116801 (2010).

[116] S. M. Cronenwett, S. M. Maurer, S. R. Patel, C. M. Marcus, C. I. Duruöz, and J. S. Harris, “Mesoscopic Coulomb Blockade in One-Channel Quantum Dots”, Physical Review Letters **81**, 5904–5907 (1998).

[117] C. Marcus, R. Westervelt, P. Hopkins, and A. Gossard, “Conductance fluctuations in a quantum dot in the tunneling regime: Crossover from aperiodic to regular behavior”, Surface Science **305**, 480–489 (1994).

[118] L. A. Ponomarenko, F. Schedin, M. I. Katsnelson, R. Yang, E. W. Hill, K. S. Novoselov, and A. K. Geim, “Chaotic Dirac billiard in graphene quantum dots”, Science **320**, 356–358 (2008).

Appended Papers

Paper I

Materials Today Energy 19 (2021) 100587

Contents lists available at ScienceDirect

Materials Today Energy

journal homepage: www.journals.elsevier.com/materials-today-energy/

Thickness-dependent properties of ultrathin bismuth and antimony chalcogenide films formed by physical vapor deposition and their application in thermoelectric generators

J. Andzane [a], A. Felsharuk [a, c], A. Sarakovskis [d], U. Malinovskis [a], E. Kauranens [a],
M. Bechelany [e], K.A. Niherysh [a, c], I.V. Komissarov [c], D. Erts [a, b, *]

[a] Institute of Chemical Physics, Riga, LV-1586, Latvia
[b] Faculty of Chemistry, University of Latvia, Riga, LV-1586, Latvia
[c] Belarusian State University of Informatics and Radioelectronics, Minsk, Republic of Belarus
[d] Institute of Solid State Physics, University of Latvia, Riga, LV-1063, Latvia
[e] Institut Européen des Membranes, IEM – UMR 5635, ENSCM, CNRS, University of Montpellier, Montpellier, France

ARTICLE INFO

Article history:
Received 9 June 2020
Received in revised form
6 November 2020
Accepted 15 November 2020
Available online 27 November 2020

Keywords:
Ultrathin film
Narrow band gap layered semiconductor
Bismuth chalcogenide
Antimony telluride
Thickness-dependent thermoelectric properties

ABSTRACT

In this work, a simple cost-effective physical vapor deposition method for obtaining high-quality Bi_2Se_3 and Sb_2Te_3 ultrathin films with thicknesses down to 5 nm on mica, fused quartz, and monolayer graphene substrates is reported. Physical vapor deposition of continuous Sb_2Te_3 ultrathin films with thicknesses 10 nm and below is demonstrated for the first time. Studies of thermoelectrical properties of synthesized Bi_2Se_3 ultrathin films deposited on mica indicated opening of a hybridization gap in Bi_2Se_3 ultrathin films with thicknesses below 6 nm. Both Bi_2Se_3 and Sb_2Te_3 ultrathin films showed the Seebeck coefficient and thermoelectrical power factors comparable with the parameters obtained for the high-quality thin films grown by the molecular beam epitaxy method. Performance of the best Bi_2Se_3 and Sb_2Te_3 ultrathin films is tested in the two-leg prototype of a thermoelectric generator.

1. Introduction and background

Thermoelectric materials and based technologies, enabling the direct conversion of heat to electricity, are expected to play an important role in solving one of the biggest global challenges, which is increase of energy efficiency of domestic and industrial processes by waste heat capturing and conversion to useful energy. A simplest thermoelectric generator (TEG) for heat-to-electricity conversion consists of two semiconductors with different (n- and p-) types of electrical conductivity, joined at their ends. The performance of thermoelectric materials and devices is characterized by a dimensionless figure of merit ZT, defined as $S^2\sigma T/k$, where S is the Seebeck coefficient of the material, σ is its electrical conductivity, T is absolute temperature, and k is thermal conductivity of the material. $S^2\sigma$ is usually referred as the power factor (PF) of thermoelectric material. The common approaches in enhancement of ZT is maximizing of PF and/or reduction of thermal conductivity of the material [1]. However, interdependency of electrical and thermal conductivities hampers breakthrough enhancement of ZT of materials.

Bismuth and antimony chalcogenides (Bi_2Se_3, Bi_2Te_3, Sb_2Te_3), layered narrow–band-gap semiconductors with recently discovered 3D topological insulator (TI) properties [2–4], are widely known as the best near–room temperature thermoelectric materials with n-type (Bi_2Se_3, Bi_2Te_3) and p-type conductivity, useful for domestic waste heat conversion applications. These materials consist of charge neutralized layers (QLs) bonded together by van der Waals interaction. Each QL is formed by five covalently bonded atomic sheets (for example, Se–Bi–Se–Bi–Se) and is ~1 nm thick.

Recently, it was predicted that quantum confinement introduced by downsizing of the thermoelectric materials may result in enhancement of ZT of thermoelectric materials [5,6]. For example, it has been shown theoretically that the multiple sub-band structure, small band gap, and vicinity of materials with TI properties to

---

[*] Corresponding author.
E-mail address: donats.erts@lu.lv (D. Erts).

https://doi.org/10.1016/j.mtener.2020.100587
2468-6069/

a metallic state associated with an electronic topological transition are responsible for their superior TE performance [7]. Theoretical calculations performed for TI bismuth chalcogenide films [8,9] proved that the reduction of the thickness of thin film below 10 nm will result in noticeable quantum tunneling between the top and bottom surfaces and inducing of hybridization band gap near the Dirac point, resulting in improvement of existing ZT of the material by nearly an order of magnitude due to the disengagement of electrical and thermal conductivities of this material. At the same time, the other research groups predicted that the parallel contributing of coexisting in such TI systems surface and bulk states to the thermoelectric properties of the TI material may tend to cancel each other out, and ZT cannot be enhanced dramatically; however, some improvement of thermoelectrical properties of material could still be observed at optimal positions of Fermi levels [10]. Experimental investigation of properties of nanostructured materials of the bismuth and antimony chalcogenide family also showed different results. For example, properties of nanostructured n-type BiTe showed coexistence of distinct topological quantum phases in this material resulting on potential decoupling of thermal and electronic transport properties, which is the fundamentals for efficient thermoelectrics [11].

On the other hand, while the theoretically proposed thicknesses for the hybridization gap opening, leading to the disengagement of electrical and thermal conductivities and consequent improvement of ZT of the material are below 6 nm and 3 nm for Bi_2Se_3 and Bi_2Te_3, respectively [10], the experimental investigation of grown by molecular beam epitaxy (MBE) ~5 nm thin $(Bi_{1-x}Sb_x)_2Te_3$ and ~5–30 nm thin Bi_2Se_3 films did not show any significant improvement from the bulk values of ZT [12,13]. Regarding Sb_2Te_3 thin films, while theoretical studies predicted significant sensitivity of Seebeck coefficient and electrical conductivity of these thin films to the thickness reduction down to 2 nm, the experimental measurements were performed only for the Sb_2Te_3 thin films with thicknesses down to 30 nm fabricated by atomic layer deposition and revealed increase of the electrical conductivity but at the same time decrease of the Seebeck coefficient, resulting to reduction of thermoelectric efficiency of the material related to the contribution of surface states [14]. The method for gaining a thermoelectrical benefit from the Sb_2Te_3 thin film proposed by the aforementioned research was gapping the surface states and tuning the charge carrier concentration. However, the theoretically proposed thickness for hybridization gap opening in Sb_2Te_3 is 4 nm [10], and, to the best of our knowledge, the experimental research of the thermoelectric properties of Sb_2Te_3 thin films with thicknesses below 30 nm has not been yet performed.

This work is focused on development of a simple and cost-effective physical vapor deposition (PVD) method of synthesis of Bi_2Se_3 and Sb_2Te_3 ultrathin films of thicknesses down to 5 nm on different (natural mica, quartz, graphene) substrates. Mica is recognized as an excellent non-electrically conductive substrate for the growth of layered materials as bismuth and antimony chalcogenides. Mica is a chemically inert substrate with atomically flat surface ideal for ultrathin films growth by van der Waals epitaxy. For example, the minimal reported thicknesses of the separate Bi_2Se_3 nanoplates PVD-deposited on synthetic fluorophlogopite mica were as small as 2–3 nm [15]. In this work, natural muscovite mica is used, which is much cheaper alternative to the synthetic mica. However, the drawbacks of mica substrates for thermoelectric measurements are its relatively high thermal conductivity, masking the real thermal conductivity of ultrathin films deposited on its surface. A good alternative to mica substrates for the thermoelectric measurements is fused quartz substrates, having low thermal conductivity. However, deposition of the ultrathin films on quartz substrates is challenging because of the presence of variety of chemical and mechanical defects on its surface. Finally, graphene is a very attractive substrate for the epitaxial growth of ultrathin Bi_2Se_3 and Sb_2Te_3 films because of the small lattice mismatch with these materials (2.9% [16] and 4% [17] for Bi_2Se_3 and Sb_2Te_3, respectively). Moreover, because of high electrical conductance graphene has a potential to be used simultaneously as the substrate for ultrathin films deposition and as the electrode for the measurements. Electrical and thermoelectric properties of Bi_2Se_3 and Sb_2Te_3 ultrathin films of thicknesses ranging from 5 to 15 nm are investigated, discussed, and compared with the properties of thin films grown by the MBE method. Performance of Bi_2Se_3 and Sb_2Te_3 ultrathin films with the best thermoelectric performance is tested in a prototype of the two-leg TEG.

2. Results and discussion

2.1. Synthesis

Previously, our group developed the PVD method for the Volmer–Weber growth of Bi_2Se_3 thin films on mica, glass, and graphene surfaces, using Bi_2Se_3 compound as a source material [18–20]. However, the minimal thicknesses of thin films grown by this method exceeded 50 nm. In this work, to achieve deposition of thinner thin films, the Bi_2Se_3 source material was replaced with separate Bi and Se sources. The use of separate sources allowed to differentiate their evaporation rates by placing them in different temperature zones as shown in Fig. 1a.

The substrate was placed in the temperature region ensuring formation of stoichiometric Bi_2Se_3 [18,20]. Presumably, the layer-by-layer growth of Bi_2Se_3 ultrathin films when separate Bi and Se sources are used instead of Bi_2Se_3 powder can be explained by specifics of evaporation and deposition processes of different source materials. The evaporation of Bi_2Se_3 at temperatures above 427 °C has dissociative nature: $Bi_2Se_3 \leftrightarrow 2BiSe(gas) + 1/2Se_2(gas)$ [21]. Because of the higher heat of formation of BiSe (~167 kJ mol^{-1}) than Bi_2Se_3 (~140 kJ mol^{-1}) [22], the adsorbed on the substrate BiSe molecules diffuse across the surface until they reach the energetically favorable position. This process results in nucleation and further growth of Bi_2Se_3 islands [18]. In case of the use of separate Bi and Se sources, heat of vaporization of Se is nearly five times smaller than of Bi (37.7 and 179 kJ mol^{-1}, respectively) [22]. The deposition process starts with evaporation and impinging of Se atoms on the whole substrate surface followed by evaporation of Bi and formation of the Bi_2Se_3 compound over all the surface of the substrate. Using this method, Bi_2Se_3 ultrathin films with thicknesses 5, 6, and 15 nm on mica substrates were prepared.

For the deposition of Sb_2Te_3 ultrathin films, the source material was placed in the center of the furnace hot zone (Fig. 1b). The mechanism of the Sb_2Te_3 growth differs from that of Bi_2Se_3, where Bi is mainly in the atomistic form. The dissociative evaporation of the Sb_2Te_3 compound can be described by the equation $Sb_2Te_3 \leftrightarrow 1/2Sb_4(gas) + 3/4Te_2(gas)$ [21]. Because of the high stability of Sb_4 tetramers and their lower sticking coefficient to the substrate than Sb_2Te_3 [21,23], the Sb_2Te_3 deposition process occurs in three steps. Initially, the optimal for Sb_2Te_3 nucleation substrate temperature must be lower than the threshold for Sb_2Te_3 nucleation (~190 °C), but high enough to avoid Sb clustering. In the developed synthesis method, this condition is fulfilled when the temperature in the center of the quartz tube reaches 405–410 °C and the nucleation of Sb_2Te_3 on the substrate takes place and may be visually observed. However, after the nucleation stage the substrate temperature can be increased by 10–20 °C to improve the Sb_2Te_3 film quality [21,23]. At this step, the further increase of the temperature in the furnace tube center up to 415 or 420 °C and consequent increase of the substrate temperature resulted in formation of 5 nm and 7 nm thin

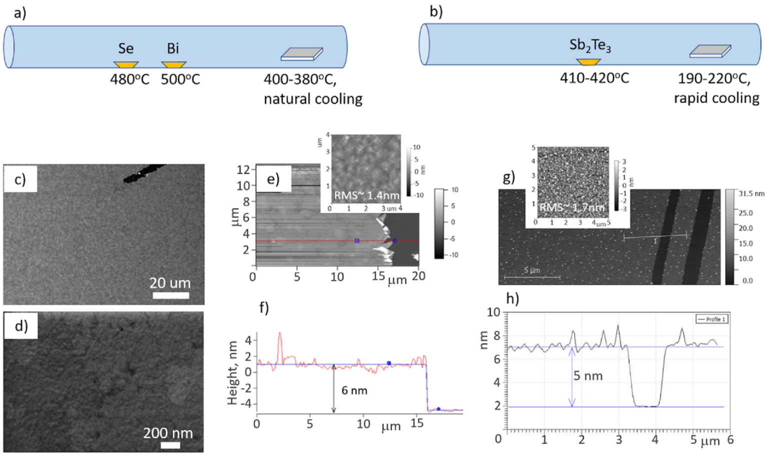

Fig. 1. a—b) Schematics of the experimental setup for Bi_2Se_3 (a) and Sb_2Te_3 (b) ultrathin films synthesis; c—f) The SEM (c,d), AFM (e) image and thickness profile (f) of 6 nm thin Bi_2Se_3 film; g—h) The AFM (g) image and thickness profile (h) of 5 nm thin Sb_2Te_3 film. AFM, atomic force microscope; SEM, scanning electron microscope; RMS, root mean square roughness.

Sb_2Te_3 films, respectively. This step is followed by immediate rapid cooling of the substrate in the inert atmosphere to preserve the Sb_2Te_3 ultrathin film of desired thickness.

The described methods of deposition of Bi_2Se_3 and Sb_2Te_3 films are effective for obtaining of ultrathin films with thicknesses down to 5 nm on the mica surface (Fig. 1 e-h) and down to 8—10 nm on fused quartz and graphene substrates (Fig. S1).

2.2. Structural characterization

Low- and high-magnification scanning electron microscope (SEM) images (Fig. 1c,d; an artificial scratch in Fig. 1c is introduced for the thickness measurements) show that the obtained ultrathin films are uniform and fully fused. Surface scans (Fig. 1 e,g) and thickness profiles (Fig. 1 f,h) performed by the atomic force microscope (AFM) for 6 nm thin Bi_2Se_3 film and 5 nm thin Sb_2Te_3 film show that these ultrathin films have smooth surface with the root mean square roughness (RMS) ~1.4 nm and ~1.7 nm, respectively (insets in Fig. 1 e,g). Energy-dispersive X-ray spectroscopy (EDX) measurements of the ultrathin Bi_2Se_3 and Sb_2Te_3 films deposited on quartz substrates confirmed within the standard deviations the stoichiometric composition (40 [Bi, Sb]: 60 [Bi, Te] at %) of these films. These results were supported by the X-ray photoelectron spectroscopy (XPS) analysis and Raman spectroscopy of ultrathin Bi_2Se_3 and Sb_2Te_3 films.

An example of XPS spectra of the 6 nm thin Bi_2Se_3 film is shown in Fig. 2 a,b. The XPS analysis showed the presence of Bi and Se in the material. In high-resolution spectra, the peaks corresponding to Bi4f$_{7/2}$ and Bi4f$_{5/2}$ are located at 158.5 eV and 163.8 eV, while the positions of Se3d$_{5/2}$ and Se3d$_{3/2}$ peaks are located at 53.8 eV and 54.6 eV, respectively.

The analysis of the presented in Fig. 2 c,d representative XPS spectra of the 5 nm thin Sb_2Te_3 film showed the presence of Sb and Te in the material. The detailed study of the spectra revealed the positions of Sb3d$_{5/2}$ and Sn3d$_{3/2}$ peaks located at 529.1 eV and 538.5 eV, respectively, identified as metallic Sb. The analysis of the Te signal revealed the presence of metallic Te3d$_{5/2}$ and Te3d$_{3/2}$ peaks located at 573.2 and 583.6 eV, respectively.

For the both Bi_2Se_3 and Sb_2Te_3 ultrathin films, the detailed analysis of the XPS spectra revealed the presence of peaks related to the oxidized material. Shoulders in Bi4f spectra located at 159.3 eV and 164.6 eV (Fig. 2 a) corresponded to the oxidized surface of the Bi_2Se_3 film. A similar small intensity feature corresponding to oxidized Se is present in the spectrum of Se3d in the region of 59 eV (Fig. 2 b). For Sb_2Te_3, the oxidized Sb peaks located at 530.8 eV (3d$_{5/2}$) and 540.2 eV (3d$_{3/2}$) with the additional peak located at 531.5 eV corresponding to O1s signal (Fig. 2 c), as well as oxidized Te3d$_{5/2}$ and Te3d$_{3/2}$ peaks located at 576.8 and 587.2 eV and Te monoxide located at 575.0 eV and 585.5 eV (Fig. 2 d) were identified. The presence of oxidation-related peaks in the XPS spectra of ultrathin Bi_2Se_3 and Sb_2Te_3 films is related to the susceptibility of these materials to rapid oxidation in air [24,25], as the synthesized ultrathin films were stored under ambient conditions for several months.

Chemical composition of the samples based on the measured XPS deconvoluted peak intensities has been evaluated to confirm the stoichiometry of the material (Table 1).

Raman spectroscopy of the deposited on different substrates ultrathin Bi_2Se_3 and Sb_2Te_3 films identified typical characteristic $E^2{}_g$ and $A^2{}_{1g}$ vibration modes appearing at the peak positions of ~130 cm^{-1} and ~173 cm^{-1} corresponding to Bi_2Se_3 (Fig. 3 a), and ~117 cm^{-1} and ~165 cm^{-1} corresponding to Sb_2Te_3 (Fig. 3 b), which is consistent with the previous reports [26,27]. No significant deviations in the positions of the peak maxima were observed.

The X-ray diffraction (XRD) characterization of the ultrathin Bi_2Se_3 and Sb_2Te_3 films deposited on mica revealed that because of the very small thickness of the deposited Bi_2Se_3 films, the XRD diffraction peaks related to both Bi_2Se_3 and mica are overlapping, which greatly complicates spectra analysis (Fig. S2), while the XRD spectra of the ultrathin films deposited on quartz and graphene substrates allow to distinguish diffraction peaks related to the reflection planes of Bi_2Se_3 and Sb_2Te_3. Fig. 4 shows the representative XRD spectra of 6 nm thin Bi_2Se_3 film and 10 nm thin Sb_2Te_3

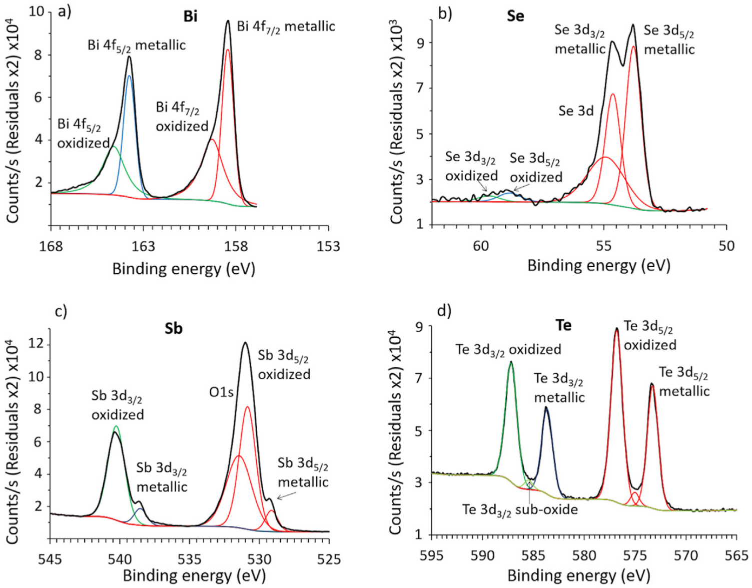

Fig. 2. Representative deconvoluted XPS spectra of a-b) 6 nm thin Bi_2Se_3 film and c-d) 5 nm thin Sb_2Te_3 film deposited on mica substrates. XPS, X-ray photoelectron spectroscopy.

Table 1
Comparison of the chemical compositions of the Bi_2Se_3 and Sb_2Te_3 source materials and ultrathin films deposited on mica substrates revealed by the XPS measurements.

Chemical element	Bi_2Se_3 source material	Bi_2Se_3 6 nm thin film on mica	Chemical element	Sb_2Te_3 source material	Sb_2Te_3 5 nm thin film
	at %	at %		at %	at %
Bi	37.1	36.7	Sb	41.6	44.9
Se	62.9	63.3	Te	58.4	55.1

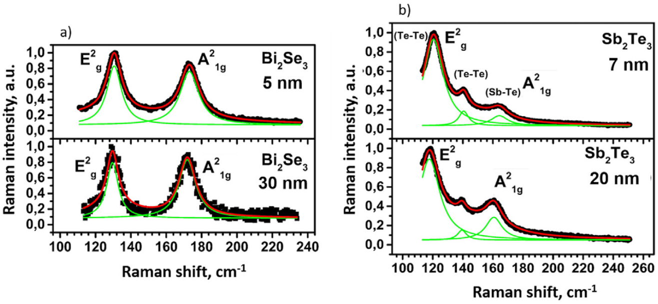

Fig. 3. Representative deconvoluted Raman spectra of a) 5 nm and 30 nm thin Bi_2Se_3 films deposited on quartz substrates, and b) 7 nm and 20 nm thin Sb_2Te_3 films deposited on mica substrates.

film deposited on graphene substrates. The XRD spectra of thicker (20 nm) Bi_2Se_3 and Sb_2Te_3 thin films are shown for the comparison.

The XRD analysis of the Bi_2Se_3 thin films spectra (Fig. 4 a) revealed the presence of peaks related the (003n) group and the absence of peaks characteristic for polycrystalline Bi_2Se_3 (015) and $(10\underline{1}0)$ reflection planes for both 6 nm and 20 nm thin films (ref. code 00-033-0214 [28]). This indicates well-oriented growth of Bi_2Se_3, with crystallographic c-axis oriented perpendicularly to the

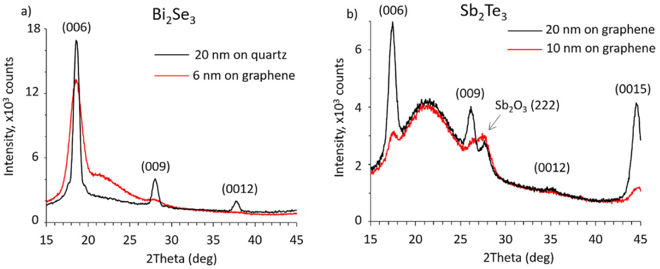

Fig. 4. Representative XRD spectra of a) Bi_2Se_3 and b) Sb_2Te_3 ultrathin films deposited on quartz and graphene substrates. XRD, X-ray diffraction.

substrate surface [20,29]. The intensity ratios for the peaks related to (006) and (009) reflection planes are 4.2 and 6.3 for the 20 nm thin film deposited on quartz and 6 nm thin film deposited on graphene, respectively, indicating a more uniform orientation of the ultrathin films grown on graphene in comparison with the ultrathin films grown on quartz, which is related to the epitaxial growth [20].

Similarly to the Bi_2Se_3, the most of peaks presented in the XRD spectra of the Sb_2Te_3 thin films (Fig. 4 b) were related to the (003n) group (ref. code 01-071-0393, calculated from ICSD 002084 using POWD-12++). Besides these peaks, a peak located at 2Theta ~27.7 deg was observed in both Sb_2Te_3 spectra. This peak may be attributed to the (222) reflection plane of the Sb_2O_3 oxide (ref. code 01-075-1565, calculated from ICSD 031102 using POWD-12++) and confirms the XPS data, where slight excess of Sb presented in the oxidized form on the surface of the Sb_2Te_3 thin film was identified.

2.3. Electrical and thermoelectric characterization

Despite the same deposition method and similar growth orientation and chemical composition, the in-plane electrical and thermoelectric properties of the deposited under identical conditions on mica and quartz substrates Bi_2Se_3 and Sb_2Te_3 ultrathin films differ (Table 2).

As it is seen fromTable 2, the ultrathin films deposited on quartz are few nm thicker and have higher Seebeck coefficients. However, because of the higher resistivity of these films, the resulting PF of these ultrathin films is lower than Bi_2Se_3 and Sb_2Te_3 ultrathin films deposited on mica. The reason for such a difference in properties may be mechanical and chemical defects of the quartz substrates, serving as multiple nucleation centers and resulting in formation of the film having more grain boundaries (boundaries between the coalesced nanoplates) than the ultrathin films deposited on mica, which is supported by the difference in intensity ratios of the XRD peaks, as well as by the previously reported structural investigation of the thicker films deposited on mica, quartz, and graphene [18,20]. While measurements of in-plane thermoelectric properties of ultrathin films deposited on graphene are challenging due to the high electrical and thermal conductivity of graphene, it is expected that because of the epitaxial growth they will be similar to the ultrathin films deposited on mica. Multiple grain boundaries reduce electrical conductance of the ultrathin films, but at the same time may serve as energy filters for the charge carriers, which results in an increase of the Seebeck coefficient. The following sections of the manuscript are focused on the in-detail investigation of the properties of showing better thermoelectric performance Bi_2Se_3 and Sb_2Te_3 ultrathin films deposited on mica substrates.

2.4. Thickness-dependent electrical properties of ultrathin films deposited on mica

Fig. 5 a illustrates temperature dependence of the resistivity of the Bi_2Se_3 and Sb_2Te_3 ultrathin films. The Bi_2Se_3 ultrathin film with thicknesses 6 and 15 nm exhibit metallic behavior typical for thin Bi_2Se_3 nanostructures (Fig. 5 a) [30]. For these thin films, the higher decrease rate of resistivity of the latter possibly indicates higher concentration of contributing to the conductivity defects as Se vacancies [31]. In turn, the resistivity of the Bi_2Se_3 ultrathin film with thickness 5 nm reaches its minimal value at temperature 257 K and then increases with decreasing temperature.

Such upturn in the resistivity of 5 nm thin Bi_2Se_3 film is consistent with some previous reports related to the opening of an energy band gap in very thin Bi_2Se_3 samples due to the quantum confinement effects resulting in reduction of electrical conductance at low temperatures [32,33]. While the precise determination of the band gaps of the Bi_2Se_3 ultrathin films was outside the scope of this work, the relation of the band gap value to the thickness of the thin film can be roughly evaluated by the estimation of the Fermi energy and the assumption that in the non-doped semiconductor the band gap energy approximately equals to the double of it. The Fermi energy can be estimated from the experimentally determined Seebeck coefficient by the simplified formula $E_F \approx \pi^2 k_B^2 T / 3eS$ [34], where k_B is Boltzmann constant, T is the background temperature, e is the elementary charge, and S is the absolute value of the Seebeck coefficient. As it is seen from Fig. 6, the Fermi energy of the Bi_2Se_3 thin films tends to increase with the decrease of the

Table 2
Representative comparison data between the properties of ultrathin Bi_2Se_3 and Sb_2Te_3 films deposited on mica and quartz substrates.

Compound	Substrate	Film thickness, nm	Seebeck coefficient, $\mu V \cdot K^{-1}$	Resistivity, $\Omega \cdot m$	PF, $\mu W \cdot K^{-2} \cdot cm^{-1}$
Bi_2Se_3	mica	6	−55	$1.23 \cdot 10^{-5}$	2.46
Bi_2Se_3	quartz	8	−75	$1.7 \cdot 10^{-4}$	0.33
Sb_2Te_3	mica	7	132	$0.8 \cdot 10^{-5}$	23
Sb_2Te_3	quartz	10	154	$2.1 \cdot 10^{-5}$	11

PF, power factor.

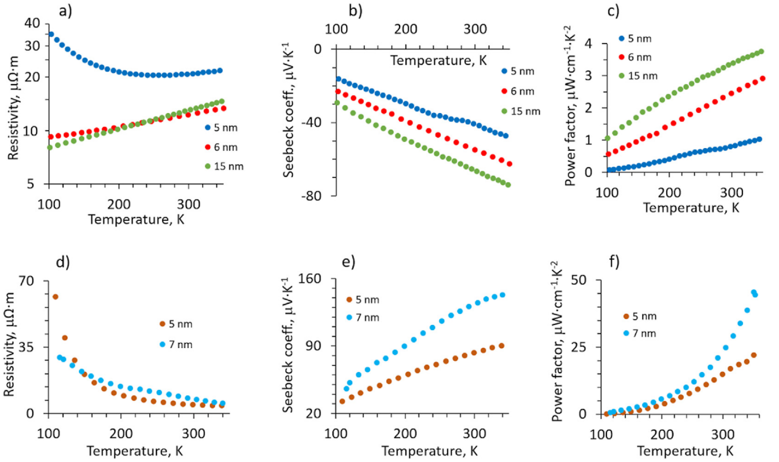

Fig. 5. Temperature dependencies of resistivity, Seebeck coefficient and PF of Bi_2Se_3 (a–c) and Sb_2Te_3 (d–f) ultrathin films of different thicknesses. PF, power factor.

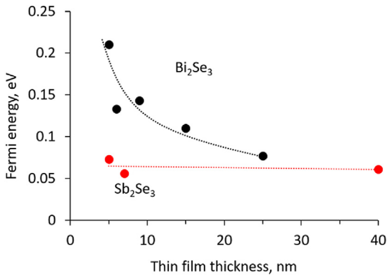

Fig. 6. Estimated values of the Fermi level for deposited on mica substrates Bi_2Se_3 and Sb_2Te_3 thin films of different thicknesses.

film thickness, proving the influence of the film thickness on the band gap size.

In contrast with the Bi_2Se_3 ultrathin films, the 5 nm and 7 nm thin Sb_2Te_3 showed the semiconductor type of conductivity (Fig. 5 d), with 5 nm thin film showing more pronounced temperature-dependent increase of resistivity and at a higher rate than 7 nm thin film. Accordingly to Hinsche et al. [14], such behavior of the resistivity may be attributed to significant contribution of surface states to the total conductivity of the thin films, whose hole concentration is in the order of 10^{18} cm^{-3}. Increase of the Fermi level with the reduction of the film thickness was not observed for the 5–7 nm Sb_2Te_3 ultrathin films, which is in agreement with Osterhage et al. [10] which proposed opening of the hybridization gap in Sb_2Te_3 when its thickness is reduced below 4 nm.

2.5. The Seebeck coefficient and power factor of the ultrathin films deposited on mica

At 300 K, the Seebeck coefficient of the Bi_2Se_3 ultrathin films varied from −67 μV K^{-1} for 15 nm thick film to −40 μV K^{-1} for 5 nm thick film (Fig. 5b). Negative values of Seebeck coefficients indicate n-type of conductivity of Bi_2Se_3. The PF calculated for 300 K varied from 3.4 μW K^{-2} cm^{-1} for 15 nm thick film to 0.8 μW K^{-2} cm^{-1} for 5 nm thick film. These values are comparable with the values obtained for the MBE-grown Bi_2Se_3 thin films ($S = -85$ μV K^{-1} and $PF = 4$ μW K^{-2} cm^{-1} for 15 nm thin film and $S = -64.6$ μV K^{-1} and $PF = 1.4$ μW K^{-2} cm^{-1} for 5 nm thin film) [13] and indicate usability of our PVD method for obtaining of high-quality Bi_2Se_3 ultrathin films. For the Sb_2Te_3 ultrathin films, Seebeck coefficients were positive, indicating p-type conductivity as is expected for this material. 7 nm thin film showed significantly higher Seebeck coefficient than the 5 nm thin film ($S = 130$ μV K^{-1} vs. $S = 82$ μV K^{-1}). The calculated PF for 7 nm and 5 nm thin Sb_2Te_3 films were 23 μW K^{-2} cm^{-1} and 15 μW K^{-2} cm^{-1}, respectively. These values are comparable with ones reported for ~1 μm thick Sb_2Te_3 thin films grown by MBE ($S = 130$ μV K^{-1}, $PF = 29$ μW K^{-2} cm^{-1}) [35], co-evaporation technique ($S = 160$ μV K^{-1}, $PF = 20$ μW K^{-2} cm^{-1}) [36], and bulk Sb_2Te_3 grown by the Bridgman method ($S = 79$ μV K^{-1}, $PF = 30$ μW K^{-2} cm^{-1}) [35]. There is a lack of experimental data on thermoelectrical properties on the ultrathin (below 30 nm) Sb_2Te_3 films; however, accordingly to the theoretical studies, the significant difference in Seebeck coefficients of 5 nm and 7 nm thin Sb_2Te_3 films may be related to the larger contribution of topological conductive surface states in thinner films [14]. For easier reading, Table 3 summarizes Seebeck coefficient and PF of the thin films obtained in this work and reported by other research groups, including data for bulk Bi_2Se_3 and Sb_2Te_3 materials.

Temperature dependence of experimentally determined Seebeck coefficients and estimated PF of Bi_2Se_3 and Sb_2Te_3 ultrathin films of different thicknesses are shown in Fig. 5 b,c,e,f. All Bi_2Se_3 films showed quasilinear decrease of the Seebeck coefficient and PF with the decrease of temperature (Fig. 5 b,c), which indicates prevailing degenerate electron state [13]. Determined from the slopes of the PF curves decrease rates showed clear dependence of PF on the ultrathin films thickness, and ranged from 0.0113 μW cm^{-1} K^{-2} per K for 15 nm thin film down to 0.0038 μW cm^{-1} K^{-2} per K for 5 nm thin film. Lower PF decrease rates of thinner Bi_2Se_3 films indicate their better applicability for

Table 3
Comparison between the Seebeck coefficients and PF of Bi_2Se_3 and Sb_2Te_3 thin films obtained in this work and by other research groups.

Sample	Seebeck coefficient, $\mu V \cdot K^{-1}$	PF, $\mu W \cdot K^{-2} \cdot cm^{-1}$	Research group
5 nm thin Bi_2Se_3 film	−40	0.8	this work
6 nm thin Bi_2Se_3 film	−55	2.45	this work
15 nm thin Bi_2Se_3 film	−67	3.5	this work
MBE-grown 5 nm thin Bi_2Se_3 film	−64.6	1.4	Guo et al. [13]
MBE-grown 15 nm thin Bi_2Se_3 film	−85	4.0	Guo et al. [13]
Bulk Bi_2Se_3 (Bridgman method)	−59	9.4	Navrátil et al. [37]
5 nm thin Sb_2Te_3 film	82	15	this work
7 nm thin Sb_2Te_3 film	130	23	this work
MBE-grown 1 μm thin Sb_2Te_3 film	130	29	Peranio et al. [35]
Co-evaporated 1 μm thin Sb_2Te_3 film	160	20	Huang et al. [36]
Bulk Sb_2Te_3 (Bridgman method)	79	30	Peranio et al. [35]

MBE, molecular beam epitaxy.

wide-range temperature applications. Observed for the considered temperature range systematic decrease of the Seebeck coefficient and PF with the decrease of Bi_2Se_3 ultrathin film thickness is consistent with the previous report on thermoelectrical properties of Bi_2Se_3 MBE thin films with thicknesses 5−30 nm [13]. It can be attributed to the increase of the contribution of Dirac-like topological surface states, whose linear dispersion is not optimal for the increase of the Seebeck coefficient [13]. The possible measures for improvement of the power factor of ultrathin films may include further decrease of the film thickness below 5 nm to completely gap the surface states, as well as tuning of the Fermi level by doping. Temperature dependencies of Seebeck coefficient of Sb_2Te_3 ultrathin films showed slight deviations from linear behavior, but their PF exhibited power-law increase (especially for the 7 nm thin Sb_2Te_3 film) with the increase of temperature (Fig. 5 e,f). The non-linear behavior of Seebeck coefficient and PF of ultrathin Sb_2Te_3 films is consistent with the remarkable contribution of topological surface states of the nanoscale Sb_2Te_3 with charge carrier concentrations in the order 10^{18}−10^{19} [14]. However, further experimental work is required for clarification of the observed dependencies. Significant increase of the PF of the 7 nm thin Sb_2Te_3 film above the room temperature makes it attractive for application in thermoelectrical devices for domestic waste heat conversion.

Showing the best PF Bi_2Se_3 and Sb_2Te_3 ultrathin films of 15 nm and 7 nm thickness, respectively, were tested in a prototype of two-leg TEG as described in the Experimental section.

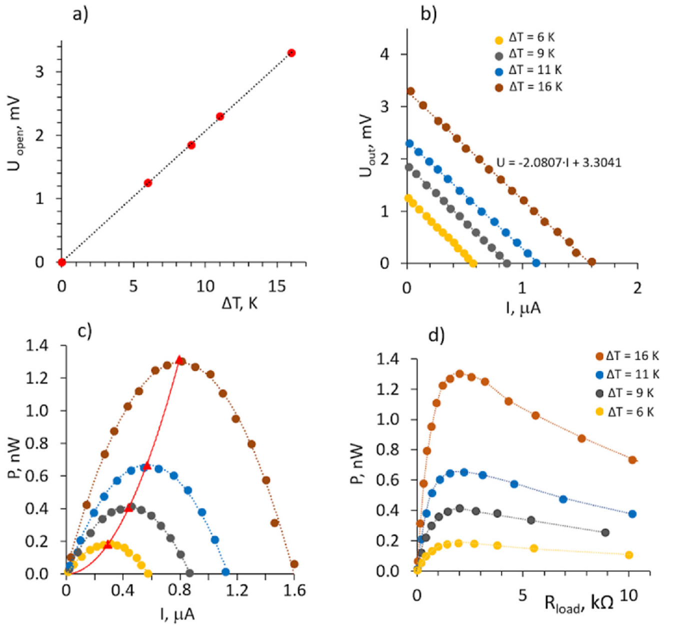

Fig. 7. Characterization of load-dependent behavior of the TEG prototype: a) thermally generated open circuit voltage vs. temperature gradient b) output voltage vs. output current; c) output power vs. output current; red triangles represent maximal power for each temperature gradient; d) output power vs. external load.

Performance of the TEG prototype was characterized by measuring the load-dependence behavior [38]. The open circuit output voltage generated by the TEG showed linear dependence on the temperature gradient (Fig. 7 a) that can be described by function U_{out} [mV] = 0.2·ΔT[K]. This result is roughly 2 times lower in comparison with the $U_{open}(\Delta T)$ function obtained for commercial thermoelectric module TEC1-12707 (U_{open}[mV] = 53.17·ΔT for 127 leg couples, which equals U_{open}[mV] = 0.42·ΔT per one leg pair) [38]. Most likely, the poorer performance of the demonstrated prototype in comparison with the commercial device is related to the heat dissipation at the ultrathin film–mica substrate interface and in the electrical contacts to the ultrathin films, which should be optimized in future. The output voltage vs. output current of the TEG at different external loads and temperature gradients is shown in Fig. 7 b. Dependencies of output voltage vs. output current are linear and of equal slope, proving stable operation of the device and allowing to extract the thermopower and internal resistance of the TEG from the linear fittings (Fig. 7 b), as well as to calculate the output power vs. output current (Fig. 7 c) and vs. the external load (Fig. 7 d) (Table 4). It was found that the maximal output power produced by the TEG prototype shows power-law increase with the increase of the temperature gradient (Fig. 7 c), which makes these devices attractive for applications involving low temperature gradients, for example, for domestic waste heat conversion. As the maximal power generated by the two-leg TEG prototype was in the range of nW for the nanosized cross-section, the comparison of its performance with the performance of the commercially available thermoelectric module was performed per cross-section unit. The maximal powers per cross-section area generated by the two-leg TEG prototype and 127 leg couple TEC1-12707 [38] were found to be 1.2 mW cm^{-2} and 6.25 mW cm^{-2}, respectively, indicating a high potential of the demonstrated TEG prototype for further development and application in domestic waste heat conversion devices.

As it can be seen from Table 4, the main drawback of the developed two-leg TEG prototype is high internal resistance in comparison with the bulk materials because of the very high length-to–cross-section ratios of the ultrathin films. This puts limitation to the resistance of the external devices as it is well known that power transfer between a voltage source and an external load is at its most efficient when the resistance of the load matches the internal resistance of the voltage source. However, such TEGs may find application for powering of potential devices having the resistance in the range 1–10 kΩ as their operation at such external loads is quite stable (Fig. 7 d). Comparison of the properties (measured at room temperature) of ultrathin films used for development of two-leg TEG prototype with the properties of the thin films used for development of the superlattice-based thin film thermoelectric modules, capable of producing a cooling flux of double that of the current state-of-the-art value [39]; however, not tested under different external loads is shown in Table 5.

As it is seen from the data in Table 5 and also supported by the research performed by other groups [40], the improvement of the thermoelectric efficiency of thin films may be achieved by consecutive deposition of different materials having the same type of conductivity and similar crystal lattices, which is in the scope of the following work of our group.

Table 4
The main parameters of the ultrathin films–based two-leg TEG prototype.

Temperature gradient, K	Thermopower, μV/K	Internal resistance, Ω	Maximal output power, nW	Optimal load resistance, Ω
6	204.9	2195	0.184	2188
9	203.6	2158	0.406	2136
11	205.5	2061	0.666	2057
16	200.6	2081	1.316	2087

Table 5
Comparison between properties of thin films synthesized in this work and reported by the other group.

Type of the thin film	Electrical resistivity, μΩ·m	Seebeck coefficient, $\mu V \cdot K^{-1}$	PF, $\mu W \cdot K^{-2} \cdot cm^{-1}$	Reference
p-type Bi_2Te_3/Sb_2Te_3	10.2	238	55	Bulman et al. [39]
p-type Sb_2Te_3	7.5	132	23	This work
n-type δ-doped $Bi_2Te_{3-x}Se_x$	13.7	−276	56	Bulman et al. [39]
n-type Bi_2Se_3	13	−67	3.5	This work

3. Conclusions

In summary, the PVD method for obtaining of Bi_2Se_3 and Sb_2Te_3 ultrathin films of thicknesses 5–10–15 nm on different substrates as mica, fused quartz, and monolayer graphene has been developed. 5–7 nm thin Sb_2Te_3 films were synthesized for the first time. Deposited on mica 5–15 nm thin Bi_2Se_3 films and 5–7 nm thin Sb_2Te_3 films showed thermoelectrical properties comparable with MBE-grown thin films. 5 nm thin Bi_2Se_3 film showed pronounced unusual upturn in resistance at temperatures below 257 K. These results are consistent with recent theoretical research gapping of topological surface states in Bi_2Se_3 thin films with thicknesses below 6 nm, which may potentially result in enhancement of thermoelectrical efficiency of this material. However, the observed systematic decrease of the Seebeck coefficient and power factor with the decrease of thickness of the Bi_2Se_3 ultrathin films indicates necessity of additional downsizing measures for effective enhancement of thermoelectric properties of this material. In turn, 7 nm thin Sb_2Te_3 film showed significant thermoelectric properties, which are comparable with 1 μm–thick MBE-grown film. Performance of 15 nm thin Bi_2Se_3 film and 7 nm thin Sb_2Te_3 film was tested in the two-leg prototype of the TEG. It showed stable operation under different external loads and temperature gradients and performance comparable with the commercial thermoelectric module; however, because of the high internal resistance it was found useful for powering devices with resistances in the range 1–10 kΩ. Potential routes for the improvement of the thermoelectric performance of the ultrathin films–based TEGs include replacement of the single ultrathin film with multilayered structures, the use of substrates with low thermal conductivity, and optimization of the electrical contacts to ultrathin films.

4. Materials and methods

4.1. Deposition of ultrathin films

The ultrathin films were deposited using a single-zone quartz tube furnace GCL-1100X (MTI Corp.). Bismuth (Bi) (≥99.99%, CAS: 7440-69-9, Sigma Aldrich), selenium (Se) (99+, CAS: 7782-49-2, Emsure) and antimony telluride (Sb_2Te_3) (99.999%, CAS: 1327-50-0, Alfa Aesar) powders were used as source materials. Evaporation temperatures were 500 °C for Bi, 480 °C for Se, and 415–420 °C for Sb_2Te_3. The substrate – freshly cleaved natural mica sheets – of thickness ~60 μm (Agar Scientific) or fused quartz 2 cm × 2 cm x 1 mm (Agar Scientific) or grown by chemical vapor deposition and transferred to the quartz substrate monolayer graphene [29] was placed downstream from the source materials located in the central area of the furnace tube. After the placement of the source materials and the substrate, the furnace tube was ventilated with the nitrogen flow and pumped down to the base pressure of 150 mTorr, which was kept constant during the deposition process. The heating rate of the source materials was 48 °C/min. The maximal substrate temperature during the deposition process was 400 °C for deposition of Bi_2Se_3 selenide and 220 °C for deposition of Sb_2Te_3. The furnace was held at the maximal source materials evaporation temperature for 1–3 min for deposition of Bi_2Se_3 of different thicknesses, followed by natural cooling down to the room temperature. For obtaining of the ultrathin Sb_2Te_3 films, after reaching the maximal temperature in the center of the furnace hot zone, the substrate and the source material were rapidly cooled down by extracting the quartz furnace tube out of the hot zone of the furnace and simultaneous filling it with nitrogen up to the atmospheric pressure.

4.2. Characterization

Morphology, thickness, and structure of the deposited ultrathin films were inspected using the field emission SEM Hitachi S-4800, AFM Asylum Research MFP-3D, and X-ray diffraction spectroscopy (powder diffractometer X'PERT MRD with Cu K_α radiation source). XPS analyses were carried out using the ThermoFisher ESCALAB Xi^+ instrument using a monochromatic Al K_α X-ray source. The instrument binding-energy scale was calibrated to give a binding energy at 932.6 eV for Cu $2p_{3/2}$ line of freshly etched metallic copper. The charge compensation system was used on all non-conductive specimen samples. The surface of each sample was irradiated with a flood of electrons to produce a nearly neutral surface charge. The spectra were recorded by using an X-ray beam size 900x10 μm, a pass energy of 20 eV, and step size 0.1 eV. Data from all materials have been referenced using the main signal of the carbon 1s spectrum assigned to occur at 285.0 eV. The carbon 1s spectrum was collected using high energy resolution settings. Raman spectra were recorded at the room temperature using scanning laser confocal micro-Raman spectrometer Confotec NR 500 with 785 nm excitation wavelength, 0.86 mW power, and 100x objective. The accumulation time of the signal for each spectrum was 10 s. The laser beam diameter was about 600 nm. Raman spectra were registered using 1800 l/mm grating, and spectral resolution ~0.2 cm^{-1}. Throughout these measurements, the edge filter cutting at ~85 cm^{-1} was used.

Electrical and thermoelectric characterization: Resistance and Seebeck coefficients of the ultrathin films were performed using thermal transport option of Physical Property Measurement System DynaCool9T (Quantum Design) in 4-point configuration for elimination of the influence of contact resistance. For determination of the Seebeck coefficient, the temperature difference between the sides of the ultrathin films did not exceed 3% from the measurement temperature.

4.3. Fabrication and testing of a TEG prototype

For the fabrication of the TEG prototype consisting of one p-type and one n-type leg, the 5 mm × 15 mm large stripes of Bi_2Se_3 and Sb_2Te_3 ultrathin films deposited on mica were used. 5 mm × 5 mm gold contacts (thickness ~ 100 nm) were deposited over the sides of the thermoelectric stripes using the thermal deposition method (SIDRABE SAF EM sputtering vacuum system), leaving 5 mm × 5 mm of the ultrathin film between the electrodes free. Copper wires were attached to the gold electrodes using electrically conductive adhesive (EPO-TEK®H20E). Thermally generated by the TEG prototype voltage was measured using a homemade device for thermoelectrical measurements [20] under temperature gradients from 6 up to 12 K, as open circuit and under different (from 1 kΩ up to 100 kΩ) external loads.

Credit author statement

Jana Andzane: Investigation, Formal analysis, Visualization, Writing – original draft **Andrei Felsharuk:** Investigation, Methodology, Validation **Anatolijs Sarakovskis:** Investigation, Formal analysis, Visualization, Writing – original draft **Uldis Malinovskis:** Investigation, Formal analysis **E. Kauranens:** Investigation, Formal analysis, Visualization **Mikhael Bechelany:** Investigation, Formal analysis **Kiryl A. Niherysh:** Investigation, Formal analysis, Visualization **Ivan V. Komissarov:** Conceptualization, Supervision **Donats Erts:** Conceptualization, Methodology, Supervision, Writing – review & editing

Declaration of competing interest

The authors declare that they have no known competing financial interests or personal relationships that could have appeared to influence the work reported in this paper.

Acknowledgements

This work was supported by the European Regional Development Fund (ERDF) project No 1.1.1.1/16/A/257. J. A. acknowledges the ERDF project No. 1.1.1.2/1/16/037. Institute of Solid State Physics, University of Latvia, Latvia as the Center of Excellence has received funding from the European Union's Horizon 2020 Framework Programme H2020-WIDESPREAD-01-2016-2017-TeamingPhase2 under grant agreement No. 739508, project CAMART².

The raw/processed data required to reproduce these findings cannot be shared at this time as the data also form a part of an ongoing study.

Appendix A. Supplementary data

Supplementary data to this article can be found online at https://doi.org/10.1016/j.mtener.2020.100587.

References

[1] J.R. Sootsman, D.Y. Chung, M.G. Kanatzidis, New and old concepts in thermoelectric materials, Angew. Chem. Int. Ed. 48 (2009) 8616–8639, https://doi.org/10.1002/anie.200900598.

[2] Y.L. Chen, J.G. Analytis, J. Chu, Z.K. Liu, S. Mo, X.L. Qi, H.J. Zhang, D.H. Lu, X. Dai, Z. Fang, S.C. Zhang, I.R. Fisher, Z. Hussain, Z. Shen, Experimental realization of a three-dimensional topological insulator, Bi_2Te_3, science 178 (2009) 1–4, https://doi.org/10.1126/science.1173034.

[3] H. Zhang, C.X. Liu, X.L. Qi, X. Dai, Z. Fang, S.C. Zhang, Topological insulators in Bi_2Se_3, Bi_2Te_3 and Sb_2Te_3 with a single Dirac cone on the surface, Nat. Phys. 5 (2009) 438–442, https://doi.org/10.1038/nphys1270.

[4] Q. Liu, C.X. Liu, C. Xu, X.L. Qi, S.C. Zhang, Magnetic impurities on the surface of a topological insulator, Phys. Rev. Lett. 102 (2009) 1–4, https://doi.org/10.1103/PhysRevLett.102.156603.

[5] L. Hicks, M.S. Dresselhaus, Thermoelectric figure of merit of a one-dimensional semiconductor, Phys. Rev. B 47 (1993) 8–11, https://doi.org/10.1103/PhysRevB.47.16631.

[6] L. Hicks, M.S. Dresselhaus, Effect of quantum-well structures on the thermoelectric figure of merit, Phys. Rev. B 47 (1993) 12727, https://doi.org/10.1103/PhysRevB.47.12727.

[7] K. Pal, S. Anand, U.V. Waghmare, Thermoelectric properties of materials with nontrivial electronic topology, J. Mater. Chem. C 3 (2015) 12130–12139, https://doi.org/10.1039/c5tc02344k.

[8] P. Ghaemi, R.S.K. Mong, J.E. Moore, In-plane transport and enhanced thermoelectric performance in thin films of the topological insulators Bi_2Te_3 and Bi_2Se_3, Phys. Rev. Lett. 105 (2010) 1–4, https://doi.org/10.1103/PhysRevLett.105.166603.

[9] M. Tahir, A. Manchon, U. Schwingenschlögl, Enhanced thermoelectric power in ultrathin topological insulators with magnetic doping, J. Appl. Phys. 116 (2014), https://doi.org/10.1063/1.4894283.

[10] H. Osterhage, J. Gooth, B. Hamdou, P. Gwozdz, R. Zierold, K. Nielsch, Thermoelectric properties of topological insulator Bi_2Te_3, Sb_2Te_3, and Bi_2Se_3 thin film quantum wells, Appl. Phys. Lett. 105 (2014), https://doi.org/10.1063/1.4896680.

[11] M. Samanta, K. Pal, U.V. Waghmare, K. Biswas, Intrinsically low thermal conductivity and high carrier mobility in dual topological quantum material, n-type BiTe, Angew. Chem. 132 (2020) 4852–4859, https://doi.org/10.1002/ange.202000343.

[12] J. Zhang, X. Feng, Y. Xu, M. Guo, Z. Zhang, Y. Ou, Y. Feng, K. Li, H. Zhang, L. Wang, X. Chen, Z. Gan, S.C. Zhang, K. He, X. Ma, Q.K. Xue, Y. Wang, Disentangling the magnetoelectric and thermoelectric transport in topological insulator thin films, Phys. Rev. B Condens. Matter 91 (2015) 1–7, https://doi.org/10.1103/PhysRevB.91.075431.

[13] M. Guo, Z. Wang, Y. Xu, H. Huang, Y. Zang, C. Liu, W. Duan, Z. Gan, S.C. Zhang, K. He, X. Ma, Q. Xue, Y. Wang, Tuning thermoelectricity in a Bi_2Se_3 topological insulator via varied film thickness, New J. Phys. 18 (2016), https://doi.org/10.1088/1367-2630/18/1/015008.

[14] N.F. Hinsche, S. Zastrow, J. Gooth, L. Pudewill, R. Zierold, F. Rittweger, T. Rauch, J. Henk, K. Nielsch, I. Mertig, Impact of the topological surface state on the thermoelectric transport in Sb_2Te_3 thin films, ACS Nano 9 (2015) 4406–4411, https://doi.org/10.1021/acsnano.5b00896.

[15] H. Li, X. Chen, Y. Zhang, K. He, J. Cao, W. Zheng, C.-L. Song, Y. Chen, C.-Z. Chang, D. Wu, W. Dang, L.-L. Wang, K. Wang, J.-F. Jia, H. Peng, Z. Fang, Z. Liu, X. Dai, W.-Y. Shan, S.-Q. Shen, X.-L. Qi, Q. Niu, X.-C. Ma, S.-C. Zhang, Q.-K. Xue, Controlled synthesis of topological insulator nanoplate arrays on mica, J. Am. Chem. Soc. 134 (2012) 6132–6135. http://www.nature.com/doifinder/10.1038/nphys1689%0Apapers3://publication/doi/10.1021/ja3021395.

[16] L. Kou, B. Yan, F. Hu, S.C. Wu, T.O. Wehling, C. Felser, C. Chen, T. Frauenheim, Graphene-based topological insulator with an intrinsic bulk band gap above room temperature, Nano Lett. 13 (2013) 6251–6255, https://doi.org/10.1021/nl4037214.

[17] S. Singh, S. Kim, W. Jeon, K.P. Dhakal, J. Kim, S. Baik, Graphene grain size-dependent synthesis of single-crystalline Sb_2Te_3 nanoplates and the interfacial thermal transport analysis by Raman thermometry, Carbon N. Y 153 (2019) 164–172, https://doi.org/10.1016/j.carbon.2019.07.017.

[18] J. Andzane, L. Britala, E. Kauranens, A. Neciporenko, M. Baitimirova, S. Lara-Avila, S. Kubatkin, M. Bechelany, D. Erts, Effect of graphene substrate type on formation of Bi_2Se_3 nanoplates, Sci. Rep. 9 (2019) 1–8, https://doi.org/10.1038/s41598-019-41178-1.

[19] J. Andzane, G. Kunakova, S. Charpentier, V. Hrkac, L. Kienle, M. Baitimirova, T. Bauch, F. Lombardi, D. Erts, Catalyst-free vapour-solid technique for deposition of Bi_2Te_3 and Bi_2Se_3 nanowires/nanobelts with topological insulator properties, Nanoscale 7 (2015) 15935–15944, https://doi.org/10.1039/c5nr04574f.

[20] J. Andzane, K. Buks, M.N. Strakova, M. Zubkins, M. Bechelany, M. Marnauza, M. Baitimirova, D. Erts, Structure and doping determined thermoelectric properties of Bi_2Se_3 thin films deposited by vapour-solid technique, IEEE Trans. Nanotechnol. 18 (2019) 948–954, https://doi.org/10.1109/TNANO.2019.2939862.

[21] N. Sirota, Chemical Bonds in Solids, Consultants bureau, New York-London, 1972, https://doi.org/10.1007/978-1-4684-1686-2 n.d.

[22] Y. Luo, Bond dissociation energies Yu-ran Luo table 1, Bond dissociation energies in diatomic molecules, CRC Handb. Chem. Phys (2009) 65–98. https://notendur.hi.is/agust/rannsoknir/papers/2010-91-CRC-BDEs-Tables.pdf.

[23] Y. Jiang, Y.Y. Sun, M. Chen, Y. Wang, Z. Li, C. Song, K. He, L. Wang, X. Chen, Q.K. Xue, X. Ma, S.B. Zhang, Fermi-level tuning of epitaxial Sb_2Te_3 thin films on graphene by regulating intrinsic defects and substrate transfer doping, Phys. Rev. Lett. 108 (2012) 1–5, https://doi.org/10.1103/PhysRevLett.108.066809.

[24] A.J. Green, S. Dey, Y.Q. An, B. O'Brien, S. O'Mullane, B. Thiel, A.C. Diebold, Surface oxidation of the topological insulator Bi_2Se_3, J. Vac. Sci. Technol. A Vacuum, Surfaces, Film 34 (2016), 061403, https://doi.org/10.1116/1.4964637.

[25] J. Schaumann, M. Loor, D. Ünal, A. Mudring, S. Heimann, U. Hagemann, S. Schulz, F. Maculewicz, G. Schierning, Improving the zT value of thermoelectrics by nanostructuring: tuning the nanoparticle morphology of Sb_2Te_3 by using ionic liquids, Dalton Trans. 46 (2017) 656–668, https://doi.org/10.1039/c6dt04323b.

[26] G. Hao, X. Qi, Y. Fan, L. Xue, X. Peng, X. Wei, J. Zhong, Spiral growth of topological insulator Sb_2Te_3 nanoplates, Appl. Phys. Lett. 102 (2013) 1–5, https://doi.org/10.1063/1.4773587.

[27] J. Zhang, Z. Peng, A. Soni, Y. Zhao, Y. Xiong, B. Peng, J. Wang, M.S. Dresselhaus, Q. Xiong, Raman spectroscopy of few-quintuple layer topological insulator Bi_2Se_3 nanoplatelets, Nano Lett. 11 (2011) 2407–2414, https://doi.org/10.1021/nl200773n.

[28] M.C. Morris, H.F. McMurdie, E.H. Evans, B. Paretzkin, H.S. Parker, N.C. Panagiotopoulos, Nat. Bur. Stand, (U.S.), Monogr, 1981.

[29] M. Baitimirova, J. Andzane, G. Petersons, R. Meija, R. Poplausks, M. Romanova, D. Erts, Vapor–solid synthesis and enhanced thermoelectric properties of non-planar bismuth selenide nanoplates on graphene substrate, J. Mater. Sci. 51 (2016) 8224–8232, https://doi.org/10.1007/s10853-016-0097-z.

[30] G. Kunakova, L. Galletti, S. Charpentier, J. Andzane, D. Erts, F. Léonard, C.D. Spataru, T. Bauch, F. Lombardi, Bulk-free topological insulator Bi_2Se_3 nanoribbons with magnetotransport signatures of Dirac surface states, Nanoscale 10 (2018) 19595–19602, https://doi.org/10.1039/c8nr05500a.

[31] B. Wiendlocha, Resonant levels, vacancies, and doping in Bi_2Te_3, Bi_2Te_2Se, and Bi_2Se_3 tetradymites, J. Electron. Mater. 45 (2016) 3515–3531, https://doi.org/10.1007/s11664-016-4502-9.

[32] Y. Zhang, K. He, C.Z. Chang, C.L. Song, L.L. Wang, X. Chen, J.F. Jia, Z. Fang, X. Dai, W.Y. Shan, S.Q. Shen, Q. Niu, X.L. Qi, S.C. Zhang, X.C. Ma, Q.K. Xue, Crossover of the three-dimensional topological insulator Bi_2Se_3 to the two-dimensional limit, Nat. Phys. 6 (2010) 584–588, https://doi.org/10.1038/nphys1689.

[33] L. Zhang, M. Dolev, Q.I. Yang, R.H. Hammond, B. Zhou, A. Palevski, Y. Chen, A. Kapitulnik, Weak localization effects as evidence for bulk quantization in Bi_2Se_3 thin films, Phys. Rev. B Condens. Matter 88 (2013) 2–5, https://doi.org/10.1103/PhysRevB.88.121103.

[34] M.I. Alomar, D. Sánchez, Thermoelectric effects in graphene with local spin-orbit interaction, Phys. Rev. B Condens. Matter 89 (2014), https://doi.org/10.1103/PhysRevB.89.115422.

[35] N. Peranio, M. Winkler, Z. Aabdin, J. König, H. Böttner, O. Eibl, Room temperature MBE deposition of Bi_2Te_3 and Sb_2Te_3 thin films with low charge carrier densities, Phys. Status Solidi Appl. Mater. Sci 209 (2012) 289–293, https://doi.org/10.1002/pssa.201127440.

[36] B. Huang, C. Lawrence, A. Gross, G.S. Hwang, N. Ghafouri, S.W. Lee, H. Kim, C.P. Li, C. Uher, K. Najafi, M. Kaviany, Low-temperature characterization and micropatterning of coevaporated Bi_2Te_3 and Sb_2Te_3 films, J. Appl. Phys. 104 (2008) 1–9, https://doi.org/10.1063/1.3033381.

[37] J. Navrátil, J. Horák, T. Plecháček, S. Kamba, P. Lošt'ák, J.S. Dyck, W. Chen, C. Uher, Conduction band splitting and transport properties of Bi_2Se_3, J. Solid State Chem. 177 (2004) 1704–1712, https://doi.org/10.1016/j.jssc.2003.12.031.

[38] J.P. Carmo, J. Antunes, M.F. Silva, J.F. Ribeiro, L.M. Goncalves, J.H. Correia, Characterization of thermoelectric generators by measuring the load-dependence behavior, Meas. J. Int. Meas. Confed 44 (2011) 2194–2199, https://doi.org/10.1016/j.measurement.2011.07.015.

[39] G. Bulman, P. Barletta, J. Lewis, N. Baldasaro, M. Manno, A. Bar-Cohen, B. Yang, Superlattice-based thin-film thermoelectric modules with high cooling fluxes, Nat. Commun. 7 (2016) 1–7, https://doi.org/10.1038/ncomms10302.

[40] Y. Min, G. Park, B. Kim, A. Giri, J. Zeng, J.W. Roh, S. Il Kim, K.H. Lee, U. Jeong, Synthesis of multishell nanoplates by consecutive epitaxial growth of Bi_2Se_3 and Bi_2Te_3 nanoplates and enhanced thermoelectric properties, ACS Nano 9 (2015) 6843–6853, https://doi.org/10.1021/nn507250r.

Paper II

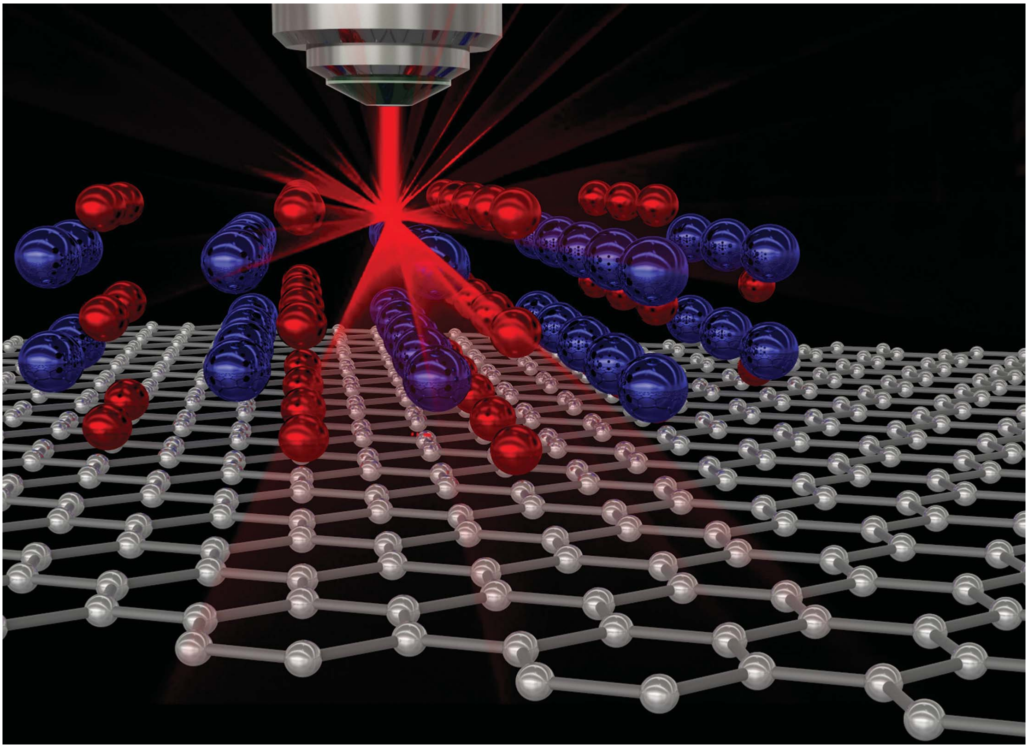

Showcasing research from Professor Donats Erts's laboratory, Institute of Chemical Physics, University of Latvia, Riga, Latvia and Dr Ivan Komissarov's group, Belarusian State University of Informatics and Radioelectronics, Minsk, Belarus.

Correlation analysis of vibration modes in physical vapour deposited Bi_2Se_3 thin films probed by Raman mapping technique

Raman spectroscopy mapping technique is used for analysis of mechanical strain in Bi_2Se_3 thin films of various thicknesses synthesized by physical vapour deposition on amorphous quartz and single-layer graphene substrates. The evaluation of strain effects is based on correlation analysis of in-plane (E_g^2) and out-of-plane (A_{1g}^2) Raman modes positions. The algorithm of phonon deformation potential (PDP) calculation based on proposed strain analysis for the 3 nm thick Bi_2Se_3 film deposited on graphene substrate, where the strain considered to be coherent across the thickness is demonstrated.

As featured in:

See I. V. Komissarov, D. Erts *et al.*, *Nanoscale Adv.*, 2021, **3**, 6395.

rsc.li/nanoscale-advances

Registered charity number: 207890

Nanoscale
Advances

PAPER

View Article Online
View Journal | View Issue

Check for updates

Cite this: *Nanoscale Adv.*, 2021, 3, 6395

Correlation analysis of vibration modes in physical vapour deposited Bi_2Se_3 thin films probed by the Raman mapping technique†

K. A. Niherysh,[ab] J. Andzane,[a] M. M. Mikhalik,[b] S. M. Zavadsky,[b] P. L. Dobrokhotov,[c] F. Lombardi,[d] S. L. Prischepa,[bc] I. V. Komissarov *[bc] and D. Erts *[ae]

Received 26th May 2021
Accepted 7th September 2021

DOI: 10.1039/d1na00390a

rsc.li/nanoscale-advances

In this work, the Raman spectroscopy mapping technique is used for the analysis of mechanical strain in Bi_2Se_3 thin films of various (3–400 nm) thicknesses synthesized by physical vapour deposition on amorphous quartz and single-layer graphene substrates. The evaluation of strain effects is based on the correlation analysis of in-plane (E_g^2) and out-of-plane (A_{1g}^2) Raman mode positions. For Bi_2Se_3 films deposited on quartz, experimental datapoints are scattered along the line with a slope $(\Delta\omega_{A_{1g}^2}/\Delta\omega_{E_g^2})$ of ~0.85, related to the distribution of hydrostatic strain. In contrast to quartz/Bi_2Se_3 samples, for graphene/Bi_2Se_3 heterostructures with the same thicknesses, an additional negative slope of ~−0.85, which can be associated with the distribution of the in-plane (*a*–*b*) biaxial tensile strain due to the film–substrate lattice mismatch, is observed. The algorithm of phonon deformation potential (PDP) calculation based on the proposed strain analysis for the 3 nm thick Bi_2Se_3 film deposited on the graphene substrate, where the strain is considered to be coherent across the thickness, is demonstrated. The PDPs for biaxial in-plane strain of the Bi_2Se_3 3 nm film in in-plane and out-of-plane modes are equal to −7.64 cm^{-1}/% and −6.97 cm^{-1}/%, respectively.

Introduction

Linear energy–momentum dispersion in graphene and topological insulators (TIs) has made these materials as well as van der Waals heterostructures based on them the focus of scientific interest for the last decade. Various devices for electronic, spintronic and even domestic waste heat conversion applications can be realised based on graphene/TI heterostructures.[1–6] Although the physical properties of these 2D materials are rather well understood, their wide practical applications are still challenging due to the extreme sensitivity of these materials to the substrates they are supported by. Strain is one of the most prominent phenomena occurring at the interface of the contacting materials which can change their band structure.[7–10] Therefore, strain can be considered not only as a problem that must be taken into account when designing a device, but also as an opportunity to tune the properties of the material. In the case of topological insulators, theoretical studies indicate that the bulk band gap and the spin-polarized Dirac surface states can be tailored by strain.[11,12] It was experimentally demonstrated that compressive strain in the out-of-plane direction reduces the bandgap of the surface state of Bi_2Se_3 films on epi-graphene on SiC.[5] Previously, it was also theoretically indicated that variations in the concentration of charge carriers caused by doping and the presence of mechanical strain in TIs can affect the thermoelectric power of these materials.[13]

Strain, defined as the lattice parameter deviation of a material from its bulk value quantitatively expressed as $\varepsilon = (a - a_0)/a_0$, where a is the lattice parameter of the strained material and a_0 is the value of the bulk, is most commonly caused by the lattice mismatch between the deposited material and the substrate.[14,15] However, as the growth of materials is usually performed at elevated temperatures, the difference in the thermal expansion coefficients (TECs) of the deposited material and the substrate is also a source of strain.[16] Separation of the impact and control of strain sources are required for precise engineering of the physical properties of TI materials.

Besides the measurement techniques commonly applied for the *ex situ* and *in situ* structural characterization of 3D materials such as X-ray diffraction (XRD) or reflection high-energy electron diffraction (RHEED), micro-Raman spectroscopy is considered as a powerful and non-destructive tool for the determination of mechanical strain in materials with

---

[a] *Institute of Chemical Physics, University of Latvia, Riga, Latvia. E-mail: donats.erts@lu.lv*

[b] *Belarusian State University of Informatics and Radioelectronics, Minsk, Belarus. E-mail: komissarov@bsuir.by*

[c] *National Research Nuclear University MEPhI (Moscow Engineering Physics Institute), Moscow, Russia*

[d] *Quantum Device Physics Laboratory, Department of Microtechnology and Nanoscience, Chalmers University of Technology, Gothenburg, Sweden*

[e] *Faculty of Chemistry, University of Latvia, Riga, Latvia*

† Electronic supplementary information (ESI) available. See DOI: 10.1039/d1na00390a

micrometric spatial resolution.[17] The micro-Raman spectroscopy technique is especially useful for the structural characterization of graphene and ultrathin films deposited by PVD as it is not subject to the technical limitations typical of the XRD and RHEED methods.[18,19] For example, in the case of graphene the correlation analysis of G and 2D Raman mode positions can be used not only to separate the impact of strain and charge carrier density on the phonon spectrum, but also to calculate the absolute values of these parameters.[20–23] This fact makes the correlation analysis of Raman modes a unique tool for studying the properties of materials.

In Raman spectroscopy, the phonon deformation potential (PDP) is the quantity connecting strain and Raman shift. It strongly depends on the thickness of the material, and sophisticated experiments have been performed to extract this dependency for bismuth chalcogenides.[24,25] In these studies strain was introduced *via* either artificial[24] or natural bending[25] in the transferred film and nanoribbons, respectively; the Raman shift coefficients were evaluated for thickness in the range of 79–260 nm, limiting their applicability to the case of epitaxial ultrathin films. The theoretically estimated value of PDP for a 2 nm thin chalcogenide film is expected to be ~5 cm^{-1}/%.[10]

In this work, a systematic study of mechanical strain in single-layer graphene/Bi_2Se_3 (SLG/Bi_2Se_3) heterostructures with different Bi_2Se_3 layer thicknesses, and in Bi_2Se_3 films of the same thicknesses deposited on quartz substrates (Q/Bi_2Se_3) is performed. The methodological approach based on the correlation analysis of the experimental Raman data was applied to evaluate the nature of strain in the deposited films. To the best of our knowledge, such a kind of correlation analysis for topological insulator ultrathin films has been performed for the first time. In addition, an original method is proposed for estimating the phonon deformation potential in Bi_2Se_3 ultrathin films based on the correlation analysis approach presented in this work.

Methods

Bi_2Se_3 films of various thicknesses (3–400 nm) were synthesized by the physical vapour deposition technique (PVD)[4,6,26,27] using a single-zone quartz tube furnace (GCL-1100X, MTI Corp.). SLG was synthesized using a First Nano Easy tube 101 CVD reactor and transferred from copper foil (GoodFellow) onto quartz (fused silica) slides (Agar scientific) by the methyl methacrylate (PMMA) polymer-assisted method.[28] Based on the results of the structural analysis of graphene performed by the reflection high energy electron diffraction (RHEED) technique and the results of the structural analysis of copper foil performed by X-ray diffraction (XRD) we conclude that the graphene synthesized in our work can be described as a set of differently oriented domains with limited azimuthal angle distribution (see ESI S1†). These graphene as well as quartz samples were used as substrates for Bi_2Se_3 film deposition.

The structure, morphology and stoichiometry of the deposited Bi_2Se_3 films were inspected using a field emission scanning electron microscope (FESEM), Hitachi S-4800, equipped with a Bruker XFlash Detector 5010 for energy dispersive X-ray spectrometry (EDS).

Thicknesses of SLG/Bi_2Se_3 heterostructures and Q/Bi_2Se_3 samples were measured using an atomic force microscope (AFM), Asylum Research MFP-3D. To measure the thickness of the films an artificial scratch was introduced. The mechanical hardness of the tool for creating a scratch exceeds the hardness of Bi_2Se_3, but is softer than quartz, which excludes deformation of the substrate.

XRD patterns of SLG/Bi_2Se_3 were obtained using CuKα radiation with an Ultima IV (Rigaku) diffractometer (λ = 0.15406 nm). XRD patterns of the copper foil were obtained using CuKα radiation with a DRON-3 diffractometer (λ = 0.15406 nm).

RHEED patterns of graphene were recorded in a custom-made (Chalmers University of Technology) pulsed laser deposition system, the base pressure is 2×10^{-7} mbar and the electron energy is 30 keV.

Raman spectra of SLG (see ESI S2†), SLG/Bi_2Se_3 and Q/Bi_2Se_3 structures were obtained at room temperature using a scanning laser confocal micro-Raman spectrometer, Confotec NR 500, by scanning sample areas of 20×20 μm^2 with 785 nm (for Bi_2Se_3 films) and 473 nm (for graphene) excitation wavelengths and 100× objective. The accumulation time of the signal for each spectrum was 10 seconds. The laser beam diameter was about 600 nm. Raman spectra were recorded using 1800 l mm^{-1} and 1200 l mm^{-1} gratings, and spectral resolution of ~0.2 cm^{-1} and ~1 cm^{-1} for Bi_2Se_3 thin films and graphene, respectively. Throughout these measurements the edge filter cutting at ~85 cm^{-1} was used.

Results

Bi_2Se_3 thin films with thicknesses 3–400 nm deposited on SLG and on quartz substrates were found to have uniform distribution of Bi and Se chemical elements over the area of ~100 × 100 mm^2 at a chemical composition of 40 at% for Bi and 60 at% for Se, which corresponds to a stoichiometry of Bi_2Se_3. Fig. 1a illustrates an example of the EDS spectrum and SEM image of the 11 nm thick Bi_2Se_3 film deposited on SLG. The XRD spectrum analysis of the SLG/Bi_2Se_3 structures revealed the presence of diffraction peaks related only to the (0 0 3*n*) family group, thus confirming the epitaxial growth of the Bi_2Se_3 thin film with the crystallographic *c*-axis oriented perpendicularly to the substrate surface.[4,29] The XRD spectrum of the SLG/Bi_2Se_3 heterostructure with Bi_2Se_3 thickness of 11 nm and the pole figure taken from the diffraction maximum (0 0 6) are shown in Fig. 1b. The pole figure was recorded in a sweep from 0 to 70 degrees. The presence of only one (central) broad maximum on the pole figure means that the crystals of Bi_2Se_3 are coherently oriented in the *c*-direction, revealing good quality of epitaxial growth. All Bi_2Se_3 films were continuous with the relatively smooth surface. The representative AFM images and height profiles of Bi_2Se_3 (11 nm) film deposited on quartz and graphene are shown in Fig. 1c and d, respectively. AFM images of all samples as well as values of root mean square (RMS) roughness are presented in ESI S3.†

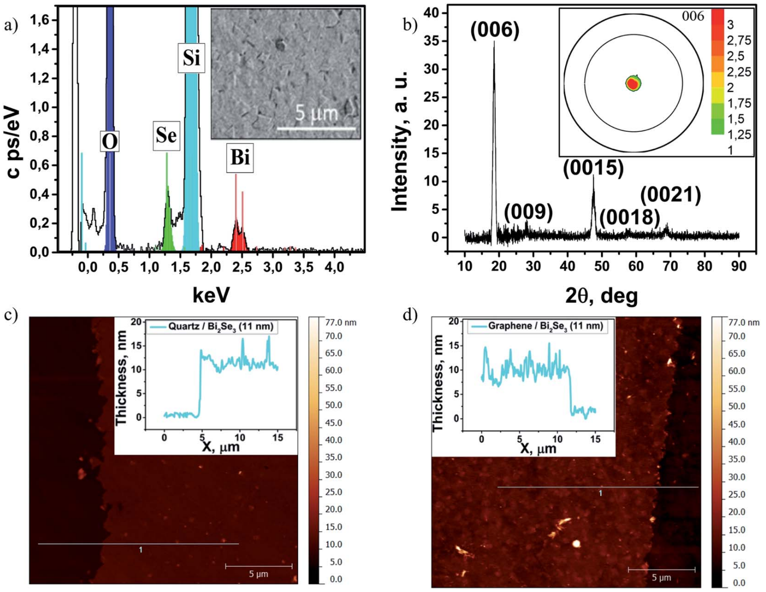

Fig. 1 (a) Energy-dispersive spectroscopy (EDS) spectrum of Bi_2Se_3 film (11 nm); inset – scanning electron microscopy (SEM) image of Bi_2Se_3 (11 nm) film deposited on SLG; (b) 2θ X-ray diffraction pattern of Bi_2Se_3 thin film (11 nm) deposited on SLG; inset – pole figure along the (0 0 6) plane; (c) atomic force microscopy (AFM) image of Bi_2Se_3 (11 nm) film on quartz and (d) on graphene with artificial scratches introduced to determine the thickness; insets – the height profiles of these films.

A typical Raman spectrum of the SLG/Bi_2Se_3 (3 nm) in the range of 85 to 350 cm^{-1} for Bi_2Se_3 and of 650 to 3000 cm^{-1} for SLG is presented in Fig. 2a. It should be noted that the D band intensity of graphene, which is responsible for defects, is at the noise level before deposition of Bi_2Se_3 films (ESI S2†). And there is an appearance of insignificant peak D (still close to the noise level) after the deposition of Bi_2Se_3 films (ESI S4†). Two characteristic peaks at ~131 cm^{-1} and ~174 cm^{-1} respectively correspond to the in-plane (E_g^2) and out-of-plane (A_{1g}^2) vibrational modes of the rhombohedral crystal structure of Bi_2Se_3 (Fig. 2a, inset).[30] Raman E_g^2 and A_{1g}^2 band mappings performed for SLG/Bi_2Se_3 and Q/Bi_2Se_3 samples with Bi_2Se_3 layer thicknesses of 3–400 nm showed Bi_2Se_3 peaks (without distortion and additional peaks) at each mapping point, which are well fitted by Lorentzian functions. This fact is consistent with the XRD data and confirms the uniformity, continuity and high quality of homogeneous ultrathin Bi_2Se_3 films grown on graphene and quartz substrates. The representative Raman mappings for the SLG/Bi_2Se_3 heterostructure with a 3 nm thin Bi_2Se_3 layer are shown in Fig. 2b and c.

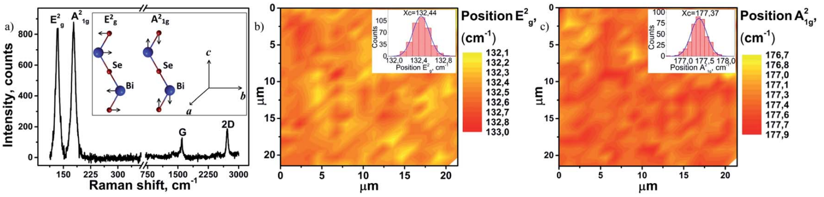

Fig. 2 (a) Raman spectrum of graphene and 3 nm Bi_2Se_3 film synthesized on it; inset – the displacement patterns of phonon modes in the Bi_2Se_3 structure; (b and c) Raman mapping images of the 3 nm Bi_2Se_3 film with the corresponding histograms (insets): (b) E_g^2 band position; (c) A_{1g}^2 band position; the colour scales represent the amplitude of measured values.

Discussion

To perform the correlation analysis of Bi_2Se_3 films deposited on quartz (Fig. 3a) and graphene (Fig. 3b) the experimental Raman datapoints of Bi_2Se_3 were plotted in the coordinates of a higher frequency mode *vs.* lower frequency mode (A^2_{1g} *vs.* E^2_g).

Fig. 3a indicates the pronounced scattering of data points (A^2_{1g} on E^2_g positions) of the Bi_2Se_3 ultrathin films deposited on quartz along the straight lines with the slope of ∼0.85 (this value was obtained from a linear fitting of datapoints for Bi_2Se_3 films deposited on quartz, Fig. 3a, inset). The deviation of experimental data from their linear fit is less than 0.5 cm^{-1}, which is comparable with the spectral resolution of the Raman measurements and reveals strong reliability of the claimed dependency. The Raman frequency vibrations in topological insulators such as Bi_2Se_3 are governed by various thickness-dependent factors, including spin orbit coupling,[31] charge carrier concentration,[32] and strain.[24] The linear scattering of A^2_{1g} on E^2_g experimental points is most probably related to the distribution of strain value in the films. Indeed, for the experimental values of Raman hydrostatic pressure coefficients $\left(\frac{d\omega_{A^2_{1g}}}{dP}\right)_T = 2.68\ cm^{-1}\ GPa^{-1}$ and $\left(\frac{d\omega_{E^2_g}}{dP}\right)_T = 3.13\ cm^{-1}\ GPa^{-1}$,[33,34] their ratio is $\left(\frac{d\omega_{A^2_{1g}}}{dP}\right)_T \Big/ \left(\frac{d\omega_{E^2_g}}{dP}\right)_T = 0.856$, which is in good agreement with the experimental data presented above. The scatter of the experimental datapoints along solid lines with a slope of ∼0.85 (Fig. 3a) indicates that Bi_2Se_3 films deposited on quartz experience strain *distributed* hydrostatically throughout the film (*i.e.* crystal lattices are strained or expanded both in-plane and out-of-plane simultaneously as illustrated in Fig. 3d). Presumably, this distribution of the strain may be related to the growth process specifics such as different TECs of the quartz substrate ($\sim 0.5 \times 10^{-6}\ K^{-1}$ (ref. 35)) and PVD-grown Bi_2Se_3 ($\sim 11–19 \times 10^{-6}\ K^{-1}$ (ref. 36)) and Volmer–Weber thin film growth mode, where growth occurs not layer-by-layer, but by the formation of separate islands, which subsequently coalesce.[6,26,29] Indeed, the Volmer–Weber growth mechanism of Bi_2Se_3 films leads to the appearance of strain which is mainly concentrated in the grooves between the grains. In the case of strong interaction of the deposited material with the substrate, this type of strain is considered to be hydrostatic.[37]

In contrast to the scatter of the A^2_{1g} *vs.* E^2_g datapoints of Q/Bi_2Se_3 samples, the scatter of the datapoints for Bi_2Se_3 thin films deposited on SLG does not show a pronounced linear shape (Fig. 3b), but rather rhomb-shaped spots with additional scatter of experimental datapoints along the dashed line with a negative slope (∼−0.85) are observed. This could be explained

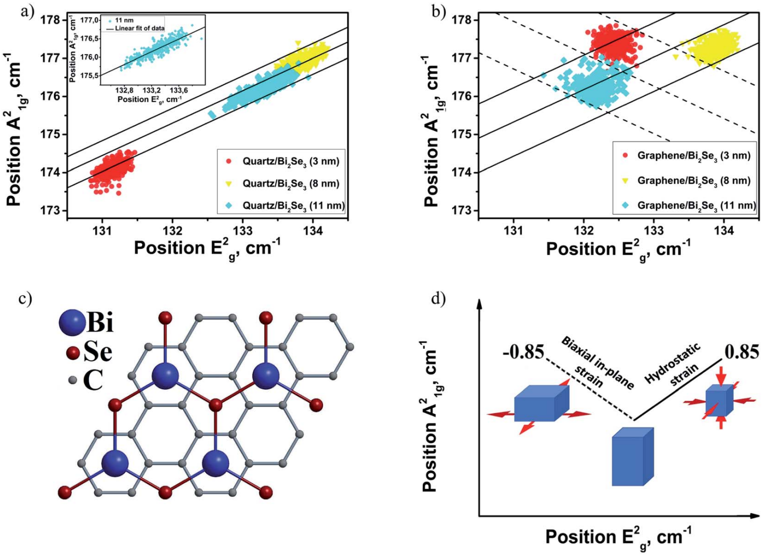

Fig. 3 The positions of the A^2_{1g} band as a function of E^2_g band positions for Bi_2Se_3 ultrathin films deposited on quartz (a) and graphene (b); the inset in Fig. 3a is a linear fit of A^2_{1g} *vs.* E^2_g dependency for 11 nm Bi_2Se_3; (c) top view of the SLG/Bi_2Se_3 interlayer stacking pattern. (d) Bi_2Se_3 strain distribution scheme based on the A^2_{1g} band as a function of E^2_g Raman band positions scattered along different slopes. The solid line with the slope of 0.85 corresponds to the hydrostatic strain of Bi_2Se_3. The dashed line with the slope of −0.85 corresponds to the biaxial in-plane tensile strain of Bi_2Se_3 (see the text for more details).

by the red-shift of the in-plane E_g^2 Raman mode positions and simultaneous blue-shift of the out-of-plane A_{1g}^2 mode positions, which are related to the in-plane tensile strain, originating from the lattice mismatch between the SLG and Bi_2Se_3. Assuming the same absolute values of Raman pressure coefficients for both compressive and tensile strains, in the case of biaxial strain a scatter of the experimental datapoints along the line with the slope ~ -0.85 should be obtained, in contrast with the hydrostatic strain (Fig. 3a). As the hexagonal lattice constant of the SLG is smaller than the Bi_2Se_3 lattice constant (Fig. 3c), the Bi_2Se_3 epitaxial film should experience in-plane tensile strain and compressive strain parallel to the *c*-axis.[1] Indeed, due to the hexagonal honeycomb lattice of graphene (the lattice constant $a_{Gr} = 2.46$ Å), the stacking pattern between single layer graphene and Bi_2Se_3 with surface Se atoms in the hollow centres of carbon hexahedral rings (Fig. 3c) has the lowest binding energy and thus is a stable structure.[38] The relationship between Bi_2Se_3 and graphene lattice parameters is $a_{Bi_2Se_3} = a_{Gr}\sqrt{3}$. For this stacking order the lattice mismatch for Bi_2Se_3 (tensile strain) is 2.9%. The experimental value of lattice parameter *c* for 11 nm Bi_2Se_3 film deposited on graphene, extracted from the most intensive XRD peaks 006 ($2\theta_{006} = 18.584°$) and 0015 ($2\theta_{0015} = 47.615°$) (Fig. 1b), is equal to 28.624 Å, which is less than the lattice constant for the relaxed bulk value (28.636 Å).[39] However, it is worth mentioning here that the obtained experimental value may differ from the real crystal lattice parameter. The accurate evaluation of lattice parameters in our case cannot be performed because amorphous quartz used as the supporting substrate for the graphene/TI heterostructure does not possess any XRD reflections which can be used for the precise positioning of the sample in the XRD goniometer.

Thus, the approach to the separation of the origin of strain in PVD-deposited ultrathin Bi_2Se_3 films on quartz and SLG substrates based on the correlation analysis of Raman mode behaviour is as follows (Fig. 3d): scatter of the experimental A_{1g}^2 *vs.* E_g^2 datapoints along the solid line with a positive slope (~ 0.85) is associated with simultaneous compression or extension both in-plane and along the *c*-axis (hydrostatic strain); in turn, scatter of these datapoints along the dashed line with a negative slope (~ -0.85) is associated with the biaxial in-plane strain caused by the lattice mismatch of the heterostructure layers.

It is important to note here that the scattering of experimental datapoints for thicker Bi_2Se_3 films synthesized on quartz and graphene substrates retained the claimed behaviour and is discussed in ESI S5.†

As was pointed out above, the Raman technique has the advantage of providing non-contact probing of physical properties and provides access for simultaneous measurements of materials in heterostructures. Therefore, the developed theory of Raman scattering in SLG allows calculation of the lattice parameter of graphene in the studied heterostructures based on the correlation analysis of 2D and G band positions.[23] In turn, the Bi_2Se_3 in-plane lattice parameter can be calculated according to the atomic arrangement presented in Fig. 3c. Thus, the in-plane strain in Bi_2Se_3 film deposited on graphene can be evaluated. It is worth mentioning that this approach is applicable only to thin coherently strained films. Indeed, the crystal size calculation for 11 nm thick film from the 006 XRD reflection (ESI S6†) is in good agreement with AFM thickness measurements. Thus, the coherence condition is satisfied.

Fig. 4 shows the dependency of the 2D band on G band positions for graphene with Bi_2Se_3 ultrathin films of different thicknesses deposited on it.

It was previously shown that the position of the G band of graphene does not depend on the wavelength of the excitation laser,[41] whereas the 2D band has dispersion $dPos(2D)/d\omega_L \sim 100$ cm^{-1} eV^{-1}.[42] Considering the nondispersive behaviour of the G band and using the dispersion together with the known position of the 2D band for the ideal unstrained and undoped graphene excited with 514 nm wavelength, ~ 2677 cm^{-1},[23,40] Raman shifts of G and 2D bands (the purple star mark ($X = 1577.5$ cm^{-1}, $Y = 2698$ cm^{-1})) for the ideal graphene excited with 473 nm wavelength were obtained.

The Raman band shift related to the biaxial strain in the ideal graphene with a fixed charge carrier concentration is represented by the bold solid line (the slope of ~ 2.2). In turn, the change of charge-carrier concentration at a fixed biaxial strain in ideal graphene is represented by a bold dashed line (the slope of ~ 0.7).[23]

It is important to note that the strain and charge carrier concentration in CVD-grown graphene transferred on the surface of a solid substrate depend on transfer conditions and

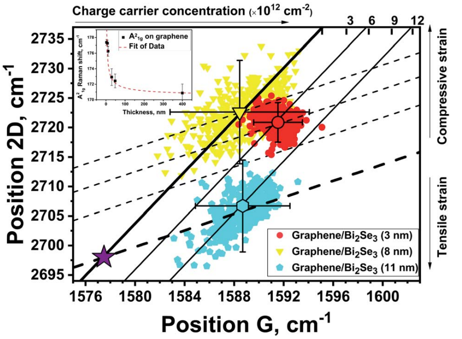

Fig. 4 Position of the 2D band as a function of the G band position for graphene/Bi_2Se_3 heterostructures with different thicknesses of Bi_2Se_3 (listed in the inbox) deposited on graphene. The purple star mark is the position of unstrained and undoped graphene.[23,40] The central large symbols of the same color as the marks of the samples represent the averaged value for 400 spectra recorded for each sample and its standard deviation in ΔG and Δ2D, respectively. The bold solid line (with a slope of ~ 2.2) passing through the purple star mark is responsible for the biaxial strain in the ideal graphene. Solid lines (with a slope of ~ 2.2) parallel to the bold solid line are responsible for the biaxial strain with fixed charge carrier concentrations. The bold dashed line (with a slope of ~ 0.7) passing through the purple star mark is responsible for the charge carrier concentration in the ideal graphene. Dashed lines (with a slope of ~ 0.7) parallel to the bold dashed line are responsible for the charge carrier concentration with fixed biaxial strain.

may vary from experiment to experiment, and even within the same sample.[23,40] In accordance with the experimental Raman data (Fig. 4), SLG from the sample with 8 nm Bi_2Se_3 deposited on it is the most strained (yellow datapoints); then for the 3 nm thick film (red datapoints) graphene is slightly relaxed, whereas for the 11 nm thick film (cyan datapoints) graphene can be considered as completely unstrained. In compliance with the atomic arrangement presented in Fig. 3c, the in-plane strain in Bi_2Se_3 films behaves in the opposite manner (11 nm thick film on graphene is the most tensile strained, then 3 nm and, finally, 8 nm thick film).

The larger tensile in-plane strain should lead to the larger red-shift of the E_g^2 Raman mode (in-plane vibrations). Indeed, that kind of a pattern is observed in the experimental data (Fig. 3b). In line with this logic, the 11 nm thick film on graphene should have the most blue-shifted A_{1g}^2 Raman mode (out-of-plane vibrations), but the experimental observation contradicts this prediction. This contradiction can be resolved by taking into account the thickness dependency of the A_{1g}^2 position, see the inset of Fig. 4. Indeed, such dependency is usually observed for Bi_2Se_3 films and explained by mechanisms other than strain such as charge transfer, spin–orbit coupling, confinement effect, and intersurface coupling.[31,32] It means that these mechanisms have a much stronger influence upon the position of the A_{1g}^2 mode than the strain itself.

Even though the absolute value of the Raman shift cannot be directly linked to the strain in the films, the deviation of the strain can be calculated from the approach discussed above. In the framework of this approach, the distribution of the experimental data points along the negative slope in Fig. 3b should be associated with the distribution of graphene lattice parameter.

Using the proposed strain separation method (Fig. 3d), the PDP for the thinnest Bi_2Se_3 (3 nm) film deposited on graphene, where the film is fully strained by the substrate and strain is considered to be coherent across the thickness,[1,31,43,44] can be calculated. This calculation is based on a simple idea. The in-plane tensile strain in 3 nm thin Bi_2Se_3 associated with the negative (~ -0.85) slope originates only from the lattice mismatch between the graphene and Bi_2Se_3. Therefore, the change in the Bi_2Se_3 lattice parameter is directly related to the change in the graphene lattice parameter (see Fig. 3c). Thus, the variation of the graphene lattice parameter can be easily transformed into variations of the Bi_2Se_3 plane lattice parameters. In combination with the variations of the A_{1g}^2 and E_g^2 shifts, the PDP values of these modes for the Bi_2Se_3 in-plane strain can be obtained. The detailed step-by-step description of the PDP calculation is presented below.

For the strain range evaluation of the graphene layer in the SLG/Bi_2Se_3 heterostructure with the 3 nm thick Bi_2Se_3 layer such a $\Delta\omega_{2D}/\Delta\omega_G$ Raman data difference is plotted in Fig. 5a.

Two dashed lines with a slope of ~0.7 were drawn through the upper and lower points of the 2D *vs.* G plot to the intersection with the bold solid line (with a slope of ~2.2) as shown in Fig. 5a. The strain range variation of the graphene layer can be calculated by determination of the difference $\Delta\omega_G$ between the intersection points of the lines with a slope of ~0.7 with the bold solid line, and the G band position for the ideal SLG (Fig. 5a, purple star mark), followed by dividing the calculated $\Delta\omega_G$ values by the averaged sensitivity factor for the G band (-69.1 ± 3.4 cm^{-1}/%[23]). Following the strain calculation procedure for the graphene layer in the SLG/Bi_2Se_3 heterostructures described above, the graphene strain range from -0.165% to -0.078% for the SLG/Bi_2Se_3 heterostructure with the 3 nm thin Bi_2Se_3 layer was determined. The lattice parameter of the strained graphene $a_{Gr}{}^{3\ nm}$ was found to vary from 2.456 to 2.458 Å. Using these values, the lattice parameter for the Bi_2Se_3 layer in the SLG/Bi_2Se_3 heterostructure $a_{Bi_2Se_3}{}^{3\ nm} = a_{Gr}{}^{3\ nm}\sqrt{3}$ was found to vary from 4.254 to 4.258 Å, which is equal to 2.80 to 2.89% tensile strain in the 3 nm thick Bi_2Se_3 film ($a_{Bi_2Se_3}^{bulk} = 4.138$ Å). The A_{1g}^2 *vs.* E_g^2 plot for the 3 nm thick Bi_2Se_3 film deposited on SLG is shown in Fig. 5b. The dashed line with a slope of ~ -0.85 indicates the in-plane tensile strain introduced by Bi_2Se_3 and graphene lattice mismatch, and is associated with the blue and red shift of A_{1g}^2 and E_g^2 modes respectively, which is consistent with other reports.[1] Raman shifts corresponding to ΔE_g^2 and

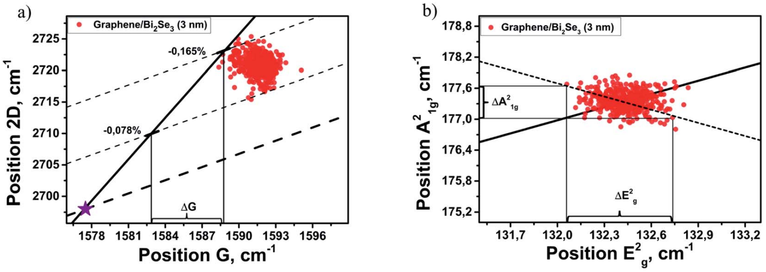

Fig. 5 (a) 2D *vs.* G dependency of the graphene layer in the SLG/Bi_2Se_3 (3 nm) heterostructure. The purple star mark is the position of unstrained and undoped graphene.[23,40] The bold solid line (slope ~2.2) is related to the biaxial strain in the ideal graphene. Dashed lines (slope ~0.7) are the change of charge-carrier concentration while biaxial strain is fixed; (b) A_{1g}^2 *vs.* E_g^2 dependency for 3 nm Bi_2Se_3 film deposited on graphene. The solid line (slope ~0.85) is related to the hydrostatic strain distribution. The dashed line (slope ~ -0.85) is related to the strain caused by graphene (lattice mismatch).

ΔA_{1g}^2 estimated from Fig. 5b are equal to 0.68 cm^{-1} and 0.62 cm^{-1}, respectively. This results in PDP values for biaxial in-plane strain for 3 nm thin Bi_2Se_3 film deposited on graphene of -7.64 cm^{-1}/% for the in-plane mode and -6.97 cm^{-1}/% for the out-of-plane mode.

Finally, let's compare our findings for PDP in Bi_2Se_3 with the literature results. In ref. 24 the A_{1g}^2, E_g^2, and A_{1g}^1 modes are red-shifted with increase of applied strain and the Raman shift strain coefficient of the A_{1g}^2 mode is -1.68 cm^{-1}/%, for the 79 nm thick film. A similar value for a 100 nm thick nanoribbon value has been reported in ref. 25 where the authors found the PDP (or the Raman shift strain coefficient) of A_{1g}^2 to be -1.78 cm^{-1}/%. As mentioned by the authors of ref. 24 and 25 these values are already much larger than those reported for bulk materials,[33] which implies strong inverse dependence of PDP on thickness.[25] Therefore, our results for the 3 nm thick film correspond to this tendency. Moreover, we evaluated the Raman shift strain coefficient of A_{1g}^2 for the 2 nm Bi_2Se_3 thick film based on the estimated deformation given in ref. 24, which varies with the film thickness, ~ -4.83 cm^{-1}/%. Considering the strong dependence of PDP (Raman shift strain coefficient) on the thickness together with 2 times difference in the out of plane strain for the same applied in-plane stress, $\varepsilon_{zz}^{\text{biaxial}} = 2 \times \varepsilon_{zz}^{\text{uniaxial}}$, (please see the ESI of ref. 24 and 45), we conclude a very good correlation of our results with those reported in the cited literature. It is worth mentioning that in both references considered, ref. 24 and 25, single spectra have been measured which may cause uncertainty in the measured value. In contrast, the proposed approach of strain separation using datapoint scatter along the straight lines with certain slopes is more statistically reliable than those presented previously[24,25] since the tensile in-plane strain applied to the Bi_2Se_3 ultrathin film originates from the lattice mismatch between the film and graphene, as well as the calculation process uses all data recorded from a large area by the Raman mapping technique. The application of the proposed method of PDP calculation makes it possible to estimate this coefficient regardless of the deformation type (both under compression and tension) in the system (Fig. 3d).

Conclusion

The method of separation of two different origins of strain (hydrostatic and in-plane tensile caused by lattice mismatch) using Raman data analysis is developed and applied to Bi_2Se_3 films PVD-grown on quartz and CVD-graphene substrates. All samples were investigated using the Raman mapping technique over a 20 × 20 μm^2 area. The correlation analysis of A_{1g}^2 and E_g^2 position modes revealed that films grown on a quartz substrate experienced a hydrostatic strain distribution, which is evidenced by the location of A_{1g}^2 *vs.* E_g^2 points along the line with a slope of ~0.85 which is in good quantitative agreement with the ratio of Raman shift hydrostatic pressure induced coefficients reported in the literature. The Bi_2Se_3 films deposited on SLG substrates experience additional in-plane tensile strain, originating from the lattice mismatch between the graphene and Bi_2Se_3, accompanied by compression in the *c*-axis. The approach for the separation of these two types of strain, based on the analysis of A_{1g}^2 *vs.* E_g^2 datapoint scatter, is proposed. Application of the proposed strain separation approach for the calculation of phonon deformation potential for the thinnest Bi_2Se_3 (3 nm) film on graphene, where the film is fully strained by the substrate and strain is considered to be coherent across the thickness, is demonstrated. The PDPs for biaxial in-plane strain of the Bi_2Se_3 3 nm film in in-plane and out-of-plane modes were calculated to be -7.64 cm^{-1}/% and -6.97 cm^{-1}/%, respectively.

Conflicts of interest

There are no conflicts to declare.

Acknowledgements

This work was supported by the European Research and Development Fund (ERDF) project No. 1.1.1.1/16/A/257 and European Union's Horizon 2020 research and innovation programme (grant agreement No. 766714/HiTIMe). I. V. Komissarov and S. L. Prischepa acknowledge the financial support of the "Improving the Competitiveness Program" of the National Research Nuclear University (MEPhI). The authors would like to thank A. Felsharuk for help with the AFM images, A. Kalaboukhov for help with the RHEED measurements and G. Rimsky for XRD analysis of copper foil.

References

1 W. Dang, H. Peng, H. Li, P. Wang and Z. Liu, *Nano Lett.*, 2010, **10**, 2870–2876.
2 X. L. Qi and S. C. Zhang, *Rev. Mod. Phys.*, 2011, **83**, 1057–1110.
3 M. Z. Hasan and C. L. Kane, *Rev. Mod. Phys.*, 2010, **82**, 3045–3067.
4 M. Baitimirova, J. Andzane, G. Petersons, R. Meija, R. Poplausks, M. Romanova and D. Erts, *J. Mater. Sci.*, 2016, **51**, 8224–8232.
5 J. Chae, S. H. Kang, S. H. Park, H. Park, K. Jeong, T. H. Kim, S. B. Hong, K. S. Kim, Y. K. Kwon, J. W. Kim and M. H. Cho, *ACS Nano*, 2019, **13**, 3931–3939.
6 J. Andzane, A. Felsharuk, A. Sarakovskis, U. Malinovskis, E. Kauranens, M. Bechelany, K. A. Niherysh, I. V Komissarov and D. Erts, *Mater. Today Energy*, 2021, **19**, 100587.
7 W. Liu, X. Peng, H. Yang, X. Wei and J. Zhong, *J. Phys.: Condens. Matter*, 2015, **27**, 435003–435129.
8 R. Roldán, A. Castellanos-Gomez, E. Cappelluti and F. Guinea, *J. Phys.: Condens. Matter*, 2015, **27**, 313201.
9 T. Y. Lü, X. X. Liao, H. Q. Wang and J. C. Zheng, *J. Mater. Chem.*, 2012, **22**, 10062–10068.
10 H. J. Conley, B. Wang, J. I. Ziegler, R. F. Haglund, S. T. Pantelides and K. I. Bolotin, *Nano Lett.*, 2013, **13**, 3626–3630.
11 H. Aramberri and M. C. Muñoz, *Phys. Rev. B*, 2017, **95**, 205422.

12 J. Liu, Y. Xu, J. Wu, B. L. Gu, S. B. Zhang and W. Duan, *Acta Crystallogr., Sect. C: Struct. Chem.*, 2014, **70**, 118–122.

13 X. Luo, M. B. Sullivan and S. Y. Quek, *Phys. Rev. B: Condens. Matter Mater. Phys.*, 2012, **86**, 184111.

14 B. Li, X. Guo, W. Ho and M. Xie, *Appl. Phys. Lett.*, 2015, **107**, 081604.

15 N. Bansal, Y. S. Kim, E. Edrey, M. Brahlek, Y. Horibe, K. Iida, M. Tanimura, G. H. Li, T. Feng, H. D. Lee, T. Gustafsson, E. Andrei and S. Oh, *Thin Solid Films*, 2011, **520**, 224–229.

16 S. Linas, Y. Magnin, B. Poinsot, O. Boisron, G. D. Förster, V. Martinez, R. Fulcrand, F. Tournus, V. Dupuis, F. Rabilloud, L. Bardotti, Z. Han, D. Kalita, V. Bouchiat and F. Calvo, *Phys. Rev. B: Condens. Matter Mater. Phys.*, 2015, **91**, 075426.

17 F. Bianco, K. Fedus, F. Enrichi, R. Pierobon, M. Cazzanelli, M. Ghulinyan, G. Pucker and L. Pavesi, *Semicond. Sci. Technol.*, 2012, **27**, 085009.

18 P. C. Hsu, T. A. Lin and I. S. Tsai, *Micro Nano Lett.*, 2014, **9**, 922–926.

19 M. O'Steen, E. Readinger, S. Farrell, M. Marek, M. Doran and D. Hanser, in *Molecular Beam Epitaxy*, Elsevier, 2018, pp. 649–675.

20 J. Zabel, R. R. Nair, A. Ott, T. Georgiou, A. K. Geim, K. S. Novoselov and C. Casiraghi, *Nano Lett.*, 2012, **12**, 617–621.

21 M. Mohr, J. Maultzsch and C. Thomsen, *Phys. Rev. B: Condens. Matter Mater. Phys.*, 2010, **82**, 201409.

22 D. Metten, F. Federspiel, M. Romeo and S. Berciaud, *Phys. Rev. Appl.*, 2014, **2**, 054008.

23 J. E. Lee, G. Ahn, J. Shim, Y. S. Lee and S. Ryu, *Nat. Commun.*, 2012, **3**, 1–8.

24 Q. Li, Y. Wang, T. Li, W. Li, F. Wang, A. Janotti, S. Law and T. Gu, *ACS Omega*, 2020, **5**, 8090–8096.

25 Y. Yan, X. Zhou, H. Jin, C. Z. Li, X. Ke, G. Van Tendeloo, K. Liu, D. Yu, M. Dressel and Z. M. Liao, *ACS Nano*, 2015, **9**, 10244–10251.

26 J. Andzane, K. Buks, M. N. Strakova, M. Zubkins, M. Bechelany, M. Marnauza, M. Baitimirova and D. Erts, *IEEE Trans. Nanotechnol.*, 2019, **18**, 948–954.

27 J. Andzane, G. Kunakova, S. Charpentier, V. Hrkac, L. Kienle, M. Baitimirova, T. Bauch, F. Lombardi and D. Erts, *Nanoscale*, 2015, **7**, 15935–15944.

28 M. T. Ghoneim, C. E. Smith and M. M. Hussain, *Appl. Phys. Lett.*, 2013, **102**, 183115.

29 J. Andzane, L. Britala, E. Kauranens, A. Neciporenko, M. Baitimirova, S. Lara-Avila, S. Kubatkin, M. Bechelany and D. Erts, *Sci. Rep.*, 2019, **9**, 1–8.

30 W. Richter and C. R. Becker, *Phys. Status Solidi*, 1977, **84**, 619–628.

31 Y. Zhao, X. Luo, J. Zhang, J. Wu, X. Bai, M. Wang, J. Jia, H. Peng, Z. Liu, S. Y. Quek and Q. Xiong, *Phys. Rev. B: Condens. Matter Mater. Phys.*, 2014, **90**, 245428.

32 Y. D. Glinka, S. Babakiray, T. A. Johnson and D. Lederman, *J. Phys.: Condens. Matter*, 2015, **27**, 52203.

33 R. Vilaplana, D. Santamaría-Pérez, O. Gomis, F. J. Manjón, J. González, A. Segura, A. Muñoz, P. Rodríguez-Hernández, E. Pérez-González, V. Marín-Borrás, V. Muñoz-Sanjose, C. Drasar and V. Kucek, *Phys. Rev. B: Condens. Matter Mater. Phys.*, 2011, **84**, 184110.

34 M. P. Deshpande, S. V. Bhatt, V. Sathe, R. Rao and S. H. Chaki, *Phys. B*, 2014, **433**, 72–78.

35 *Technical information for type GE 124 fused quartz*, 2015, https://www.microtonano.com.

36 X. Chen, H. D. Zhou, A. Kiswandhi, I. Miotkowski, Y. P. Chen, P. A. Sharma, A. L. Lima Sharma, M. A. Hekmaty, D. Smirnov and Z. Jiang, *Appl. Phys. Lett.*, 2011, **99**, 261912.

37 S. G. Mayr and K. Samwer, *Phys. Rev. Lett.*, 2001, **87**, 361051–361054.

38 L. Kou, B. Yan, F. Hu, S. C. Wu, T. O. Wehling, C. Felser, C. Chen and T. Frauenheim, *Nano Lett.*, 2013, **13**, 6251–6255.

39 S. Nakajima, *J. Phys. Chem. Solids*, 1963, **24**, 479–485.

40 S. Berciaud, S. Ryu, L. E. Brus and T. F. Heinz, *Nano Lett.*, 2009, **9**, 346–352.

41 R. P. Vidano, D. B. Fischbach, L. J. Willis and T. M. Loehr, *Solid State Commun.*, 1981, **39**, 341–344.

42 A. C. Ferrari and D. M. Basko, *Nat. Nanotechnol.*, 2013, **8**, 235–246.

43 T. H. Kim, K. Jeong, B. C. Park, H. Choi, S. H. Park, S. Jung, J. Park, K. H. Jeong, J. W. Kim, J. H. Kim and M. H. Cho, *Nanoscale*, 2016, **8**, 741–751.

44 C. Wang, X. Zhu, L. Nilsson, J. Wen, G. Wang, X. Shan, Q. Zhang, S. Zhang, J. Jia and Q. Xue, *Nano Res.*, 2013, **6**, 688–692.

45 W. G. Cady and J. Valasek, *Phys. Teach.*, 1965, **3**, 130.

Paper III

nanomaterials

Article

Magnetotransport Studies of Encapsulated Topological Insulator Bi_2Se_3 Nanoribbons

Gunta Kunakova [1,*], Edijs Kauranens [1], Kiryl Niherysh [1,2], Mikhael Bechelany [3], Krisjanis Smits [4], Gatis Mozolevskis [4], Thilo Bauch [5], Floriana Lombardi [5] and Donats Erts [1]

[1] Institute of Chemical Physics, University of Latvia, 19 Raina Blvd., LV-1586 Riga, Latvia; edijs.kauranens@lu.lv (E.K.); kiryl.niherysh@lu.lv (K.N.); donats.erts@lu.lv (D.E.)
[2] Research and Development Department, Integrated Micro- and Nanosystems, Belarusian State University of Informatics and Radioelectronics, P. Brovki Str. 6, 220013 Minsk, Belarus
[3] Institut Européen des Membranes, IEM, UMR 5635, University of Montpellier, ENSCM, CNRS, 34095 Montpellier, France; mikhael.bechelany@umontpellier.fr
[4] Institute of Solid State Physics, University of Latvia, Kengaraga 8, LV-1063 Riga, Latvia; smits@cfi.lu.lv (K.S.); gatis.mozolevskis@cfi.lu.lv (G.M.)
[5] Quantum Device Physics Laboratory, Department of Microtechnology and Nanoscience, Chalmers University of Technology, SE-41296 Goteborg, Sweden; thilo.bauch@chalmers.se (T.B.); floriana.lombardi@chalmers.se (F.L.)
* Correspondence: gunta.kunakova@lu.lv

Abstract: The majority of proposed exotic applications employing 3D topological insulators require high-quality materials with reduced dimensions. Catalyst-free, PVD-grown Bi_2Se_3 nanoribbons are particularly promising for these applications due to the extraordinarily high mobility of their surface Dirac states, and low bulk carrier densities. However, these materials are prone to the formation of surface accumulation layers; therefore, the implementation of surface encapsulation layers and the choice of appropriate dielectrics for building gate-tunable devices are important. In this work, all-around ZnO-encapsulated nanoribbons are investigated. Gate-dependent magnetotransport measurements show improved charge transport characteristics as reduced nanoribbon/substrate interface carrier densities compared to the values obtained for the as-grown nanoribbons on SiO_2 substrates.

Keywords: Bi_2Se_3 nanoribbons; ZnO; magnetotransport

check for updates

Citation: Kunakova, G.; Kauranens, E.; Niherysh, K.; Bechelany, M.; Smits, K.; Mozolevskis, G.; Bauch, T.; Lombardi, F.; Erts, D. Magnetotransport Studies of Encapsulated Topological Insulator Bi_2Se_3 Nanoribbons. *Nanomaterials* **2022**, *12*, 768. https://doi.org/10.3390/nano12050768

Academic Editors: Yanquan Geng, Emmanuel Brousseau, Bo Xue, Jingran Zhang and Jiqiang Wang

Received: 27 January 2022
Accepted: 20 February 2022
Published: 24 February 2022

1. Introduction

Three-dimensional topological insulators (3D-TIs) are among the major materials in the class of topological materials. 3D-TIs have attracted significant research interest due to their unusual surface properties. Carriers originating from topological surface states exhibit a Dirac cone in the band structure [1] and charge transport via these states is protected against backscattering from non-magnetic impurities [2,3]. If proximitized with an s-wave superconductor, superconductivity induced in the topological surface states is unconventional and predicted to host Majorana fermions [4,5]. The exploitation of these exotic surface properties is advantageous for a variety of applications, for example, in topological quantum computing [6], spintronics [7,8], and in the development of new-concept electronic devices [9]. The surface states of TIs are metallic while the bulk of the material, which is expected to be an insulator, is highly doped due to the formation of native defects [10]. This aspect remains the main challenge in accessing the surface-state charge transport, hampering progress towards the development of applications beyond fundamental studies.

Owing to their large surface-to-volume ratio, 3D-TI nanowires and nanoribbons are promising candidates with which to achieve truly topological surface-state-dominated charge transport without any contribution from the bulk. Their nanosized geometry provides even more functionalities because of the low number of transport modes [11], which is particularly important for probing Majorana states [6]. Remarkable improvements in material quality have been demonstrated in 3D-TIs doped with native-defect-compensating substitutions. Nearly insulating bulk with a charge carrier density of ~10^{15} cm^{-3} has been reported in single crystals of $BiSbTeSe_2$ [12] (BSTS), but this approach is not fully successful in nanowires and nanoribbons. Here, precise and reproducible concentrations of dopants are challenging to obtain, and they are achieved at the expense of charge carrier mobility [13].

Nanoribbons of Bi_2Se_3 have been reported to be nearly ideal 3D-TIs, practically without any bulk conduction, and with exceptionally high carrier mobilities [14,15]. However, Bi_2Se_3 is prone to the formation of surface accumulation layers [16]; this is particularly evident in thin nanoribbons, where the thickness is comparable with the Debye screening length [14,17,18]. The majority of the proposed 3D-TI-nanoribbon-based electronic devices require good tunability of their chemical potential for accessing surface Dirac carriers in a controlled manner. This can be achieved by employing electrostatic gating techniques. However, additional trivial carriers with large densities form at the nanoribbon surfaces, or at the interface with the substrate, which cannot be effectively depleted by common electrostatic gating techniques. Therefore, more effort is needed to prevent the uncontrolled formation of surface accumulation layers in Bi_2Se_3 nanoribbons.

The use of surface-capping layers for Bi_2Se_3 and Bi_2Te_3 has proven to be beneficial to protect against environmental doping [19] and to probe surface state transport. Widely used capping layer materials are Te or Se, and the oxide layers of ZnO or Al_2O_3 [13,20,21], deposited on the top surface of the material. This allows more efficient electrostatic tuning of the Fermi level [21], while in the case of Bi_2Se_3 nanoribbons, where the accumulation layer is formed at the nanoribbon/substrate interface [14,17], other approaches have to be considered.

In this work, we used atomic layer deposition (ALD) to fabricate all-around ZnO-capped or -encapsulated Bi_2Se_3 nanoribbons. The choice of selecting ZnO as an encapsulation layer material was based on the fact that thin layers of high-quality ZnO are possible to grow at moderate temperatures. This is particularly important for preserving the stoichiometry of Bi_2Se_3, as elevated temperatures may cause the unwanted out-diffusion of Se, which increases the doping of the bulk. Comparative magnetotransport studies of individual encapsulated and as-grown Bi_2Se_3 nanoribbons from the same batch synthesis show that the encapsulation layer of ZnO helps to minimize the impact of the accumulation layer at the nanoribbon/substrate interface and improves the tunability of the chemical potential using a back-gate. These findings are important for the implementation of 3D-TI-nanoribbon-based topological quantum devices.

2. Materials and Methods

Free-standing Bi_2Se_3 nanoribbons were grown on glass substrates using catalyst-free physical vapor deposition (PVD). The growth procedure is described in detail elsewhere [22]. As-grown nanoribbons were mechanically transferred to prepatterned Si/300 nm SiO_2 chips by bringing the chip and the glass substrate into contact with each other. The glass substrate with the remaining free-standing nanoribbons was then covered with 2 nm of ZnO, using ALD at ~100 °C, in a home-built set-up.

Flakes of hexagonal boron nitride (h-BN) were exfoliated from h-BN single crystals (2D semiconductors) and transferred to prepatterned Si/300 nm SiO_2 chips. ZnO-encapsulated Bi_2Se_3 nanoribbons were then transferred to the chips partially covered with thin flakes of h-BN. Standard electron beam lithography processing was used to define electrical contacts to individual Bi_2Se_3 and ZnO/Bi_2Se_3 nanoribbons. After developing the resist, the samples were etched for 60 s in $H_2O/HCl/H_2O_2/CH_3COOH$ solution [23] at room temperature to remove the surface oxide layer, and layers of Ti (3 nm) and Au (80 nm) were evaporated shortly after the etching to ensure formation of ohmic contacts.

Charge transport measurements were conducted in a Physical Property Measurement System (PPMS) Dynacool, equipped with a 9 T magnet, at a base temperature of 2 K. In magnetoresistance measurements, a magnetic field *B* was applied perpendicularly to the nanoribbon surface. Electrode pair I^+/I^- (see Figure 2a) was used as the current electrodes to ensure a uniform flow of current in the nanoribbon, while the remaining electrodes V_1 to V_8 were employed as the voltage probes. Longitudinal resistance R_{xx} was recorded using, for example, electrode pair V_3/V_7 while the transversal resistance R_{xy} was measured across the pair V_5/V_6. For this particular nanoribbon device, voltage electrodes V_1 to V_4 are positioned where the nanoribbon is on top of the h-BN flake (~30 nm in thickness), while the other voltage electrodes are located on the nanoribbon part, which is in direct contact with the SiO_2.

In order to determine whether the ZnO had covered the free standing Bi_2Se_3 nanoribbons, the nanoribbons were transferred to Cu grids and imaged through high-resolution transmission electron microscope (HR-TEM Technai, Fei, Eindhoven, Netherland).

3. Results and Discussion

Simplified schematics illustrating the free-standing nanoribbons and encapsulation with a thin ZnO layer are shown in Figure 1a. The HR-TEM studies of the ZnO/Bi_2Se_3 nanoribbons reveal a crystalline layer, with a thickness of ~2 nm, at the nanoribbon surfaces. In total, five different nanoribbons of various geometries were examined, and a crystalline surface layer was formed in all of them. The *d*-spacing value estimated from the lattice fringes of Bi_2Se_3 is 0.21 nm, which is in good agreement with the previous studies [22]. The *d*-spacing value determined for the ZnO of 0.28 nm corresponds to (100) planes of hexagonal wurtzite [24]. The interface between the Bi_2Se_3 and ZnO is separated by a layer of amorphous material, with a thickness of ~1.5–2 nm. This layer corresponds to native oxide of Bi_2Se_3, BiO_x (see Figure 1b), which is always present on surfaces of Bi_2Se_3 [19].

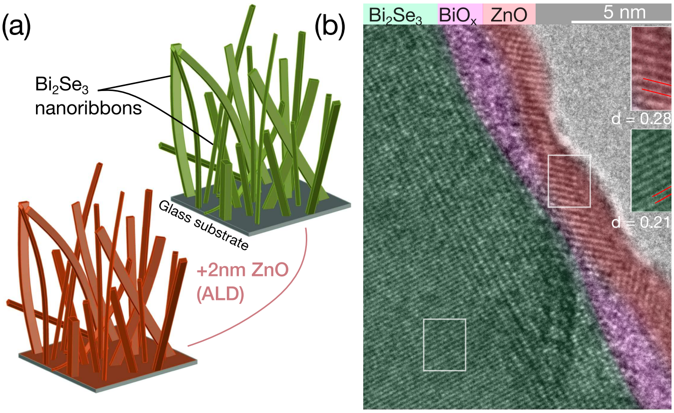

Figure 1. (**a**) Schematic representation of catalyst-free PVD-synthesized free-standing Bi_2Se_3 nanoribbons on glass substrate; (**b**) false-colored HR-TEM image of a Bi_2Se_3 nanoribbon after encapsulation with a thin layer of ZnO.

One of the fabricated nanoribbon Hall-bar devices used in the magnetotransport measurements is depicted in Figure 2a. The measured $R_{xy}(B)$ at zero back-gate voltage is shown in Figure 2b. In order to minimize the error from misaligned electrodes, the data were anti-symmetrized as a function of the magnetic field (see inset of Figure 2b). The $R_{xy}(B)$ dependences for all the measured nanoribbons were nonlinear. The absolute value of the slope calculated from the high magnetic field range 7–9 T was always smaller than the value determined from the 0–2.5 T range. This nonlinearity points to the charge carriers originating from two or more carrier bands characterised by different densities/mobilities.

The initial carrier density n_{3D} can be calculated from the low or high magnetic field slope of $R_{xy}(B)$ as:

$$\frac{1}{n_{3D}e} = t\frac{\mathrm{d}R_{xy}}{\mathrm{d}B} \times \frac{w}{w_h}. \tag{1}$$

Here, t is the nanoribbon thickness, w is the nanoribbon width, w_h is the distance between the Hall contacts, and e is the elementary charge. The calculated values for the 2D carrier densities ($n_{2D} = n_{3D}\cdot t$) from both the 0–2.5 T and 7–9 T regions for the as-grown and ZnO-encapsulated nanoribbons from the same batch synthesis are listed in Table S1 (see Supplementary Information (SI)). The values estimated from the 7–9 T range are about 20–30% higher than those obtained from the 0–2.5 T range.

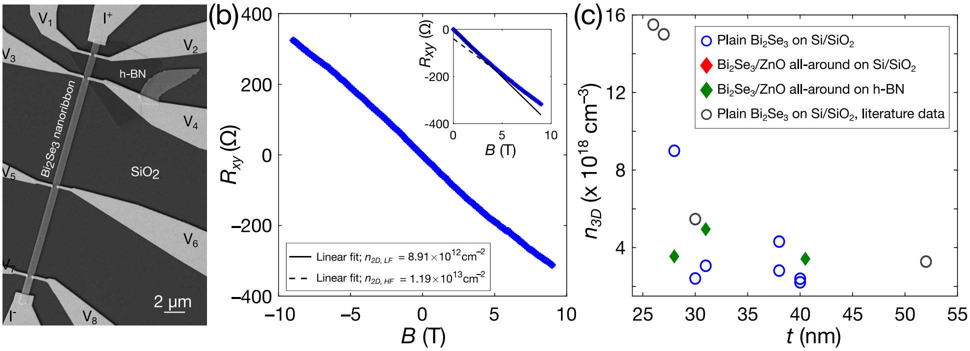

Figure 2. (**a**) SEM image of a Bi_2Se_3 nanoribbon Hall-bar device; (**b**) Hall resistance $R_{xy}(B)$ for the ZnO/Bi_2Se_3 nanoribbon device A3t (see Table S1), measured at back-gate voltage V_g = 0 V. The inset shows anti-symmetrized $R_{xy}(B)$ data with linear fit in the 0–2.5 T range (black solid curve), and in the 7–9 T range (black dashed curve); (**c**) Hall carrier density of Bi_2Se_3 and ZnO/Bi_2Se_3 nanoribbons, plotted versus the nanoribbon thickness. In the case of the ZnO/Bi_2Se_3 nanoribbons, total thickness t is reduced by 4 nm, accounting for the two ~2 nm thick ZnO layers. Gray data points correspond to the data from [14]; here, the carrier density is calculated from the same magnetic field range (0–2.5 T).

Figure 2c shows the n_{3D} of the as-grown Bi_2Se_3 and ZnO/Bi_2Se_3 nanoribbons, plotted as a function of the nanoribbon thickness. The data correspond to the values calculated from the 0–2.5 T range, since in high magnetic fields, some nanoribbons showed the presence of Shubnikov–de Haas oscillations in $R_{xx}(B)$, additionally impacting the $R_{xy}(B)$ dependence.

The charge carrier density n_{3D} for the as-grown Bi_2Se_3 nanoribbons with thicknesses of ~30–40 nm is about ~3.5 × 10^{18} cm^{-3}, and it increases to ~9 × 10^{18} cm^{-3} for the 28-nanometer-thin nanoribbon. This peculiar $n_{3D}(t)$ dependence of the catalyst-free PVD-grown Bi_2Se_3 nanoribbons has been reported previously [14]. The increased 3D charge carrier density for nanoribbons of thicknesses below ~30 nm is due to the accumulation layer of a large carrier density of ~1.3 × 10^{13} cm^{-2} (see Table 1), formed at the nanoribbon's bottom surface/substrate interface [14]. Figure 2c also includes the values of the carrier densities reported in [14] (gray points). In this work, the obtained $n_{3D}(t)$ for the as-grown ribbons is similar to those previously reported in the literature.

The n_{3D} values for the ZnO-encapsulated Bi_2Se_3 nanoribbons are close to those determined for the as-grown nanoribbons with thicknesses of ~30–40 nm, and are also about ~3.5 × 10^{18} cm^{-3}. A pronounced increase of n_{3D} of the thin ZnO-encapsulated nanoribbons (t < 30 nm) is not observed, indicating that the overall carrier density in the accumulation layer could be smaller compared to the as-grown Bi_2Se_3 nanoribbons.

The charge carrier density n_{2D} as a function of the back-gate voltage V_g for a 28-nanometer-thin ZnO-encapsulated Bi_2Se_3 nanoribbon on h-BN is plotted in Figure 3a.

The applied back-gate voltage directly affects the nanoribbon bottom surface/substrate interface, and at higher V_g values, some parts of the nanoribbon bulk as well. The slope of the $n_{2D}(V_g)$ gives an indication of the capacitance of this field-effect device, and $C \approx 6.2 \times 10^{-5}$ F/m^2. In order to effectively deplete the majority of the initial carriers of ~9 × 10^{12} cm^{-2}, one would need to apply approximately twice as high a voltage to the back-gate, which is not feasible for this device. Nevertheless, the $n_{2D}(V_g)$ data are helpful for the study of the properties of the nanoribbon/substrate interface. The $R_{xx}(V_g)$ data of the same ribbon reflect the $n_{2D}(V_g)$ characteristics (see inset of Figure 3a). The absence of maxima or saturation in the $R_{xx}(V_g)$ indicates that the Fermi energy E_F remained above the Dirac point in the entire measured V_g range. To tune the E_F to the Dirac point, which is important for accessing the charge carriers exclusively from the surface Dirac states, ultra-thin (t ~ 10 nm) Bi_2Se_3 nanoribbons would be needed. Another aspect for improving the gate tunability is the thickness and permittivity of the gate dielectric, i.e., a thinner dielectric layer than the 32 nm of h-BN on 300 nm of SiO_2 could be used ($\varepsilon \sim$ 3–4), or, alternatively, one could choose a $SrTiO_3$ substrate, in which the relative dielectric constant at low temperatures is in the order of 10^3–10^4.

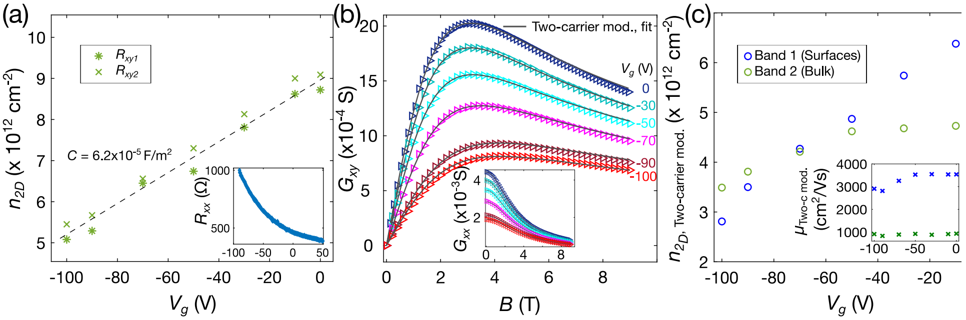

Figure 3. (**a**) Charge carrier density $n_{2D}(= n_{3D}t)$ as a function of the back-gate voltage V_g. Here, n_{2D} is calculated from the anti-symmetrized $R_{xy}(B)$ data in the 0–2.5 T range. R_{xy1} and R_{xy2} represent the Hall resistances measured using two different pairs of transversal electrodes, on the same nanoribbon. Black dashed line is the linear fit, and the capacitance estimated from the slope is 6.2 × 10^{-5} F/m^2. In the inset—longitudinal resistance R_{xx} as a function of the V_g; (**b**) conductance tensor element $G_{xy}(B)$ at different applied V_g, fitted with the two-carrier model, inset shows fitted $G_{xx}(B)$ curves; (**c**) from the two-carrier model extracted parameters of the two bands: carrier densities n_1; n_2, and mobilities μ_1; μ_2 (in the inset) versus the back-gate voltage. All the data shown correspond to the ZnO/Bi_2Se_3 nanoribbon A3t.

Since the $R_{xy}(B)$ curves clearly indicate the presence of charge carriers from several carrier bands, we analysed the magnetotransport data using the two-carrier model.

Here, the conductance tensor elements G_{xy} and G_{xx} as a function of the magnetic field can be written as [25,26]:

$$G_{xy}(B) = eB \left. \frac{n_1\mu_1^2}{1+\mu_1^2B^2} + \frac{n_2\mu_2^2}{1+\mu_2^2B^2} \right) \tag{2a}$$

$$G_{xx}(B) = e \left. \frac{n_1\mu_1}{1+\mu_1^2B^2} + \frac{n_2\mu_2}{1+\mu_2^2B^2} \right) \tag{2b}$$

with parameters n_1, n_2 and μ_1, μ_2 representing the carrier densities and mobilities of the two bands, respectively. G_{xy} and G_{xx} from the measured resistances are calculated as:

$$G_{xy}(B) = -\frac{R'_{xy}}{R'^2_{xy} + R'^2_{xx}} \tag{3a}$$

$$G_{xx}(B) = -\frac{R'_{xx}}{R'^2_{xy} + R'^2_{xx}} \tag{3b}$$

R'_{xy} is the Hall resistance, corrected considering the geometry of a nanoribbon Hall-bar device, and is equal to $R_{xy}\ w/w_c$. R'_{xx} is the sheet resistance, equal to $R_{xx}\ w/L$. The calculated conductance tensor elements as a function of magnetic field for different applied back-gate voltages are fitted with Equations (2a) and (2b) and plotted in Figure 3b. For the nanoribbon A3t, the extracted value of the charge carrier density of band 1 is $n_1 = 6.43 \times 10^{12}$ cm^{-2} and the mobility $\mu_1 = 3530$ cm^2/Vs, while the carrier density and mobility of band 2 are $n_2 = 4.74 \times 10^{12}$ cm^{-2} and $\mu_2 = 990$ cm^2/Vs, respectively. These parameters of the two bands are similar to those estimated for other ZnO-encapsulated Bi_2Se_3 nanoribbons (see Table 1).

The extracted carrier density values n_1 and n_2 of the two bands change with the applied back-gate voltage. The value n_1 scales linearly with the applied back-gate voltage and is reduced by ~50% at $V_g = -100$ V. Instead, n_2 is practically insensitive to V_g in the 0–-50 V range, while at $V_g > -50$, V starts to decrease more rapidly.

Table 1. Summary of the carrier densities (cm^{-2}) and mobilities (cm^2/Vs) extracted from the two-band analysis and from the SdH oscillations for ZnO-encapsulated Bi_2Se_3 nanoribbons on h-BN and SiO_2 substrates, and comparison with the literature data (refs. [14,15,17]).

		Surfaces (Band 1)		**Bulk (Band 2)**		**Top Surface ***	**Bulk ***
ZnO/Bi_2Se_3 NR on h-BN:	**t_{NR}, nm**	n_1	μ_1	n_2	μ_2	$n_{2D,\ SdH}$	$n_{3D,\ SdH}$
A3t	29	6.43×10^{12}	3540	$4.74 \times 10^{12}/1.64 \times 10^{18}$	930	2.40×10^{12}	1.44×10^{18}
A1b	35	7.18×10^{12}	4700	$5.31 \times 10^{12}/1.52 \times 10^{18}$	2052		
D3b	34	6.24×10^{12}	4800	$4.99 \times 10^{12}/1.46 \times 10^{18}$	1350		
Bi_2Se_3 NR on SiO_2, sample E5 [14]	30	15.0×10^{12} **				2.40×10^{12}	
Bi_2Se_3 NR on SiO_2, sample BR3-10R2 [14]	63	-				2.50×10^{12}	1.70×10^{18}
Bi_2Se_3 NR on SiO_2, sample E [17]	79	13.0×10^{12} *				2.90×10^{12}	6.60×10^{17}
Bi_2Se_3 NR on STO, sample B51-10 [15]	9	5.55×10^{12} **	1232				

* Extracted from analysis of the SdH oscillations. ** These values account only carrier density of the nanoribbon bottom surface/substrate interface.

In what follows, we discuss a possible scenario that would account for this behaviour. Band 1 is affected by the back-gate voltage much more strongly; therefore, the carrier density n_1 can most likely be associated with the surface states. As the nanoribbons are fully encapsulated by the ZnO protection layer, the mobilities of the nanoribbon top and bottom surfaces can be expected to have similar values, and carriers from both surfaces would appear in the same channel (n_1) of the two-band model. The bulk mobilities are typically reported to be of much lower values [27], and the μ_1 of 3530 cm^2/Vs is more than three times larger than the value of μ_2. For nanoribbon A1b, where the μ_1 is 4700 cm^2/Vs, SdH oscillations with two dominating frequencies are observed (see Figure S2, SI). One of the frequencies of ~99 T is similar to that observed in the catalyst-free PVD-grown Bi_2Se_3 nanoribbons, which have previously been reported to represent the surface Dirac states from the nanoribbon top surfaces [14,22,28]. This gives the carrier density of the nanoribbon top surface of $n_{TS\ SdH}$~2.4×10^{12} cm^{-2}. The carriers from the top surface are most likely insensitive to the back-gate voltage, as the nanoribbon is of a relatively large thickness. The bottom surface/interface $n_{BS,\ Int.}$ carrier density at V_g = 0 V would be then $n_1 - n_{TS\ SdH} \approx 4 \times 10^{12}$ cm^{-2}, which would not be very different from all the ZnO/Bi_2Se_3 nanoribbons transferred onto the h-BN (4.03, 3.84 and 4.78 × 10^{12} cm^{-2} for the nanoribbons A3t, D3b, and A1b, respectively). These low values corroborate that the ZnO encapsulation of Bi_2Se_3 nanoribbons mitigates the creation of an accumulation layer.

Band 2 with carrier density n_2 can be assumed to correspond to the bulk carriers. Above −50 V, when the bottom surface/interface carriers are partly depleted, a fraction of the bulk carriers also starts to be affected by the back-gate voltage, and at V_g = −100 V, the n_2 is reduced to ~3.5 × 10^{12} cm^{-2}. At V_g = 0 V, the n_2 is 4.74–5.31 × 10^{12} cm^{-2} (see Table 1), and if rescaling to the 3D values: 1.46–1.64 × 10^{18} cm^{-3}. Peculiarly enough, the second frequency of the aforementioned SdH oscillations of the nanoribbon A1b (Figure S2, SI), with the highest μ_2, gives 1.44 × 10^{18} cm^{-3}. This value is close to the 3D bulk carrier densities determined from band 2.

4. Conclusions

To conclude, the application of a ZnO encapsulation layer to topological insulator Bi_2Se_3 nanoribbons and the use of h-BN as a substrate help to improve the nanoribbon/substrate interface properties. Thin layers of crystalline ZnO have no degrading impact on the overall transport characteristics of Bi_2Se_3 nanoribbons. The 3D charge carrier densities for nanoribbons of different thicknesses are of the same order as the values determined for as-grown nanoribbons with thicknesses of 30–40 nm. The reduced surface carrier density extracted from two-band Hall analysis points towards a reduction in the interface accumulation layer when encapsulating Bi_2Se_3 nanoribbons with a thin ZnO layer. Moreover, the ZnO-encapsulated nanoribbons show excellent Hall mobility. The presence of the Shubnikov–de Haas oscillations confirms that the high quality of catalyst-free PVD-grown Bi_2Se_3 nanoribbons stays preserved if ZnO is used as an encapsulation layer. This approach of all-around encapsulation in combination with ultra-thin Bi_2Se_3 nanoribbons, transferred to mono or few layer h-BN substrates, would be beneficial to controllably achieve ambipolar transport in Bi_2Se_3.

Supplementary Materials: The following supporting information can be downloaded at: https://www.mdpi.com/article/10.3390/nano12050768/s1.

Author Contributions: Conceptualization, G.K.; investigation E.K. and K.N.; resources K.S., G.M., T.B., F.L., D.E. and M.B.; writing—review and editing, G.K., T.B., F.L. and D.E. All authors have read and agreed to the published version of the manuscript.

Funding: This research was funded by the Latvian Council of Science, project "Highly tunable surface state transport in topological insulator nanoribbons", No. lzp-2020/2-0343, and by the European Union's Horizon 2020 research and innovation program, Grant Agreement No. 766714/HiTIMe.Institute of Solid-State Physics, University of Latvia as the Center of Excellence has received funding from the European Union's Horizon 2020 Framework Programme H2020-WIDESPREAD-01-2016-2017-TeamingPhase2 under grant agreement No. 739508, project CAMART2.

Institutional Review Board Statement: Not applicable.

Informed Consent Statement: Not applicable.

Data Availability Statement: The data presented are available on request from the corresponding author.

Conflicts of Interest: The authors declare no conflict of interest.

References

1. Zhang, H.; Liu, C.-X.; Qi, X.-L.; Dai, X.; Fang, Z.; Zhang, S.-C. Topological insulators in Bi_2Se_3, Bi_2Te_3 and Sb_2Te_3 with a single Dirac cone on the surface. *Nat. Phys.* **2009**, *5*, 438–442. [CrossRef]
2. Hsieh, D.; Xia, Y.; Wray, L.; Qian, D.; Pal, A.; Dil, J.H.; Osterwalder, J.; Meier, F.; Bihlmayer, G.; Kane, C.L.; et al. Observation of Unconventional Quantum Spin Textures in Topological Insulators. *Science* **2009**, *323*, 919–922. [CrossRef] [PubMed]
3. Hasan, M.Z.; Kane, C.L. Colloquium: Topological insulators. *Rev. Mod. Phys.* **2010**, *82*, 3045–3067. [CrossRef]

4. Fu, L.; Kane, C.L. Superconducting Proximity Effect and Majorana Fermions at the Surface of a Topological Insulator. *Phys. Rev. Lett.* **2008**, *100*, 096407. [CrossRef]
5. Fu, L.; Kane, C.L. Josephson current and noise at a superconductor/quantum-spin-Hall-insulator/superconductor junction. *Phys. Rev. B* **2009**, *79*, 161408. [CrossRef]
6. Manousakis, J.; Altland, A.; Bagrets, D.; Egger, R.; Ando, Y. Majorana qubits in a topological insulator nanoribbon architecture. *Phys. Rev. B* **2017**, *95*, 165424. [CrossRef]
7. Shiomi, Y.; Nomura, K.; Kajiwara, Y.; Eto, K.; Novak, M.; Segawa, K.; Ando, Y.; Saitoh, E. Spin-Electricity Conversion Induced by Spin Injection into Topological Insulators. *Phys. Rev. Lett.* **2014**, *113*, 196601. [CrossRef]
8. Khokhriakov, D.; Hoque, A.M.; Karpiak, B.; Dash, S.P. Gate-tunable spin-galvanic effect in graphene-topological insulator van der Waals heterostructures at room temperature. *Nat. Commun.* **2020**, *11*, 3657. [CrossRef]
9. Yasuda, K.; Mogi, M.; Yoshimi, R.; Tsukazaki, A.; Takahashi, K.S.; Kawasaki, M.; Kagawa, F.; Tokura, Y. Quantized chiral edge conduction on domain walls of a magnetic topological insulator. *Science* **2017**, *358*, 1311–1314. [CrossRef]
10. Xue, L.; Zhou, P.; Zhang, C.X.; He, C.Y.; Hao, G.L.; Sun, L.; Zhong, J.X. First-principles study of native point defects in Bi_2Se_3. *AIP Adv.* **2013**, *3*, 052105. [CrossRef]
11. Kunakova, G.; Surendran, A.P.; Montemurro, D.; Salvato, M.; Golubev, D.; Andzane, J.; Erts, D.; Bauch, T.; Lombardi, F. Topological insulator nanoribbon Josephson junctions: Evidence for size effects in transport properties. *J. Appl. Phys.* **2020**, *128*, 194304. [CrossRef]
12. Xu, Y.; Miotkowski, I.; Liu, C.; Tian, J.; Nam, H.; Alidoust, N.; Hu, J.; Shih, C.-K.; Hasan, M.Z.; Chen, Y. Observation of topological surface state quantum Hall effect in an intrinsic three-dimensional topological insulator. *Nat. Phys.* **2014**, *10*, 956–963. [CrossRef]
13. Hong, S.S.; Cha, J.J.; Kong, D.; Cui, Y. Ultra-low carrier concentration and surface-dominant transport in antimony-doped Bi_2Se_3 topological insulator nanoribbons. *Nat. Commun.* **2012**, *3*, 757. [CrossRef]
14. Kunakova, G.; Galletti, L.; Charpentier, S.; Andzane, J.; Erts, D.; Léonard, F.; Spataru, C.D.; Bauch, T.; Lombardi, F. Bulk-free topological insulator Bi_2Se_3 nanoribbons with magnetotransport signatures of Dirac surface states. *Nanoscale* **2018**, *10*, 19595–19602. [CrossRef]
15. Kunakova, G.; Bauch, T.; Palermo, X.; Salvato, M.; Andzane, J.; Erts, D.; Lombardi, F. High-Mobility Ambipolar Magnetotransport in Topological Insulator Bi_2Se_3 Nanoribbons. *Phys. Rev. Appl.* **2021**, *16*, 024038. [CrossRef]
16. Brahlek, M.; Kim, Y.S.; Bansal, N.; Edrey, E.; Oh, S. Surface versus bulk state in topological insulator Bi_2Se_3 under environmental disorder. *Appl. Phys. Lett.* **2011**, *99*, 012109. [CrossRef]
17. Veyrat, L.; Iacovella, F.; Dufouleur, J.; Nowka, C.; Funke, H.; Yang, M.; Escoffier, W.; Goiran, M.; Eichler, B.; Schmidt, O.G.; et al. Band Bending Inversion in Bi_2Se_3 Nanostructures. *Nano Lett.* **2015**, *15*, 7503–7507. [CrossRef]
18. Brahlek, M.; Koirala, N.; Bansal, N.; Oh, S. Transport properties of topological insulators: Band bending, bulk metal-to-insulator transition, and weak anti-localization. *Solid State Commun.* **2015**, *215–216*, 54–62. [CrossRef]
19. Kong, D.; Cha, J.J.; Lai, K.; Peng, H.; Analytis, J.G.; Meister, S.; Chen, Y.; Zhang, H.-J.; Fisher, I.R.; Shen, Z.-X.; et al. Rapid Surface Oxidation as a Source of Surface Degradation Factor for Bi_2Se_3. *ACS Nano* **2011**, *5*, 4698–4703. [CrossRef]
20. Lang, M.; He, L.; Xiu, F.; Yu, X.; Tang, J.; Wang, Y.; Kou, X.; Jiang, W.; Fedorov, A.V.; Wang, K.L. Revelation of Topological Surface States in Bi_2Se_3 Thin Films by In Situ Al Passivation. *ACS Nano* **2012**, *6*, 295–302. [CrossRef] [PubMed]
21. Ngabonziza, P.; Stehno, M.P.; Myoren, H.; Neumann, V.A.; Koster, G.; Brinkman, A. Gate-Tunable Transport Properties of In Situ Capped Bi_2Te_3 Topological Insulator Thin Films. *Adv. Electron. Mater.* **2016**, *2*, 1600157. [CrossRef]
22. Andzane, J.; Kunakova, G.; Charpentier, S.; Hrkac, V.; Kienle, L.; Baitimirova, M.; Bauch, T.; Lombardi, F.; Erts, D. Catalyst-free vapour–solid technique for deposition of Bi2Te3and Bi2Se3nanowires/nanobelts with topological insulator properties. *Nanoscale* **2015**, *7*, 15935–15944. [CrossRef]
23. Singh, A. Growth, Structural and Electrical Characterization of Topological Dirac Materials. Ph.D. Thesis, University of Cambridge, Cambridge, UK, 28 June 2018.
24. Ghosh, R.; Kundu, S.; Majumder, R.; Roy, S.; Das, S.; Banerjee, A.; Guria, U.; Bera, M.K.; Subhedar, K.M.; Chowdhury, M.P.; et al. One-pot synthesis of multifunctional ZnO nanomaterials: Study of superhydrophobicity and UV photosensing property. *Appl. Nanosci.* **2019**, *9*, 1939–1952. [CrossRef]
25. Ashcroft, N.W.; Mermin, N.D. *Solid State Physics*; Harcourt College Publishers: San Diego, CA, USA, 1976.
26. Bansal, N.; Kim, Y.S.; Brahlek, M.; Edrey, E.; Oh, S. Thickness-Independent Transport Channels in Topological InsulatorBi_2Se_3Thin Films. *Phys. Rev. Lett.* **2012**, *109*, 116804. [CrossRef] [PubMed]
27. Qu, D.-X.; Hor, Y.S.; Xiong, J.; Cava, R.J.; Ong, N.P. Quantum Oscillations and Hall Anomaly of Surface States in the Topological Insulator Bi_2Te_3. *Science* **2010**, *329*, 821–824. [CrossRef] [PubMed]
28. Kunakova, G.; Meija, R.; Andzane, J.; Malinovskis, U.; Petersons, G.; Baitimirova, M.; Bechelany, M.; Bauch, T.; Lombardi, F.; Erts, D. Surface structure promoted high-yield growth and magnetotransport properties of Bi_2Se_3 nanoribbons. *Sci. Rep.* **2019**, *9*, 11328. [CrossRef] [PubMed]

Paper IV

ADVANCED MATERIALS INTERFACES
www.advmatinterfaces.de

Synthesis and Properties of Bismuth Selenide Based Nanolaminates for Application in Thermoelectrics

Jana Andzane, Andrei Felsharuk, Krisjanis Buks, Anatolijs Sarakovskis, Kiryl Niherysh, Jevgenijs Gabrusenoks, and Donats Erts*

In this work, simple and cost-effective phyiscal vapor deposition method is applied for deposition of single Bi_2Se_3, $Bi_{1.925}Sn_{0.075}Se_3$, $Bi_2Se_{2.975}Te_{0.025}$ ultrathin films of average thickness 10–12 nm, and for the fabrication of n-type 5-layer nanolaminates. The nanolaminates are composed from alternating doped and undoped ultrathin films. Electrical and thermoelectric properties (Seebeck coefficient, resistivity, electron thermal conductivity, charge carrier concentration, and mobility) of nanolaminates as well as single ultrathin undoped and doped films are studied at room temperature under ambient conditions. Both types of nanolaminates show 75–125% increase of the Seebeck coefficient accompanied by the 65–85% reduction of the electron thermal conductivity in comparison with the nanostructured bulk materials of similar chemical compositions. The mechanisms underlying such improvement of properties of studied nanolaminates in comparison with the nanostructured bulk counterparts are discussed.

1. Introduction

Thermoelectric (TE) materials-based technologies enable direct conversion of heat to electricity and are expected to play an important role in waste heat capturing and conversion to useful energy. The architectures of TE devices are diverse and include flat bulk devices, thin- and thick-film devices, as well as flexible TE devices, which are of great importance for development of wearable electronics.[1,2] However, up to now the application of TE devices is limited to niche fields due to the low efficiency of the conventional TE materials. Improvement of TE performance of materials is of great importance for boosting TE technology.

The efficiency of TE materials is determined by a dimensionless figure of merit (ZT). In a typical definition, ZT is defined as $S^2\sigma T \cdot \kappa^{-1}$, where S is the Seebeck coefficient of the material, б is its electrical conductivity, T is the absolute temperature and κ is the thermal conductivity of the material, which is the sum of contributions from charge carriers κ_e and from lattice vibrations κ_L. Expression $S^2\sigma$ is usually referred as power factor (PF) of the TE material. The common approaches in the enhancement of ZT are maximizing of PF and/or the reduction of thermal conductivity of the material.[3] An effective for tuning the PF of the TE materials is the introduction of dopants in it.

Bismuth chalcogenides (Bi_2Se_3, Bi_2Te_3), layered narrow band gap semiconductors with recently discovered 3D topological insulator (TI) properties,[4–6] are known as one of the best near-room temperature n-type TE materials, useful for domestic waste heat conversion applications. Despite the lower TE efficiency of Bi_2Se_3 in comparison with Bi_2Te_3, it is significantly less rare, less expensive, and less toxic near-room temperature TE material. In addition, in contrast with the Bi_2Te_3, the growth mechanism of Bi_2Se_3 during the physical vapor deposition (PVD) allows to synthesize uniform ultrathin films on fused quartz substrates.[7]

Recently, it has been shown that introduction of tellurium (Te) in the Bi_2Se_3 polycrystalline bulk material may result in reduction of its thermal conductivity up to 40% depending on dopant concentration.[8] Introduction of tin (Sn) in concentration of 3–8% or Te in concentrations 6–50% in Bi_2Se_3 material resulted also in an increase of the Seebeck coefficient of these thin films up to 90% and 35% respectively in comparison with undoped bulk Bi_2Se_3.[8,9] However, such an increase of the Seebeck coefficient and reduction of thermal conductivity of the doped material did not result in significant increase of its ZT of the doped material in comparison with the undoped bulk due to the simultaneous reduction of its electrical conductance. However, has been proposed theoretically that introduction of Sn into Bi_2Se_3 in concentrations 1–2%, or the 0.5% change in the amount of Te or Se vacancies in the Bi_2Se_3 or Bi_2Te_3 material may result in formation of resonant impurity levels (RL) in their electronic structures near the Fermi level, which hybridize with the host electronic states, creating a redistribution of the

---

J. Andzane, A. Felsharuk, K. Buks, K. Niherysh, D. Erts
Institute of Chemical Physics
University of Latvia
Raina blvd. 19, Riga LV-1586, Latvia
E-mail: jana.andzane@lu.lv

A. Sarakovskis, J. Gabrusenoks
Institute of Solid State Physics
University of Latvia
Kengaraga str. 8, Riga LV-1063, Latvia

D. Erts
Faculty of Chemistry
University of Latvia
Raina blvd. 19, Riga LV-1586, Latvia

The ORCID identification number(s) for the author(s) of this article can be found under https://doi.org/10.1002/admi.202200385.

DOI: 10.1002/admi.202200385

electronic states around a valence or conduction band, which may lead to the enhancement of the Seebeck coefficient without affecting the electrical conductance of the material, and thus, to the PF of the material.[10–12]

Regarding reduction of thermal conductivity of TE materials, it was predicted theoretically that a significant decrease of the thermal conductivity due to the phonon scattering at the boundaries/interfaces is expected when the thickness of the material is reduced down to few tens of nm, as well as when the material consists of periodic thin-film structures with in the direction parallel to the film plane.[13–15] Recently, it also has been shown on an example of Bi_2Se_3 nanowires that downsizing of the Bi_2Se_3 below 20 nm results in significant suppression of the bulk conductance of this material,[16] while further downsizing of the TE materials-TI below 10 nm was proposed to result in enhancement of ZT of TE materials due to the opening of hybridization gap between the surface states.[17–19] However, the experimental investigation of properties of ultrathin films of bismuth chalcogenide family did not show any significant improvement from the bulk values of ZT, but at the same time identified significant sensitivity of Seebeck coefficient and electrical conductivity of these thin films to thickness reduction and position of Fermi level.[7,20–22] Also, it has been shown recently on an example of PbX (X = Se, Te) nanolaminates deposited by atomic layer deposition method, such structures showed significant enhancement of ZT in comparison with the single films due to the enhancement of the Seebeck coefficient and reduction of thermal conductivity owing to the processes occurring at the interfaces between the nanolaminate layers.[15] To the best of our knowledge, the TE properties of multi-layered periodic structures fabricated by PVD and composed of ultrathin (≈10–12 nm) layers of TE materials (nanolaminates) have not been yet studied. Development of simple and economically affordable technique as PVD for fabrication of high-quality ultrathin films based nanolaminates would significantly contribute of the application of such structures at industrial scale.

In this work, the previously demonstrated simple and cost-effective PVD method for deposition of ultrathin films[7] is applied for synthesis of single Bi_2Se_3 ultrathin films doped with low concentrations of Sn (1.5%) or Te (0.5%) for potential inducing of the RL in the material, and for the fabrication of n-type nanolaminates, composed of 5 intermittent doped and undoped ultrathin (≈10–12 nm) layers. Electrical and TE properties of single ultrathin undoped and doped films, as well as of 5-layer nanolaminates obtained by consecutively deposited doped and undoped layers are investigated and discussed.

2. Results and Discussion

2.1. Structural Characterization of Undoped and Doped Single Ultrathin Films and Nanolaminates

Figure 1 illustrates the representative images of the deposited on quartz substrates Te-doped (Figure 1a) and Sn-doped (Figure 1b) Bi_2Se_3 ultrathin films. 5-layer nanolaminates were

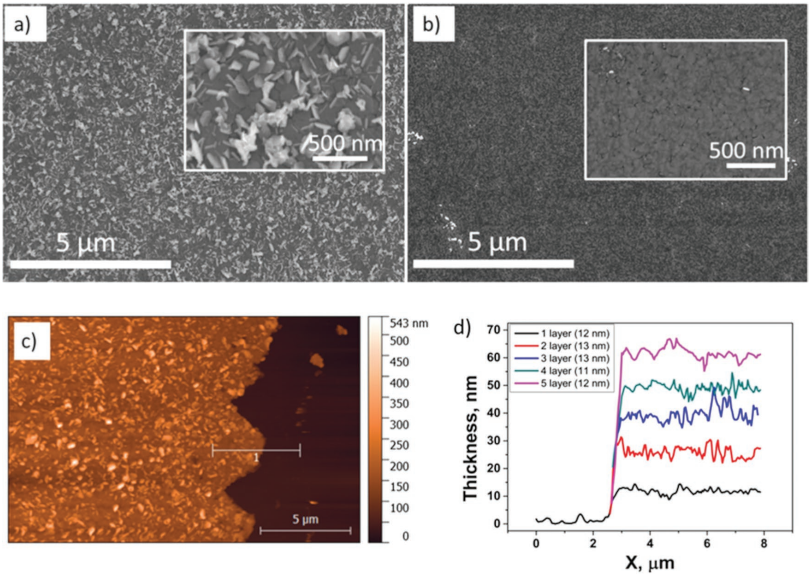

Figure 1. Representative scanning electron microscopy (SEM) images of 10–12 nm thin a) Te-doped and b) Sn-doped Bi_2Se_3 ultrathin films deposited on quartz substrates; insets—closer look on the surfaces of these ultrathin films; c) representative atomic force microscopy (AFM) image of the 5-layer Bi_2Se_3:Te nanolaminate and d) height profiles of each layer of a 5-layer Bi_2Se_3:Sn nanolaminate.

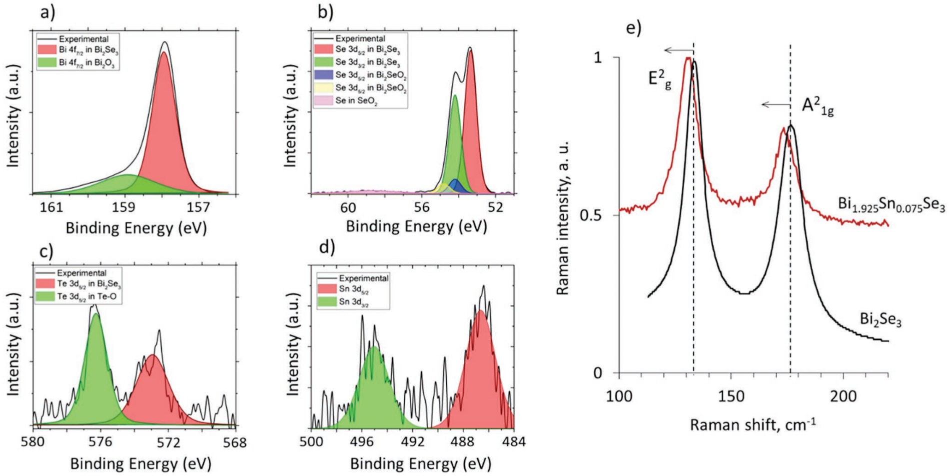

Figure 2. a–d) Representative deconvoluted X-ray photoelectron spectroscopy spectra of $Bi_2Se_{2.975}Te_{0.025}$ and $Bi_{1.925}Sn_{0.075}Se_3$ ultrathin films; e) Raman spectra of Bi_2Se_3 and $Bi_{1.925}Sn_{0.075}Se_3$ ultrathin films.

fabricated by consecutive deposition of 3 undoped (layers No 1, 3, and 5, Figure 1d) and two Sn- or Te- doped layers (layers No 2 and 4, Figure 1d). Depending on the dopant used, the nanolaminates are further in the text referred to as Bi_2Se_3:Sn and Bi_2Se_3:Te.

The concentration of Sn and Te dopants in the Bi_2Se_3 was proved by the energy-dispersive X-ray diffraction which showed chemical composition of doped films within the standard deviation as Bi (≈40 ± 4):Se (≈60 ± 3):Sn (≈1.5 ± 0.5)/Te (≈0.5 ± 0.2) at%. Bi_2Se_3 ultrathin films doped with 1.5 at% of Sn and ≈0.5 at% for Te are further referred to as $Bi_{1.925}Sn_{0.075}Se_3$ and $Bi_2Se_{2.975}Te_{0.025}$. The presence of dopants in the Bi_2Se_3 ultrathin films was confirmed by complementary methods such as Raman and X-ray photoelectron spectroscopy (XPS) spectroscopy (**Figure 2**).

In high resolution Bi 4f and Se 3d spectra of the $Bi_2Se_{2.975}Te_{0.025}$ ultrathin film the peak corresponding to Bi $4f_{7/2}$ is located at 157.9 eV (Figure 2a), while the peaks Se $3d_{5/2}$ and Se $3d_{3/2}$ are located at 53.4 and 54.2 eV respectively (Figure 2b). An additional peak in the Bi 4f spectrum located at 158.9 eV corresponds to the oxidized Bi_2Se_3 arising from the 1–2 nm thin native oxide formed under the air impact.[23] In turn, two low intensity peaks at 54.2 and 54.8 eV in the Se 3d spectra (Figure 2b) may be related to selenium in an elemental or Bi_2SeO_2 environment, while the very low intensity peak located at 59 eV corresponds to the Se in a SeO_2 chemical environment. The obtained data are in good agreement with the previously reported XPS measurements of 13 nm thin Bi_2Se_3 nanosheets.[24] The high-resolution Te 3d spectrum pointed to the presence of Te in Bi_2Se_3 (peak located at 572.9 eV corresponding to Te $3d_{5/2}$, Figure 2c), as well as to the presence of Te in TeO_2 chemical environment (peak located at 576.3 eV). The oxidation of the surface of $Bi_2Se_{2.975}Te_{0.025}$ most likely is related to the sample handling and storage in the air.[25] Presumably, the presence of the ≈1–2 nm thin native oxide on the surface of ultrathin films has no negative effect on their TE properties due to the TE properties of these oxides, comparable with the TE properties the not-oxidized materials.[26,27] Based on the XPS measurements, the chemical composition of the Te-doped Bi_2Se_3 ultrathin film was determined to be Bi (38 ± 4):Se (≈62 ± 4):Te (≈0.6 ± 0.2), which supports the energy-dispersive X-ray diffraction measurements. XPS analysis of $Bi_{1.925}Sn_{0.075}Se_3$ ultrathin film showed the presence of Sn in a concentration ≈1% at% (Bi (36 ± 3):Se (64 ± 4):Sn (1 ± 0.5). High resolution spectra of Sn revealed presence of two bands 486.6 and 495.0 eV corresponding to $3d_{5/2}$ and $3d_{3/2}$, respectively. The bands are considerably shifted from the positions corresponding to metallic Sn (485.2 and 493.9 eV),[28] suggesting that the observed Sn forms bonds within Bi_2Se_3 structure. In addition, Raman spectra obtained for $Bi_{1.925}Sn_{0.075}Se_3$ ultrathin films showed left-shift (Figure 2e) of the Bi_2Se_3 characteristic peaks in comparison with the typical characteristic E^2_g and A^2_{1g} vibration modes of undoped Bi_2Se_3 appearing at the peak positions ≈134 cm^{-1} and ≈177 cm^{-1} (Figure 2e) and consistent with the previous reports for stoichiometric Bi_2Se_3 nanostructures.[29] The left-shift of peak positions of $Bi_{1.925}Sn_{0.075}Se_3$ in comparison with undoped Bi_2Se_3 ultrathin films indirectly proves the substitution of Bi atoms with Sn atoms in the doped material.[30]

2.2. TE Properties of Undoped and Doped Ultrathin Films and Nanolaminates

Values of the Seebeck coefficient indicate n-type conductivity of all Bi_2Se_3-based ultrathin films and nanolaminates (**Table 1**). Properties of the Bi_2Se_3 ultrathin film (Seebeck coefficient −50 µV K^{-1}, resistivity $1.2 \cdot 10^{-5}$ Ω m, PF ≈0.2 mW m^{-1} K^{-2}) at

Table 1. Charge carrier concentration, mobility, electron thermal conductivity, Seebeck coefficient (S), resistivity (ρ), and power factor (PF) of single doped and undoped Bi_2Se_3 ultrathin films and 5-layer nanolaminates at 300 K.

Sample	n, $\times 10^{19}$ cm^{-3}	μ, cm^2 V^{-1} s^{-1}	κ_e, W m^{-1} K^{-1}	S, μV K^{-1}	ρ, $\times 10^{-5}$ Ω m	PF, mW m^{-1} K^{-2}
Single Bi_2Se_3 ultrathin film	2.35 ± 0.05	32.8 ± 0.4	0.52	−50 ± 2	1.20 ± 0.05	0.21 ± 0.02
Single $Bi_{1.925}Sn_{0.075}Se_3$ ultrathin film	3 ± 0.1	21.3 ± 0.6	0.82	−70 ± 3	0.75 ± 0.05	0.65 ± 0.03
Single $Bi_2Se_{2.975}Te_{0.025}$ ultrathin film	2.8 ± 0.6	11.3 ± 2.5	0.016	−68 ± 2	39.5 ± 0.05	0.012 ± 0.003
5-layer Bi_2Se_3:Sn nanolaminate	–	–	0.176	−124 ± 4	3.10 ± 0.05	0.5 ± 0.03
5-layer Bi_2Se_3:Te nanolaminate	–	–	0.08	−153 ± 5	6.7 ± 0.05	0.35 ± 0.02
Ref. Bi_2Se_3 pellets sintered from 13 nm thin sheets[31]	–	–	–	−105	4.3	0.25
Ref. $Bi_{1.925}Sn_{0.075}Se_3$ nanomaterial[24]	1.34	239	0.5	−100	1.6	0.6
Ref. $Bi_2Se_{2.975}Te_{0.025}$ polycrystalline bulk[8]	2.2	209	0.54	−74	1.1	0.45

room temperature are in good agreement with previously reported by our group.[7] Comparison of the properties of Bi_2Se_3 ultrathin films with the properties reported for the bulk nanostructured pellets consisting of sintered 13 nm thin Bi_2Se_3 nanosheets synthesized by solvothermal method[31] showed that the Seebeck coefficient of the former is approximately two times smaller than that of the latter (Table 1). However, the Bi_2Se_3 ultrathin films also showed significantly lower resistivity in comparison with these nanostructured pellets, presumably due to the lower impact of the interfacial charge carrier scattering.[32] This resulted in PF of 0.2 mW m^{-1} K^{-2}, which is similar to the previously reported for the nanostructured pellets PF of 0.25 mW m^{-1} K^{-2} (ref. [31], Table 1).

Doping of the Bi_2Se_3 ultrathin film with low amounts of Sn or Te resulted in an increase of the Seebeck coefficient of the ultrathin films at room temperature by ≈40% from −50 μV K^{-1} for Bi_2Se_3 ultrathin film to ≈−70 μV K^{-1} for both $Bi_{1.925}Sn_{0.075}Se_3$ and $Bi_2Se_{2.975}Te_{0.025}$ ultrathin films (Table 1). Such an increase of the Seebeck coefficient was accompanied by the decrease of the resistivity of the $Bi_{1.925}Sn_{0.075}Se_3$ ≈40% from $1.2\cdot10^{-5}$ Ω m down to $0.75\cdot10^{-5}$ Ω m in comparison with the undoped Bi_2Se_3 film, presumably due to the increase of the charge carrier concentration from $2.35\cdot10^{19}$ cm^{-3} to $3\cdot10^{19}$ cm^{-3} (Table 1) as a result of the Sn doping, which was previously observed also for the Sn-doped Bi_2Se_3 thin films.[33] This resulted in a significant increase of the PF of the $Bi_{1.925}Sn_{0.075}Se_3$ ultrathin film in comparison with Bi_2Se_3 ultrathin films (0.65 mW m^{-1} K^{-2} versus 0.2 mW m^{-1} K^{-2}, Table 1). The increase of the Seebeck coefficient and simultaneous decrease of the resistivity of the $Bi_{1.925}Sn_{0.075}Se_3$ ultrathin film may also indicate the formation of the RL in the Bi_2Se_3 band gap, and thus, optimal Sn dopant concentration for the enhancement of the PF of Bi_2Se_3 ultrathin films.

In contrast, despite the increase of the charge carrier concentration from $2.35\cdot10^{19}$ cm^{-3} to $2.8\cdot10^{19}$ cm^{-3} (Table 1), the resistivity of the $Bi_2Se_{2.975}Te_{0.025}$ increased by ≈30 times in comparison with undoped Bi_2Se_3 ultrathin film, resulting in significant decrease of the resulting PF (0.01 mW m^{-1} K^{-2} for $Bi_2Se_{2.975}Te_{0.025}$ vs 0.2 mW m^{-1} K^{-2} for Bi_2Se_3, Table 1). Such decrease in the electrical conductivity upon introduction of Te in the Bi_2Se_3 ultrathin film may be related to a significant decrease of charge carrier mobility from ≈33 cm^2 V^{-1} s^{-1} down to ≈11.3 cm^2 V^{-1} s^{-1} (Table 1) due to the enhanced scattering at the introduced point defects caused by the different mass and size between Te and Se atoms.[8] Comparison calculated from the experimental data electron thermal conductivities κ_e of the single ultrathin films showed that while κ_e of the undoped and Sn-doped ultrathin films are close to the values reported for nanomaterials of the same chemical compositions, the κ_e of $Bi_2Se_{2.975}Te_{0.025}$ single ultrathin film (0.016 W m^{-1} K^{-1}) was ≈33 times lower in comparison with the κ_e values for the Bi_2Se_3 ultrathin film and Te-doped polycrystalline bulk material (0.54 W m^{-1} K^{-1}) (Table 1). Presumably, the lower values of κ_e of the $Bi_2Se_{2.975}Te_{0.025}$ in comparison with $Bi_{1.925}Sn_{0.075}Se_3$ and Bi_2Se_3 ultrathin films may be related to the difference in morphologies of these ultrathin films (Figure 1a,b), resulting in more pronounced electron scattering at the boundaries between the randomly oriented nanostructures, composing the $Bi_2Se_{2.975}Te_{0.025}$ ultrathin films.

The 5-layer Bi_2Se_3:Sn and Bi_2Se_3:Te nanolaminates showed an increase of the Seebeck coefficient by 75 and 125% in comparison with the single ultrathin films, and significantly higher in comparison with the Seebeck coefficient values reported for bulk nanostructured materials of similar compositions (Table 1). Most likely, the increase of the Seebeck coefficient is related to the phonon scattering and carrier filtering at the inner interfaces between the layers in the nanolaminates.[34] Simultaneously, the resistivity of the Bi_2Se_3:Sn nanolaminate increased by ≈2 times, while the resistivity of the Bi_2Se_3:Te nanolaminate decreased by approximately five times in comparison with single doped films (Table 1). Increase of the resistivity of the Bi_2Se_3:Sn nanolaminate presumably may be related to the significant electrical resistance of grain and interlayer boundaries in it.[35] In turn, decrease in the resistivity of the Bi_2Se_3:Te nanolaminate may be related to the presence of Te atoms with low electronegativity at the interfaces between the nanolaminate layers as Te atoms preferentially substitute Se atoms in the outer atomic sheets of Bi_2Se_3 quintuple layers.[12,36] Consequently, the PF of the Bi_2Se_3:Sn nanolaminate was found to be slightly lower than the PF of $Bi_{1.925}Sn_{0.075}Se_3$ ultrathin film, while the PF of the Bi_2Se_3:Te showed a dramatic increase by 35 times in comparison with the $Bi_2Se_{2.975}Te_{0.025}$ ultrathin film (Table 1). Calculated from the experimental data, electron thermal conductivity κ_e of both types on Bi_2Se_3-based nanolaminates was also found to be significantly reduced in comparison with the κ_e reported for nanostructured bulk materials of similar chemical compositions (Table 1), presumably due to the electron scattering/filtering at the interfaces between the nanolaminate layers, as well as at the boundaries between the nanostructures, composing the layers. Reduced contribution of κ_e to the total thermal conductivity κ_{tot} of the nanolaminates may result in an increase of ZT of these materials in comparison with their nanostructured bulk counterparts, which makes the nanolaminates perspective for application in thin films TE generators.

3. Conclusions

In summary, PVD method was applied for deposition of single Bi_2Se_3, $Bi_{1.925}Sn_{0.075}Se_3$, and $Bi_2Se_{2.975}Te_{0.025}$ ultrathin films of average thickness 10–12 nm, and for consecutive deposition of alternating doped and undoped layers for fabrication of 5-layer nanolaminates employing Sn- or Te-doped layers. To the best of knowledge, thermoelectrical properties of PVD-deposited 5-layer n-type nanolaminates were studied for the first time. It was found that the Seebeck coefficient of both types of nanolaminates increases by ≈75–125% and the calculated from the experimental data electron thermal conductivity κ_e decreases by 65–85% in comparison with the single ultrathin films and the values reported for the nanostructured bulk materials of similar chemical compositions, presumably due to the filtering and scattering of the charge carriers at the interfaces between the nanolaminate layers. Although the electrical resistivity of the nanolaminates was 3–6 times higher in comparison with the data reported for the nanostructured bulk materials of similar chemical compositions, resulting in power factors, not exceeding these of the nanostructured bulk materials, the reduced contribution of electron thermal conductivity of the nanolaminates to their total thermal conductivity points to significant potential of PVD-deposited nanolaminates for the applications in thin film TE devices.

4. Experimental Section

Sample Preparation: Deposition of ultrathin undoped and doped ultrathin films and fabrication of nanolaminates. The thin films were deposited using single-zone quartz tube furnace GCL-1100X (MTI Corp.) using PVD method initially developed for deposition of Bi_2Se_3 nanowires[37] and further modified for deposition of ultrathin films.[7,38,39] Bismuth (Bi) (≥99.99%, CAS: 7440-69-9, Sigma Aldrich) and selenium (Se) (99+, CAS: 7782-49-2, Emsure) powders were used as basic source materials. Tin (Sn) (99.998%, CAS: 7440-31-5, Sigma Aldrich) and Tellurium (Te) (99.999%, CAS: 13494-80-9, Alfa Aesar) were used as dopants. Evaporation temperatures were 500 °C for Bi and Te, and 480 °C for Se. The substrate fused quartz 2 cm × 2 cm × 1 mm (Agar Scientific) was washed in 2-propanol and distilled water and placed downstream from the source materials located in the central area of the furnace tube. After the placement of the source materials and the substrate, the furnace tube was ventilated with nitrogen flow and pumped down to the base pressure of 150 mTorr, which was kept constant during the deposition process. The heating rate of the source materials was 48 $°C\ min^{-1}$. The maximal substrate temperature during the deposition process was 400 °C. For the deposition of Bi_2Se_3, the furnace was held at maximal source materials evaporation temperature for 1 min, followed by natural cooling down to the room temperature. For the deposition of Sn-doped Bi_2Se_3 films, the dopant source was prepared by thermal evaporation of Sn layer of size 3 mm × 3 mm × 1 nm on a quartz substrate, which was placed together with the Bi source material. For the deposition of Te-doped ultrathin Bi_2Se_3 films, the 0.8 mg of the dopant source in a form of powder was placed together with the Se source material. The amount of dopant in the ultrathin film was controlled by the amount of the source dopant. For the deposition of nanolaminates, consecutive syntheses were performed, where the deposition of a doped ultrathin film on the surface of previously deposited undoped ultrathin film after its cool-down.

Structural Characterization: Morphology, thickness, and structure of the deposited thin films were inspected using field emission SEM Hitachi S-4800 and AFM Asylum Research MFP-3D. XPS analyses were carried out using ThermoFisher ESCALAB Xi+ instrument using monochromatic Al Kα X-ray source. The instrument binding energy scale was calibrated to give a binding energy at 932.6 eV for Cu $2p_{3/2}$ line of freshly etched metallic copper. The charge compensation system was used on all non-conductive specimen samples. The surface of each sample was irradiated with a flood of electrons to produce nearly neutral surface charge. The spectra were recorded by using an X-ray beam size 900 × 10 microns, a pass energy of 20 eV, and step size 0.1 eV. Data from all materials have been referenced using the main signal of the carbon 1s spectrum assigned to occur at 285.0 eV. The carbon 1s spectrum was collected using high energy resolution settings.

Raman spectra were recorded at room temperature using scanning laser confocal micro-Raman spectrometer Confotec NR 500 with 785 nm excitation wavelength, 0.86 mW power, 100× objective and spectral resolution ≈0.2 cm^{-1}, and by TriVista CRS Confocal Raman Microscope system equipped with triple spectrometer setup (750 mm focal length) and cooled CCD camera, with 532 nm excitation wavelength, 0.5 mW power and the ultimate resolution of the spectrometer ≈0.1 cm^{-1}.

Electrical and TE Characterization: Resistance and Seebeck coefficient of the thin films were measured at room temperature using thermal transport option of physical property measurement system (PPMS) DynaCool9T (Quantum Design) in 4-point configuration for elimination of the influence of contact resistance, and MultiVu software. The sample size was 15 mm × 5 mm, with the 7 mm distance between the inner electrodes, as described elsewhere.[40] For determination of Seebeck coefficient, the temperature difference between the sides of the thin films did not exceed 3% from the measurement temperature.

Hall mobility and sheet resistance were measured using electron transport option of the PPMS at magnetic field values from −9T to +9T. For these measurements, square samples of 10 mm × 10 mm were prepared and supplied by Cr (5 nm)/Au (70 nm) electrodes in the Van der Pauw configuration. The measurements were carried out following the methodology described by Werner et al.[41]

Determination of Thermal Conductivity: The total thermal conductivity of the material κ_{tot} was the sum of contributions of lattice (phonon) thermal conductivity κ_L and electron thermal conductivity κ_e. The ultrathin films and nanolaminates were deposited on the quartz glass substrates without the lift-off possibility, thus, the direct measurement of the total thermal conductivity using the PPMS system was not possible as the main contribution to the measured κ_{tot} of the sample would be from the quartz substrate. The contribution of the electron thermal conductivity κ_e to the total thermal conductivity was evaluated using the Wiedemann–Franz law: $\kappa_e = L\sigma T$, where L is the Lorentz number, σ is the electrical conductivity, and T is the absolute temperature. For the most materials with metallic type of conductance, L equals to $2.44 \cdot 10^{-8}$ ($W\ \Omega\ K^{-2}$). However, for the considered in this work materials having charge carriers between non-degenerate and degenerate states,[42] the use of the above value of L can result in errors of up to 40%.[43] Thus, for the estimation of L the equation proposed by Kim et al.[44] was used: $L = 1.5 + \exp(-|S|/116)$, where S was the experimentally determined Seebeck coefficient of the material.

Statistical Analysis: The resistance and Seebeck coefficient of the samples was calculated as the mean of 5 consecutive measurements (± standard deviation (SD) estimated from these 5 measurements). The values of the Hall resistance at each magnetic field value correspond to the average of 50–250 measurements, depending on the stability of the measurement, determined prior to the measurement. Charge carrier mobility was calculated using weighted linear regression of the normalized Hall resistance and magnetic field strength in RStudio, using the inverse standard deviation of the data point as statistical weights. Error propagation was considered using the general formula for error propagation.

Supporting Information

Supporting Information is available from the Wiley Online Library or from the author.

Acknowledgements

This work was funded by the ERDF project 1.1.1.2/1/16/037. A.S. and J.G. acknowledge the support from the European Union's Horizon 2020 Framework Programme H2020-WIDESPREAD-01-2016-2017-TeamingPhase2 under grant agreement No. 739508, project CAMART^2.

Conflict of Interest

The authors declare no conflict of interest.

Data Availability Statement

The data that support the findings of this study are available from the corresponding author upon reasonable request.

Keywords

bismuth selenide, doping, nanolaminate, physical vapor deposition, thermoelectric properties, ultrathin films

Received: February 21, 2022
Revised: May 22, 2022
Published online: June 27, 2022

---

[1] R. He, G. Schierning, K. Nielsch, *Adv. Mater. Technol.* **2018**, *3*, 1700256.
[2] S. Yang, P. Qiu, L. Chen, X. Shi, *Small Sci.* **2021**, *1*, 2100005.
[3] J. R. Sootsman, D. Y. Chung, M. G. Kanatzidis, *Angew. Chem., Int. Ed.* **2009**, *48*, 8616.
[4] Y. L. Chen, J. G. Analytis, J. Chu, Z. K. Liu, S. Mo, X. L. Qi, H. J. Zhang, D. H. Lu, X. Dai, Z. Fang, S. C. Zhang, I. R. Fisher, Z. Hussain, Z. Shen, *Science* **2009**, *325*, 178.
[5] H. Zhang, C. X. Liu, X. L. Qi, X. Dai, Z. Fang, S. C. Zhang, *Nat. Phys.* **2009**, *5*, 438.
[6] Q. Liu, C. X. Liu, C. Xu, X. L. Qi, S. C. Zhang, *Phys. Rev. Lett.* **2009**, *102*, 156603.
[7] J. Andzane, A. Felsharuk, A. Sarakovskis, U. Malinovskis, E. Kauranens, M. Bechelany, K. A. Niherysh, I. V. Komissarov, D. Erts, *Mater. Today Energy* **2020**, *19*, 100587.
[8] R. Liu, X. Tan, G. Ren, Y. Liu, Z. Zhou, C. Liu, Y. Lin, C. Nan, *Crystals* **2017**, *7*, 257.
[9] J. Andzane, K. Buks, M. N. Strakova, M. Zubkins, M. Bechelany, M. Marnauza, M. Baitimirova, D. Erts, *IEEE Trans. Nanotechnol.* **2019**, *18*, 948.
[10] R. J. Mehta, Y. Zhang, H. Zhu, D. S. Parker, M. Belley, D. J. Singh, R. Ramprasad, T. Borca-Tasciuc, G. Ramanath, *Nano Lett.* **2012**, *12*, 4523.
[11] J. U. Lee, D. H. Lee, B. Kwon, D. Bin Hyun, S. Nahm, S. H. Baek, J. S. Kim, *J. Electron. Mater.* **2015**, *44*, 1926.
[12] B. Wiendlocha, *J. Electron. Mater.* **2016**, *45*, 3515.
[13] G. Chen, *J. Heat Transfer* **1997**, *119*, 220.
[14] G. Chen, C. L. Tien, *J. Thermophys. Heat Transfer* **1993**, *7*, 311.
[15] X. Chen, H. Baumgart, *Materials* **2020**, *13*, 1283.
[16] G. Kunakova, L. Galletti, S. Charpentier, J. Andzane, D. Erts, F. Léonard, C. D. Spataru, T. Bauch, F. Lombardi, *Nanoscale* **2018**, *10*, 19595.
[17] L. D. Hicks, M. S. Dresselhaus, *Phys. Rev. B* **1993**, *47*, 8.
[18] P. Ghaemi, R. S. K. Mong, J. E. Moore, *Phys. Rev. Lett.* **2010**, *105*, 166603.
[19] M. Tahir, A. Manchon, U. Schwingenschlögl, *J. Appl. Phys.* **2014**, *116*, 093708.
[20] J. Zhang, X. Feng, Y. Xu, M. Guo, Z. Zhang, Y. Ou, Y. Feng, K. Li, H. Zhang, L. Wang, X. Chen, Z. Gan, S. C. Zhang, K. He, X. Ma, Q. K. Xue, Y. Wang, *Phys. Rev. B: Condens. Matter Mater. Phys.* **2015**, *91*, 075431.
[21] M. Guo, Z. Wang, Y. Xu, H. Huang, Y. Zang, C. Liu, W. Duan, Z. Gan, S. C. Zhang, K. He, X. Ma, Q. Xue, Y. Wang, *New J. Phys.* **2016**, *18*, 015008.
[22] H. Osterhage, J. Gooth, B. Hamdou, P. Gwozdz, R. Zierold, K. Nielsch, *Appl. Phys. Lett.* **2014**, *105*, 123117.
[23] D. Kong, J. J. Cha, K. Lai, H. Peng, J. G. Analytis, S. Meister, Y. Chen, H. J. Zhang, I. R. Fisher, Z. X. Shen, Y. Cui, *ACS Nano* **2011**, *5*, 4698.
[24] M. Li, Y. Zhang, T. Zhang, Y. Zuo, K. Xiao, J. Arbiol, J. Llorca, Y. Liu, A. Cabot, *Nanomaterials* **2021**, *11*, 4.
[25] D. Erts, J. Katkevics, M. Sjomkane, J. Andzane, A. Sarakovskis, K. Smits, A. Viksna, Y. Rublova, R. Meija, *Nano-Struct. Nano-Objects* **2022**, *30*, 100847.
[26] R. A. Horne, *J. Appl. Phys.* **1959**, *30*, 393.
[27] X. Tan, Y. Liu, K. Hu, G. Ren, Y. Li, R. Liu, Y. H. Lin, J. L. Lan, C. W. Nan, *J. Am. Ceram. Soc.* **2018**, *101*, 326.
[28] F. Lu, X. Ji, Y. Yang, W. Deng, C. E. Banks, *RSC Adv.* **2013**, *3*, 18791.
[29] J. Zhang, Z. Peng, A. Soni, Y. Zhao, Y. Xiong, B. Peng, J. Wang, M. S. Dresselhaus, Q. Xiong, *Nano Lett.* **2011**, *11*, 2407.
[30] C. C. Wang, F. S. Shieu, H. C. Shih, *Nanomaterials* **2021**, *11*, 1352.
[31] M. Hong, Z. G. Chen, L. Yang, G. Han, J. Zou, *Adv. Electron. Mater.* **2015**, *1*, 1500025.
[32] A. J. Minnich, M. S. Dresselhaus, Z. F. Ren, G. Chen, *Energy Environ. Sci.* **2009**, *2*, 466.
[33] G. M. Stephen, I. Naumov, S. Tyagi, O. A. Vail, J. E. Demell, M. Dreyer, R. E. Butera, A. T. Hanbicki, P. J. Taylor, I. Mayergoyz, P. Dev, A. L. Friedman, *J. Phys. Chem. C* **2020**, *124*, 27082.
[34] A. Nadtochiy, V. Kuryliuk, V. Strelchuk, O. Korotchenkov, P. W. Li, S. W. Lee, *Sci. Rep.* **2019**, *9*, 16335.
[35] J. J. Kuo, M. Wood, T. J. Slade, M. G. Kanatzidis, G. J. Snyder, *Energy Environ. Sci.* **2020**, *13*, 1250.
[36] T. Lei, K. H. Jin, N. Zhang, J. L. Zhao, C. Liu, W. J. Li, J. O. Wang, R. Wu, H. J. Qian, F. Liu, K. Ibrahim, *J. Phys.: Condens. Matter* **2016**, *28*, 255501.
[37] J. Andzane, G. Kunakova, S. Charpentier, V. Hrkac, L. Kienle, M. Baitimirova, T. Bauch, F. Lombardi, D. Erts, *Nanoscale* **2015**, *7*, 15935.
[38] J. Andzane, L. Britala, E. Kauranens, A. Neciporenko, M. Baitimirova, S. Lara-Avila, S. Kubatkin, M. Bechelany, D. Erts, *Sci. Rep.* **2019**, *9*, 4791.
[39] M. Baitimirova, J. Andzane, G. Petersons, R. Meija, R. Poplausks, M. Romanova, D. Erts, *J. Mater. Sci.* **2016**, *51*, 8224.
[40] K. Buks, J. Andzane, L. Bugovecka, M. V. Katkov, K. Smits, O. Starkova, J. Katkevics, A. Bērziņš, L. Brauna, V. Voikiva, D. Erts, *Adv. Mater. Interfaces* **2022**, 2200318.

Paper V

nanomaterials

MDPI

Article

Low-Vacuum Catalyst-Free Physical Vapor Deposition and Magnetotransport Properties of Ultrathin Bi_2Se_3 Nanoribbons

Raitis Sondors [1,†], Kiryl Niherysh [1,†], Jana Andzane [1], Xavier Palermo [2], Thilo Bauch [2], Floriana Lombardi [2] and Donats Erts [1,3,*]

[1] Institute of Chemical Physics, University of Latvia, LV-1586 Riga, Latvia
[2] Quantum Device Physics Laboratory, Department of Microtechnology and Nanoscience, Chalmers University of Technology, 41296 Gothenburg, Sweden
[3] Faculty of Chemistry, University of Latvia, LV-1586 Riga, Latvia
* Correspondence: donats.erts@lu.lv
† These authors contributed equally to this work.

Abstract: In this work, a simple catalyst-free physical vapor deposition method is optimized by adjusting source material pressure and evaporation time for the reliable obtaining of freestanding nanoribbons with thicknesses below 15 nm. The optimum synthesis temperature, time and pressure were determined for an increased yield of ultrathin Bi_2Se_3 nanoribbons with thicknesses of 8–15 nm. Physical and electrical characterization of the synthesized Bi_2Se_3 nanoribbons with thicknesses below 15 nm revealed no degradation of properties of the nanoribbons, as well as the absence of the contribution of trivial bulk charge carriers to the total conductance of the nanoribbons.

Keywords: bismuth selenide; ultrathin nanoribbons; bulk-free topological insulator; catalyst-free physical vapor deposition; magnetotransport properties

check for updates

Citation: Sondors, R.; Niherysh, K.; Andzane, J.; Palermo, X.; Bauch, T.; Lombardi, F.; Erts, D. Low-Vacuum Catalyst-Free Physical Vapor Deposition and Magnetotransport Properties of Ultrathin Bi_2Se_3 Nanoribbons. *Nanomaterials* **2023**, *13*, 2484. https://doi.org/10.3390/nano13172484

Academic Editor: Zhidong Zhang

Received: 29 July 2023
Revised: 26 August 2023
Accepted: 31 August 2023
Published: 3 September 2023

1. Introduction

Bismuth selenide (Bi_2Se_3) is a semiconducting material that belongs to the 3D topological insulators (3D TIs) [1–3]. The properties of Bi_2Se_3 nanostructures have been extensively studied for potential applications in a variety of fields, including spintronic devices [4,5], sensors [6–8], photodetectors [9–11], battery electrodes [12–14], as well as thermoelectric [15–19] and nanoelectromechanical devices [16]. While unique surface states have made Bi_2Se_3 an attractive candidate for the realization of various quantum phenomena, they are often masked by the contribution of bulk charge carriers [20]. It has been reported that the bulk conductivity of TIs was successfully suppressed by introducing chemical compensating dopants into nanostructures [21–23]. However, due to scattering on dopant impurities in such doped materials, the mobility of charge carriers often does not exceed ~500 $cm^2 \cdot (Vs)^{-1}$ [23,24]. Thus, undoped Bi_2Se_3 nanostructures as ultrathin films, nanoribbons (elongated nanostructures with a rectangular cross-section in which the width is much larger than the thickness) [3,25] and nanoplates are great candidates for the effective utilization of their topological surface states due to the high surface-to-volume ratio, suppressing the bulk charge carriers [26] and high mobility.

On the other hand, the use of TIs nanoplates, nanowires, and nanoribbons in various types of electrical applications requires the transfer of the nanostructures to a dielectric substrate. While applying an electrostatic field via gate electrode to the TI-based device, the additional carriers dope the nanostructure, forming an accumulation layer at the dielectric–topological insulator interface. As a result, the energy band bending effect occurs [22]. The depth of the accumulation layer D can be estimated by solving Poisson equation in the full depletion approximation to yield $D = (2\kappa\varepsilon_0\Delta E/(e^2 n))^{-1/2}$ [22,24], where κ is the dielectric permittivity, ΔE is the shift of Fermi energy across the bang-bending region due to the applied gate voltage ($\Delta E \leq$ 100–300 meV (TIs bandgap [27])), and n is the carrier density. The values of the accumulation layer depth ranging from 10 to 35 nm for samples with carrier density n ~10^{19} cm^{-3} were reported in the literature [22–24,28–32]. To fully suppress bulk conduction, the sample thickness should be smaller than D so that the gate can effectively modulate the charge carrier density of the entire sample. Considering the slight variation of carrier density between the nanoribbons, as well as the non-ideality in the samples, such as compositional inhomogeneity and the possible presence of the defect states, the thickness of 15 nm can be chosen as a top limit reference for optimizing growth parameters in order to achieve an increased yield of such nanoribbons. In addition, some unique effects, such as the formation of a hybridization gap, resulting in the disengaging of electrical and thermal conductance, may occur in topological insulators with thickness reduced below 10 nm [33].

The physical vapor deposition (PVD) method is attractive for the synthesis of Bi_2Se_3 nanoribbons due to its simplicity and easily adjustable synthesis parameters such as partial pressure of vaporized source material, heating and deposition time and rate, substrate temperature, which make it an ideal candidate for high-yield synthesis of chemically pure nanostructures. Another advantage of the catalyst-free PVD is no need for expensive single-crystalline substrates. Previously, the successful synthesis of Bi_2Se_3 nanoribbons has been demonstrated via catalyst-free [34,35] and catalyst-assisted [36–38] PVD techniques. Both catalyst-free and catalyst-assisted methods allowed for freestanding Bi_2Se_3 nanoribbons to be obtained, permitting their easy handling and transfer to the desired substrates and positions [26,34,36]. However, the thicknesses of the vast majority of these nanoribbons ranged from ~20 to ~100 nm, with a negligible number of nanoribbons with thicknesses below 15 nm [39]. The nanoribbon thicknesses above 20 nm are too large for utilizing TI properties of the nanoribbons as the increased thickness increases the contribution of bulk conductivity. In turn, the use of the ultrathin nanoribbons obtained in these syntheses is complicated by their extremely small number. Previously, our group reported strong gate tunability of the Fermi level (ambipolar transport) for a 9 nm-thick Bi_2Se_3 nanoribbon occasionally formed during the catalyst-free physical vapor deposition [38]. These findings became a trigger for the optimization of the synthesis process to achieve an increased yield of ultrathin nanoribbons.

In the present work, the main parameters (synthesis temperature, time, and vapor pressure) of previously developed catalyst-free physical vapor deposition method for the obtaining of freestanding Bi_2Se_3 nanoribbons [34] were systematically optimized to achieve the outcome of the Bi_2Se_3 nanoribbons with thicknesses below 15 nm. The optimum parameters were determined for maximizing the yield of ultrathin nanoribbons. To reveal their topological states, magnetotransport properties were investigated for the ultrathin ($\leq$15 nm) Bi_2Se_3 nanoribbons obtained using the optimized synthesis parameters.

2. Materials and Methods

2.1. Synthesis of Bi_2Se_3 Nanoribbons

Bi_2Se_3 nanoribbons were synthesized via catalyst-free physical vapor deposition, similarly as reported in [34] in a GSL-1100X tube furnace (length 60 cm, diameter 46 mm) (MTI Corporation, Richmond, CA, USA). The calibration curve for the temperature profile along the furnace tube was taken prior to the synthesis of the Bi_2Se_3 nanostructures under the same conditions (temperature, time, and pressure) as for the synthesis of the nanostructures using a K-type thermocouple installed in the flange of the furnace tube and allowing to monitor the temperature in different locations inside it. The pressure inside the furnace tube was measured using NIST Traceable Digital Convection Vacuum Gauge (Stinger, InstruTech, Inc., Longmont, CO, USA), which passed the certified calibration for direct readout of nitrogen. The maximum expected error for the pressure readout does not exceed 0.1 Torr). Bi_2Se_3 flakes (99.999%, Sigma Aldrich, St. Louis, MO, USA) were used as the source material, and 25 × 75 mm glass microscope slides were used as the substrate. 90 mg of the source material was placed in the center of the tube furnace, where the temperature during the synthesis reached 585 °C. The substrate was placed downstream from the source material in a zone where the temperature (based on the calibration curve) during the synthesis reaches 320 °C at the cold side of the substrate to 450 450 °C at the hot side of the substrate. The temperature in the center of the substrate during the synthesis was 400–410 °C. The furnace tube was first flushed with N_2 gas for 5 min to create an inert atmosphere. The initial temperature in all syntheses was 25 °C. The furnace heating rate from the room temperature to 575–590 °C was ~12.5 °C/min (45 min). The start pressure in the furnace tube varied from 0.1 to 18 Torr. During the deposition process, the furnace was kept at a temperature of 575–590 °C for a time ranging from 0 up to 30 min, after which the furnace heater was turned off to cool down naturally. After the temperature in the furnace center had decreased to 540 °C, an N_2 gas flow was introduced with a dynamic pressure of ~25 Torr. After the temperature had decreased to 475 °C, the flow was terminated, and the tube was rapidly filled with N_2 to an atmospheric pressure.

2.2. Characterization of Morphology of Bi_2Se_3 Nanoribbons

Field emission scanning electron microscope (SEM, Hitachi S-4800, Hitachi Ltd., Chiyoda, Tokyo, Japan) equipped with an energy-dispersive X-ray (EDX) analyzer Bruker XFLASH 5010 (Bruker Corporation, Billerica, MA, USA) was used for the inspection of morphology and chemical composition of nanostructures grown on the substrate. The as-grown Bi_2Se_3 nanoribbons were mechanically transferred from the glass substrate to flat Si substrates, and an atomic force microscope (AFM, Bruker Dimension ICON, Bruker Corporation, Billerica, MA, USA) was used to measure the thicknesses of more than 1000 individual Bi_2Se_3 nanoribbons. The *R* language for statistical computing was used for data analysis and visualization [40].

2.3. Magnetotransport Measurements

Electron beam lithography (JEOL JBX 9300FS, JEOL Ltd., Akishima, Tokyo, Japan), Ar-ion beam etching (Oxford Ionfab 300 Plus, Oxford Instruments, Abington, UK) and vacuum evaporator (Lesker PVD 225, Kurt J. Lesker Company, Pittsburgh, PA, USA) were used to create electrical contacts to individual nanoribbons. Magnetotransport measurements were performed in the four-terminal configuration using the physical property measurement system (Quantum Design DynaCool (14T), Quantum Design, Inc., San Diego, CA, USA) in the temperature range 2–300 K.

3. Results and Discussion

3.1. Optimization of Synthesis Parameters for Obtaining Ultrathin Bi_2Se_3 Nanoribbons

As reported previously [34], the growth of the Bi_2Se_3 nanoribbons during the catalyst-free vapor-solid deposition is initiated by the temporary N_2 gas flow, which is introduced in the furnace tube during the cooling stage. The real-time temperature profiles in the center of the furnace tube and in the center of the substrate during the synthesis and at the moment of N_2 flow introduction are shown in Figure 1a. Later, it was demonstrated in [41] that the growth of the Bi_2Se_3 nanoribbons in the catalyst-free PVD process occurs from the edges of the Bi_2Se_3 nanoplates seeds (Figure 1a, inset). The stoichiometry of the obtained nanoribbons was confirmed by the EDX analysis, showing a Bi:Se proportion of 37 ± 3 (Bi):62 ± 4 (Se). The representative AFM image and related height profiles illustrate the rectangular cross-section of the nanoribbon with the width exceeding the thickness of the nanoribbon by a factor of ~13 (Figure 1b). Height profiles obtained at three different positions across the nanoribbon match well with each other, indicating uniform shape and thickness of the nanoribbon's cross-section.

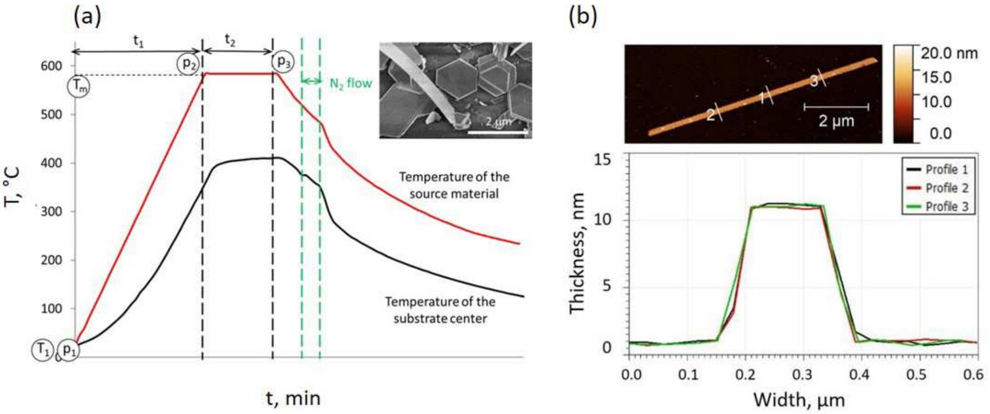

Figure 1. (**a**) An example of temperature profiles measured in real-time prior to the synthesis of Bi_2Se_3 nanostructures under the same conditions (temperature, time, and pressure) as for the synthesis of the nanostructures: at the center of the furnace (location of the Bi_2Se_3 source material—solid red line) and at the center of the substrate (the region where the stoichiometric Bi_2Se_3 nanoribbons are obtained—solid black line); Inset—secondary electron SEM image of a Bi_2Se_3 nanoribbon growing from the edge of Bi_2Se_3 nanoplate-seed; (**b**) atomic force microscope image of ~10 nm thin Bi_2Se_3 nanoribbon (top) and height profiles at three different positions demonstrating an identical shape and thickness of the cross-section of the nanoribbon (bottom).

The growth of the Bi_2Se_3 nanoribbons from the edges of the nanoplates can be explained by the Bi_2Se_3 deposition kinetics. As Bi_2Se_3 is a highly anisotropic layered material, its growth occurs much faster in the lateral direction (perpendicular to the crystallographic *c*-axis) compared to the vertical. As the top and bottom surfaces of the Bi_2Se_3 nanoplates are chemically saturated with selenium [42], the Bi and Se adatoms cannot form covalent bonds with the atoms on the surface and diffuse to the edges of the growing nanoplate, having a number of dangling bonds. Without the carrier gas flow, the growth of the Bi_2Se_3 nanoplates is a result of a natural diffusion of the vaporized source material to the substrate and following the motion of the adatoms to the energetically favorable edges of the nanoplates. This leads to the formation of symmetrical nanoplates or stacks of nanoplates (Figure 1a, inset). However, the introduction of the N_2 gas flow provides a rapid increase in the concentration of the evaporated source material near the substrate, accompanied by the change of the temperature gradient along the substrate due to the approaching hot carrier gas from the center of the furnace tube (Figure 1a, black solid line) as well as an insignificant change of the temperature of the source material (Figure 1a, red solid line). The introduction of the gas flow results in directed diffusion of the adatoms, leading to a much faster growth rate in the N_2 flow direction and to the formation of long crystalline nanoribbons starting from the edge of the nanoplates [41]. The rapid decrease in the temperature after the N_2 gas flow is turned off (Figure 1a) is related to the filling of the furnace tube with N_2 up to atmospheric pressure for the termination of the nanoribbon growth process. The thickness of the nanoribbons is most likely determined by the thickness of the nanoplates or, in the case of a step-like structure of the nanoplates, by the thickness of the step. In turn, the growth rate and, consequently, the thickness of the nanoplates/nanoplate steps depend on the amount and diffusion rate of the vaporized source material. The rate of evaporation can be approximated by the Hertz–Knudsen evaporation equation [43]:

$$\frac{dN}{dt} = \frac{\alpha_e N_A (p_e - p_h)}{\sqrt{2\pi MRT}},$$

where N—number of evaporated atoms per surface area, t—time, α_e—the coefficient of evaporation, N_A—Avogadro number, p_e—equilibrium pressure, p_h—hydrostatic pressure, M—molecular weight of the evaporated species, R—is universal gas constant, T—absolute temperature. Considering the constant initial mass of the source material and its heating rate in all syntheses, the amount and diffusion rate of the vaporized source Bi_2Se_3 is governed by the three variable parameters of the synthesis: maximal heating temperature of the source material T_m (Figure 1a), the initial pressure in the furnace tube p_1 (Figure 1a), which determines the pressure p_2 at the end of the heating stage (Figure 2a), and time t_2, during which the source material is kept at T_m (Figure 1a). In the synthesis process, t_2 determines the pressure p_3 at the end of the heating stage (Figures 1a and 2b).

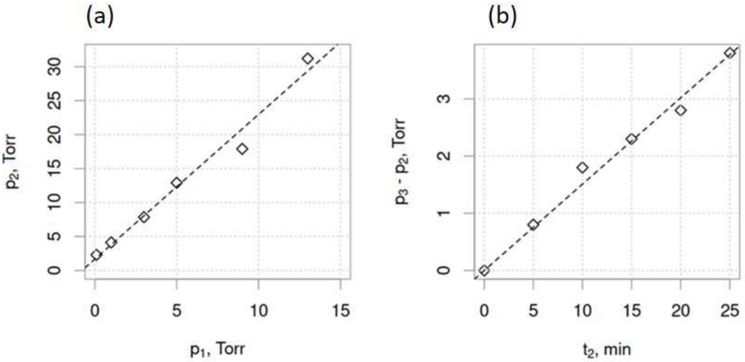

Figure 2. Charts illustrating relation between the (**a**) pressure p_2 at the end of the furnace heating to maximal synthesis temperature and the initial pressure p_1, and (**b**) between the heating time t_2 of the source material at maximal temperature T_m and the pressure increase during the t_2 time. All p_1, p_2, and p_3 measurement errors did not exceed 1% of the measured value.

In the previously demonstrated syntheses of the Bi_2Se_3 nanoribbons on glass [34,39] and anodized alumina [41] substrates, these parameters were T_m = 585 °C, p_1 = 0.5–5 Torr and t_2 = 15 min. The syntheses based on these parameters resulted in the formation of free-standing nanoribbons with thicknesses starting from 7–9 nm [39] and up to 100 nm [34,39,41] within one batch of nanoribbons. However, the vast majority of the Bi_2Se_3 nanoribbons had thicknesses between 25 nm [26] and 80 nm [41], with the number of ultrathin nanoribbons being negligible, which makes their use for practical applications extremely challenging.

To optimize the synthesis parameters to reach a sufficient outcome of the Bi_2Se_3 nanoribbons with reduced thicknesses, the parameters T_m, p_1 and t_2 were varied in the ranges 575–590 °C, 0.1–18 Torr and 0–30 min, respectively, to determine the optimal growth conditions for the nanoribbons with thicknesses below 25 nm, and especially for obtaining ultrathin nanoribbons with thicknesses below 10–15 nm. The tested synthesis parameters and the outcome of nanoribbons of different thicknesses are summarized in Table 1, with emphasis on the proportions of nanoribbons with thicknesses in the ranges of <10 nm, 10–15 nm, 15–20 nm, 20–25 nm, and >25 nm.

Table 1. Synthesis parameters, percentage of Bi_2Se_3 nanoribbons with thicknesses <10 nm, 10–15 nm, 15–20 nm, 20–25 nm, and >25 nm, and mean thickness (nm). In all experiments, the initial temperature T_1 = 25 °C and heating time t_1 = 45 min.

No.	**Synthesis Parameters:**					**Results:**					
	Temperature [°C]	**Time [min]**	**Pressure [Torr]**			**Nanoribbon Thickness, nm/%**					**Mean Thickness [nm]**
	T_m	**t_2**	**p_1**	**p_2**	**p_3**	**<10**	**10–15**	**15–20**	**20–25**	**>25**	
1.	575	15	5.00	11		0%	0%	0%	0%	100%	52
2.	590	15	5.00	14		Poor quality of nanoribbons: defects in crystal structure					
3	585	30	5.00	12.8	16.2	0%	0%	2.8%	8.5%	88.7%	51
4	585	25	5.00	13.2	17	0%	0%	7.8%	7.7%	84.5%	53
5	585	20	5.00	12.4	15.2	0%	0%	20%	20%	60%	50
6	585	15	5.00	12.4	14.7	0%	2.7%	8%	16%	73.3%	36
7	585	10	5.00	13	14.8	0%	6.3%	18.8%	43.8%	31.1%	38
8	**585**	**5**	**5.00**	**12.3**	**13.1**	**0%**	**18.2%**	**27.3%**	**45.5%**	**9%**	**27**
9	**585**	**0**	**5.00**	**12.9**	**—**	**1.7%**	**13.6%**	**28.8%**	**42.4%**	**13.5%**	**24**
10	585	0	0.10	2.3	—	0%	2.7%	9.5%	27%	60.8%	53
11	585	0	1.00	4.13	—	0%	0%	10%	20%	70%	49
12	585	0	3.00	7.85	—	0%	0%	20%	20%	60%	35
13	585	0	9.00	17.9	—	0%	11.1%	11.1%	22.2%	55.6%	33
14	585	0	13.0	31.2	—	0%	0%	0%	12.5%	87.5%	30
15	585	0	18.0	40.5	—	No nanoribbons observed					

Variation of T_m did not result in the increased outcome of the ultrathin nanoribbons compared to the standard T_m = 585 °C (yellow part of Table 1). Reduction of T_m by 10 °C (from 585 °C down to 575 °C) resulted in the outcome of nanoribbons with thicknesses above 25 nm, with the mean value of the nanoribbon thickness of 52 nm (Table 1, row 1), which is higher in comparison with the value of 36 nm obtained for the similar synthesis performed with the T_m = 585 °C (Table 1, row 6). In turn, an increase in T_m by 5 °C up to 590 °C resulted in the poor quality of the nanoribbons, expressed in a high number of defects in their crystal structure, presumably due to the excess of Bi (Table 1, row 2), which was confirmed by the EDX analysis which showed Bi:Se proportion of (45 ± 3)% (Bi):(55 ± 3)% (Se). Thus, T_m = 585 °C, which was used in the previously developed synthesis, and resulted in a reliable outcome of stoichiometric nanoribbons, was selected as the constant parameter. Furthermore, only parameters t_2 (green part of Table 1) and p_1 (blue part of Table 1) were varied.

Generally, the mean thickness of the nanoribbons linearly decreased with the decrease in the source material heating time t_2 while keeping the pressure p_1 constant (Figure 3a, and the green part of Table 1, including row 9), which is most likely related to the decreased amount of the evaporated source material, and consequently, the thickness of the nanoplate seeds. In contrast, an increase in the initial pressure p_1 while keeping t_2 constant resulted in a slight decrease in the mean thickness $\langle t \rangle$ of the nanoribbons from ~50 nm down to 0 nm when the p_1 increased from 0.1 to 18 Torr (Figure 3, blue part of Table 1, including row 9).

As can be seen from the inset in Figure 3a, an increase in the t_2 at constant pressure p_1 impacts not only the mean thickness of the nanoribbons $\langle t \rangle$, but also the distribution of the actual thicknesses of the nanoribbons. The thickness distribution at t_2 = 0 min has a majority of the nanoribbons within the range 10–40 nm with the maximum at the nanoribbon thickness values of ~20 nm (Figure 3a (inset), red pillars). In contrast, the thickness distribution of the nanoribbons obtained in the synthesis with t_2 = 30 min is more uniform and has maximum shifted to the thicknesses 50 nm (Figure 3a (inset), blue pillars). Consequently, t_2 = 0 min is an optimal choice for obtaining the highest number of ultrathin nanoribbons. The thickness distribution for most of the nanoribbons obtained in the synthesis with p_1 = 5 Torr is mainly between 0 and 40 nm, with the maximum at the nanoribbon thickness 10–20 nm (Figure 3b (inset), red pillars). In contrast, the thickness distribution for the nanoribbons obtained in the synthesis with p_1 = 9 Torr was wider and shifted to the higher thickness values, covering the range 10–60 nm (Figure 3b (inset), blue pillars), with the maximum shifted to the 20–30 nm-thick nanoribbons, which may be related to the formation of thicker nanoplates seeds as explained further in the text. Thus, the p_1 of 5 Torr may be considered as optimal pressure for the obtaining of ultrathin nanoribbons.

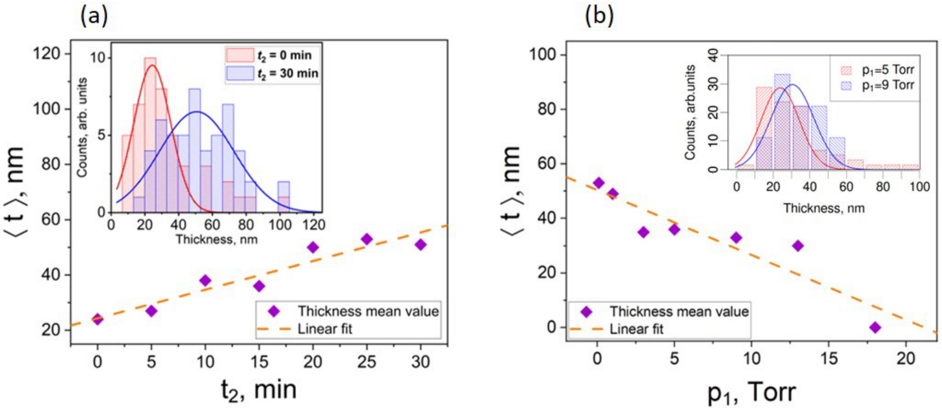

Figure 3. Bi_2Se_3 nanoribbon mean thickness ⟨t⟩ vs. (**a**) time t_2 at a constant initial pressure p_1 = 5 Torr, and (**b**) vs. the initial pressure p_1 at constant time t_2 = 0 min. The orange dashed lines correspond to a linear fit of the experimental data. Insets: Bi_2Se_3 nanoribbon thickness histograms for t_2 = 0 min and 30 min at constant p_1 = 5 Torr (left), and for p_1 = 5 Torr and 9 Torr at constant t_2 = 0 min (right). Solid lines correspond to the Gaussian distribution of experimental data, from which the mean thickness ⟨t⟩ was calculated.

The ranges of the synthesis parameters t_2 and p_1 suitable for obtaining ultrathin Bi_2Se_3 nanoribbons of thicknesses <10 nm, 10–15 nm, 15–20 nm, and 20–25 nm are illustrated in Figure 4a and b, respectively. While nanoribbons with thicknesses 20–25 nm may be obtained within the wide range of parameters with t_2 ranging from 0 to 25 min and p_1 ranging from 0.1 to 13 Torr (Figure 4a,b, blue area), the optimal parameters, resulting in a yield of ~42–46% of nanoribbons with these thicknesses are T_m = 585 °C, t_2 = 0–10 min, and p_1 = 5 Torr (Table 1, rows 7–9). These synthesis parameters also result in narrow nanoribbon thickness distributions, with most of the nanoribbons having thicknesses below 25 nm. As suggested by the Hertz–Knudsen evaporation equation, increasing the initial pressure effectively reduces the diffusion rate of the source material, resulting in slower nucleation and growth of the nanoplate seeds; however, this does not hamper their formation.

However, increasing the time t_2 above 10 min while keeping p_1 = 5 Torr results in an increase in the yield of Bi_2Se_3 nanoribbons with thicknesses above 25 nm up to ~60–89% (Table 1, rows 3–6), which indicates that the growth of nanoplates seeds starts before the heating stage at constant T_m (Figure 1) and continues during the full period of the heating time t_2. A similar increase in the outcome of the nanoribbons with thicknesses above 25 nm was observed with the decrease in p_1 below 5 Torr (Table 1, rows 10–12) or its increase above 5 Torr (Table 1, rows 13–14) while keeping t_2 = 0 min. The decrease in p_1 may lead to the formation of thicker nanoplate seeds due to the increased evaporation and diffusion rate of the source material. In turn, the increase in p_1 may result in the formation of nanoplates with a high number of surface defects, hampering the diffusion of adatoms to the edges of the nanoplates and promoting the formation of the step-like structure of the nanoplates with high step thicknesses. The evaporation equation suggests that no more evaporation occurs when the hydrostatic pressure exceeds the equilibrium pressure of the source material. This was experimentally confirmed by observing that synthesis at a pressure p_1 = 18 Torr did not yield any nanoribbons (Table 1, row 15), indicating that the synthesis pressure was close to or above the equilibrium pressure of the source material.

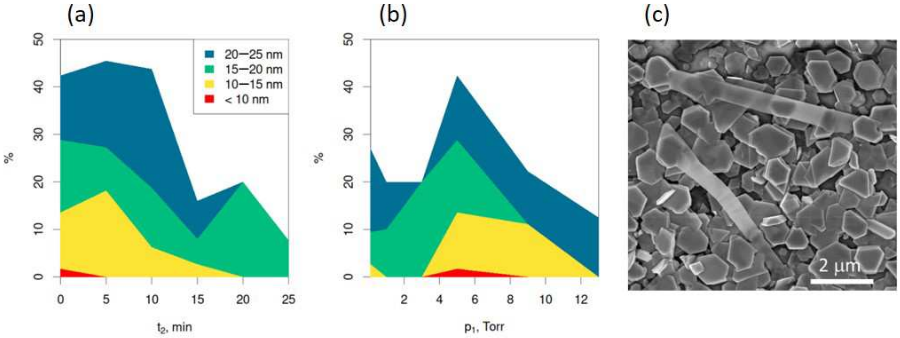

Figure 4. Stacked area plots of Bi_2Se_3 nanoribbon mean thicknesses (**a**) from syntheses with p_1 = 5.0 Torr with various heating times t_2, and (**b**) t_2 = 0 min with various starting pressure p_1. (**c**) The secondary electron scanning electron microscope image of ultrathin Bi_2Se_3 nanoribbons grown from the step-like structure at the top surfaces of Bi_2Se_3 nanoplate seeds.

While the nanoribbons with thicknesses of 15–20 nm may also be obtained in quite wide range of synthesis parameters: t_2 ranging from 0 to 25 min and p_1 ranging from 0.1 to 13 Torr (Figure 4a,b, green area), the range of synthesis parameters for obtaining nanoribbons with thicknesses 10–15 nm required reduction of t_2 below 20 min and p_1 falling in the range 3–13 Torr (Figure 4a,b, yellow area). For both 10–15 nm and 15–20 nm thickness ranges, the initial pressure p_1 = 5 Torr was found to be optimal for obtaining the highest yield of the nanoribbons. However, for obtaining maximal yield (~27–29% of 15–20 nm thin nanoribbons and ~13.5–18% of 10–15 nm thin nanoribbons, Table 1, rows 8. and 9), the time t_2 had to be reduced to 0–5 min with the optimal value of t_2 = 0 min. While there was no significant difference in the yields of the 15–20 nm thin nanoribbons obtained in the syntheses with t_2 being 0 min and 5 min (28.8% vs. 27.3%), the difference in the yields of the 10–15 nm at these values of t_2 was noticeable (13.6% vs. 18.2%). Presumably, this effect may be related to the dynamics of the formation of the step-like structure of the nanoplates seeds formed before the start of the second stage of the synthesis—heating the source material at constant temperature T_m—and further initiation of the nanoribbon growth from the edges of these steps. In the synthesis with t_2 = 0, the step-like morphology starts its formation, and at t_2 = 5 min, more step-like structures are formed, resulting in an increased yield of the nanoribbons. This hypothesis is indirectly supported by the fact that the nanoribbons with thicknesses below 10 nm (Figure 4a,b, red area) can be formed in the narrow range of the synthesis parameters of t_2 varying from 0 to 5 min and p_1 varying between 3 and 9 Torr with the optimal parameters p_1 = 5 Torr and t_2 = 0 min when the yield of 1.7% of the total number of characterized nanoribbons can be reached (Table 1, row 9). These nanoribbons were grown from the edges of newly formed step-like structures on the surfaces of the Bi_2Se_3 nanoplates seeds, as illustrated in Figure 4c. It should be noted that the minimal detected thickness of the nanoribbons obtained under these synthesis parameters was 8 nm, which presumably may be the lower limit for the controlled synthesis of ultrathin nanoribbons by physical vapor deposition.

3.2. Magnetotransport Properties of Ultrathin Bi_2Se_3 Nanoribbons

The freestanding stoichiometric Bi_2Se_3 nanoribbons synthesized with adjusted parameters on a glass substrate (Figure 5a) were transferred to Si/SiO_2 (7 × 7 mm) substrates with marks via simple flip-chip (slight pressing of the chip to the glass with nanoribbons) method. The transferred nanoribbons were analyzed using an optical (Figure 5b) and atomic force microscope (Figure 1b) to distinguish the thinnest ones. The selected ultrathin nanoribbons were patterned using electron-beam lithography to create electrical contacts in a four-terminal measuring configuration. Since the surfaces of Bi_2Se_3 nanoribbons oxidize in the air faster than a cleaved single crystal [44], and for our nanoribbons, synthesized by the standard method, ~1 nm oxide layer formed in one week, but after 3 years, their surface is covered with a 10 nm-thick oxide layer [45] (other groups also show higher oxidation rates ~2 nm oxide layer is formed in 2 days of exposure to air [46]), the samples were stored in an inert atmosphere after the synthesis to reduce the thickness of the formed native oxide layer. To remove the oxide layer and provide an ohmic contact, approximately 3–4 nm thin layers were etched off the nanoribbon surfaces with Ar ions prior to the formation of the metal electrodes to the nanoribbons by the evaporation method. After etching, the sample was immediately loaded into a vacuum chamber of a metal evaporator. To enhance adhesion, an extremely thin adhesion layer of Ti (3 nm) was deposited before the gold evaporation (80 nm). SEM image of a device with Hall bar electrodes geometry based on a single ultrathin (15 nm) nanoribbon is shown in Figure 5c. The six-contacts geometry (two large electrodes at the ends of nanoribbon for passing current and two pairs of Hall bars) allows measurements of the longitudinal (V_{xx}) and transverse (V_{xy}) voltages in a four-probe configuration, thus eliminating the contact resistance effects. However, the overlapping of the nanoribbon with gold electrodes (Figure 5d) results in an error in Hall voltage measurements due to the non-ideal Hall bar geometry. Thus, similarly to reported in [39], the measured value of V_{xy} must be corrected using a numerically calculated geometrical correction factor for the specific device geometry.

For all measured devices, the sheet resistance linearly decreased with the decrease in temperature (a metallic transition), reaching saturation at about 30 K (Figure 6a). Such behavior was also observed previously for Bi_2Se_3 nanoribbons with different thicknesses [26,34] since the PVD-grown Bi_2Se_3 nanostructures are usually excessively doped with selenium vacancies (electron donors), which contribute to the conducting states from the bulk [2]. Such a phenomenon complicates tuning the Fermi level close/through the Dirac point via applying electrostatic gate potential to the nanostructures. Reducing the thickness of nanoribbons increases their surface-to-volume ratio, which can effectively reduce the metallic bulk conduction of Bi_2Se_3 nanostructures. This is evidenced by the increase in the sheet resistance of the nanoribbons with the decrease in their thickness (Figure 6b) and may help to reveal the topological surface states (TSSs) transport signatures [2].

To estimate the three-dimensional concentration of charge carriers $n_{3D\text{-}Hall}$ of individual nanoribbons, the Hall resistance R_{xy} was measured as a function of the magnetic field at the base temperature of 2 K. The negative $R_{xy}(B)$ slope indicates n-type carriers for all measured devices (Figure 6e). The values of the carrier concentration were calculated from the Hall resistance as [39]:

$$\frac{1}{n_{3D-Hall} \cdot e} = t\frac{dR_{xy}}{dB} \times g,$$

where e is the elementary charge, t is the thickness of the measured nanoribbon, and $g \approx 4$ (for this experiment) is a correction factor for the shunting of the Hall effect by the gold electrodes (Figure 5d) [39]. The $n_{3D\text{-}Hall}$ values as a function of the nanoribbon thickness are presented in Figure 6c. The increase in the $n_{3D\text{-}Hall}$ while the thickness of the nanoribbons is decreasing indicates a stronger contribution of TI surface carriers since the bulk contribution becomes less dominant [26].

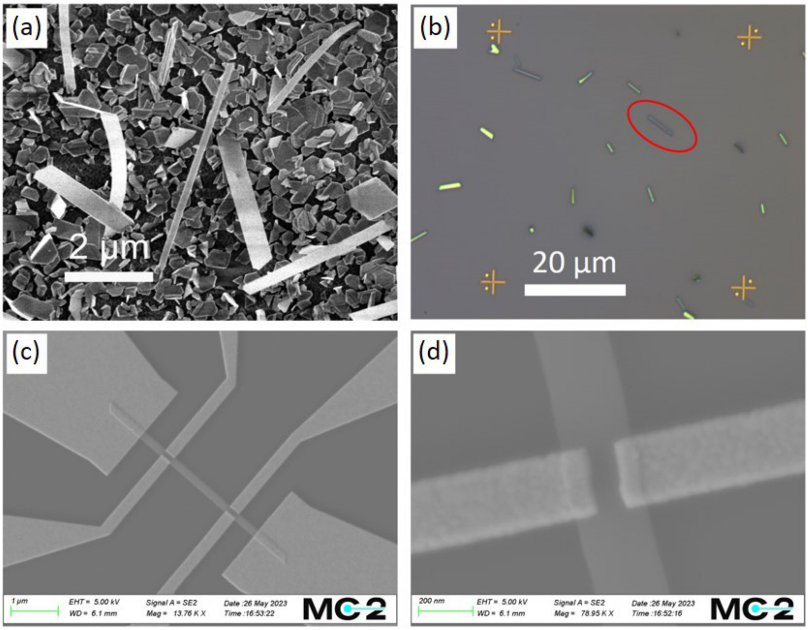

Figure 5. (**a**) Secondary electron SEM image of grown freestanding Bi_2Se_3 nanoribbons on a glass substrate. (**b**) Optical image of transferred nanoribbons to Si/SiO_2 substrate. The red circle highlights the nanoribbon (15 nm thick) selected for further fabrication. (**c**) SEM image of Bi_2Se_3 nanoribbon-based (from (**b**)) device with patterned electrodes for the Hall-effect measurement; (**d**) Hall bars overlapping the Bi_2Se_3 nanoribbon; this configuration requires a correction factor g when calculating the $n_{3D\text{-}Hall}$ concentration.

To probe the TI properties of obtained nanoribbons, the magnetoresistance R_{xx} as a function of the magnetic field applied perpendicularly to the nanoribbon's surface was measured. All devices exhibited pronounced oscillations in high magnetic fields. This effect is associated with the Shubnikov–de Haas (SdH) oscillations. After subtracting a polynomial background, the strictly periodic residual magnetoresistance ΔR_{xx} was obtained in 1/B (Figure 6d). The Fourier transform of the oscillations gives a single frequency at F = 96 T (inset of Figure 6d), which, according to the Onsager relationship, corresponds to $n_{2D} = 2.32 \times 10^{12}$ cm^{-2} [26]. Any deviation from periodicity should lead to the appearance of another (additional) frequency (corresponding to the bulk) in the Fourier transform spectrum. This was not observed, so a clear signature of a bulk-free transport nature was found in the obtained nanoribbons. Moreover, the observed SdH frequency can be attributed to the top Dirac surface states (at the interface of nanoribbon with vacuum). This is supported by our previous results [26,39], where it was shown that the charge accumulation layer formed at the nanoribbon–substrate interface dominates in the Hall conductance. Due to the overlapping of the bottom topological surface states with the accumulation layer having lower charge carrier mobility [26], the bottom surface SdH oscillations do not usually appear in the magnetoresistance. Moreover, the linear fit of Hall resistance (blue dashed line in Figure 6e) in the low magnetic field range depicts the deviation from the linearity at higher magnetic fields. This non-linearity indicates the contribution of another band (accumulation layer) with different concentrations of carriers and mobility. Indeed, the values of the 2D carrier concentrations extracted from the SdH oscillations analysis and Hall effect measurements (which include all existing types of carriers) showed a large discrepancy ($n_{2D\ SdH}$ = 2.32 × 10^{12} cm^{-2} and $n_{2D\text{-}Hall}$ = 8.93 × 10^{12} cm^{-2}). Applying the two-band model analysis for the longitudinal and transverse magnetoconductance to extract the carrier concentration and the mobility of the two types of carriers [26,39], it can be assumed that one band is represented by the Dirac electrons (at the interface of the nanoribbon with vacuum) and the other band includes both the charge accumulation layer and the Dirac electrons at the bottom surface of the nanoribbon. In the fits, the value of n_1 was set equal to $n_{2D\text{-}SdH}$ = 2.32 × 10^{12} cm^{-2} extracted from the SdH measurements. Figure 6f shows the fitting results with the experimental data, which yields μ_1 = 1.08 × 10^3 $cm^2 \cdot (Vs)^{-1}$ for the mobility of the carriers from the topological surface states at the nanoribbon top surface, and n_2 = 7.89 × 10^{12} cm^{-2} and μ_2 = 5.11 × 10^2 $cm^2 \cdot (Vs)^{-1}$ are representing parameters for second band. The extracted top surface mobility is in good agreement with previously published results [39,47], while the mobility of the second band is slightly lower than that published in the literature. This may be due to the possible non-uniformity of the oxide layer on the surface of the substrate, the presence of local defects, and the non-homogeneity of the accumulation layer, and may also vary from device to device.

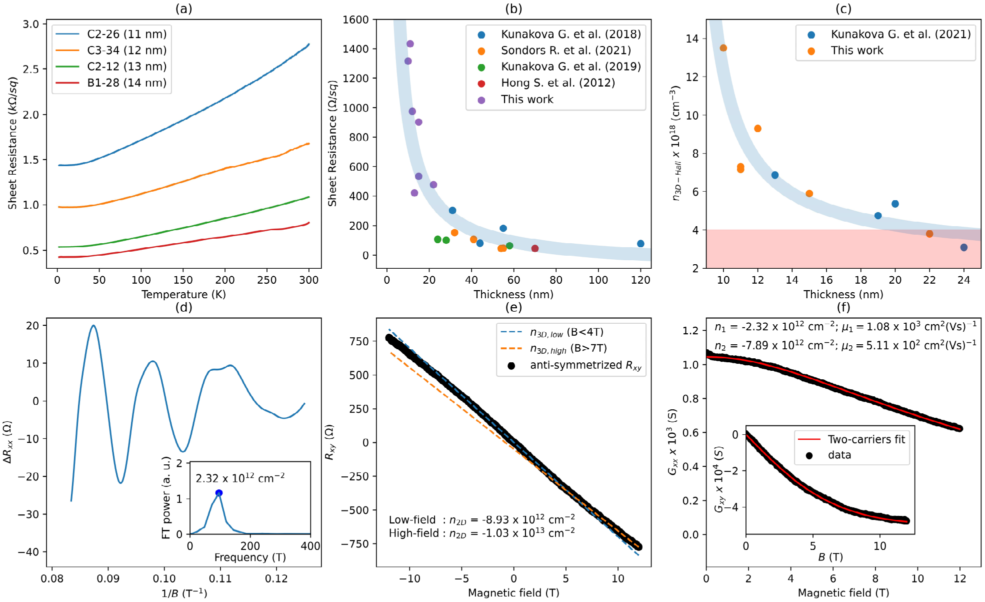

Figure 6. Magnetotransport of Bi_2Se_3 nanoribbons with thickness below 15 nm. (**a**) Sheet resistance as a function of temperature; (**b**) Sheet resistance as a function of nanoribbon thickness measured at 2 K. Purple marks are data from this work, the colored marks (blue, orange, green and red) are data from Kunakova G, et al. (2018) [26], Sondors R. et al. (2021) [36], Kunakova G, et al. (2019) [41] and Hong S. et al. (2012) [24], respectively. The light-blue shaded region is a guide to the eye (1/t), indicating a dramatic increase in sheet resistance as thickness decreases; (**c**) The three-dimensional concentration of charge carriers $n_{3D\text{-}Hall}$ as a function of nanoribbons thickness. Orange marks are data from this work; the blue marks are data from Kunakova G, et al. (2021) [39], respectively. The

light-blue shaded region is a guide to the eye, and the pink-shaded region indicates the upper bound for the bulk carrier concentration [26]; (**d**) Shubnikov–de Haas magnetoresistance oscillations as a function of 1/B for the 15 nm-thick nanoribbons measured at 2 K. The inset: the Fourier transform power spectra of $\Delta R_{xx}(1/B)$ shown in (**d**); (**e**) Anti-symmetrized $R_{xy}(B)$. The blue dashed lines are the linear fit in the range of 0 to 4 T. The orange dashed lines are the linear fit in the range of 7 to 12 T. (**f**) Longitudinal (G_{xx}) and transverse (G_{xy}) magnetoconductance as a function of the magnetic field. The solid red lines correspond to the fit of the two-carrier model. All the data refer to the same nanoribbon as shown in (**d**).

4. Conclusions

A systematic study of the correlation of the main parameters (synthesis pressure and time) of the catalyst-free physical vapor deposition synthesis and the thickness of the synthesized Bi_2Se_3 nanoribbons showed that the optimal combination of these parameters allows the successful synthesis of ultrathin Bi_2Se_3 nanoribbons with thicknesses below 15 nm. Decreasing the time of heating the source material at maximal temperature during the synthesis correlated with an increased percentage of ultrathin nanoribbons, as well as a lower mean nanoribbon thickness overall. The optimal synthesis parameters for obtaining the highest yield of the Bi_2Se_3 nanoribbons with thicknesses below 15 nm were the temperature of the source material of 585 °C, initial pressure of the inert gas in the synthesis tube of 5 Torr, and time of heating of the source material at a maximal temperature of 0–5 min, meaning that for obtaining the ultrathin nanoribbons cooling process should start immediately or within 5 min from the moment when the maximal synthesis temperature of 585 °C has been reached.

Investigation of the transport properties of the obtained Bi_2Se_3 nanoribbons with thicknesses below 15 nm showed that the values of the sheet resistance for these nanoribbons are by approximately an order of magnitude higher compared to the values reported previously for the thicker Bi_2Se_3 nanoribbons synthesized using catalyst-free PVD. Potentially, this could lead to better tuning of the chemical potential through electrostatic gating and help access transport through topological surface states. The single frequency extracted from SdH oscillations corresponded to the topological surface states at the top surface of the nanoribbon (at the interface with the vacuum). There is no signature of 3D bulk carriers. The presence of the accumulation layer (with lower mobility) was observed at the nanoribbon–substrate interface. The topological surface states observed in the studied nanostructures confirmed that the Bi_2Se_3 thin (below 15 nm) nanoribbons synthesized with modified parameters do not result in a degradation of the transport properties.

Author Contributions: Conceptualization, F.L. and D.E.; investigation, R.S., K.N., J.A., X.P. and T.B.; writing—original draft preparation, R.S., K.N. and J.A.; writing—review and editing, J.A. and D.E.; visualization R.S., K.N. and J.A.; supervision, F.L. and D.E. All authors have read and agreed to the published version of the manuscript.

Funding: This research was funded by the Latvian Council of Science (project No. lzp-2019/1-0349) and the European Union's Horizon 2020 Research and Innovation program (grant agreement No. 766714/HiTIMe). K.N acknowledges the financial support of the "Strengthening of the capacity of doctoral studies at the University of Latvia within the framework of the new doctoral model", identification no. 8.2.2.0/20/I/006. X.P., F.L. and T.B. also acknowledge support from the Swedish infrastructure for micro- and nanofabrication—MyFab.

Data Availability Statement: The raw/processed data required to reproduce these findings cannot be shared at this time as the data also forms part of an ongoing study.

Conflicts of Interest: The authors declare no conflict of interest.

References

1. Mazumder, K.; Shirage, P.M. A brief review of Bi_2Se_3 based topological insulator: From fundamentals to applications. *J. Alloys Compd.* **2021**, *888*, 161492. [CrossRef]
2. Cao, H.; Xu, S.; Miotkowski, I.; Tian, J.; Pandey, D.; Hasan, M.Z.; Chen, Y.P. Structural and electronic properties of highly doped topological insulator Bi_2Se_3 crystals. *Phys. Status Solidi—Rapid Res. Lett.* **2013**, *7*, 133–135. [CrossRef]
3. Cui, Y.; Kong, D.S.; Randel, J.C.; Peng, H.L.; Cha, J.J.; Meister, S.; Lai, K.J.; Chen, Y.L.; Shen, Z.X.; Manoharan, H.C. Topological Insulator Nanowires and Nanoribbons. *Nano Lett.* **2010**, *10*, 329–333.
4. Park, H.; Jeong, K.; Maeng, I.H.; Sim, K.I.; Pathak, S.; Kim, J.; Hong, S.B.; Jung, T.S.; Kang, C.; Kim, J.H.; et al. Enhanced Spin-to-Charge Conversion Efficiency in Ultrathin Bi_2Se_3Observed by Spintronic Terahertz Spectroscopy. *ACS Appl. Mater. Interfaces* **2021**, *13*, 23153–23160. [CrossRef]
5. Yan, Y.; Wang, L.X.; Ke, X.; Van Tendeloo, G.; Wu, X.S.; Yu, D.P.; Liao, Z.M. High-Mobility Bi_2Se_3 nanoplates manifesting quantum oscillations of surface states in the sidewalls. *Sci. Rep.* **2014**, *4*, 3817. [CrossRef] [PubMed]
6. Fan, H.; Zhang, S.; Ju, P.; Su, H.; Ai, S. Flower-like Bi_2Se_3 nanostructures: Synthesis and their application for the direct electrochemistry of hemoglobin and H_2O_2 detection. *Electrochim. Acta* **2012**, *64*, 171–176. [CrossRef]
7. Du, B.; Kang, W.; He, Y.; Wang, Y.; Yang, X.; Meng, G.; Zhu, Z.; Lin, X.; Tan, Y.; Liang, C.; et al. Topological insulator Bi_2Se_3 for highly sensitive, selective and anti-humidity gas sensors. *iScience* **2023**, *26*, 106387. [CrossRef] [PubMed]
8. Du, F.; Zheng, K.; Zeng, S.; Yuan, Y. Sensitivity Enhanced Plasmonic Biosensor Using Bi_2Se_3-Graphene Heterostructures: A Theoretical Analysis. *Nanomaterials* **2022**, *12*, 4078. [CrossRef] [PubMed]
9. Yang, M.; Zhou, H.; Wang, J. Topological insulators photodetectors: Preparation, advances and application challenges. *Mater. Today Commun.* **2022**, *33*, 104190. [CrossRef]
10. Kim, J.; Park, S.; Jang, H.; Koirala, N.; Lee, J.B.; Kim, U.J.; Lee, H.S.; Roh, Y.G.; Lee, H.; Sim, S.; et al. Highly Sensitive, Gate-Tunable, Room-Temperature Mid-Infrared Photodetection Based on Graphene-Bi_2Se_3 Heterostructure. *ACS Photonics* **2017**, *4*, 482–488. [CrossRef]
11. Sharma, A.; Bhattacharyya, B.; Srivastava, A.K.; Senguttuvan, T.D.; Husale, S. High performance broadband photodetector using fabricated nanowires of bismuth selenide. *Sci. Rep.* **2016**, *6*, 19138. [CrossRef] [PubMed]
12. Zhi, J.; Zehtab Yazdi, A.; Valappil, G.; Haime, J.; Chen, P. Artificial solid electrolyte interphase for aqueous lithium energy storage systems. *Sci. Adv.* **2017**, *3*, e1701010. [CrossRef] [PubMed]
13. Xie, L.; Yang, Z.; Sun, J.; Zhou, H.; Chi, X.; Chen, H.; Li, A.X.; Yao, Y.; Chen, S. Bi_2Se_3/C Nanocomposite as a New Sodium-Ion Battery Anode Material. *Nano-Micro Lett.* **2018**, *10*, 50. [CrossRef] [PubMed]
14. Ud Din, M.A.; Irfan, S.; Jamil, S.; Dar, S.U.; Khan, Q.U.; Saleem, M.S.; Cheng, N. Graphene-like ultrathin bismuth selenide nanosheets as highly stable anode material for sodium-ion battery. *J. Alloys Compd.* **2022**, *901*, 163572. [CrossRef]
15. Andzane, J.; Felsharuk, A.; Buks, K.; Sarakovskis, A.; Niherysh, K.; Gabrusenoks, J.; Erts, D. Synthesis and Properties of Bismuth Selenide Based Nanolaminates for Application in Thermoelectrics. *Adv. Mater. Interfaces* **2022**, *9*, 2200385. [CrossRef]
16. Jasulaneca, L.; Meija, R.; Kauranens, E.; Sondors, R.; Andzane, J.; Rimsa, R.; Mozolevskis, G.; Erts, D. Cryogenic nanoelectromechanical switch enabled by Bi_2Se_3 nanoribbons. *Mater. Sci. Eng. B Solid-State Mater. Adv. Technol.* **2022**, *275*, 115510. [CrossRef]
17. Ali, Z.; Butt, S.; Cao, C.; Butt, F.K.; Tahir, M.; Tanveer, M.; Aslam, I.; Rizwan, M.; Idrees, F.; Khalid, S. Thermochemically evolved nanoplatelets of bismuth selenide with enhanced thermoelectric figure of merit. *AIP Adv.* **2014**, *4*, 117129. [CrossRef]
18. Hong, M.; Chen, Z.G.; Yang, L.; Han, G.; Zou, J. Enhanced Thermoelectric Performance of Ultrathin Bi_2Se_3 Nanosheets through Thickness Control. *Adv. Electron. Mater.* **2015**, *1*, 1500025. [CrossRef]
19. Osterhage, H.; Gooth, J.; Hamdou, B.; Gwozdz, P.; Zierold, R.; Nielsch, K. Thermoelectric properties of topological insulator Bi_2Te_3, Sb_2Te_3, and Bi_2Se_3 thin film quantum wells. *Appl. Phys. Lett.* **2014**, *105*, 123117. [CrossRef]
20. Stephen, G.M.; Naumov, I.; Tyagi, S.; Vail, O.A.; Demell, J.E.; Dreyer, M.; Butera, R.E.; Hanbicki, A.T.; Taylor, P.J.; Mayergoyz, I.; et al. Effect of Sn Doping on Surface States of Bi_2Se_3Thin Films. *J. Phys. Chem. C* **2020**, *124*, 27082–27088. [CrossRef]
21. Ju, Z.; Hou, Y.; Bernard, A.; Taufour, V.; Yu, D.; Kauzlarich, S.M. Ambipolar Topological Insulator and High Carrier Mobility in Solution Grown Ultrathin Nanoplates of Sb-Doped Bi_2Se_3. *ACS Appl. Electron. Mater.* **2019**, *1*, 1917–1923. [CrossRef]
22. Kong, D.; Chen, Y.; Cha, J.J.; Zhang, Q.; Analytis, J.G.; Lai, K.; Liu, Z.; Hong, S.S.; Koski, K.J.; Mo, S.-K. Ambipolar field effect in the ternary topological insulator $(Bi_xSb_{1-x})_2Te_3$ by composition tuning. *Nat. Nanotechnol.* **2011**, *6*, 705–709. [CrossRef]
23. Lee, J.; Park, J.; Lee, J.-H.; Kim, J.S.; Lee, H.-J. Gate-tuned differentiation of surface-conducting states in $Bi_{1.5}Sb_{0.5}Te_{1.7}Se_{1.3}$ topological-insulator thin crystals. *Phys. Rev. B* **2012**, *86*, 245321. [CrossRef]
24. Hong, S.S.; Cha, J.J.; Kong, D.; Cui, Y. Ultra-low carrier concentration and surface-dominant transport in antimony-doped Bi_2Se_3 topological insulator nanoribbons. *Nat. Commun.* **2012**, *3*, 757. [CrossRef]
25. Pan, Z.W.; Dai, Z.R.; Wang, Z.L. Nanobelts of semiconducting oxides. *Science* **2001**, *291*, 1947–1949. [CrossRef]
26. Kunakova, G.; Galletti, L.; Charpentier, S.; Andzane, J.; Erts, D.; Léonard, F.; Spataru, C.D.; Bauch, T.; Lombardi, F. Bulk-free topological insulator Bi_2Se_3 nanoribbons with magnetotransport signatures of Dirac surface states. *Nanoscale* **2018**, *10*, 19595–19602. [CrossRef] [PubMed]
27. Zhang, H.; Liu, C.X.; Qi, X.L.; Dai, X.; Fang, Z.; Zhang, S.C. Topological insulators in Bi_2Se_3, Bi_2Te_3 and Se_2Te_3 with a single Dirac cone on the surface. *Nat. Phys.* **2009**, *5*, 438–442. [CrossRef]

28. Wang, Y.; Xiu, F.; Cheng, L.; He, L.; Lang, M.; Tang, J.; Kou, X.; Yu, X.; Jiang, X.; Chen, Z. Gate-controlled surface conduction in Na-doped Bi_2Te_3 topological insulator nanoplates. *Nano Lett.* **2012**, *12*, 1170–1175. [CrossRef]
29. Xiu, F.; He, L.; Wang, Y.; Cheng, L.; Chang, L.T.; Lang, M.; Huang, G.; Kou, X.; Zhou, Y.; Jiang, X.; et al. Manipulating surface states in topological insulator nanoribbons. *Nat. Nanotechnol.* **2011**, *6*, 216–221. [CrossRef] [PubMed]
30. Bianchi, M.; Guan, D.; Bao, S.; Mi, J.; Iversen, B.B.; King, P.D.C.; Hofmann, P. Coexistence of the topological state and a two-dimensional electron gas on the surface of Bi_2Se_3. *Nat. Commun.* **2010**, *1*, 128. [CrossRef] [PubMed]
31. King, P.D.C.; Hatch, R.C.; Bianchi, M.; Ovsyannikov, R.; Lupulescu, C.; Landolt, G.; Slomski, B.; Dil, J.H.; Guan, D.; Mi, J.L. Large tunable Rashba spin splitting of a two-dimensional electron gas in Bi_2Se_3. *Phys. Rev. Lett.* **2011**, *107*, 96802. [CrossRef]
32. Benia, H.M.; Lin, C.; Kern, K.; Ast, C.R. Reactive chemical doping of the Bi_2Se_3 topological insulator. *Phys. Rev. Lett.* **2011**, *107*, 177602. [CrossRef]
33. Ghaemi, P.; Mong, R.S.K.; Moore, J.E. In-plane transport and enhanced thermoelectric performance in thin films of the topological insulators Bi_2Te_3 and Bi_2Se_3. *Phys. Rev. Lett.* **2010**, *105*, 166603. [CrossRef]
34. Andzane, J.; Kunakova, G.; Charpentier, S.; Hrkac, V.; Kienle, L.; Baitimirova, M.; Bauch, T.; Lombardi, F.; Erts, D. Catalyst-free vapour–solid technique for deposition of Bi_2Te_3 and Bi_2Se_3 nanowires/nanobelts with topological insulator properties. *Nanoscale* **2015**, *7*, 15935–15944. [CrossRef]
35. Fang, L.; Jia, Y.; Miller, D.J.; Latimer, M.L.; Xiao, Z.L.; Welp, U.; Crabtree, G.W.; Kwok, W.K. Catalyst-free growth of millimeter-long topological insulator Bi_2Se_3 nanoribbons and the observation of the π-berry phase. *Nano Lett.* **2012**, *12*, 6164–6169. [CrossRef]
36. Sondors, R.; Kunakova, G.; Jasulaneca, L.; Andzane, J.; Kauranens, E.; Bechelany, M.; Erts, D. High-yield growth and tunable morphology of Bi_2Se_3 nanoribbons synthesized on thermally dewetted au. *Nanomaterials* **2021**, *11*, 2020. [CrossRef] [PubMed]
37. Zhang, K.; Pan, H.; Wei, Z.; Zhang, M.; Song, F.; Wang, X.; Zhang, R. Synthesis and magnetotransport properties of Bi_2Se_3 nanowires. *Chin. Phys. B* **2017**, *26*, 96101. [CrossRef]
38. Gao, L.; Li, H.; Ren, W.; Wang, G.; Li, H.; Ashalley, E.; Zhong, Z.; Ji, H.; Zhou, Z.; Wu, J.; et al. The high-yield growth of Bi_2Se_3 nanostructures via facile physical vapor deposition. *Vacuum* **2017**, *140*, 58–62. [CrossRef]
39. Kunakova, G.; Bauch, T.; Palermo, X.; Salvato, M.; Andzane, J.; Erts, D.; Lombardi, F. High-Mobility Ambipolar Magnetotransport in Topological Insulator Bi_2Se_3 Nanoribbons. *Phys. Rev. Appl.* **2021**, *16*, 024038. [CrossRef]
40. R Core Team. *A Language and Environment for Statistical Computing*; R Foundation for Statistical Computing: Vienna, Austria, 2022.
41. Kunakova, G.; Meija, R.; Andzane, J.; Malinovskis, U.; Petersons, G.; Baitimirova, M.; Bechelany, M.; Bauch, T.; Lombardi, F.; Erts, D. Surface structure promoted high-yield growth and magnetotransport properties of Bi_2Se_3 nanoribbons. *Sci. Rep.* **2019**, *9*, 11328. [CrossRef] [PubMed]
42. Kong, D.; Dang, W.; Cha, J.J.; Li, H.; Meister, S.; Peng, H.; Liu, Z.; Cui, Y. Few-layer nanoplates of Bi_2Se_3 and Bi_2Te_3 with highly tunable chemical potential. *Nano Lett.* **2010**, *10*, 2245–2250. [CrossRef]
43. Mattox, D.M. *Handbook of Physical Vapor Deposition (PVD) Processing*; William Andrew: Amsterdam, The Netherlands, 2010; ISBN 0815520387.
44. Tereshchenko, O.E.; Kokh, K.A.; Atuchin, V.V.; Romanyuk, K.N.; Makarenko, S.V.; Golyashov, V.A.; Kozhukhov, A.S.; Prosvirin, I.P.; Shklyaev, A.A. Stability of the (0001) surface of the Bi_2Se_3 topological insulator. *JETP Lett.* **2011**, *94*, 465–468. [CrossRef]
45. Erts, D.; Katkevics, J.; Sjomkane, M.; Andzane, J.; Sarakovskis, A.; Smits, K.; Viksna, A.; Rublova, Y.; Meija, R. EIS characterization of aging and humidity-related behavior of Bi_2Se_3 films of different morphologies. *Nano-Struct. Nano-Objects* **2022**, *30*, 100847. [CrossRef]
46. Kong, D.; Cha, J.J.; Lai, K.; Peng, H.; Analytis, J.G.; Meister, S.; Chen, Y.; Zhang, H.J.; Fisher, I.R.; Shen, Z.X.; et al. Rapid surface oxidation as a source of surface degradation factor for Bi_2Se_3. *ACS Nano* **2011**, *5*, 4698–4703. [CrossRef] [PubMed]
47. Steinberg, H.; Gardner, D.R.; Lee, Y.S.; Jarillo-Herrero, P. Surface state transport and ambipolar electric field effect in Bi_2Se_3 nanodevices. *Nano Lett.* **2010**, *10*, 5032–5036. [CrossRef]

Paper VI

Quantum Confinement and Coherent Transport in Ultrathin Bi_2Se_3 Nanoribbons

Kiryl Niherysh,[1, 2, *] Xavier Palermo,[1] Ananthu P. Surendran,[1] Alexei Kalaboukhov,[1]
Raitis Sondors,[2] Jana Andzane,[2] Donats Erts,[2, 3] Thilo Bauch,[1] and Floriana Lombardi[1, †]
[1]*Quantum Device Physics Laboratory, Department of Microtechnology and Nanoscience,*
Chalmers University of Technology, Göteborg, Sweden
[2]*Institute of Chemical Physics, University of Latvia, Riga, Latvia*
[3]*Faculty of Chemistry, University of Latvia, Riga, Latvia*
(Dated: August 11, 2024)

In recent years much progress has been made in realizing topological insulator (TI) nanostructures where the reduced dimensions should help to diminish the contributions from bulk carriers and enhance quantum confinement. Though nm thick 3D-TI nanoribbons exhibiting topological properties are still difficult to reproducibly synthesize. Here we demonstrate the growth of ultrathin Bi_2Se_3 nanoribbons by a simple catalyst-free physical-vapour deposition, where the tuning of the material evaporation time plays a crucial role in determining the ultimate thickness of the nanoribbons. Magnetotransport and Hall effect measurements show that at thicknesses close to 10 nm the transport features are affected by Altshuler-Aronhov-Spivak like coherent orbits at low magnetic fields, while Shubnikov-de Haas oscillations take over at high fields. The observed phenomena originate from the topological surface states and dominate the nanoribbon transport. Ultrathin nanoribbons also show pronounced conductance oscillations as a function of gate voltage, that can be attributed to ballistic transport and quantized sub-bands. The results highlight the importance of material growth and quantum confinement to exploit the unique properties of topological surface states, establishing 3D-TI nanoribbons as a promising platform for a variety of novel applications.

DOI:

I. INTRODUCTION

The properties of the topologically protected Dirac surface states in 3D topological insulator (3D TI) nanostructures are promising for a variety of applications including quantum computing [1–4], spintronics [5–8], thermoelectric device [9–12], and realization of single-electron charge pumps with high accuracy for metrology [13]. However, the contribution from the trivial bulk charge carriers often masks the exotic properties of the topological surface states. To take full advantage of the protected surface states, one needs to tune the chemical potential inside the band gap and close to the Dirac point. One effective way to eliminate the bulk contribution is chemical compensation doping of nanoribbons [14–16]; however, this procedure significantly reduces the mobility of surface Dirac electrons [17, 18]. An alternative approach to reduce the bulk contribution maintaining high mobility is to increase the surface-to-volume ratio by growing 3D-TI materials with reduced dimension such as nanoribbons [19, 20].

In our previous work we demonstrated the growth of Bi_2Se_3 nanoribbons using our standard catalyst-free physical-vapour deposition (PVD) [21]. However, in this study, we had a lower yield of nanoribbons with a thickness of less than 15 nm. Here we show that by properly tuning the deposition conditions of our PVD technique, we can identify a regime of growth that allows to obtain Bi_2Se_3 nanoribbons with thicknesses below 15 nm and lengths up to 5-10 µm. For the thinnest nanoribbons, the growth mechanism changes from a layered to rough regime, varying the morphology of nanostructures, which affects the transport properties of the topological surface states of nanoribbons. We show that quantum oscillations in a magnetic field can be clearly detected even in the thinnest nanoribbons and that therefore the transport properties are dominated by the surface states. By combining magnetoresistance and Hall effect measurements, we have discovered a regime of thicknesses (below 15 nm) where Altshuler-Aronhov-Spivak (AAS) like orbits dominate the transport at low magnetic fields, while Shubnikov-de Haas (SdH) oscillations are observed at high fields. In addition, we demonstrate a clear signature of quantized energy band structure in the form of an oscillatory behaviour of the longitudinal zero-bias resistance as a function of back-gate voltage. The results highlight the importance of material growth and geometrical confinement for the correct use of the unique properties of topological surface states.

II. EXPERIMENTAL RESULTS AND DISCUSSION

A. Synthesis of ultrathin Bi_2Se_3 nanoribbons

Bi_2Se_3 nanoribbons were synthesized via catalyst-free physical vapour deposition in a GSL-1100X tube furnace (MTI Corporation). Bi_2Se_3 powder was used as a source

---

[*] e-mail: kiryl.niherysh@lu.lv
[†] e-mail: floriana.lombardi@chalmers.se

material, and placed in the center of the furnace tube where the temperature reaches 585 °C during the synthesis. A glass substrate (25×75 mm) was placed downstream from the source material. Before the synthesis, the tube was first flushed with N_2 gas for 5 min to create an inert atmosphere. The scheme of the synthesis process is shown in Fig. 1.

First, the furnace was heated up from room temperature to 585 °C in a time interval t_1 = 45 min. The substrate temperature at this moment was from 430 to 230 °C at its “hot” and “cold” ends, respectively. After that, the furnace was kept at the temperature of 585 °C for a time t_2 that was varied between 15 (standard growth [21]) and 0 min (modified growth, these work), and afterwards the furnace was turned off to cool down naturally. When the temperature in the furnace center decreased to 540 °C, an N_2 gas flow was introduced in the tube with a dynamic pressure of 26 Torr, initiating the growth of the nanoribbons. The flow was terminated once temperature reached 475 °C, and the tube was filled with N_2 to atmospheric pressure.

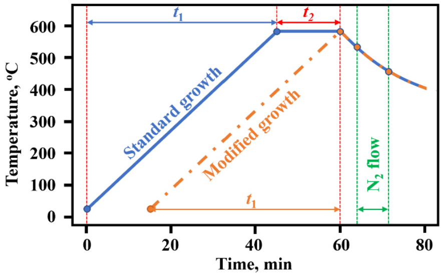

FIG. 1. Schematic of the synthesis process. The solid blue line corresponds to the standard growth described in [21], and the orange dot-dashed line corresponds to a modified growth with t_2 = 0 min.

During the standard growth process [21], nanoplates are deposited on the substrate for a time t_1+t_2. They serve as seeds for the subsequent formation of nanoribbons during the N_2 streaming. As the top surface of the nanoplate is chemically saturated by selenium atoms [22], adatoms adsorbed there from the gas phase cannot form covalent bonds. Thus, they diffuse in the direction of the gas flow and bond to the nanoplate crystal at the edges, which leads to a much faster growth rate in the N_2 flow direction, forming long crystalline nanoribbons [21]. Since the cross-section of the nanoribbons is correlated to that of the seed nanoplates from which they grow, as shown in Fig. 2, it can be influenced by changing the conditions in which the nanoplates are grown. The amount of deposited material is proportional to the partial pressure of the evaporated source and evaporation time [23], and then the thickness of nanoribbons can be changed by adjusting only these parameters. In this work, the deposition time t_2 was reduced from 15 to 0 min, and the pressures p_1 and p_2 which represent respectively the value measured when the heater is switched on and when the heater reaches the set temperature of 585 °C, were kept constant.

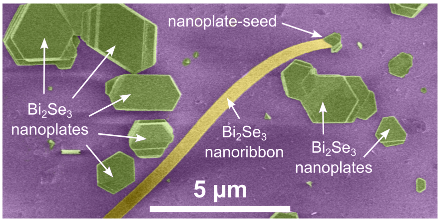

FIG. 2. False-color SEM image of a Bi_2Se_3 nanoribbon and the nanoplate seed.

The synthesis parameters not only influence the geometry of the nanoribbons, but also determine their growth mechanism, affecting their transport properties [24]. Fig. 3a and 3b show atomic force microscopy (AFM) images and surface profiles for 12 and 22 nm thick nanoribbons, respectively. The thin nanoribbon (Fig. 3a) shows the presence of small grains on the surface, while the thicker one (Fig. 3b) has an atomically flat surface. The average surface roughness for the thin nanoribbon is ∼ 0.67 nm, while for the thicker ribbon this parameter is ∼ 0.13 nm. These images seem to indicate that the growth kinetics of thin nanoribbons differ from that of thick ones. Here we propose a possible growth scenario that can occur when time t_2 is changed. During the vapour-solid (VS) process, the formation of nanoribbon/nanowire-like nanostructures is determined by growth kinetics [25, 26]. As mentioned earlier, the top surface of the nanoplates (seeds) is chemically saturated. As a result, newly arriving growth species (adatoms) will diffuse to side edges with atomic steps, ledges, and kinks [27, 28]. Previously, it was shown that the two-dimensional nucleation probability on the surface of nanoribbons can be described as [25–27]:

$$P_N = B\exp\left\{\left(-\frac{\pi\sigma^2}{k^2T^2\ln(p/p_0)}\right)\right\} \tag{1}$$

where P_N is the nucleation probability, B is a constant, σ is the surface energy, k is the Boltzmann constant, T is the absolute temperature, p is the actual vapour pressure, and p_0 is the equilibrium vapour pressure corresponding to temperature T. If the vapour pressure $p < p_0$, the chemical potential of the crystal is larger than that of the vapour and the crystal should sublimate. However, if $p > p_0$ the vapour should crystallize. In our experiment, the deposition of nanostructures proceeds in the supersaturated state $(p/p_0) > 1$. Therefore, the supersaturation ratio (p/p_0) and temperature are two dominant processing factors in controlling the morphology of the products in the VS growth process [27].

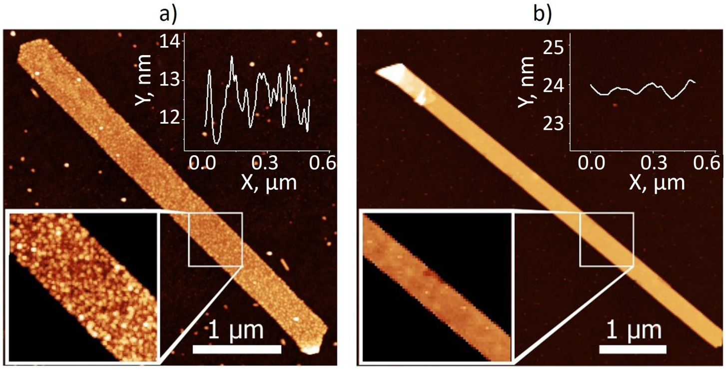

FIG. 3. a) AFM image of a 12 nm thick nanoribbon grown with the rough mechanism. The inset is the surface profile with RMS roughness around ∼ 670 pm. b) AFM image of a 22 nm thick nanoribbon in which the rough-to-smooth growth transition mechanism occurred. The inset is the surface profile with RMS roughness around ∼ 130 pm. The y-axis range is identical to the one of the inset in panel a) to emphasize the significant difference.

The amount of evaporated material at the start of nanoribbons growth in the case of $t_2 = 0$ min is much less than in the case of the standard growth, where $t_2 = 15$ min. Nanoplates (seeds) deposited only over time t_1 have smaller thicknesses in comparison with flakes deposited during time t_1+t_2. However their side edges with atomically rough steps, regardless of the plate thickness, act as effective "catalyst" that initiates the growth of nanoribbons in the lateral direction. As in the case of the vapour-liquid-solid growth mechanism, the edge side area of the "catalyst" plate, from which the nanoribbon growth occurs, can be saturated with adatoms more easily for thinner seeds compared to thicker ones [29]. The value of supersaturation at the edge surface tends to decrease for plates with higher thicknesses. Previously, it was also shown that a decrease in supersaturation may lead to the rough-to-smooth transition of the crystal growth mechanism [30–32]. We have experimentally found that during the same deposition process, nanoribbons less than 15 nm thick have a rough surface, while ribbons more than 15 nm thick have a smooth morphology, indicating a 2D growth mechanism. This suggests that a transition from rough to smooth growth takes place in our experiment. Moreover, this growth scenario is consistent with the appearance of a high yield of thin nanoribbons. At some point, the growth particles from the vapour cannot saturate the side edge of very thick seeds, and the chemical potential of the crystal itself becomes larger than that of the vapour ($p_0 > p$). In this case, the growth of the thickest nanoribbons may stop, while the growth rate of crystals from saturated seeds increases with a decrease in their thickness [29]. As we will show below, the difference in morphology between thicker and thinner nanoribbons strongly affects the transport properties of the topological surface states.

B. Transport measurements of Bi_2Se_3 nanoribbons

Bi_2Se_3 nanoribbons synthesized using the parameter $t_2 = 0$ min were transferred to a Si/SiO_2 (300 nm) substrate for transport measurements. After the transfer, several nanoribbons were selected using optical and atomic force microscopies. The electrical leads were patterned via electron-beam lithography to create contacts for magnetoresistance and Hall effect measurements. Ar^+-ion beam etching was used to remove the native oxide from the top surface of the nanoribbons prior to the deposition of Ti/Au contacts (3/80 nm) (Fig. 4). The longitudinal resistance R_{xx} was measured from the room temperature down to 2 K (shown in the insets of Fig. 5a). For all measured devices, R_{xx} decreases with tempera-

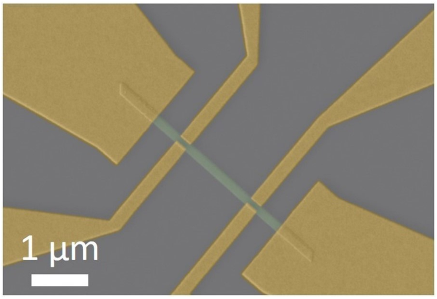

FIG. 4. False-color SEM image of a fabricated device based on a Bi_2Se_3 nanoribbon (green) transferred to a Si/SiO_2 substrate (grey). The metal electrodes are shown in yellow.

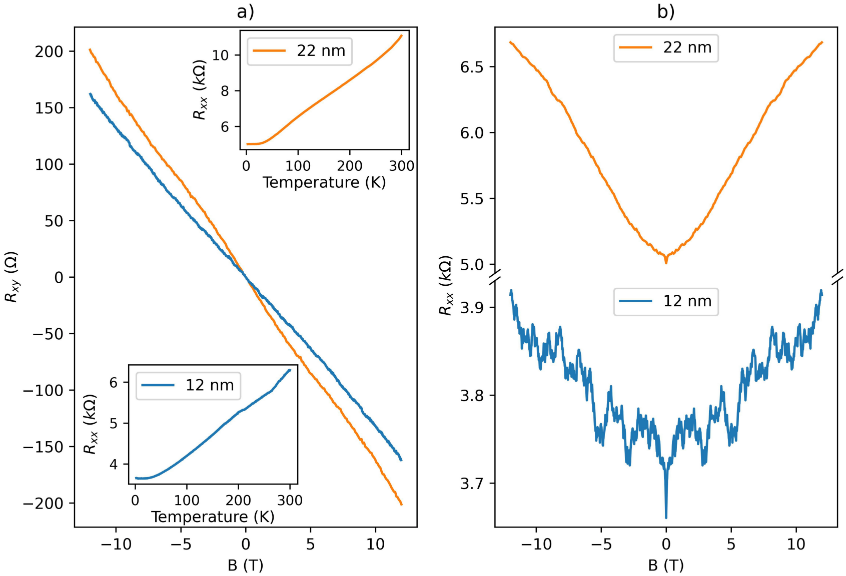

FIG. 5. The magnetic field dependence of the a) transverse R_{xy} and b) longitudinal R_{xx} resistances for 12 nm (blue, **Device I**) and 22 nm (orange, **Device II**) thick ribbons measured at 2 K, respectively. The insets in a) represent the temperature dependence of R_{xx} for the two devices.

ture and saturates at about 30 K. The metallic behavior is observed for both thin and thick ribbons as well as for previously reported Bi_2Se_3 nanoribbons/nanowires with different thicknesses [21, 33]. This dependence is expected since the Bi_2Se_3 nanostructures grown by PVD method usually have native defects such as selenium vacancies, which act as electron donors ($n-$type doping) [34, 35]. We measured the magnetoresistance R_{xx} as a function of a magnetic field (up to 12 T) applied perpendicularly to the surface of the nanoribbons at low temperatures (2 K). Thin Bi_2Se_3 nanoribbons with thickness below 15 nm show well-pronounced magnetoresistance oscillations in the entire range of the magnetic fields, while for thicker nanoribbons they are only visible at high fields (Fig. 5b). As we will discuss, this difference can be explained by the coherent scattering of electron waves from surface irregularities associated with the peculiar morphology of the thin nanoribbons (due to different growth mechanisms compared to the thicker ones), which leads to the appearance of AAS-like orbits. The Hall resistance R_{xy} was also measured to estimate the sheet carrier density n_{2D} of individual nanoribbons (Fig. 5a). The latter is given by:

$$\frac{1}{n_{2D}e} = \frac{dR_{xy}}{dB} \times g, \qquad (2)$$

where e is the elementary charge, and g is geometrical correction factor. Due to overlapping of the nanoribbon with contact electrodes (the non-ideal Hall bar geometry, see Fig. 4), the measured Hall voltage needs to be corrected [36]. Using a finite element simulation method (COMSOL Multiphysics), we numerically solved the current continuity equation and obtained the correction factor $g \approx 4$ for our Hall bar geometries and contact resistances [19]. The values of n_{2D} extracted from the data are respectively 1.2×10^{13} cm^{-2} for **Device I** (thickness $t = 12$ nm, and width $w = 360$ nm), and 8.8×10^{12} cm^{-2} for **Device II** (thickness $t = 22$ nm, and width $w = 310$ nm), while the negative slope indicates n-type carriers for both devices.

For the thick nanoribbon ($t = 22$ nm, **Device II**), pronounced oscillations were found by subtracting a polynomial background and plotting the data in $1/B$ (see inset of Fig. 6a). The observed oscillations are associated with a quantum phenomenon known as Shubnikov-de Haas oscillations and can be related to the extreme cross-sectional area of the Fermi surface in momentum-space via the Onsager relation [33, 37]. Fourier transform (FT) analysis on the SdH oscillations was carried out to determine the oscillation frequencies. Due to the small number of oscillation periods observed in the field range of the measurements, the resolution of the FT power spectrum

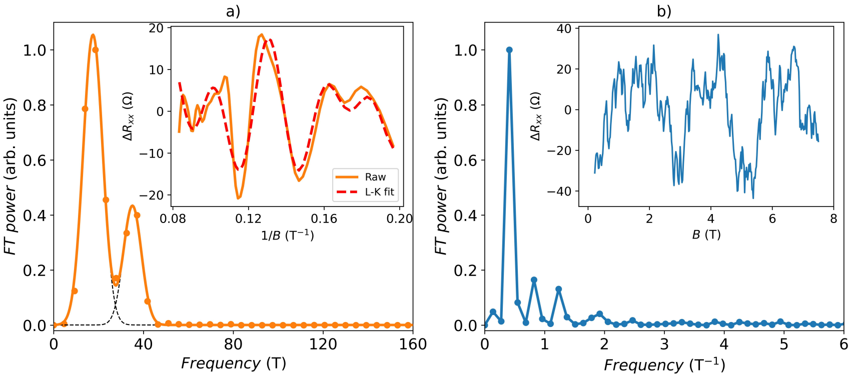

FIG. 6. Power spectra of a) ΔR_{xx} (shown in the inset) for a 22 nm thick (**Device II**) nanoribbon and b) $\Delta R_{xx}\,(B)$ (in the inset) for a 12 nm thick ribbon (**Device I**) measured at 2 K, respectively. A 5^{th}-order polynomial was subtracted to remove the magnetoresistance background from the data. The dot marks correspond to the experimental data extracted from the FT power spectra. The black dashed lines represent the Gaussian fits of the experimental points for two observed peaks (panel a)). The solid line represents the sum of Gaussian fits. The red dashed line in the inset of panel a) represents the multi-frequency Lifshitz-Kosevich fit of experimental data.

TABLE I. The parameters obtained by fitting of the spectrum shown in the inset of Fig. 6a (**Device II**) by the multi-component Lifshitz-Kosevich function. Error bars represent one standard deviation of the fitting parameters.

ΔR_{0-1}, Ω	τ_{D-1}, s	φ_1	F^{II}_{1-LK}, T	ΔR_{0-2}, Ω	τ_{D-2}, s	φ_2	F^{II}_{2-LK}, T
24.0±0.04	$(3.6\pm0.4)\times10^{-13}$	0.44±0.09	23.6±0.7	42.0±0.02	$(2.4\pm0.2)\times10^{-13}$	−0.21±0.07	35.9±0.6

is low. So, the experimental FT datapoints were fitted with a Gaussian approximation to determine the oscillation frequency more accurately. The least-square algorithm (chi-square minimization) iteratively minimized the deviation of the experimental data from the theoretical (Gaussian) model. One standard deviation of the fitting parameter defines the error bars when determining the frequency (Fig. 6a). The FT data fit of the oscillations reveals a dominant frequency $F_1^{II} = 17.5\pm4.3$ T and an additional (second) frequency $F_2^{II} = 35.1\pm4.0$ T, corresponding to $n^{II}_{2D\_1} = 4.23\pm1.04 \times 10^{11}$ cm^{-2} and $n^{II}_{2D\_2} = 8.49\pm0.97 \times 10^{11}$ cm^{-2} according to the Onsager relationship, respectively. The presence of two frequency peaks in a high magnetic field leads to the beating pattern of the SdH oscillations.

The oscillatory component of ΔR_{xx} was also fitted by the Lifshitz-Kosevich expression with a Berry phase included to take into account the topological character of the system [37–43]:

$$\Delta R_{xx} \simeq \Delta R_0 \sqrt{\frac{B}{2F}} R_T R_D \cos\left[2\pi\left(\frac{F}{B} + \frac{1}{2} + \varphi\right)\right], \quad (3)$$

where the first pre-factor ΔR_0 is the amplitude of the oscillation in the high-field limit $1/B \to 0$. The second pre-factor is the temperature reduction factor $R_T = \frac{\lambda m^* T/B}{\sinh(\lambda m^* T/B)}$, with $\lambda = \frac{2\pi^2 k_B T}{\hbar\omega_c} = \frac{2\pi^2 k_B T m^*}{\hbar e B}$, where m^* is the cyclotron mass, T is the temperature, k_B is Boltzmann's constant. The third pre-factor is the Dingle reduction factor representing the exponential decrease of ΔR_{xx} with decreasing field B: $R_D = e^{-\lambda_D}$, with $\lambda_D = \frac{2\pi^2 k_B T_D}{\hbar\omega_c} = \frac{2\pi^2 k_B T_D m^*}{\hbar e B} = \frac{\pi m^*}{\tau_D e B}$, where T_D is the Dingle temperature, τ_D is the Dingle scattering time, which is related to the quantum mobility by $\mu = e\tau_D/m^*$. The oscillation of ΔR_{xx} is described by the cosine term with a frequency F and phase factor $\varphi = \beta - \delta$. The value of the phase offset $\beta = 1/2$ should correspond to Dirac fermions with a π Berry phase, and $\beta = 0$ (or equivalently 1) should correspond to trivial fermions. In turn, the phase shift correction δ is associated with the Fermi-surface dimension ($\delta = 0$ for the 2D Fermi surface and $\delta = -1/8$ or $+1/8$ for the 3D system (− for electrons and + for holes), respectively) [42].

To approximate the complex ΔR_{xx} data, shown in Fig. 6a (inset), the multi-frequency Lifshitz-Kosevich function fit was applied. A fixed value of the cyclotron mass $m^* = 0.15m_e$ [33] was used for the fitting process. The matching of the fit and the raw data is remarkable. Moreover, two fitted frequencies converged to the values obtained from the FT analysis. All obtained fitting parameters are collected in Table I.

The quantum mobility obtained from the quantum relaxation time is: $\mu_1 = 4275$ and $\mu_2 = 2855$ cm^2/V·s, respectively.

The values of the 2D carrier densities extracted from the Hall effect measurements and SdH oscillations show almost an order of magnitude discrepancy. In our previous works we have shown that a charge accumulation layer with $n_{2DEG} \approx 1.0 \times 10^{13}$ cm^{-2} is formed at the nanoribbon-substrate interface and dominates in the Hall conductance [19, 33]. Since the bottom topological surface states (TSSs) overlap with the accumulation layer with much lower mobility [33], SdH oscillations due to this 2DEG do not usually appear in the magnetoresistance. Therefore, we attribute the observed SdH frequency $F^{II}_{1-LK} = 23.6 \pm 0.7$ T to the top Dirac surface states (at the interface of the nanoribbon with vacuum) and $F^{II}_{2-LK} = 35.9 \pm 0.6$ T to the bulk carriers.

As shown in Fig. 5b, thin nanoribbons (less than 15 nm) exhibit instead a strong oscillatory pattern in the entire range of a magnetic field. The phenomenology of these oscillations is compatible with that of universal conductance fluctuation (UCF). The latter represents quantum interferences of electron diffusion paths with different lengths, leading to aperiodic oscillations in magnetic field [44]. However, the FT calculated from $\Delta R_{xx}(B)$ below 7 T (to exclude the possible impact of SdH on the magnetoresistance) shows instead a single (dominant) peak at $F^{I}_{UCF} = 0.41 \pm 0.07$ T^{-1} (Fig. 6b, **Device I**). A well-defined periodicity is unusual for conventional UCF (Appendix A). However, it can be explained if the fluctuations originate from AAS-type orbits, with similar characteristic areas that become accessible because of the specific surface morphology of the thin nanoribbons [45, 46].

The characteristic AAS area of these orbits can be calculated as $S = \phi \times F^{I}_{UCF}$, where $\phi = h/2e$ is the magnetic flux quantum relevant for AAS oscillations. From the extracted orbit area $S = 0.0008$ μm^2 one can estimate a characteristic path length for the electrons as $L \sim 2\sqrt{\pi S} = 100$ nm. The calculated value $2R_{AAS} = 32$ nm (for circular orbits $L = 2\pi R_{AAS}$) is in good agreement with the characteristic size of the surface irregularities of about 29.4±1.6 nm, which was extracted using the two-dimensional fast Fourier transform (2D−FFT) of AFM image presented in the inset of Fig. 3a (Appendix B).

For **Device III** fabricated using a Bi$_2$Se$_3$ nanoribbon with a maximized surface-to-volume ratio (thickness $t = 12$ nm, and width $w = 85$ nm), the $R_{xx}(B)$ pattern changed after a warming up to room temperature, which excludes that the magnetoresistance oscillations can be only attributed to SdH oscillations (Fig. 7a).

In fact, the onset of SdH oscillations requires the condition $\mu B \gg 1$, where μ is the electron mobility. This condition is not usually satisfied below $5-6$ T, since typical Hall mobility values in nanoribbons are between 1200−2100 cm^2/V·s as reported in our previous works [19, 33]. Indeed, the estimated values of Hall mobility obtained for **Device I** and **Device II** are $\mu_1 = 1075$ and $\mu_2 = 1210$ cm^2/V·s, respectively.

To determine whether the UCF comes from interference effects in the bulk or from the 2D topological surface, we have studied the angular dependence of R_{xx} with respect to the out-of-plane magnetic field. In an ideal 2D electron system, the interference pattern depends only on the normal component of the magnetic field $B_\perp = B\cos\theta$, where θ is the angle between the direction normal to the nanoribbon plane and the orientation of the magnetic field [47]. After subtracting a 5^{th}-order polynomial background, the resulting oscillation patterns ΔR_{xx} measured at various angles θ superimpose if plotted against $1/B_\perp$ below 5 T, which confirms the 2D origin of UCF [46] (Fig. 7b).

However, the analysis becomes more complicated at higher fields due to the coexistence of UCF and SdH oscillations. In general, the coherence of the AAS-like orbits associated with the specific morphology of the samples is also observable at higher magnetic fields. To remove the contributions of UCF from the magnetoresistance, we applied a low-pass Butterworth filter to the $R_{xx}(B)$ curve with a cut-off frequency $F^{III}_{c} = F^{III}_{UCF} - 2\delta_G$ (Fig. 7c)), where $F^{III}_{UCF} = 0.83 \pm \delta_G$ T^{-1} is FT frequency extracted from UCF oscillations in a low magnetic field (below 5.5 T, upper panel of Fig. 7d)) and $\delta_G = 0.19$ T^{-1} is the standard deviation of the Gaussian distribution.

The filtered curve was subtracted by a 5^{th}-order polynomial background in the $1/B$ field. As the interference between UCF and SdH oscillations is observed above $5-6$ T, the subtracted curve was considered at magnetic fields above 5.5 T. As in Fig. 6a, the power spectrum data points obtained from the FT of the filtered curve were fitted by a Gaussian approximation. The resulting data fit gives one dominating frequency $F^{III}_{1-FT} = 21.9 \pm 6.8$ T and a second frequency $F^{III}_{2-FT} = 38.6 \pm 3.9$ T, with the corresponding 2D carrier concentrations about $n^{III}_{2D-1} = 5.3 \pm 1.64 \times 10^{11}$ cm^{-2} and $n^{III}_{2D-2} = 9.3 \pm 0.94 \times 10^{11}$ cm^{-2}, respectively (Fig. 7d)). The same filtering procedure of magnetoresistance oscillations was applied to $R_{xx}(B)$ measured at different θ angles.

It should be noted here that due to the different periodicity of the observed phenomena (B-periodic UCF, associated with AAS-orbits [46], and $1/B$-periodic SdH [48]) the low-pass filter can cut off the high-frequency component of SdH oscillations when filtering UCF. However, the Fourier spectrum after filtering shows a similar pattern as compared to a thicker nanoribbon (see **Device II**, Fig. 6a) in which the UCF is not so pronounced, and no filtering was applied for this analysis. This legitimates our procedure.

Finally, to show that the SdH oscillations extracted using the UCF filtering procedure can be attributed to the 2D quantum phenomena, we have studied the dependence of R_{xx} at high magnetic fields ($B \geq 5$ T) as a

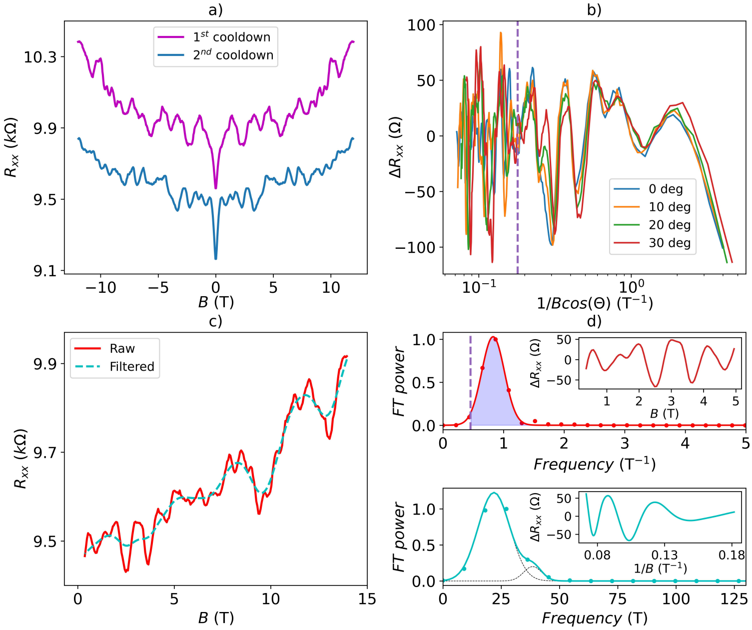

FIG. 7. a) The magnetoresistance of **Device III** (thickness $t = 12$ nm, and width $w = 85$ nm) as a function of a magnetic field after the first and second cooldowns, measured at 2 K. b) Background-removed (5^{th}-order polynomial) resistance ΔR_{xx} as a function of $1/B\cos\theta$. The x-axis is plotted on a logarithmic scale to show a clear data superimposition at low magnetic fields. The vertical dashed line denotes a magnetic field of 5.5 T. c) Filtering data to exclude UCF (**Device III**, $\theta = 30$ deg): the red curve is the original data, and the cyan dashed curve is low-pass filtered data (using cut-off frequency F_c^{III} from the top panel in d)). d) Fourier analyses of $\Delta R_{xx}(B)$ (the top panel) from the low magnetic field region (in the inset) and the obtained oscillations after filtering $\Delta R_{xx}(1/B)$ (the bottom panel (inset)).

function of the angle θ. The plots of ΔR_{xx} in $1/B$ (measured at 2 K) for several angles after applying the filtering procedure are presented in Fig. 8a. Since the resolution of the FT spectrum is low, the filtered ΔR_{xx} curves for different angles of the magnetic field were fitted by the multi-frequency Lifshitz-Kosevich function (Eq. 3) using the least-squares method. The fitted curves are presented by red dashed lines in Fig. 8a, and the corresponding fitting parameters are listed in Table II.

The frequencies $F_{1-LK}^{III} = 25.02 \pm 0.09$ T and $F_{2-LK}^{III} = 46.4 \pm 0.11$ T are very similar to the frequency values obtained using FT ($F_{1-FT}^{III} = 21.9 \pm 6.8$ T and $F_{2-FT}^{III} = 38.6 \pm 3.9$ T, Fig. 7d bottom panel). The carrier mobility: $\mu_1^{III} = 8980$ and $\mu_2^{III} = 1830$ cm^2/V·s was obtained from the Dingle scattering time ($\mu = e\tau_D/m^*$). Such a high quantum mobility (up to 10000 cm^2/V·s) was previously observed in our nanoribbons with a thickness below 30 nm [33]. The angular dependence of the obtained frequencies is presented in Fig. 8b. It is clearly visible that F_{1-LK}^{III} follows the $1/\cos\theta$ trend (typical for 2D electron systems), while F_{2-LK}^{III} exhibits a weak angular dependence, which is typical for bulk electrons [33, 40]. Thus, the high mobility, angular dependence $1/\cos\theta$ together with the phase factor $\varphi \approx 0.5$ allow us to conclude that the frequency F_{1-LK}^{III} corresponds to carriers from surface states, and the frequency F_{2-LK}^{III} represents bulk carriers. This assumption is further confirmed by measurements with an applied back-gate voltage (Fig. 9).

The R_{xx} as a function of the gate voltage has been studied for **Device III** (Fig. 9). When the back-gate voltage $V_g = -8$ V is applied to the nanoribbon, frequency $F_{1\_0V\_LK}^{III} = 21.7 \pm 0.01$ T changed slightly to $F_{1\_-8V\_LK}^{III} = 21.3 \pm 0.02$ T, while the second frequency $F_{2\_0V\_LK}^{III} = 49.1 \pm 0.01$ T shifted to $F_{2\_-8V\_LK}^{III} = 38.8 \pm 0.03$ T. Due to screening effects, the gate voltage should first be able to deplete the layers closest to the interface. Indeed, it has been recently reported that for Bi$_2$Se$_3$ nanoribbons as thin as 9 nm [19] the effect

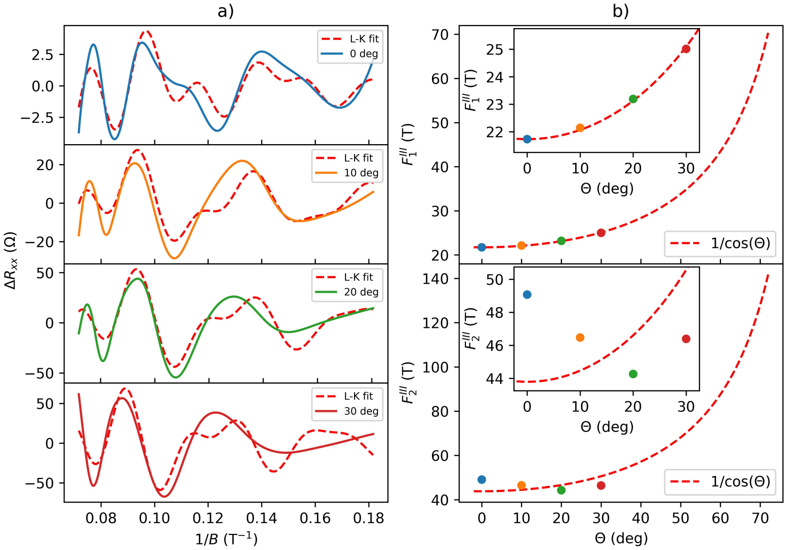

FIG. 8. a) Shubnikov-de Haas oscillations of a Bi_2Se_3 nanoribbon (**Device III**) after subtracting the background and UCF. The curves are fitted by the multi-frequency Lifshitz-Kosevich function (red dashed lines). b) SdH oscillation frequencies obtained from the Lifshitz-Kosevich fit as a function of the applied magnetic field angle (the color of the dots corresponds to the color in panel a)). The measurements were carried out at a temperature of 2 K. The red dashed lines represent the $1/\cos\theta$ fit. Insets are the zoom-in region to show a clear dependence of F^{III}_{1-LK} as a function of angle and a weak angular dependence for F^{III}_{2-LK}.

TABLE II. The parameters obtained by fitting of the spectra shown in Figs. 8a and 9b (**Device III**) by the multi-component Lifshitz-Kosevich function. Error bars represent one standard deviation of the fitting parameters.

θ, deg	ΔR_{0-1}, Ω	τ_{D-1}, s	φ_1	F^{III}_{1-LK}, T	ΔR_{0-2}, Ω	τ_{D-2}, s	φ_2	F^{III}_{2-LK}, T
0	6.0±0.002	(7.7±0.51)×10^{-13}	0.36±0.01	21.7±0.01	39.9±0.003	(1.6±0.09)×10^{-13}	−0.23±0.011	49.1±0.01
10	51.6±0.001	(7.7±0.07)×10^{-13}	0.49±0.09	22.1±0.08	192.8±0.03	(1.6±0.07)×10^{-13}	0.08±0.013	46.5±0.02
20	98.5±0.009	(7.7±0.09)×10^{-13}	0.42±0.06	23.2±0.06	397.4±0.05	(1.6±0.06)×10^{-13}	0.29±0.092	44.3±0.08
30	118.6±0.021	(7.7±0.48)×10^{-13}	0.37±0.09	25.0±0.09	546.1±0.08	(1.5±0.09)×10^{-13}	0.26±0.108	46.4±0.11
0 (−8 V)	77.3±0.006	(7.9±0.57)×10^{-13}	0.26±0.02	16.7±0.01	199.9±0.03	(2.3±0.14)×10^{-13}	−0.19±0.013	28.7±0.01

of the back-gate on the top surface electrons becomes visible only after full depletion of the bottom surface states and the accumulation layer. This fact confirms that the SdH oscillations with frequency F_1^{III}, observed in our measurements belong to the top surface states , while the second frequency F_2^{III} is attributed to the bulk states.

We now argue that size quantization effects are essential in our devices. In addition to the expected shift of frequency F_2^{III} and the increase of the resistance due to the depletion of the nanoribbon carriers by the gate, we also observe reproducible oscillations of R_{xx} as a function of back-gate voltage (Fig. 9c).

The band structure of surface carriers in TI nanoribbons is described by the momentum vector k along the nanoribbon axis and the angular momentum l: [49, 50]

$$E_l(k) = \pm\hbar v_F\sqrt{k^2 + \frac{\pi(l)^2}{S}}, \qquad (4)$$

where l is half-integer $\pm\frac{1}{2}$,$\pm\frac{3}{2}$,..., $\hbar$ is the reduced Planck constant, v_F is Fermi velocity (5×10^5 ms^{-1}), S is the cross-sectional area of the nanoribbon. In the following, we will argue that the oscillations observed in $R_{xx}(V_g)$ can be related to the sub-bands formation (Eq. 4). When the chemical potential crosses one sub-band, a new conduction channel becomes accessible, leading to

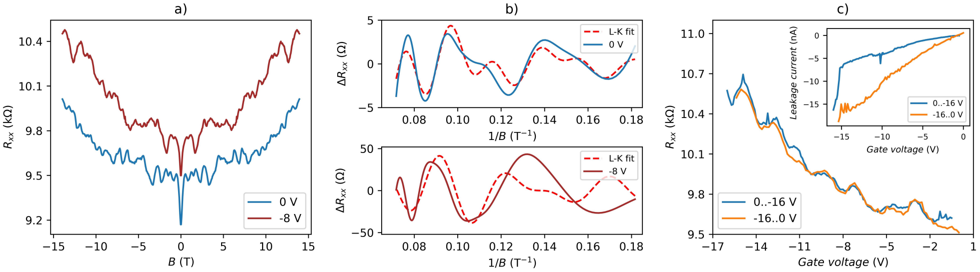

FIG. 9. a) The magnetoresistance of **Device III** as a function of a magnetic field at 0 and −8 V back-gate voltage. The measurements were carried out at a temperature of 2 K. b) Shubnikov-de Haas oscillations after subtracting the background and UCF (at 0 and −8 V back-gate voltage). The curves are fitted by the multi-frequency Lifshitz-Kosevich function (red dashed lines). c) R_{xx} as a function of back-gate voltage. The blue and orange curves represent two scan sweeps with different directions. The leakage current was monitored and kept below 3 % of the measured current during the measurements (the inset).

pronounced resistance dips [49]. To show that $R_{xx}(V_g)$ oscillations are a sign of sub-band structure, we first will calculate the carrier concentration as a function of chemical potential, and in the second step, we will estimate the change in carrier concentration with an applied gate voltage. Finally, we will compare the change in chemical potential due to the applied gate voltage to the number of resistance oscillations we observe in our measurements.

The charge carrier concentration of a trivial 2DEG is given by $n_{2DEG} = k_F^2/2\pi$. The corresponding Fermi energy can be calculated as:

$$E_{F(2DEG)} = \frac{\hbar^2 k_F^2}{2m^*} = \frac{\hbar^2 \pi}{m^*} n_{2DEG}, \tag{5}$$

where k_F is Fermi wavevector, m^* is effective mass, for the Bi_2Se_3 case $m^* = 0.15 m_e$ [33]. For Dirac fermions the carrier concentration is $n_{SS} = k_F^2/4\pi$, and the Fermi energy can be written as:

$$E_{F(SS)} = \hbar k_F v_F = \hbar v_F \sqrt{4\pi n_{SS}}. \tag{6}$$

Considering that the bottom of the conduction band is located 180 meV above the Dirac point [51] one can estimate the position of the Fermi level from the total charge carrier concentration at the substrate/nanoribbon interface using equations 5 and 6. Thus, for a typical carrier concentration in our nanoribbons on a Si/SiO$_2$ substrate of $n = 1.2 \times 10^{13}$ cm^{-2}, the calculated E_F is ≈ 270 meV. The contributions to the total carrier concentration as a function of the chemical potential measured from the Dirac point are shown in Fig. 10, where the blue line represents the bottom TSSs, the red line is the trivial 2DEG, and the yellow one is the sum of the two.

To estimate the carrier concentration change induced by the applied gate voltage, we have numerically computed the capacitance between the back-gate electrode and the bottom surface of the 3D-TI nanoribbon using COMSOL Multiphysics. So, considering a simple asymmetric metallic parallel plate geometry, where one electrode is given by the doped silicon and the other is the nanoribbon, the static surface charge carrier density per applied gate voltage $\sigma \simeq 1.5 \times 10^{-4}$ C/m^{2}V was numerically calculated. Considering this σ, one can estimate the change of the carrier concentration at the bottom interface as $\Delta n = \sigma V_g / e = 1.5 \times 10^{12}$ cm^{-2} for the maximum applied voltage ($V_g = -16$ V). We can assume that the change of carrier concentration occurs mainly in the bottom TSSs, which is justified by the fact that the trivial 2DEG at the bottom extends well inside the bulk, and therefore is screened by the TSS [51]. In this case, the Δn corresponds to a change in the chemical potential of ≈ 45 meV (see Fig. 10). For the dimensions of the nanoribbon in this study (**Device III**), we find that the distance between the sub-band minima $\Delta = h v_F / C \approx 9$ meV, where h is the Planck constant and $C = 2(w + t)$ is the circumference of the nanoribbon with rectangular cross-section [52, 53]. The change in the chemical potential would therefore correspond to the crossing of approximately 5 sub-bands which is very close to the 5 to 6 $R_{xx}(V_g)$ oscillations observed in Fig. 9c.

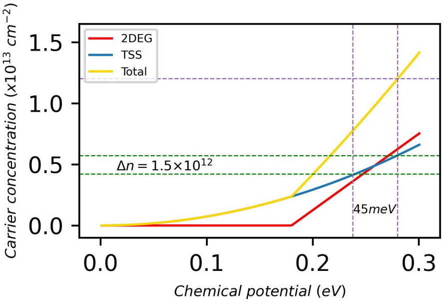

FIG. 10. The charge carrier concentration as a function of the Fermi energy. The red line is the energy dependence in the case of regular 2DEG, the blue line is the energy dependence in the case of Dirac states, and the yellow one is the energy dependence at the substrate/nanoribbon interface, where both types of carriers exist.

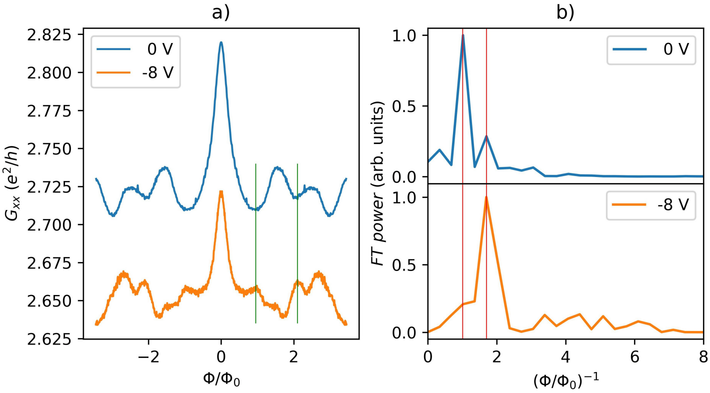

FIG. 11. a) The magnetoconductance as a function of ϕ/ϕ_0 for two different back-gate voltages 0 and -8 V. The measurements were carried out at a temperature of 2 K. b) Fourier transforms of $\partial G_{xx}/\partial(\phi/\phi_0)$ from a).

In the presence of a magnetic field applied along the topological insulator nanoribbon, Eq. 4 can be rewritten as:

$$E_l(k) = \pm\hbar v_F \sqrt{k^2 + \frac{\pi(l - \phi/\phi_0)^2}{S}}, \qquad (7)$$

where $\phi = BS$ is a magnetic flux threading the cross-section area S of the nanoribbon, and, $\phi_0 = h/e$ is the fundamental flux quantum. According to Eq. 7, the energy-momentum relation is periodic in ϕ/ϕ_0, which leads to the appearance of Aharonov-Bohm (AB) oscillations of G_{xx} [50].

In the quasi-ballistic regime, h/e AB oscillations are predicted to dominate over $h/2e$ AAS oscillations [50]. AAS oscillations originate from interference between time-reversed paths, due to weak anti-localization and, thus, differ from AB oscillations in their physical origin. In the quasi-ballistic regime, the circumference of the nanoribbon should not be much longer than the mean-free path l_e. The pattern of these oscillations also depends on the carrier density, which can be changed by applying a gate voltage. At the Dirac point, magnetoconductance minimum at $\phi/\phi_0 = 0$ and maximum at $\phi/\phi_0 = 0.5$ should be observed. However, even away from the Dirac point, the AB phase can alternate with applied gate voltage, when E_F is crossing the sub-bands [50]. Fig. 11a presents the magnetoconductance as a function of two different back-gate voltages (0 and -8 V), demonstrating that maxima and minima at finite magnetic flux alternate with an applied gate and the period oscillation at $V_g = 0$ V is close to ϕ_0 as shown by the Fourier transform of $\partial G_{xx}/\partial(\phi/\phi_0)$ (Fig. 11b).

However, there is also a component in the FT at approximately twice the frequency that can be attributed to AAS. This can be explained by a presence of a strong weak anti-localization peak (Fig. 7a) which indicates that a fraction of the modes has a more diffusive character. Since the gate voltage was not high enough to tune the chemical potential to the Dirac point, the alternating maxima and minima of G_{xx} as a function of gate voltage indicate the crossing of sub-bands by the Fermi level. This behavior has not previously been observed in non-topological systems [50]. The fact that by decreasing the gate voltage the ratio between the AB and AAS inverts (Fig. 11b) might be due to more diffusive modes contributing at $V_g = -8$ V.

III. CONCLUSIONS

In summary, we have presented the growth and transport characterization of ultrathin 3D-TI Bi_2Se_3 nanoribbons synthesized by physical vapour deposition. We show that the nanoribbon growth kinetics can be changed from a 2D layer-by-layer to rough mode by tuning the synthesis parameters. We also find a strong correlation between morphology of the nanoribbons and their transport properties. The oscillatory pattern of magnetoresistance observed over the entire range of the magnetic field for ultrathin nanoribbons is explained by coherent Altshuler-Aronov-Spivak like orbits with the similar characteristic area, which become accessible due to the specific surface morphology. In addition, an interference effect is observed between AAS and SdH oscillations at high magnetic fields. Finally, the ultrathin ribbons also show signatures of size quantization effects, manifesting as an oscillatory behaviour of the magnetoresistance as a function of back-gate voltage. Our ultrathin nanoribbons represent a promising platform to exploit the properties of topological surface states.

ACKNOWLEDGEMENTS

This work is supported by the European Union's Horizon 2020 Research and Innovation Program (Grant Agreement No. 766714/HiTIMe). Authors would like to thank "Vinnova competence center at the Chalmers University of Technology 2D-TECH" and the Latvian Council of Science (project No. lzp/2019/1/0349). K. Niherysh acknowledges the financial support of the "Strengthening of the capacity of doctoral studies at the University of Latvia within the framework of the new doctoral model", identification no. 8.2.2.0/20/I/006. We also acknowledge support from the Swedish infrastructure for micro- and nanofabrication - MyFab.

APPENDIX A: UCF ANALYSIS

Due to the specific surface morphology of our thin nanoribbons, unusually strong periodic conductance oscillations were observed across the entire range of magnetic fields. Here, we performed a more deep analysis of the unconventional behaviour of UCF, to show that these periodic oscillations originate from AAS-type orbits with a similar characteristic area, existing due to the peculiar morphology of the nanoribbons.

Since the conductance G of each sample varies from each other, the root mean square (RMS) of the statistical distribution of conductance fluctuations $\Delta G_{RMS}=\sqrt{\langle(\Delta G^2)\rangle} \approx e^2/h$ with $\Delta G = G - \langle G \rangle$ where $\langle G \rangle$ represents the ensemble averaging, is independent of material, size and degree of disorder and called Universal Conductance Fluctuation (UCF) [54]. Fig. 12a represents ΔG data measured for **Device I**. It is well known that UCF amplitudes decrease on average when the sample dimensions are longer than dephasing length L_φ [54, 55], for example UCF in range from 6 to 0.01 e^2/h have been reported in Bi_2Se_3 [47]. The values of $\Delta G^{I}_{RMS} = 0.049$ and $\Delta G^{III}_{RMS} = 0.01$ e^2/h were calculated for **Device I** and **Device III**, respectively. Considering simple 1D mesoscopic nanoribbon [54] (where only the length of the device is longer than L_φ) for our device's geometries we find that the expected ΔG_{RMS} ranges between 0.015 and 0.03 e^2/h (for L_φ of the order of 300 nm (see ref. [19]), which is comparable with what we calculated above.

As can be seen from Fig. 6b, **Device I** with the exception of the dominant frequency $F^{I}_{UCF} = 0.41 \pm 0.07$ T^{-1} attributed to AAS-type orbits also demonstrates faster oscillations. To investigate the origin of these oscillations, the following analysis was carried out. The contribution to the conductance $\Delta G(B) = \Delta G_{int}(B) + \Delta G_n(B)$ consists of static fluctuations, associated with interference (UCF) $\Delta G_{int}(B)$, and noise components $\Delta G_n(B)$, which are determined by the measuring equipment and the sample. To illustrate the effect of noise

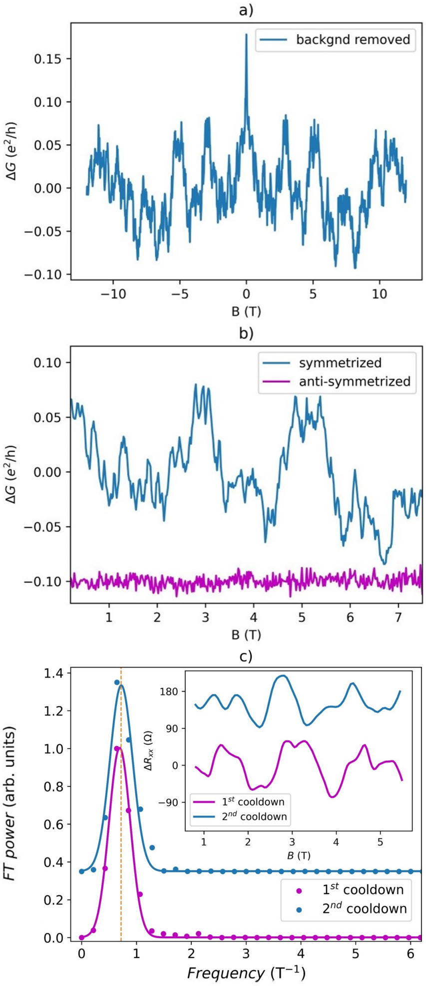

FIG. 12. a) The conductance fluctuations $\Delta G = G - \langle G \rangle$ after subtraction of quadratic polynomial background as a function of magnetic field (**Device I**). b) Splitting the conductance fluctuations from panel a) into the symmetrical $\Delta G_s(B)$ and anti-symmetrical $\Delta G_a(B)$ components. To show the significant difference, the anti-symmetrized curve is shifted by -0.1 e^2/h. c) The Fourier transform of the conductance fluctuations (**Device III**) after subtraction of polynomial background as a function of a magnetic field (inset) measured after first (purple) and second (blue) cooldown. The measurements were carried out at a temperature of 2 K. The dashed orange line represents frequency $F^{III}_{UCF\_1CD} \approx F^{III}_{UCF\_2CD} = 0.72 \pm 0.2$ T^{-1}.

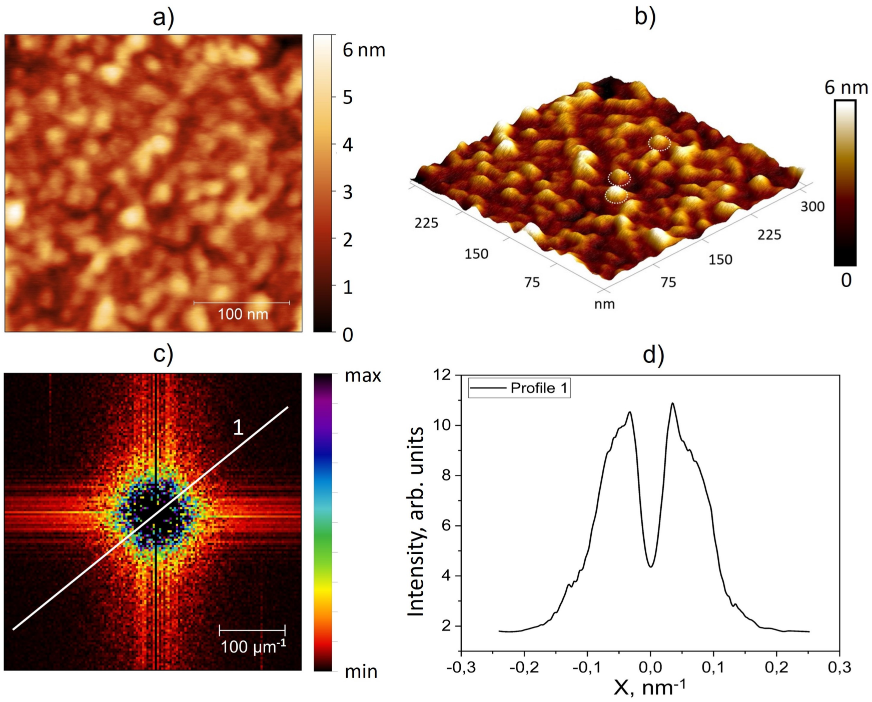

FIG. 13. AFM measurements of a nanoribbon surface (**Device I**). a) Scan size of 310 × 310 nm^2. b) 3D AFM plot of image presented in panel a). White dashed circles delimitate possible AAS orbits. c) The frequency spectrum image of data from panel a). d) Profile 1 taken from 2D FFT-map from panel c): the frequency value at the peak corresponds to 0.034 ± 0.002 nm^{-1}.

on the measured fluctuations, the fluctuations remaining after subtracting the quadratic background (Fig. 12a) have been converted to $\Delta G(B) = \Delta G_s(B) + \Delta G_a(B)$, where $\Delta G_s(B)$ is symmetrized and $\Delta G_a(B)$ is antisymmetrized components. In its turn, the symmetric part is $\Delta G_s(B) = 1/2(\Delta G(B) + \Delta G(-B))$ and the antisymmetric part is $\Delta G_a(B) = 1/2(\Delta G(B) - \Delta G(-B))$, respectively. Since interference-related conductance fluctuations must be symmetrical in the magnetic field [56], $\Delta G_{int}(B)$ can only occur in the symmetrical part of $\Delta G_s(B)$, while the noise component $\Delta G_n(B)$ will be present equally in the symmetric $\Delta G_s(B)$ and anti-symmetric component $\Delta G_a(B)$. Therefore $\Delta G_s(B) = \Delta G_{int}(B) + \Delta G_n^s(B)$, and $\Delta G_a(B) = \Delta G_n^a(B)$ [57]. In Fig 12b the conductance fluctuations $\Delta G = G - \langle G \rangle$ measured for **Device I** are presented as a function of a magnetic field $\Delta G(B)$ converted to symmetric (UCF+noise) and anti-symmetric (noise) components. It is clearly seen, that after splitting the noise component, device still experiences huge oscillations with period ≈ 2.5 T (which we classified as AAS-type oscillations) and the conventional aperiodic UCF.

Another possible mechanism explaining B-periodic oscillations of transport modes is the Sondheimer size effect [58, 59]. However, Sondheimer oscillations (SO) should influence both longitudinal and transverse magnetotransport channels. Due to the significantly larger value of R_{xx} than the Hall resistance R_{xy} the SO should be more clearly visible against the background during Hall measurements, and should also be present in the longitudinal channel [58]. Nevertheless, in our particular case (**Device I**), the measured Hall effect is linear, while pronounced oscillations are observed only in the $R_{xx}(B)$ dependence (Fig. 5a). Although derived to describe surfaces, the Fuchs-Sondheimer theory [60, 61] does not consider the influence of surface states and quantum size effects in the case of topological insulators [62, 63]. All the above-mentioned facts allow us to exclude the SO mechanism from the explanation of the transport properties of thin TI nanoribbons.

Since we associate periodic UCF fluctuations with the peculiar morphology of the nanoribbon surface, which may differ from sample to sample, we specified the UCF frequency for each measured device. For instance, $F^{I}_{UCF} = 0.41 \pm 0.07$ T^{-1} for **Device I** and $F^{III}_{UCF} = 0.72 \pm 0.2$ T^{-1} for **Device III**, respectively. We also checked the change in UCF frequency after the first and second cooldowns for **Device III**. As can be seen from Fig. 12c (inset), the oscillation pattern looks completely different for different cooldowns, however the FT of oscillations in a magnetic field below 5.5 T shows the same frequency $F^{III}_{UCF-1CD} \approx F^{III}_{UCF-2CD} = 0.72 \pm 0.2$ T^{-1}. Moreover, a shift of the above-mentioned frequency following $1/\cos\theta$ trend, when angle θ increases from 0 up to 30 deg ($F^{III}_{UCF-0deg} = 0.72 \pm 0.2$ and $F^{III}_{UCF-30deg} = 0.83 \pm 0.19$ T^{-1} (Fig. 7d)) was observed. This fact together with a clear alignment (superposition) of magnetoresistance fluctuations associated with the UCF as a function of the perpendicular component of the magnetic field $B_{\perp} = B\cos\theta$ (Fig. 7b) indicates the 2D nature of the UCF [46, 64] and is consistent with the hypothesis about Altshuler-Aronov-Spivak like orbits associated with the morphology of nanoribbons.

APPENDIX B: AAS-TYPE ORBITS SIZE DETERMINATION

To calculate the averaged size of AAS orbits an additional high-resolution AFM measurement was performed for a nanoribbon from **Device I** (Fig. 13a-b). To determine the characteristic size of the irregularities, the surface morphology was analyzed using the two-dimensional fast Fourier transform (2D-FFT).

Fig. 13c shows the frequency spectrum image. In the case of isotropic material, the power spectrum is radially symmetric, and a radial distribution can be distinguished. From the averaged distribution of the power spectrum intensity one can extract the averaged frequency and, therefore, the averaged diameter of the orbits. From the profile shown in (Fig. 13d), we determined the dominant frequency of 0.034±0.002 nm^{-1} using a Gaussian fit. This frequency corresponds to a characteristic length scale in the real space of the original image [65]. The extracted averaged size (diameter) of possible orbits $L = 29.4 \pm 1.6$ nm is in good agreement with a characteristic diameter of AAS orbits ($2R_{AAS} = 32$ nm), extracted from the transport measurements.

---

[1] J. Manousakis, A. Altland, D. Bagrets, R. Egger, and Y. Ando, Majorana qubits in a topological insulator nanoribbon architecture, Physical Review B **95** (2017).

[2] S. D. Sarma, M. Freedman, and C. Nayak, Majorana zero modes and topological quantum computation, npj Quantum Information **1**, 1 (2015).

[3] X. Sun, B. Li, E. Zhuo, Z. Lyu, Z. Ji, J. Fan, X. Song, F. Qu, G. Liu, J. Shen, and L. Lu, Realization of superconducting transmon qubits based on topological insulator nanowires, Applied Physics Letters **122** (2023).

[4] T. W. Schmitt, M. R. Connolly, M. Schleenvoigt, C. Liu, O. Kennedy, J. M. Chávez-Garcia, A. R. Jalil, B. Bennemann, S. Trellenkamp, F. Lentz, E. Neumann, T. Lindström, S. E. D. Graaf, E. Berenschot, N. Tas, G. Mussler, K. D. Petersson, D. Grützmacher, and P. Schüffelgen, Integration of topological insulator Josephson junctions in superconducting qubit circuits, Nano Letters **22** (2022).

[5] T. H. Hwang, H. S. Kim, H. Kim, J. S. Kim, and Y. J. Doh, Electrical detection of spin-polarized current in topological insulator $Bi_{1.5}Sb_{0.5}Te_{1.7}Se_{1.3}$, Current Applied Physics **19**, 917 (2019).

[6] F. Yang, S. Ghatak, A. A. Taskin, K. Segawa, Y. Ando, M. Shiraishi, Y. Kanai, K. Matsumoto, A. Rosch, and Y. Ando, Switching of charge-current-induced spin polarization in the topological insulator $BiSbTeSe_2$, Physical Review B **94**, 075304 (2016).

[7] C. M. Acosta and A. Fazzio, Spin-polarization control driven by a rashba-type effect breaking the mirror symmetry in two-dimensional dual topological insulators, Physical Review Letters **122**, 036401 (2019).

[8] H. Park, K. Jeong, I. H. Maeng, K. I. Sim, S. Pathak, J. Kim, S. B. Hong, T. S. Jung, C. Kang, J. H. Kim, J. Hong, and M. H. Cho, Enhanced spin-to-charge conversion efficiency in ultrathin Bi_2Se_3 observed by spintronic terahertz spectroscopy, ACS Applied Materials and Interfaces **13**, 23153 (2021).

[9] T. H. Wang and H. T. Jeng, Topological insulator nanoribbons – a new paradigm for high thermoelectric performance, Nano Energy **66**, 104092 (2019).

[10] Y. Xiong, G. Zhou, N. C. Lai, X. Wang, Y. C. Lu, O. V. Prezhdo, and D. Xu, Chemically switchable n-type and p-type conduction in bismuth selenide nanoribbons for thermoelectric energy harvesting, ACS Nano **15** (2021).

[11] N. X. Yang, Q. Yan, and Q. F. Sun, Linear and nonlinear thermoelectric transport in a magnetic topological insulator nanoribbon with a domain wall, Physical Review B **102**, 245412 (2020).

[12] X. Ye, H. Xu, and X. Zhu, Spin thermoelectric effects of skyrmions in ferromagnetic topological insulators, Journal of Physics D: Applied Physics **56**, 065001 (2023).

[13] R. Saxena, E. Grosfeld, S. E. D. Graaf, T. Lindstrom, F. Lombardi, O. Deb, and E. Ginossar, Electronic confinement of surface states in a topological insulator nanowire, Physical Review B **106**, 035407 (2022).

[14] T. Arakane, T. Sato, S. Souma, K. Kosaka, K. Nakayama, M. Komatsu, T. Takahashi, Z. Ren, K. Segawa, and Y. Ando, Tunable dirac cone in the topological insulator $Bi_{2-x}Sb_xTe_{3-y}Se_y$, Nature Communications **3**, 1 (2012).

[15] S. Jafarpisheh, A. Ju, K. Janßen, T. Taniguchi, K. Watanabe, C. Stampfer, and B. Beschoten, Reducing

the impact of bulk doping on transport properties of Bi-based 3D topological insulators, Physica status solidi (b) **258**, 2000021 (2021).

[16] Z. Ren, A. A. Taskin, S. Sasaki, K. Segawa, and Y. Ando, Optimizing $Bi_{2-x}Sb_xTe_{3-y}Se_y$ solid solutions to approach the intrinsic topological insulator regime, Physical Review B **84**, 165311 (2011).

[17] S. S. Hong, J. J. Cha, D. Kong, and Y. Cui, Ultra-low carrier concentration and surface-dominant transport in antimony-doped Bi_2Se_3 topological insulator nanoribbons, Nature Communications **3**, 1 (2012).

[18] K. Nowak, M. Jurczyszyn, M. Chrobak, K. Maćkosz, A. Naumov, N. Olszowska, M. Rosmus, I. Miotkowski, A. Kozłowski, M. Sikora, and M. Przybylski, Influence of doping on the topological surface states of crystalline Bi_2Se_3 topological insulators, Materials **15**, 2083 (2022).

[19] G. Kunakova, T. Bauch, X. Palermo, M. Salvato, J. Andzane, D. Erts, and F. Lombardi, High-mobility ambipolar magnetotransport in topological insulator Bi_2Se_3 nanoribbons, Physical Review Applied **16**, 024038 (2021).

[20] M. Wiesner, R. H. Roberts, J. F. Lin, D. Akinwande, T. Hesjedal, L. B. Duffy, S. Wang, Y. Song, J. Jenczyk, S. Jurga, and B. Mroz, The effect of substrate and surface plasmons on symmetry breaking at the substrate interface of the topological insulator Bi_2Te_3, Scientific Reports **9**, 1 (2019).

[21] J. Andzane, G. Kunakova, S. Charpentier, V. Hrkac, L. Kienle, M. Baitimirova, T. Bauch, F. Lombardi, and D. Erts, Catalyst-free vapour–solid technique for deposition of Bi_2Te_3 and Bi_2Se_3 nanowires/nanobelts with topological insulator properties, Nanoscale **7**, 15935 (2015).

[22] D. Kong, W. Dang, J. J. Cha, H. Li, S. Meister, H. Peng, Z. Liu, and Y. Cui, Few-layer nanoplates of Bi_2Se_3 and Bi_2Te_3 with highly tunable chemical potential, Nano Letters **10**, 2245 (2010).

[23] A. Rockett, *Physical Vapor Deposition* (Springer, Boston, MA, 2008) pp. 505–572.

[24] M. A. Lovette, A. R. Browning, D. W. Griffin, J. P. Sizemore, R. C. Snyder, and M. F. Doherty, Crystal shape engineering, Industrial and Engineering Chemistry Research **47**, 9812 (2008).

[25] Z. R. Dai, Z. W. Pan, and Z. L. Wang, Novel nanostructures of functional oxides synthesized by thermal evaporation, Advanced Functional Materials **13**, 9 (2003).

[26] Y. Li, Y. Liu, C. S. Lee, and S. T. Lee, Large-scale synthesis of Ga_2O_3 nanoribbons by a two-step gas flow control, Superlattices and Microstructures **46**, 585 (2009).

[27] C. Yan, N. Singh, and P. S. Lee, Morphology control of indium germanate nanowires, nanoribbons, and hierarchical nanostructures, Crystal Growth and Design **9**, 3697 (2009).

[28] Z. L. Wang, Nanobelts, Nanowires, and Nanodiskettes of Semiconducting Oxides - From Materials to Nanodevices, Advanced Materials **15**, 432 (2003).

[29] V. Nebol'sin, E. Levchenko, V. Yuryev, and N. Swaikat, About the Shape of the Crystallization Front of the Semiconductor Nanowires, ACS Omega **8**, 8263 (2023).

[30] M. Elwenspoek and W. Boerhof, Anisotropic growth rate of rough crystal faces, Physical Review B **36**, 5326 (1987).

[31] X. Y. Liu, P. Bennema, and J. P. V. D. Eerden, Rough–flat–rough transition of crystal surfaces, Nature **356**, 778 (1992).

[32] C. J. Tilbury and M. F. Doherty, Modeling layered crystal growth at increasing supersaturation by connecting growth regimes, AIChE Journal **63**, 1338 (2017).

[33] G. Kunakova, L. Galletti, S. Charpentier, J. Andzane, D. Erts, F. Léonard, C. D. Spataru, T. Bauch, and F. Lombardi, Bulk-free topological insulator Bi_2Se_3 nanoribbons with magnetotransport signatures of dirac surface states, Nanoscale **10**, 19595 (2018).

[34] Y. R. Sapkota, *Development of Novel Electronic and Magnetic Thin Films for Next Generation Spintronics Applications*, Ph.D. thesis, Southern Illinois University at Carbondale (2022).

[35] T. R. Devidas, E. P. Amaladass, S. Sharma, R. Rajaraman, D. Sornadurai, N. Subramanian, A. Mani, C. S. Sundar, and A. Bharathi, Role of Se vacancies on Shubnikov-de Haas oscillations in Bi_2Se_3: A combined magneto-resistance and positron annihilation study, Europhysics Letters **108**, 67008 (2015).

[36] L. Barbut, F. Jazaeri, D. Bouvet, and J. M. Sallese, Mobility measurement in nanowires based on magnetic field-induced current splitting method in H-shape devices, IEEE Transactions on Electron Devices **61**, 2486 (2014).

[37] D. Shoenberg, *Magnetic oscillations in metals* (2009).

[38] M. Brahlek, N. Koirala, M. Salehi, N. Bansal, and S. Oh, Emergence of Decoupled Surface Transport Channels in Bulk Insulating Bi_2Se_3 Thin Films, Physical Review Letters **113**, 026801 (2014).

[39] W. Zhao, C. X. Trang, Q. Li, L. Chen, Z. Yue, A. Bake, C. Tan, L. Wang, M. Nancarrow, M. Edmonds, D. Cortie, and X. Wang, Massive Dirac fermions and strong Shubnikov–de Haas oscillations in single crystals of the topological insulator Bi_2Se_3 doped with Sm and Fe, Physical Review B **104**, 085153 (2021).

[40] K. Shrestha, D. E. Graf, V. Marinova, B. Lorenz, and P. C. W. Chu, Simultaneous detection of quantum oscillations from bulk and topological surface states in metallic $Bi_2Se_{2.1}Te_{0.9}$, Philosophical Magazine **97**, 1740 (2017).

[41] J. Xiong, Y. Luo, Y. Khoo, S. Jia, R. J. Cava, and N. P. Ong, High-field shubnikov-de haas oscillations in the topological insulator bi_2te_2se, Physical Review B **86**, 045314 (2012).

[42] A. K. Okazaki, S. Wiedmann, S. Pezzini, M. L. Peres, P. H. O. Rappl, and E. Abramof, Shubnikov–de Haas oscillations in topological crystalline insulator SnTe(111) epitaxial films, Physical Review B **98**, 195136 (2018).

[43] O. Pavlosiuk, P. Swatek, and P. Wiśniewski, Giant magnetoresistance, three-dimensional Fermi surface and origin of resistivity plateau in YSb semimetal, Scientific Reports **6**, 38691 (2016).

[44] H. Pan, K. Zhang, Z. Wei, J. Wang, M. Han, F. Song, X. Wang, B. Wang, and R. Zhang, Nontrivial surface state transport in Bi_2Se_3 topological insulator nanoribbons, Applied Physics Letters **110** (2017).

[45] S. Charpentier, L. Galletti, G. Kunakova, R. Arpaia, Y. Song, R. Baghdadi, S. M. Wang, A. Kalaboukhov, E. Olsson, F. Tafuri, D. Golubev, J. Linder, T. Bauch, and F. Lombardi, Induced unconventional superconductivity on the surface states of Bi_2Te_3 topological insulator, Nature Communications **8**, 1 (2017).

[46] A. Kandala, A. Richardella, D. Zhang, T. C. Flanagan, and N. Samarth, Surface-sensitive two-dimensional magneto-fingerprint in mesoscopic Bi_2Se_3 channels, Nano Letters **13**, 2471 (2013).

[47] Z. Li, T. Chen, H. Pan, F. Song, B. Wang, J. Han, Y. Qin, X. Wang, R. Zhang, J. Wan, D. Xing, and G. Wang, Two-dimensional universal conductance fluctuations and the electron-phonon interaction of surface states in Bi_2Te_2Se microflakes, Scientific Reports **2**, 1 (2012).

[48] L. Schubnikow and W. J. de Haas, Magnetische Widerstandvergrößerung in Einkristallen von Wismut bei tiefen Temperaturen, Leiden Communications **207**, 3 (1930).

[49] F. Münning, O. Breunig, H. F. Legg, S. Roitsch, D. Fan, M. Rößler, A. Rosch, and Y. Ando, Quantum confinement of the dirac surface states in topological-insulator nanowires, Nature Communications **12**, 1 (2021).

[50] S. Cho, B. Dellabetta, R. Zhong, J. Schneeloch, T. Liu, G. Gu, M. J. Gilbert, and N. Mason, Aharonov–Bohm oscillations in a quasi-ballistic three-dimensional topological insulator nanowire, Nature Communications **6**, 1 (2015).

[51] L. Veyrat, F. Iacovella, J. Dufouleur, C. Nowka, H. Funke, M. Yang, W. Escoffier, M. Goiran, B. Eichler, O. G. Schmidt, B. Büchner, S. Hampel, and R. Giraud, Band bending inversion in Bi_2Se_3 nanostructures, Nano Letters **15**, 7503 (2015).

[52] L. A. Jauregui, M. T. Pettes, L. P. Rokhinson, L. Shi, and Y. P. Chen, Magnetic field-induced helical mode and topological transitions in a topological insulator nanoribbon, Nature Nanotechnology **11**, 345 (2016).

[53] J. Ziegler, R. Kozlovsky, C. Gorini, M. H. Liu, S. Weishäupl, H. Maier, R. Fischer, D. A. Kozlov, Z. D. Kvon, N. Mikhailov, S. A. Dvoretsky, K. Richter, and D. Weiss, Probing spin helical surface states in topological HgTe nanowires, Physical Review B **97**, 035157 (2018).

[54] P. A. Lee, A. D. Stone, and H. Fukuyama, Universal conductance fluctuations in metals: Effects of finite temperature, interactions, and magnetic field, Physical Review B **35**, 1039 (1987).

[55] J. G. Checkelsky, Y. S. Hor, M.-H. Liu, D.-X. Qu, R. J. Cava, and N. P. Ong, Quantum Interference in Macroscopic Crystals of Nonmetallic Bi_2Se_3, Physical Review Letters **103**, 246601 (2009).

[56] S. Washburn and R. A. Webb, Aharonov-Bohm effect in normal metal quantum coherence and transport, Advances in Physics **35**, 375 (1986).

[57] T. Bauch, *Quanteninterferenzeffekte und zeitabhängiger elektronischer Transport in metallischen Nanostrukturen*, Ph.D. thesis, Universität zu Köln (2000).

[58] M. R. van Delft, Y. Wang, C. Putzke, J. Oswald, G. Varnavides, C. A. Garcia, C. Guo, H. Schmid, V. Süss, H. Borrmann, J. Diaz, Y. Sun, C. Felser, B. Gotsmann, P. Narang, and P. J. Moll, Sondheimer oscillations as a probe of non-ohmic flow in WP_2 crystals, Nature Communications **12**, 1 (2021).

[59] S. Mallik, G. C. Ménard, G. Saïz, I. Gilmutdinov, D. Vignolles, C. Proust, A. Gloter, N. Bergeal, M. Gabay, and M. Bibes, From Low-Field Sondheimer Oscillations to High-Field Very Large and Linear Magnetoresistance in a $SrTiO_3$-Based Two-Dimensional Electron Gas, Nano Letters **22**, 65 (2022).

[60] E. H. Sondheimer, The Influence of a Transverse Magnetic Field on the Conductivity of Thin Metallic Films, Physical Review **80**, 401 (1950).

[61] K. Fuchs and H. H. Wills, The conductivity of thin metallic films according to the electron theory of metals, Mathematical Proceedings of the Cambridge Philosophical Society **34**, 100 (1938).

[62] N. F. Hinsche, S. Zastrow, J. Gooth, L. Pudewill, R. Zierold, F. Rittweger, T. Rauch, J. Henk, K. Nielsch, and I. Mertig, Impact of the topological surface state on the thermoelectric transport in Sb_2Te_3 thin films, ACS Nano **9**, 4406 (2015).

[63] M. Tang, J. Y. Zhang, S. Bi, Z. L. Hou, X. H. Shao, K. T. Zhan, and M. S. Cao, Ultrathin Topological Insulator Absorber: Unique Dielectric Behavior of Bi_2Te_3 Nanosheets Based on Conducting Surface States, ACS Applied Materials and Interfaces **11**, 33285 (2019).

[64] J. Lee, J. Park, J.-H. Lee, J. S. Kim, and H.-J. Lee, Gate-tuned differentiation of surface-conducting states in $Bi_{1.5}Sb_{0.5}Te_{1.7}Se_{1.3}$ topological-insulator thin crystals, Physical Review B **86**, 245321 (2012).

[65] P. Carmona, M. Röding, A. Särkkä, C. von Corswant, E. Olsson, and N. Lorén, Structure evolution during phase separation in spin-coated ethylcellulose/hydroxypropylcellulose films, Soft Matter **17**, 3913 (2021).

Paper VII

Sensors & Actuators: A. Physical 371 (2024) 115292

Contents lists available at ScienceDirect

Sensors and Actuators: A. Physical

journal homepage: www.journals.elsevier.com/sensors-and-actuators-a-physical

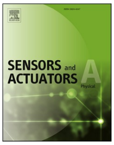

Effect of bending deformation on suspended topological insulator nanowires: Towards a topological insulator based NEM switch

Kiryl Niherysh [a], Liga Jasulaneca [a], Elza Dzene [a], Floriana Lombardi [b], Donats Erts [a,c,*]

[a] *Institute of Chemical Physics, University of Latvia, Raina blvd. 19, Riga LV-1586, Latvia*
[b] *Quantum Device Physics Laboratory, Department of Microtechnology and Nanoscience, Chalmers University of Technology, Kemivägen 9, Gothenburg 41258, Sweden*
[c] *Faculty of Chemistry, University of Latvia, Raina blvd. 19, Riga LV-1586, Latvia*

ARTICLE INFO

Keywords:
Topological insulator
Deformation
Nanoscale electromechanical (NEM) switch

ABSTRACT

Nanodevices consisting of the suspended and supported parts of topological insulator Bi_2Se_3 nanowires were fabricated and measured at low and room temperatures. Probing of topological surface states, accompanied by the electrostatic field effect used to dynamically manipulate bending deformation, was carried out to monitor the external strain introduced into the suspended and supported parts within the same Bi_2Se_3 nanowire. Depending on the device geometry, pure elastic and elastoplastic types of concave deformation, as well as convex buckling deformation, were realized in the suspended parts of the nanowires. For various types of observed deformations, different magnitudes of increase in the Source-Drain resistance of the deformed part compared to the relaxed part of the same devices were determined. All suspended devices exhibit external strain-sensitive Shubnikov-de Haas oscillation frequencies representing the carriers of top and bottom surface states and bulk, whereas, in the case of supported devices, the bottom surface states are masked by a trivial 2DEG. The obtained results may be useful for strain engineering of TI materials, as well as for applications in NEMS and other areas related to suspended nanostructures.

1. Introduction

Suspended devices based on nanosized structures in the form of nanowires (NWs), nanobelts, nanoribbons, and thin films (TF) are successfully implemented in a wide field of various applications in electronics [1-4], biosensing [5-7], gas sensing [10,8,9], photonics [11], thermoelectric performance devices [12,13], nanomechanical resonators [14-16], devices for fundamental phenomena investigations [17, 18], and nanoelectromechanical switches [19-22] due to their small size, low mass, high crystalline quality, significant anelasticity, plasticity, and ultra-high strength [23,24]. Indeed, the coupling of mechanical and other degrees of freedom, such as electrical, spin or optical, allows the creation of novel devices with improved characteristics.

One class of these devices is nanoelectromechanical (NEM) switches, which exploit mechanical and electrical interaction between movable and static elements [22,25,26]. Most of the NEM switches based on suspended TF (graphene) [27,28] or NWs [21,29,30] have previously been demonstrated at room temperature. However, the use of a material with a high melting point, such as molybdenum or silicon carbide, in NEM switches makes it possible to implement devices at high temperatures (up to 800 K) [31,32]. Thus, NEM switches have already proven their superiority as low-voltage [33-35], low standby-power devices [36], and suitability for harsh environment applications [31, 32]. These energy-efficient devices can be used as memory, logical and sensing elements, endowed with high sensitivity and speed. Moreover, the use of a material with suitable physical properties at low temperatures (e.g. graphene, or topological insulators (TIs)) as the active element of NEM switches will lead to new applications in space installations [37] or quantum computing applications [38]. Recently, a NEM switch operating at temperatures as low as 5 K has been demonstrated by our group using a layered topological insulator material – bismuth selenide (Bi_2Se_3) [39].

Three-dimensional topological insulators (3D TIs) are a novel class of quantum materials that are insulating in the bulk, but host conducting topological surface states (TSSs) protected by time-reversal symmetry. Due to spin-momentum locking of Dirac fermions originating from TSSs, the material provides an opportunity to realize a broad range of applications inaccessible in ordinary materials [40,41]. Experimentally accessing TSSs has been a challenge due to a significant contribution from the bulk carriers that place the Fermi level in the bulk conduction

---

[*] Corresponding author at: Institute of Chemical Physics, University of Latvia, Raina blvd. 19, Riga LV-1586, Latvia.
E-mail address: donats.erts@lu.lv (D. Erts).

https://doi.org/10.1016/j.sna.2024.115292
Received 23 November 2023; Received in revised form 26 February 2024; Accepted 18 March 2024

band [42-44]. To overcome this problem (reduce the concentration of bulk carriers), efforts have been aimed at: a) synthesis of 3D TIs with an increased surface-to-volume ratio [45,46], b) introduction of chemical compensating dopants into TI materials [43,47,48], and c) control of Dirac states in TIs by introducing various strain (strain engineering) [49-53]. While the synthesis of reduced-size nanostructures and the compensating doping approaches allow optimization of TI material properties before device fabrication and are irreversible, strain engineering provides a reversible route for modifying the electronic structure in TI-based devices [54]. Since 3D TI materials as Bi_2Se_3, Bi_2Te_3 and Sb_2Te_3 have a tetradymite structure formed by five covalently bonded atomic sheets (e.g., Se–Bi–Se–Bi–Se) defined as a quintuple layer (QL), which are weakly bonded between each other (van der Waals) [40], the bulk band topology of TIs would be expected to be sensitive to uniaxial in-plane stain [54]. Thus, strain is a particularly exciting way to manipulate and control the Fermi level in TIs, since different types of deformations can lead to different properties [55]. For example, strain may lead to phase transitions from topological to trivial states and vice-versa [56,57]. It has been theoretically calculated that the electronic band gap of Bi_2Se_3 decreases with tensile in-plane strain and increases with compressive in-plane strain [58].

TI-based NEM switches could take advantage of both the strain tunability of electronic properties of Bi_2Se_3 and the suitable electromechanical properties for undergoing electromechanical «ON/OFF» switching. Typically, the moment of «ON/OFF» switching is determined by a significant and sharp change in current after closing or opening the contact: in the case of a Source-Drain current a nanorelay configuration is implemented, and in the case of a Gate-Drain current a two-terminal switch is realized. The disadvantage of currently implemented 2-terminal switches based on Bi_2Se_3 nanowires is the large distribution of the geometric dimensions of the synthesized nanostructures, which causes differences in the elastic properties of nanowires. As a result, the balance between «ON» state adhesion and nanowire elastic force is different for individual nanowires, so often when the gate voltage is released, the elastic force of the nanowire does not exceed the adhesion force, and the nanowire can remain in the «ON» state. However, the strain-induced rearrangement of the electronic properties of Bi_2Se_3 makes it possible to continuously control the Source-Drain current not only at the moment of switching but also at all stages of nanowire bending, as well as to monitor the state of the nanowire under different bending modes.

The active element in the form of nanowires used in NEM devices can be repeatedly exposed to external mechanical stress (compression, tension, bending and buckling), which requires excellent resistance to bending fatigue. However, as was recently shown by *Kong at al.* [23], previous studies (theoretical and experimental) have mainly focused on the loading behavior of nanowires (tensile/compressive) in NEMS, while the bending deformation behavior of nanowires remains less studied [59-65].

In this study, based on the sensitivity of TSSs to external strain, we exploited the magnetotransport properties of the suspended and supported parts within the same Bi_2Se_3 nanowire to investigate the effects of nanowire bending/buckling deformation for further use in NEM applications. Temperature dependence of resistance, magnetoresistance as a function of a magnetic field, and Hall effect measurements are used to describe the properties of TI nanowires in relaxed and strained states. The electrostatic field effect was used to deform the nanowire at room and low temperatures. Our results may pave the way towards a single device in which «ON/OFF» switching would be complemented by the possibility of dynamical manipulation of the Fermi level and topological states via electrostatically induced strain.

2. Materials and methods

The free-standing Bi_2Se_3 nanowires were synthesized by vapor-liquid-solid (VLS) growth in a quartz tube furnace on a glass substrate using the Au catalyst nanoparticles, formed by a dewetted ultrathin Au film as described in [66]. For better comparability, nanowires from the same batch were used to fabricate samples for bending experiments. The 7 × 7 mm sized Si/SiO_2 (300 nm) chips were patterned via electron-beam lithography (EBL) to define the shape of the trenches. After that, the pre-patterned chips were etched either by reactive ion etching (RIE) in a mixture of CHF_3 (20 sccm) and O_2 (5 sccm) at 10°C and 200 W power for 8 min (using Cr metal mask) (***Device 1***) or in buffered hydrofluoric acid 7 : 1 (BOE) ($HF : NH_4F = 12.5 : 87.5\%$) for approx. 3 min to fully etch a silicon oxide layer (***Device 2*** and ***3***). Next, Ti/Au (5/95 nm) back-gate contacts were formed by the e-beam evaporator. Then the NWs were transferred to the substrate with the trenches, slightly pressing this chip (a flip-chip method) to the glass with nanowires (***Device 1*** and ***2***). For ***Device 3*** the NWs were suspended in isopropyl alcohol for alignment across the trenches with the gates using floating-electrode dielectrophoresis [39,67]. Supercritical CO_2 drying was used to remove the isopropyl residuals and avoid capillary forces between the nanowire and the gate electrode.

Then, the nanowires transferred across the trenches were patterned using EBL to create electrical contacts. To remove the native oxide layer and provide a robust ohmic contact, the surface of the nanowires was etched off (approximately 3–4 nm) with Ar-ion milling prior to the deposition of the metal electrodes.

The width, thickness and suspended/supported length of the devices were determined using an atomic force microscope (AFM, Bruker Dimension ICON). In-situ transport measurements (2-probe configuration) of ***Device 3*** at room temperature were carried out using a scanning electron microscope (SEM, Hitachi FE-SEM S-4800) equipped with a nanomanipulator.

Tilted SEM images of the devices were obtained using SEM-Zeiss Supra 60 VP. Electron-beam lithography (JEOL JBX 9300FS), Reactive Ion Etcher (Oxford Instruments PlasmaPro Cobra), Ar-ion beam etching (Oxford Ionfab 300 Plus), and vacuum evaporator (Lesker PVD 225) were used to fabricate the trenches and create electrical contacts to the individual nanowires in a cleanroom environment. Magnetotransport measurements were performed in the physical property measurement system PPMS (Quantum Design DynaCool (14 T)) equipped with external electronics at the temperature of 2 K. All devices were measured in DC bias mode. The biasing circuit consists of a voltage source V_b (Keithley 2400), a bias resistor R_b (for current biasing), and a sampling resistor R_s that is used for probing the current supplied to the device (Figs. 1a and 6b). Both the voltage drops across the supported V_{supp} and suspended V_{susp} parts of the device as well as $I_b R_s$ are measured using a setup consisting of two low-noise differential amplifiers (Stanford Instruments) connected to the digital multimeters (Keithley 2000), to get voltages and current across the device, respectively. The gate electrode was connected to another source meter V_b^G (Keithley 2400) through a bias resistor R_b^G with a nominal 1 MΩ to reduce the noise. The Gate-Drain current was simultaneously monitored during applying the back-gate voltage.

3. Results and discussion

3.1. Magnetotransport properties of synthesized Bi_2Se_3 nanowires

After synthesis, several nanowires of different thicknesses (30–120 nm) were characterized in terms of electron transport properties. All nanowires demonstrate nearly linear behavior of the longitudinal magnetoresistance as a function of temperature, which indicates metallic conduction frequently observed in Bi_2Se_3 due to conductive bulk states [68]. Magnetoresistance as a function of a magnetic field measured at 2 K exhibits oscillations at the magnetic field above ~5 T attributed to the Shubnikov–de Haas (SdH) oscillations (quantum transport phenomena representing magneto-oscillations of the resistance in systems with high-mobility electrons at sufficiently low temperatures). They arise as a result of the cyclotron motion of electrons and

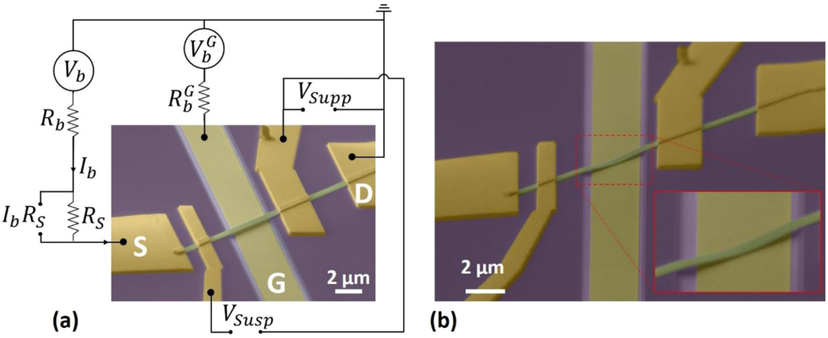

Fig. 1. Tilted false-color SEM images of fabricated ***Device 1*** based on a Bi_2Se_3 nanoribbon (green) transferred onto a Si/SiO_2 substrate (violet), containing an etched trench with a gold back-gate electrode (light-yellow) inside. The metal electrodes are shown in yellow. The device consists of the suspended and supported parts. (a) The device (with the measurements scheme) in the «OFF» configuration (an unstrained suspended wire above the back-gate electrode). (b) The device in the «ON» configuration (a wire is touching the gate). The inset is a zoom-in region showing that the suspended nanowire is deformed by the electrostatic force and attached to the gate.

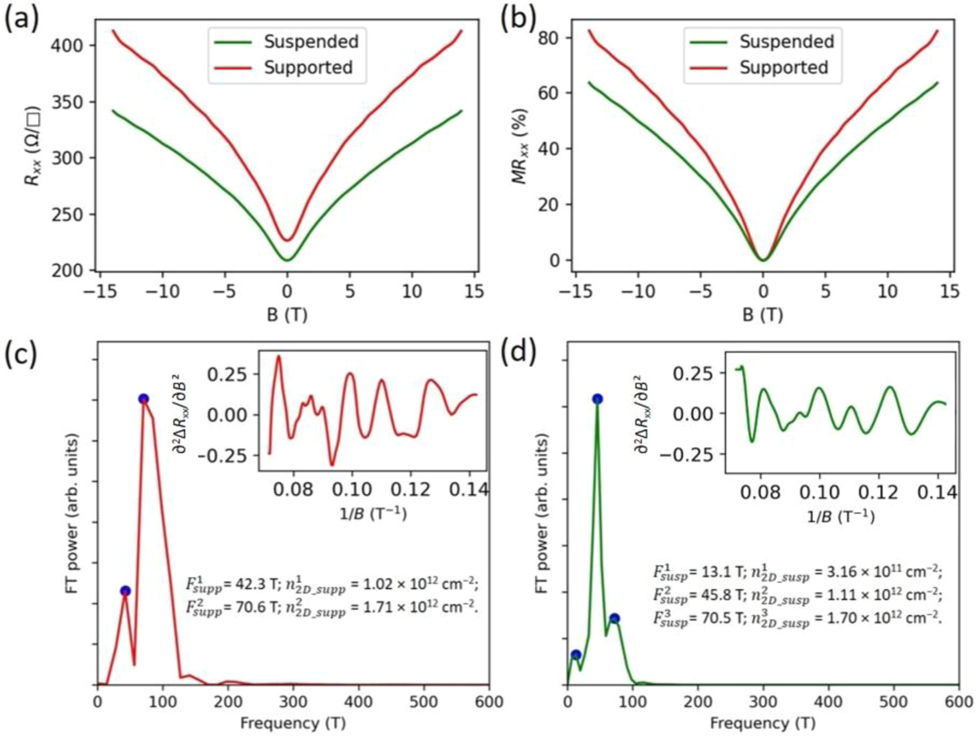

Fig. 2. Magnetotransport measurements of ***Device 1*** presented in Fig. 1a. (a) The longitudinal sheet resistance $R_{xx}(\Omega/\square)$ as a function of a magnetic field for the suspended and supported parts. (b) Magnetoresistance $MR = (R_{xx}(B) - R_{xx}(0))/R_{xx}(0))$ as a function of a magnetic field. Shubnikov-de Haas oscillations analysis: the Fourier transform power spectra of $\partial^2\Delta R_{xx}/\partial B^2$ (presented in the insets) for the supported part shown in (c), and for the suspended part shown in (d), respectively.

the sequential crossings of the discrete Landau Levels through the Fermi energy [69]. These observed oscillations are not strictly periodic in $1/B$, and the Fourier transform (FT) of them reveals a few frequencies, which leads to a beating pattern of the SdH oscillations. Such multiple frequencies for Bi_2Se_3 nanowires with thicknesses above ~30 nm have previously been reported by our group in [46,66,70] and also by other groups [71,72]. The complex pattern of the SdH oscillations originates from the coexistence of the 3D bulk carriers and the 2D topological surface states. Thus, the nanowires synthesized in this study exhibit features of both surface states and bulk carriers, which is consistent with previously observed phenomena in Bi_2Se_3 synthesized by various methods. In general, the transport behavior of measured nanowires is qualitatively the same with transport of the supported parts of the devices presented below.

3.2. Magnetotransport properties of an elastically deformed suspended nanowire

To implement a micron-sized long NEM switch based on a Bi_2Se_3 nanowire, ***Device 1*** containing the supported and the suspended over the trench with the gate electrode parts was fabricated (Fig. 1).

To study the electronic properties and distinguish the difference in Source-Drain transport between the suspended and supported parts of ***Device 1***, the magnetotransport measurements with a magnetic field applied perpendicularly to the nanowire were performed at 2 K. Fig. 2a represents the longitudinal sheet resistance, calculated as R_{xx} (Ω/□)= $R_{xx}(\Omega)\times w/L$, where w is the actual nanowire width and L is the distance between the longitudinal contacts, as a function of a magnetic field. The value R_{xx}(Ω/□) is slightly different for the suspended and supported parts. We attribute this difference to the influence of contact resistance in the case of supported part measurements (three-probe configuration). Since the values of R_{xx} are different, we plot magnetoresistance MR= $(R_{xx}(B)-R_{xx}(0))/R_{xx}(0))$ as a function of a magnetic field to show the difference between two parts within one nanowire (Fig. 2b).

For both suspended and supported parts of the wire, the ΔR_{xx} oscillations were found by subtracting a polynomial background. This effect is associated with the Shubnikov-de Haas oscillations. The Fourier transform of the $\partial^2\Delta R_{xx}/\partial B^2$ for the supported part reveals only two frequencies F^1_{supp}=42.3 T and F^2_{supp}=70.6 T. Following the Onsager relation [73], these frequencies correspond to $n^1_{2D\_supp}=1.02\times10^{12}$ cm^{-2} and $n^2_{2D\_supp}=1.71\times10^{12}$ cm^{-2}, respectively (Fig. 2c). A similar multi-frequency pattern (with two dominating frequencies) for Bi_2Se_3 nanoribbons with thicknesses above 30 nm was previously observed by our group [46]. Since the surface states (at the substrate-nanowire interface) are overlapped with the charge accumulation layer having lower charge carrier mobility, the bottom surface SdH oscillations do not usually appear in magnetoresistance. Moreover, these frequencies (previously observed in [46]) were unaffected by the applied gate voltage (up to −75 V), indicating that they correspond to either bulk or surface state carriers at the top surface (at the nanoribbon-vacuum interface) [45,46,74]. Thus, we attribute observed F^1_{supp} and F^2_{supp} to the top surface states at the interface with vacuum and to the bulk, respectively.

For the suspended part, the FT of the $\partial^2\Delta R_{xx}/\partial B^2$ oscillations demonstrates three frequencies: F^1_{susp}=13.1 T, F^2_{susp}=45.8 T and F^3_{susp}=70.5 T, which correspond to $n^1_{2D\_susp}=3.16\times10^{11}$ cm^{-2}, $n^2_{2D\_susp}=1.11\times10^{12}$ cm^{-2} and $n^3_{2D\_susp}=1.70\times10^{12}$ cm^{-2}, respectively (Fig. 2d). We attribute the appearance of the third (lowest) frequency to the states from the bottom surface, which are no longer masked by the accumulation layer. Since the SdH frequencies of TI are sensitive to external strain [53], the fact that the frequencies corresponding to the top surface states for the suspended and supported parts remain almost the same is in good agreement with the absence of deformation at the suspended part, as shown in Fig. 1a.

After examination of the suspended and supported parts in a relaxed state, the R_{xx} as a function of the gate voltage has been studied for ***Device 1***.

According to existing analytical models of bending [75,76], the strain of a bent nanowire in the thickness direction can be divided into three types: pure elastic, elastoplastic, and pure plastic deformation (Fig. 3). In the case of pure elastic deformation, the top surface (inner side) of the nanowire experiences compressive stress, while the bottom surface (outer side) is under tensile stress, and there is no stress in the middle (neutral layer (NL)). After removing the bending moment M, the elastic deformation will be restored. As shown in [77], if the radius of bending curvature R is much larger than the substrate thickness t and the dominant deformation occurs in the longitudinal direction, the bending strain can be calculated using the formula of the continuum mechanics model for elastic beams: $\varepsilon = t/2\,R$. In the case of elastoplastic deformation, the NL is displaced from the centroid of the cross-section due to the mass conservation effect, which induces a transition of tensile/-compressive stresses across the thickness of the nanowire. The direction of NL displacement is related to the material properties and the bending curvature. In most cases (for materials with similar behavior under compressive/tensile stresses), the neutral layer is shifting towards the center of curvature. After releasing the bending moment M, the elastic deformation is restored, but the plastic deformation remains, which leads to deviations in the dimensions of the nanowire. If the stretching applied during the bending process is large enough, NL can extend beyond the cross-section, thus the stress gradient across the thickness of the nanowire will reduce and elasticity will decrease sharply (plastic deformation) compared to the pure bending effect [76].

Applying a negative voltage to the gate electrode first of all leads to the formation of oppositely charged carriers (depletion layer) at the bottom surface of the naturally n-doped nanowire. As far as a depletion layer is formed, an electrostatic attractive force acts on the wire uniaxially bending it towards the gate (Fig. 1b). A similar procedure occurs if a positive voltage is applied to the gate electrode. First, an accumulation layer (negatively charged carriers) is formed at the bottom surface of the nanowire, and then, as a consequence, the nanowire bends towards the gate under the influence of the electrostatic attractive force. During such bending, the top surface of the nanowire experiences compressive stress, while the bottom surface is under tensile stress (Fig. 3b). When a negative voltage is applied to the device, there is a clear increase in the resistance of the suspended part (Fig. 4a bottom panel), while the resistance of the supported part remains unchanged (Fig. 4a top panel (inset)). As the dielectric constant of SiO_2 (ε_{SiO2}=3–4) [78] is higher than that of vacuum (ε_{vac}=1) [79], the effect of changing Fermi energy via the gating effect (at the initial moment when the distance to the wire is the same) should be more effective in the case of the supported wire, even in the presence of the accumulation layer, since the trivial 2DEG at the bottom extends well inside the bulk, and is therefore screened by topological surface states [72]. Thus, we attribute the change in resistance when the wire is suspended to the mechanical deformation (bending towards the gate).

During the gate voltage sweep, the current between the gate electrode and the nanowire I_{GD} (similar to 2-terminal switches[20,25,29,39,67]) also was monitored (Fig. 4a top panel). At a certain point (−1.45 V) the I_{GD} starts increasing because the distance (separation) between the nanowire and the gate becomes small and a tunneling effect appears. A further increase in the potential at the back gate leads to the emersion of pronounced peaks in the Gate-Drain current and resistance curves. This may be due to the logarithmically increasing tunneling current with decreasing distance [80], as well as the action of additional attractive van der Waals forces that come into play when the distance between the nanosized objects is several nanometers [81]. The change in the resistance slopes (purple dashed lines in Fig. 4a bottom panel) indicates the point of initial action of additional van der Waals forces. At −1.84 V (left orange line in Fig. 4a), I_{GD} starts to increase sharply, which is a sign of the device switching to the «ON» mode. To prove the fact that the increase in Source-Drain resistance (with gate range from 0 to −1.84 V) is

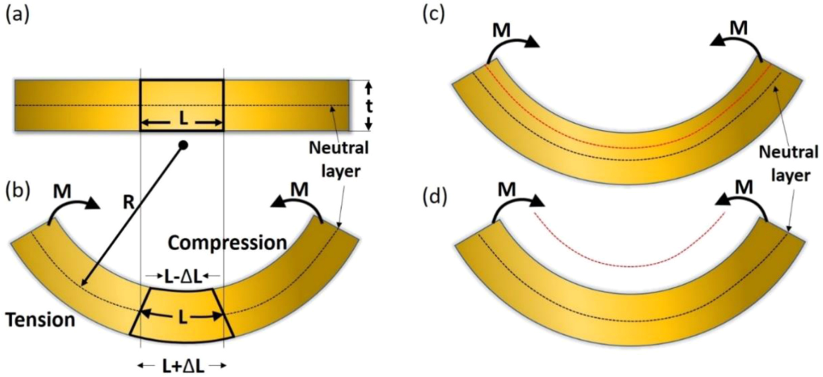

Fig. 3. The scheme of the distribution of various types of deformation along the thickness of the nanowire. (a) A nanowire before bending (relaxed state). (b) A nanowire under elastic deformation. The predominant deformation occurs in the longitudinal direction. (c) A nanowire in elastoplastic deformation regime. (d) Shift of NL beyond the nanowire cross-section (the entire cross-section is under tensile strain) (plastic deformation).

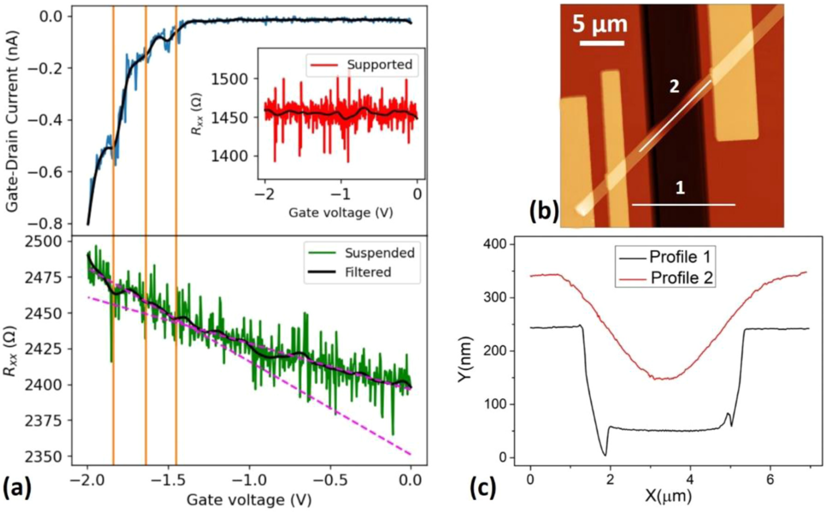

Fig. 4. (a) Gate-Drain current and R_{xx} of the suspended and supported (in the inset) parts as a function of the back-gate voltage (***Device 1***). The blue, red and green lines represent experimental data. The black lines depict filtered data. The vertical orange lines indicate pronounced peaks due to mechanical deformation. The change in the slopes of the two purple dashed lines indicates the point of the initial action of the additional van der Waals forces to the electrostatic attractive force, resulting in faster deformation of the nanowire. (b) AFM image of the device in «ON» mode. (c) Height profile of the bent nanowire, presented in (b).

a result of mechanical deformation and not of the tuning of the Fermi energy due to the field effect, we increased the back-gate voltage to −2 V. After this the Gate-Drain current value increased linearly from ≈ −0.6 nA to −1.7 μA, which means the device is in stable «ON» mode. Even after that, the increased resistance of the suspended part remains at the same value (does not decrease to the initial value before gating/-bending). It is a sign of the deformation effect since the influence of the electric field does not affect the wire anymore. SEM image as well as AFM image and height profile of the bent wire in «ON» mode are presented in Fig. 2b and Figs. 4b and 4c, respectively.

To investigate the strain-induced rearrangement of the electronic properties after bending the wire to the gate contact, magnetotransport of ***Device 1*** was remeasured in «ON» mode at a fixed voltage on the back gate of −2 V. The longitudinal sheet resistance and MR as a function of a magnetic field are presented in Fig. 5a and b, respectively. It is clearly seen, that $R_{xx}(\Omega/\square)$ value of the supported part remains unaffected by the gate voltage, while the suspended part reveals an increase in resistance (3,84%) in comparison with the data presented in Fig. 3. Following the analysis of the SdH oscillations described above, we did not find any difference for the supported part before and after applying

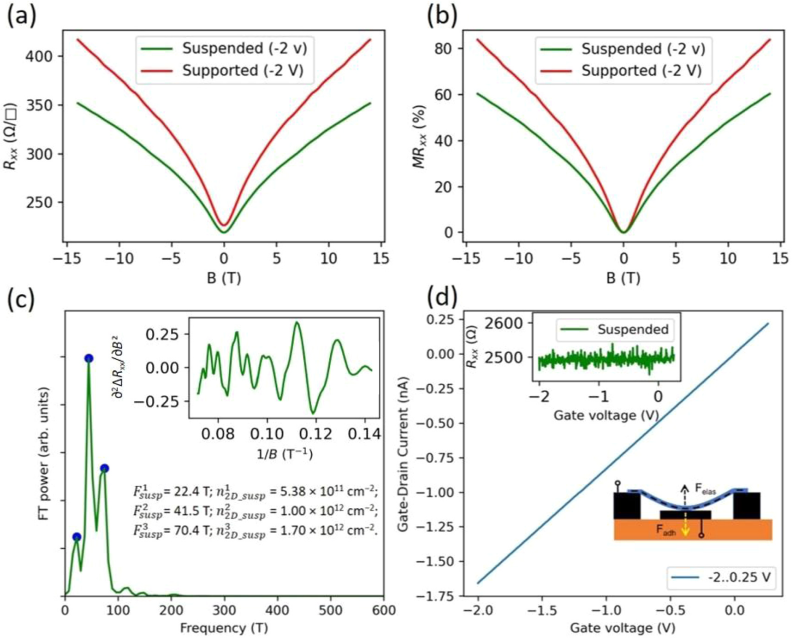

Fig. 5. Magnetotransport measurements of ***Device 1*** presented in Fig. 2b in «ON» regime (with a fixed gate voltage of −2 V). (a) The longitudinal sheet resistance $R_{xx}(\Omega/\square)$ as a function of a magnetic field for the suspended and supported parts. (b) The magnetoresistance MR = $(R_{xx}(B) - R_{xx}(0))/R_{xx}(0))$ as a function of a magnetic field. (c) The Fourier transform power spectra of $\partial^2\Delta R_{xx}/\partial B^2$ (presented in the insets) for the suspended part. (d) Gate-Drain current of the suspended parts as a function of the back-gate voltage after magnetotransport measurements. The top inset is R_{xx} as a function of the gate voltage. The bottom inset is the schematic of «ON» regime of the switch, when $F_{vdW} + F_{elec} > F_{elas}$.

the gate voltage, as expected. However, the suspended part exhibits a slight shift of F_{susp}^{2--2V}=41.5 T ($n_{2D\_susp}^{2--2V}$=1.00×10^{12} cm^{-2}) towards lower frequency in comparison with F_{susp}^{2} =45.8 T ($n_{2D\_susp}^{2}$=1.11×10^{12} cm^{-2}), as well as F_{susp}^{1--2V}=22.4 T ($n_{2D\_susp}^{1--2V}$=5.38×10^{11} cm^{-2}) towards higher value comparing to F_{susp}^{1}=13.1 T ($n_{2D\_susp}^{1}$=3.16×10^{11} cm^{-2}), while the third frequency remains the same $F_{susp}^{3--2V} \approx F_{susp}^{3}$. All values of the SdH frequencies, as well as 2D carrier concentrations in relaxed and deformed states are summarized in Table 1.

Table 1
Deformation type of the nanowire.

	Design	Channel	SdH frequency, T	n_{2D}, cm^{-2}	Deformation	Deformation type	ΔR, %
Device 1	Suspended	Top surface	45.8	1.11 × 10^{12}	relaxed	Relaxed	-
		Bottom surface	13.1	3.16 × 10^{11}	relaxed		
		Bulk	70.5	1.70 × 10^{12}	relaxed		
	Supported	Top surface	42.3	1.02 × 10^{12}	relaxed	Relaxed	-
		Bottom surface	-	-	relaxed		
		Bulk	70.6	1.70 × 10^{12}	relaxed		
Device 1 (−2 V)	Suspended	Top surface	41.5	1.00 × 10^{12}	compression	Elastic	3.84
		Bottom surface	22.4	5.38 × 10^{11}	tension		
		Bulk	70.4	1.70 × 10^{12}	relaxed		
	Supported	Top surface	42.3	1.02 × 10^{12}	relaxed	Relaxed	-
		Bottom surface	-	-	relaxed		
		Bulk	70.6	1.70 × 10^{12}	relaxed		
Device 2	Suspended	Top surface	43.4	6.29 × 10^{11}	compression	Elastoplastic	21.85
	(Deformed)	Bottom surface	25.9	1.05 × 10^{12}	tension		
		Bulk	93.6	2.26 × 10^{12}	compression		
	Supported	Top surface	52.9	1.28 × 10^{12}	relaxed	Relaxed	-
		Bottom surface	-	-	relaxed		
		Bulk	96.9	2.34 × 10^{12}	relaxed		
Device 3	Suspended	Top surface	41.4	1.00 × 10^{12}	tension	Buckled	-1.62
	(Buckled)	Bottom surface	20.7	5.01 × 10^{11}	compression		
		Bulk	69.1	1.67 × 10^{12}	-		

The observed results are consistent with [53,82], where the tensile strain shifts the Dirac point towards lower energies, while compressive strain causes a shift to higher energies. So, the SdH frequencies experience upshift/downshift with tension/compression of the nanowire on the bottom/top surface. We attribute the downshift of $F_{susp}^{2\_-2V}$ frequency (top surface states) to the induced compressive deformation on the top surface of the nanowire and the upshift of $F_{susp}^{1\_-2V}$ (bottom surface states) to the induced tensile deformation on the bottom surface of the nanowire, respectively. The fact that the SdH frequency representing bulk charge carriers remains unchanged after the performed measurements and is identical to the value of the relaxed (supported) part, indicates that the NL is not displaced from the centroid of the nanowire cross-section, and there is a balance of stresses on the top and bottom surfaces, which is a clear sign of elastic deformation regime.

Taking into consideration an elastic deformation regime, the formula $\varepsilon = t/2\ R$ can be used to estimate the amount of nanowire deformation. For given ***Device 1***, the radius of curvature is equal to R=21.5 μm (calculated based on AFM measurements (Fig. 4c)), and therefore the strain is $\varepsilon = 0.22\%$.

After completing the magnetoresistance measurements, the gate swept from −2 to 0.25 V. The Gate-Drain current as well as the gate dependence of resistance for the suspended part are shown in Fig. 5d. The linear behavior of the current-voltage characteristic and the absence of a change in resistance during the sweep indicate that the balance between attractive van der Waals F_{vdW} + electrostatic F_{elec} and repulsive elastic F_{elas} forces is violated ($F_{\text{vdW}} + F_{\text{elec}} > F_{\text{elas}}$), which results in strong attachment of the wire to the gate electrode (Fig. 2b, Fig. 5d bottom inset) [25]. In our case, this procedure was performed intentionally to demonstrate the strain distribution in the nanowire under different «ON» and «OFF» regimes. For the repeatable operation of the device in «ON – OFF» regimes (as in the electromechanical switch), the gate bias voltage must be less than the value of −1.84 V (the left vertical orange line in Fig. 4a).

In summary, uniaxial electrostatic bending of the nanowire towards the gate results in compressive strain on the top surface and tensile strain on the bottom surface, as evidenced by a shift in the SdH oscillation frequencies corresponding to these surfaces. The bulk frequency remains the same for the supported part, suspended and suspended deformed parts, which is a sign of the elastic deformation regime. During the bending process, an increase in the Source-Drain resistance by 3.84% was observed. We associate it with the effect of deformation, since after the switching to «ON» regime the resistance value remained unchanged. To regulate the distance between the nanowire and the gate electrode, an electrostatic potential should be precisely applied. It will allow to monitor the Source-Drain current continuously and to access (at certain gate voltages) the regime in which two parallel currents (Source-Drain current as well as Gate-Drain tunneling current) are present. Simultaneous control of these two currents makes it possible to accurately define the moment when it is necessary to stop bending and consider the nanowire to be in the «ON» regime. As a result, a stable balance is determined between the adhesion force and the elastic force of the nanowire, so when the gate voltage is released, the latter one exceeds the adhesion force and the device should turn into the «OFF» state, and hence the switch can operate in a repeatable manner.

3.3. Magnetotransport properties of an elastoplastically deformed suspended nanowire

To study the electrical and mechanical properties of suspended nanowires in the elastoplastic deformation mode, ***Device 2*** was fabricated. To introduce a plastic component of deformation, a certain amount of strain (greater than in the elastic mode) must be applied to the nanowire, which will cause an irreversible change in geometry. In order to introduce additional strain to the device (for example, due to the load on the sample) without significant change in the fabrication process, it was decided to increase the length of the suspended part. According to the classical beam deformation theory, in the case of the beam fixed at both ends with a uniform continuously distributed load on top, the maximum deflection of the beam at center is $\delta_{\max} = \frac{qL^4}{384EI}$, where q is the uniform load [N/m], L is the distance between fixed ends, E is the modulus of elasticity [Pa·N/m^2], I is the area moment of inertia [m^4] [83]. Indeed, due to $\delta_{\max} \sim L^4$, an increase in L at the same load on the top of the suspended nanowire (for example, a resist) will bend the nanowire more efficiently. Using the property of isotropic etching of SiO_2 with wet chemicals (BOE), we increased the trench width from 3 up to 8 μm. Since ***Device 2*** was fabricated identically to ***Device 1***, the suspended part of the nanowire experienced significant loading (resist and metal), resulting in elastoplastic bending of the nanowire towards the gate electrode. After removal of the loading from the suspended part (Lift-off), the deformation of the nanowire remains even without applying voltage to the back-gate electrode. Representative optical and AFM images of ***Device 2*** with the suspended and supported parts of the nanowire, as well as AFM profile of the deformed nanowire (in «ON» regime) are presented in Fig. 6. The provided geometry of contacts allows independent measurements of the supported and suspended parts of the nanowire in a four-probe configuration, thus eliminating the contact resistance effects. Moreover, the additional pair of Hall bars allows to measure the type and concentration of charge carriers.

Since the stress during elastoplastic deformation is distributed over the nanowire cross-section, the formula $\varepsilon = t/2\ R$ can no longer be used for strain value estimation. We carried out transport measurements to compare the relaxed (supported) part of the nanowire with the suspended part that experienced elastoplastic deformation. This comparison will help to evaluate the effect of strain on the properties of the nanowire.

First, we checked whether the nanowire was touching the gate contact by measuring the current between the gate and the nanowire (I_{GD}), which indicated an open circuit. Then, to measure transport properties in elastoplastic deformation mode, ***Device 2*** was cooled down from room temperature (RT) to 2 K. A metallic temperature dependence of the longitudinal sheet resistances $R_{\text{xx}}(\Omega/\square)$ for the supported and suspended parts was observed (Fig. 7a). As shown in Fig. 7a, the $R_{\text{xx}}(\Omega/\square)$ of the suspended part is higher than that of the supported part (21,85% at 2 K), and we attribute this fact to the bending effect and elastoplastic deformation of the nanowire introduced during fabrication.

To estimate the type and charge carrier's concentration of the examined nanowire (***Device 2***), the Hall resistance R_{xy} was measured as a function of a magnetic field at the temperature of 2 K at the supported part. The negative $R_{\text{xy}}(B)$ slope indicates n-type carriers (Fig. 7a inset). The values of the 2D carrier concentration were calculated from the Hall resistance as [46]: $n_{\text{2D\_Hall}} = (w_{\text{H}}/w)/(e \cdot \partial R_{\text{xy}}/\partial B)$, where w is the actual nanowire width, w_{H} is the distance between the Hall contacts, and e is the elementary charge. The linear fit of the Hall resistance (blue dashed line in the inset of Fig. 7a) in the low magnetic field range depicts the deviation from the linearity at higher magnetic fields (orange dashed line in the inset of Fig. 7a). This non-linearity indicates the contribution of another band (for example an accumulation layer at the interface between the nanoribbon and substrate with different mobility and concentrations of carriers) to the entire transport through the nanowire [45,46,74]. The fitting results of the experimental Hall data yield $n_{\text{2D\_Hall}}$=2.81×10^{13} cm^{-2} and μ_{Hall}=2.02×10^{3} cm^2 (Vs)$^{-1}_{,}$ which are typical values for Bi_2Se_3 nanowires synthesized by our group using physical vapor deposition method [46,66,70,74,84].

Likewise to ***Device 1***, magnetotransport measurements with a magnetic field applied perpendicularly to the nanowire at 2 K were performed for ***Device 2***. The Fourier transform of the $\partial^2\Delta R_{\text{xx}}/\partial B^2$ oscillations for the supported part reveals two frequencies F_{supp}^{1}=52.9 T and F_{supp}^{2}=96.9 T, corresponding to $n_{2D\_supp}^{1}$=1.28×10^{12} cm^{-2} and $n_{2D\_supp}^{2}$=2.34×10^{12} cm^{-2}, respectively (Fig. 7c). Similar to ***Device 1***, we

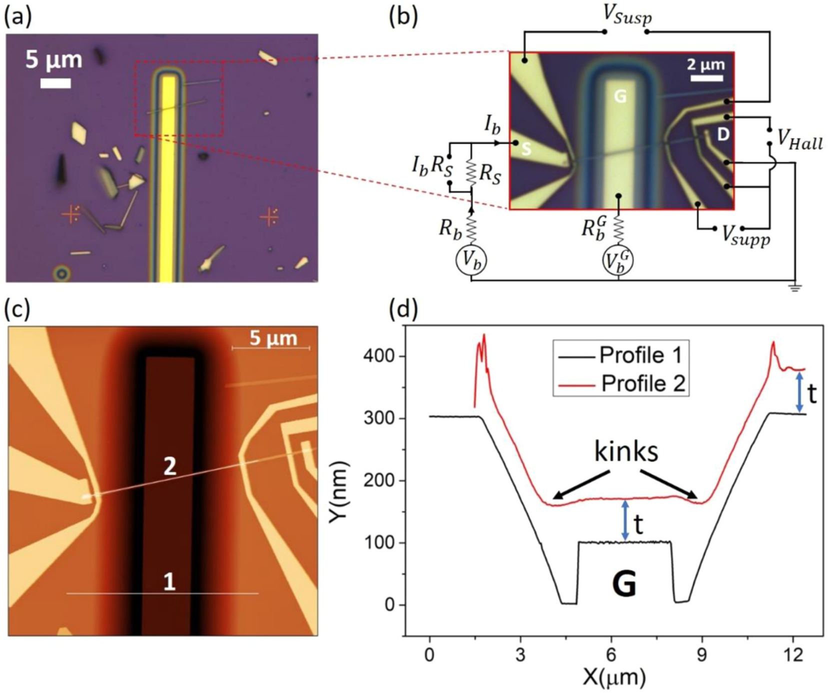

Fig. 6. (a) Optical image of a transferred Bi_2Se_3 nanowire across the pre-patterned trench with a gold electrode inside. (b) Optical image (with measurements scheme) of ***Device 2*** containing the suspended and supported nanowire parts, shown in panel (a). (c) AFM image and (d) corresponding height profiles of ***Device 2***, indicating full mechanical contact («ON» regime) of the nanowire with the gate electrode after applying gate voltage.

attribute observed F^1_{supp} and F^2_{supp} to the top surface states at the interface with vacuum and to the bulk, respectively. It should be noted here, that the deviation from the linearity at high magnetic fields for the Hall effect measurements (Fig. 7a inset) and the discrepancy in 2D carrier concentrations extracted from the SdH oscillations analysis and the Hall effect measurements confirm that the charge accumulation layer formed at the substrate-nanowire interface dominates in the Hall conductance and mask bottom topological surface states.

In the case of the suspended part, the FT of the $\partial^2\Delta R_{xx}/\partial B^2$ oscillations depicts three frequencies: F^1_{susp}=25.9 T, F^2_{susp}=43.3 T, and F^3_{susp}=93.6 T, which according to the Onsager relation correspond to $n^1_{2D\_susp}$=6.29×10^{11} cm^{-2}, $n^2_{2D\_susp}$=1.05×10^{12} cm^{-2}, and $n^3_{2D\_susp}$=2.26×10^{12} cm^{-2}, respectively (Fig. 7d). All observed frequencies are summarized in Table 1. As for ***Device 1***, the lowest frequency F^1_{susp} represents the states from the bottom surface. The frequency F^1_{supp}=52.9 T representing the top surface states carriers under relaxed condition (supported part) exhibits shift to lower frequency F^2_{susp}=43.3 T, indicating compression of the Bi_2Se_3 nanowire on the top surface. Moreover, the frequency representing bulk in the suspended case also experiences a downshift in comparison with the bulk states in a relaxed mode. This means that, due to the elastoplastic deformation regime, the NL is displaced from the centroid of the cross-section towards the center of curvature, and the balance of stresses on the top and bottom surfaces of the nanowire changes (Fig. 3c). This may result in a change in the overall conductance of the wire. Moreover, in [53] it is shown that relaxed or compressed surfaces demonstrate lower mobility of carriers than under tension, therefore $\sigma = en\mu$ for a surface deformed under compression is much lower than under tensile deformation or in a relaxed state, due to lower mobility and charge carrier concentration. Assuming that the top and bottom surface states act as parallel conductive transport channels, decrease of conductance at the top surface results in an increase in the overall resistance of the nanowire. Thus, in the particular case of ***Device 2***, we attribute the higher resistance of the suspended part (in comparison with the supported part (Fig. 7a)) to the effect of elastoplastic deformation of the nanowire.

Since the formula $\varepsilon = t/2R$ is no longer applicable, we tried to evaluate the strain by comparing the resistance for the relaxed and strained modes. As it is shown in [85] for materials based on bismuth chalcogenides, the relative changes in the resistance of the samples $\Delta R/R$ are proportional to ε. Using the coefficient of strain sensitivity $\Delta R/\varepsilon R$, which ranged from 100 to 200 for different samples measured at room temperature [85], the strain ε ≈ 0.27–0.53% (the ratio $\Delta R/R$=0.53 is extracted from Fig. 7a at 300 K) for ***Device 2*** at RT can be roughly evaluated.

Fig. 8a represents the Gate-Drain current of the suspended part as a function of the back-gate voltage. Due to a very short distance between the suspended nanowire and the gate electrode (approximately ten nanometers), upon applying negative gate voltage, the suspended nanowire is immediately attached to the gate electrode (Fig. 8b). This behavior was expected, since basing upon numerical calculation

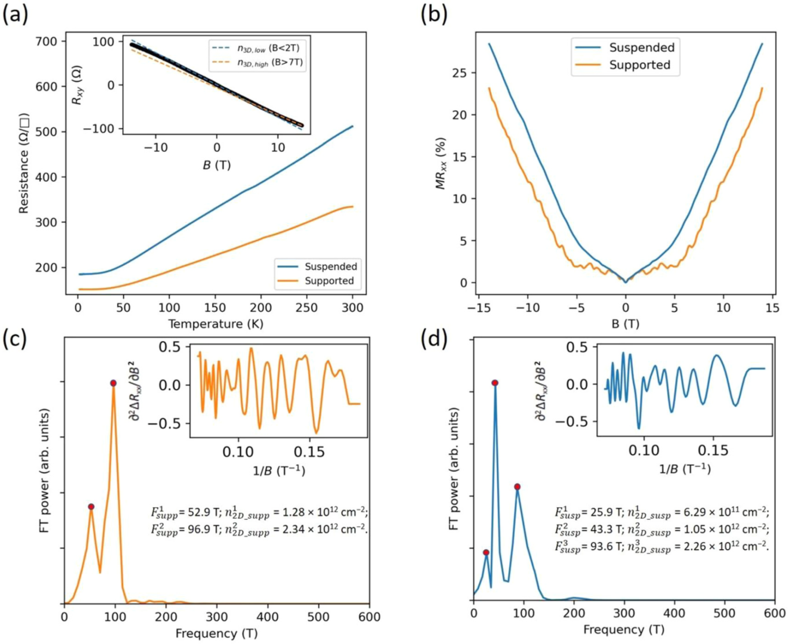

Fig. 7. Magnetotransport measurements of ***Device 2*** presented in Fig. 6. (a) Temperature dependence of R_{xx}(Ω/□) for the suspended and supported parts. The inset is anti-symmetrized Hall effect measurements $R_{xy}(B)$. The blue dashed line is the linear fit in the range from 0 to 2 T, while the orange dashed line is the linear fit in the range from 7 to 14 T. (b) Magnetoresistance MR = $(R_{xx}(B) - R_{xx}(0))/R_{xx}(0)$ as a function of a magnetic field. Shubnikov-de Haas oscillations analysis: the Fourier transform power spectra of $\partial^2\Delta R_{xx}/\partial B^2$ (presented in the insets) for the supported part shown in (c) and for the suspended part shown in (d), respectively.

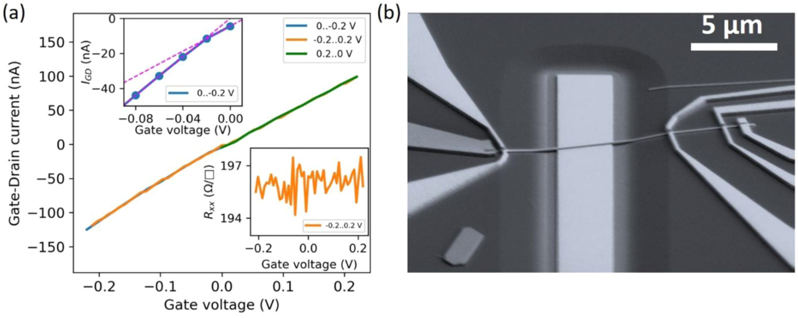

Fig. 8. (a) The gate-drain current measured as a function of the gate voltage for the suspended part of ***Device 2***. The blue, orange, and green curves represent scan sweeps with different directions. The top inset is a zoom-in view of the 0..−0.2 V sweep. The purple dashed lines show the deviation from linearity at −0.02 V, indicating the «ON» state switching. The bottom inset is R_{xx} as a function of the gate voltage, indicating a stable «ON» state even after the gate voltage is removed or swept positively. (b) SEM image of switched «ON» device after performed measurements.

described in [67], we found that for a certain device geometry (nanowire thickness t=71 nm, width w=200 nm, distance between electrodes (suspended part) L_{susp}=9.2 µm, and distance between the gate and nanowire $d\approx$6–8 nm) at back-gate voltage of ≈−25 mV, the nanowire should collapse to the gate electrode. Indeed, the current between the gate electrode and nanowire (I_{GD}), monitored during the gate sweep, shows a linear dependence (with a small deviation around 0 V gate voltage (top inset in Fig. 8a), indicating an ohmic contact between the nanowire and the back-gate electrode (Fig. 8a). After switching to the «ON» state, the Source-Drain resistance of the suspended part R_{xx} (Ω/□) increased by 6.52% compared to the wire resistance in the «OFF» state. Moreover, according to the numerical calculation of the distribution of electrostatic forces near the corner of the gate electrode, the electric field causes an infinite force on an infinitesimal part of the conductor [86], which results in the wire deformation near both sides of the gate (Fig. 6d). The radii of these bends (kinks) are much smaller than the radius of curvature of the suspended device, which causes large localized deformations. Turning off the back-gate voltage does not lead to the detaching of the nanowire from the gate. The increased Source-Drain resistance persists after the gate voltage is removed (bottom inset in Fig. 8a). We attribute this fact to the presence of van der Waals interaction between the wire and the gate electrode. Due to the very large contact area, as well as to the plastic deformation (kinks) of the nanowire, it leads to the changes in the geometry of the device. Figs. 6b and 8b show AFM and SEM images of ***Device 2*** after the measurements were performed. It is clearly visible, that the nanowire is lying on the surface of the gate electrode. According to AFM data, the bending radius of the suspended part of ***Device 2*** is equal to ≈ 53 μm, and the radii of small kinks are ≈ 23,4 μm. The overall nature of strain in the switched-«ON» ***Device 2*** becomes more complicated due to the presence of localized (at the kinks) deformations. The magnitudes of the change in Source-Drain resistance in the «OFF» and «ON» states are 21.85% and 29.80%, respectively, which is significantly higher in comparison with elastically deformed ***Device 1*** (where the difference was 3.84%).

The use of elastoplastically deformed nanowires in NEM switches will provide more effective bending in contrast to a pure elastically deformed nanowire. However, the presence of a plastic deformation term will play a negative role in the resistance to bending fatigue, which may adversely affect the repeatability of the device in «ON»–«OFF» regimes, and most probably the life-time of the device will be significantly shorter than in the case of pure elastic deformation.

3.4. Magnetotransport properties of a convex-buckled suspended nanowire

Since the distribution of stresses over the cross-section of a suspended nanowire during deformation with upward and downward bending can be different (the NL can move in different directions), ***Device 3***, which experiences a convex shape deformation, in contrast to ***Device 1*** and ***2*** (concave shape), was fabricated.

During the cooling process from RT to 2 K, the Source-Drain resistance measured in the two-probe configuration experiences a metallic behavior (Fig. 9a inset). Magnetotransport analysis of ***Device 3*** at 2 K shows similar behavior with the suspended part of ***Device 1***, demonstrating three SdH oscillation frequencies: F^1_{susp}=20.7 T, F^2_{susp}=41.4 T, and F^3_{susp}=69.1 T after the Fourier transform of the $\partial^2\Delta R_{xx}/\partial B^2$ (Fig. 9b). Observed frequencies with corresponding charge carrier densities $n^1_{2D\_susp}$=5.01×10^{11} cm^{-2}, $n^2_{2D\_susp}$=1.00×10^{12} cm^{-2}, and $n^3_{2D\_susp}$=1.67×10^{12} cm^{-2} refer to the bottom, top surface, and bulk states, respectively. All data related to the SdH oscillations are summarized in Table 1.

Then, the gate dependence of Source-Drain resistance was measured at 2 and 4 K (Fig. 10). Both negative and positive gate voltage sweeps show deviation in resistance change with gate voltage at ±35 V (denoted as the intersection of linear fits (the dashed lines in Fig. 10) of experimental data in high and low electric fields). For the buckled beam fixed at both sides, the transition from the first stable position (convex shape) (Fig. 11) to the opposite stable position (concave shape) under the influence of an electrostatic field leads to the appearance of a third (curved) intermediate state [87]. We associate the observed change in slopes with the transition of the nanowire from the initial state to the second stable (concave shape) position (via an intermediate curved mode), while a further increase in voltage leads to the deformation of the nanowire towards the gate.

Since the selenium vacancies exist in Bi_2Se_3 and are the main origin of *n*-doping, it is reasonable that charges in the Bi_2Se_3 nanowires can be redistributed under the influence of a strong external electric field. Thus, we associate the decrease in the Source-Drain resistance of the buckled nanowire (during a positive voltage sweep at the gate) with the relaxation of the nanowire from its convex shape. Changing the voltage polarity on the gate sweep leads to an increase in resistance, which is presumably related to returning the nanowire to its original (convex) shape, as well as with charge redistribution due to the electrostatic field effect. With a negative voltage sweep, we assume an additional Fermi energy tuning process, because a much higher voltage is applied to ***Device 3*** compared to ***Devices 1*** and ***2***.

The observed magnitude of the change in Source-Drain resistance with a positive gate sweep between 0 and 80 V is −1.62%, which is twice less in comparison to the elastically deformed ***Device 1*** (which has a similar lateral geometry). Here, the change in resistance is calculated as the difference from 0 V, however, the nanowire is not relaxed at this point due to its buckled nature. Thus, this value indicates the change in resistance that occurred during bending from the first stable point to the maximum deformed position for ***Device 3***. However, it is worth noting here that the bending distance in the case of ***Device 3*** is much higher compared to ***Device 1***, but the resistance changes during bending are still lower. Negative strain values indicate a relaxation process after the initial convex state. Due to the smaller resistance change during the operation of buckled ***Device 3*** (with a significantly larger initial distance

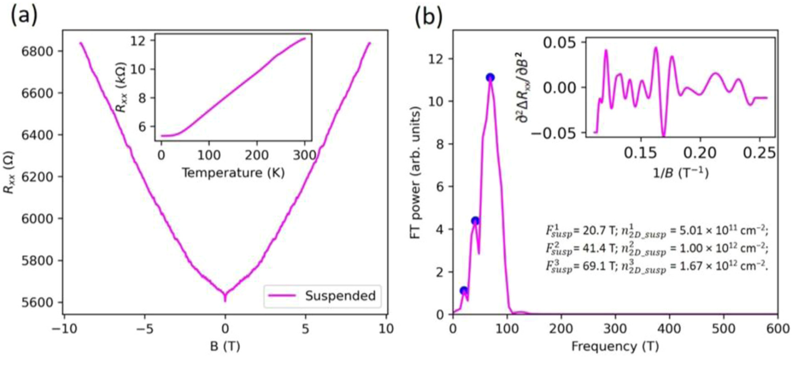

Fig. 9. Magnetotransport measurements of ***Device 3***. (a) R_{xx} as a function of a magnetic field. The inset is the temperature dependence of R_{xx}. (b) Shubnikov-de Haas oscillations analysis: the Fourier transform power spectra of $\partial^2\Delta R_{xx}/\partial B^2$ (presented in the inset).

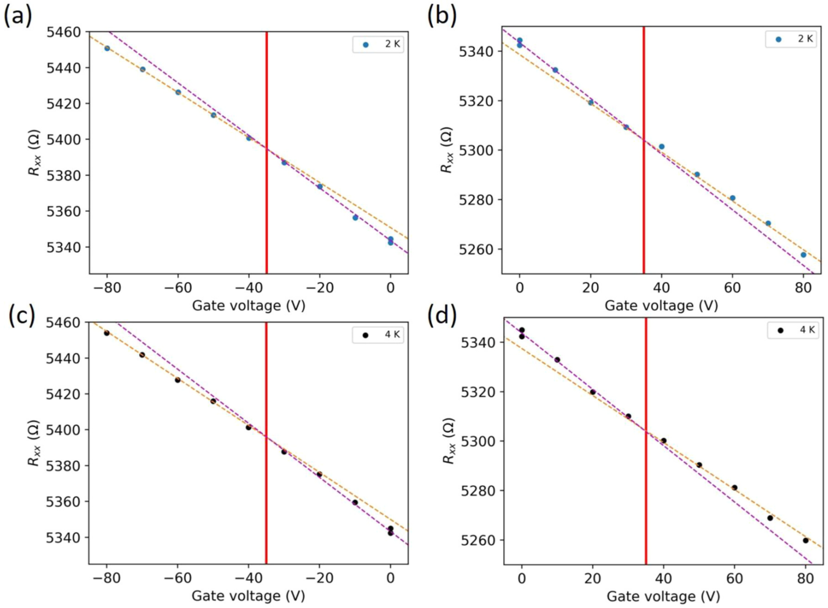

Fig. 10. Source-Drain R_{xx} as a function of back-gate voltage measured at 2 K (a-b) and 4 K (b-c) for ***Device 3***. Each data point represents the averaged R_{xx} value extracted from twenty *I-V* curves measured at a certain voltage value. The orange dashed line is the linear fit in the high electric field range, while the purple dashed line is the linear fit in the low electric field range. The solid red lines indicate the voltage value of ±35 V.

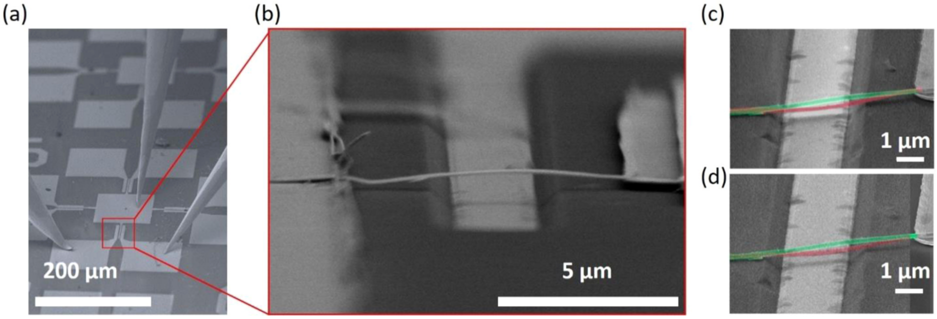

Fig. 11. (a) SEM image of suspended ***Device 3***, connected via an on-SEM manipulator (two-probe configuration) and (b) zoom-in tilted SEM image of the nanowire suspended across the back-gate electrode after transfer and contacts fabrication. (c, d) Overlayed SEM images, showing sharp deformation of the nanowire as the applied gate voltage changes from 0 V (green) to −40 V (c, red) and 40 V (d, red). Images are colored for improved comprehension.

between the nanowire and the gate) compared to the conventional ***Device 1***, buckled devices are promising candidates for NEM switches. This fact is a good advantage of buckled devices in terms of the resistance to bending fatigue. In addition, the convex shape allows the use of an additional (top gate) electrode to implement a three-terminal switch, and also such devices can be used for non-volatile memory applications.

To confirm that the wire deforms from the initial state (convex) to a second stable state (concave) after the gate voltage reaches ±35 V, we used an on-SEM nanomanipulator equipped with sharp gold tips to electrically connect the nanowire and the back-gate electrode to perform an in-situ measurement at room temperature, as shown in Fig. 11 and S1 (Supplementary material). Figs. 11c and 11d show in-situ measured SEM images of the buckled nanowire in the initial state (green) and after applying a voltage of ±40 V (red in panel c and d). It is clearly seen that the shape of the nanowire changes to concave. This fact is in good agreement with the low temperature gate measurements (Fig. 10), in which the change in resistance slopes occurred at ±35 V.

4. Conclusions

Suspended devices based on VLS-grown topological insulator Bi_2Se_3 nanowires were fabricated using different methods. The effect of mechanical deformation on the suspended part of the devices was studied using magnetotransport measurements (at low temperature), as well as in-situ SEM measurements at room temperature. The electrostatic field effect was used to dynamically manipulate bending deformation, while the magnetotransport measurements were performed to monitor the external strain introduced into the suspended and supported parts within the same Bi_2Se_3 nanowire. The pure elastic and elastoplastic types as well as a buckled deformation were realized in the suspended parts of the nanowires. All devices exhibit the Shubnikov-de Haas oscillation frequencies representing the carriers of the top and bottom surface states and the bulk (see Table 1). In the case of supported devices, the bottom surface states are masked by the trivial 2DEG, and only two frequencies were observed, whereas for the suspended parts, a third frequency appears because the carriers of the bottom surface states are not masked by trivial 2DEG, formed at the interface between the substrate and the nanowire. It can be seen that, regardless of the type of deformation (elastic, elastoplastic), the SdH frequencies experienced downshift and upshift with compressive and tensile strain, respectively. Changes in the Source-Drain resistance as well as the Gate-Drain current were continuously monitored as the nanowire was bent towards the gate electrode to determine the moment of contact with the gate, as well as to monitor the type of deformation induced and changes in the electrical transport properties of the device. During the bending of the suspended nanowires, an increase in the Source-Drain resistance was observed by 3.84% for elastic deformation, 21.85% for elastoplastic deformation, and only 1.62% for deformation of the buckled nanowire. Thus, elastoplastic deformation provides more effective bending compared to the pure elastically deformed and buckled nanowire. However, the presence of a plastic term will play a negative role in the resistance to bending fatigue compared to pure elastic deformation. The buckled devices are also promising candidates for NEM switches because the convex shape allows the use of an additional electrode to implement a three-terminal switch, and such devices can also be used for non-volatile memory applications. It should be noted here, that the results presented in this work are in good agreement and extend previous study [53], where Bi_2Se_3 nanowires were initially (statically) deformed (without the gate effect). We implemented more precise control during strain injection and demonstrated three different deformation regimes. The obtained results can be useful for strain engineering of TI materials, as well as for applications in NEMS and other fields related to suspended nanostructures (thermoelectric, sensing, etc.).

CRediT authorship contribution statement

Kiryl Niherysh: Writing – original draft, Investigation, Formal analysis. **Elza Dzene:** Writing – review & editing, Investigation. **Liga Jasulaneca:** Writing – review & editing, Visualization, Investigation. **Donats Erts:** Writing – review & editing, Validation, Supervision, Project administration, Methodology. **Floriana Lombardi:** Writing – review & editing, Supervision, Resources, Conceptualization.

Declaration of Competing Interest

The authors declare that they have no known competing financial interests or personal relationships that could have appeared to influence the work reported in this paper.

Data Availability

Data will be made available on request.

Acknowledgements

This research was funded by the Latvian Council of Science (project No. lzp-2019/1-0349). Authors would also like to acknowledge support from the Swedish infrastructure for micro- and nanofabrication - MyFab.

Appendix A. Supporting information

Supplementary data associated with this article can be found in the online version at doi:10.1016/j.sna.2024.115292.

References

[1] K. Akarvardar, C. Eggimann, D. Tsamados, Y.S. Chauhan, G.C. Wan, A. Mihai Ionescu, R.T. Howe, H.-S.P. Wong, Analytical modeling of the suspended-gate FET and design insights for low-power logic, IEEE Trans. Electron Devices (2008) *55*.

[2] N. Abelé, R. Fritschi, K. Boucart, F. Casset, P. Ancey, A.M. Ionescu, Suspended-Gate MOSFET: Bringing New MEMS Functionality into Solid-State MOS Transistor. IEEE International Electron Devices Meeting, 2005, IEDM Tech. Dig. (2005) 479–481.

[3] S. Sasaki, K. Tateno, G. Zhang, H. Suominen, Y. Harada, S. Saito, A. Fujiwara, T. Sogawa, K. Muraki, Encapsulated Gate-All-around InAs Nanowire Field-Effect Transistors, Appl. Phys. Lett. *103* (2013) 213502.

[4] H.-C. Lin, C.-H. Kuo, G.-J. Li, C.-J. Su, T.-Y. Huang, Operation of a Novel Device with Suspended Nanowire Channels, IEEE Electron Device Lett. (2010) *31*.

[5] A. Thiha, F. Ibrahim, S. Muniandy, I.J. Dinshaw, S.J. Teh, K.L. Thong, B.F. Leo, M. Madou, All-carbon suspended nanowire sensors as a rapid highly-sensitive label-free chemiresistive biosensing platform, Biosens. Bioelectron. *107* (2018) 145–152.

[6] A. Boisen, T. Thundat, Design & fabrication of cantilever array biosensors, Mater. Today *12* (2009) 32–38.

[7] F. Bendriaa, F. Le Bihan, A.C. Salaün, T. Mohammed-Brahim, O. Bonnaud, Study of mechanical stability of suspended bridge devices used as PH sensors, J. Non Cryst. Solids *352* (2006) 1246–1249.

[8] K.-W. Choi, M.-S. Jo, J.-S. Lee, J.-Y. Yoo, J.-B. Yoon, K. Choi, M. Jo, J. Lee, J. Yoo, J. Yoon, Perfectly aligned, air-suspended nanowire array heater and its application in an always-on gas sensor, Adv. Funct. Mater. *30* (2020) 2004448.

[9] Y. Lim, Y. Lee, J.Il Heo, H. Shin, Highly sensitive hydrogen gas sensor based on a suspended palladium/carbon nanowire fabricated via batch microfabrication processes, Sens Actuators B Chem. *210* (2015) 218–224.

[10] J. Choi, J. Kim, Highly sensitive hydrogen sensor based on suspended, functionalized single tungsten nanowire bridge, Sens Actuators B Chem. *136* (2009) 92–98.

[11] D. Hatanaka, A. Bachtold, H. Yamaguchi, Electrostatically induced phononic crystal, Phys. Rev. Appl. *11* (2019) 024024.

[12] G. Li, D. Liang, R.L.J. Qiu, X.P.A. Gao, Thermal conductivity measurement of individual Bi_2Se_3 nano-ribbon by self-heating Three-ω method, Appl. Phys. Lett. *102* (2013) 43104.

[13] Dedi, P.C. Lee, P.C. Wei, Y.Y. Chen, Thermoelectric characteristics of a single-crystalline topological insulator Bi_2Se_3 nanowire, Nanomaterials *11* (2021) 819.

[14] M. Kim, J. Kim, Y. Hou, D. Yu, Y.J. Doh, B. Kim, K.W. Kim, J. Suh, Nanomechanical characterization of quantum interference in a topological insulator nanowire, Nat. Commun. *10* (2019) 1–7.

[15] C.B. Maliakkal, J.P. Mathew, N. Hatui, A.A. Rahman, M.M. Deshmukh, A. Bhattacharya, Fabrication and characterization of GaN nanowire doubly clamped resonators, J. Appl. Phys. *118* (2015) 114301.

[16] A. Husain, J. Hone, H.W.C. Postma, X.M.H. Huang, T. Drake, M. Barbic, A. Scherer, M.L. Roukes, Nanowire-based very-high-frequency electromechanical resonator, Appl. Phys. Lett. *83* (2003) 1240–1242.

[17] A. Iorio, M. Rocci, L. Bours, M. Carrega, V. Zannier, L. Sorba, S. Roddaro, F. Giazotto, E. Strambini, Vectorial control of the spin-orbit interaction in suspended InAs nanowires, Nano Lett. *19* (2019) 652–657.

[18] R.I. Shekhter, F. Santandrea, G. Sonne, L.Y. Gorelik, M. Jonson, Nonequilibrium and quantum coherent phenomena in the electromechanics of suspended nanowires (Review Article), Low. Temp. Phys. *35* (2009) 662–678.

[19] M. Liao, S. Hishita, E. Watanabe, S. Koizumi, Y. Koide, Suspended single-crystal diamond nanowires for high-performance nanoelectromechanical switches, Adv. Mater. *22* (2010) 5393–5397.

[20] K.J. Ziegler, D.M. Lyons, J.D. Holmes, D. Erts, B. Polyakov, H. Olin, K. Svensson, E. Olsson, Bistable nanoelectromechanical devices, Appl. Phys. Lett. *84* (2004) 4074–4076.

[21] L. Boodhoo, L. Crudgington, H.M.H. Chong, Y. Tsuchiya, Z. Moktadir, T. Hasegawa, H. Mizuta, Fabrication and characterisation of suspended narrow silicon nanowire channels for low-power nano-electro-mechanical (NEM) switch applications, Micro Eng. *145* (2015) 66–70.

[23] L. Kong, G. Cao, H. Zhou, J. Wang, In Situ observation of high bending strain recoverability in Au nanowires, Crystals *13* (2023) 1159.

[22] O.Y. Loh, H.D. Espinosa, Nanoelectromechanical contact switches, Nat. Nanotechnol. *7* (2012) 283–295.

[24] W. Tomita, S. Sasaki, K. Tateno, H. Okamoto, H. Yamaguchi, Novel fabrication technique of suspended nanowire devices for nanomechanical applications, Phys. Status Solidi (b) *257* (2020) 1900401.

[25] L. Jasulaneca, J. Kosmaca, R. Meija, J. Andzane, D. Erts, Review: electrostatically actuated nanobeam-based nanoelectromechanical switches – materials solutions and operational conditions, Beilstein J. Nanotechnol. *9* (2018) 271–300.

[26] L. Wang, P. Zhang, Z. Liu, Z. Wang, R. Yang, On-chip mechanical computing: status, challenges, and opportunities, Chip *2* (2023) 100038.

[27] N. Huynh Van, M. Muruganathan, J. Kulothungan, H. Mizuta, Fabrication of a three-terminal graphene nanoelectromechanical switch using two-dimensional materials, Nanoscale *10* (2018) 12349.

[28] P. Li, G. Jing, B. Zhang, S. Sando, T. Cui, Single-crystalline monolayer and multilayer graphene nano switches, Appl. Phys. Lett. *104* (2014) 39.

[29] J. Andzane, R. Meija, A.I. Livshits, J. Prikulis, S. Biswas, J.D. Holmes, D. Erts, An AC-assisted single-nanowire electromechanical switch, J. Mater. Chem. C. Mater. *1* (2013) 7134–7138.

[30] R. He, X.L. Feng, M.L. Roukes, P. Yang, Self-transducing silicon nanowire electromechanical systems at room temperature, Nano Lett. *8* (2008) 1756–1761.

[31] Y. Qian, B.W. Soon, P. Singh, H. Campanella, C. Lee, All metal nanoelectromechanical switch working at 300 °C for rugged electronics applications, Nanoscale *6* (2014) 5606–5611.

[32] T.H. Lee, S. Bhunia, M. Mehregany, Electromechanical computing at 500°C with silicon carbide, Science *1979* (2010) 1316–1318. *329*.

[33] J. Kulothungan, K. Kandhasamy, Large scale fabrication of graphene based nanoelectromechanical (NEM) contact switches with Sub-0.5 volt actuation, Adv. Phys. Res. *2* (2023) 2200050.

[34] J.O. Lee, Y.H. Song, M.W. Kim, M.H. Kang, J.S. Oh, H.H. Yang, J.B. Yoon, A Sub-1-Volt Nanoelectromechanical Switching Device, Nat. Nanotechnol. *8* (2012) 36–40.

[35] S. Rana, J. Mouro, S.J. Bleiker, J.D. Reynolds, H.M.H. Chong, F. Niklaus, D. Pamunuwa, Nanoelectromechanical Relay without Pull-in Instability for High-Temperature Non-Volatile Memory, Nat. Commun. *11* (2020) 1–10.

[36] A. Peschot, C. Qian, T.-J.K. Liu, Nanoelectromechanical Switches for Low-Power Digital Computing, Micromachines *6* (2015) 1046–1065.

[37] R.R. Benoit, N.S. Barker, Reliability of RF MEMS Switches at Cryogenic (Liquid He) Temperatures, Microelectron. Reliab. *111* (2020) 113706.

[38] E. Lee, J.W. Kang, Molecular Dynamics Analysis of Graphene-Based Nanoelectromechanical Switch, ECS Trans. *72* (2016) 1–6.

[39] L. Jasulaneca, R. Meija, E. Kauranens, R. Sondors, J. Andzane, R. Rimsa, G. Mozolevskis, D. Erts, Cryogenic Nanoelectromechanical Switch Enabled by Bi_2Se_3 Nanoribbons, Mater. Sci. Eng.: B *275* (2022) 115510.

[40] Y. Ando, T, opological Insul. Mater. *82* (2013).

[41] C. Felser, S. Zhang, B. Yan, J.J. Cha, K.J. Koski, Y. Cui, Topological Insulator Nanostructures. Physica status solidi (RRL), Rapid Res. Lett. *7* (2013) 15–25.

[42] S.S. Hong, J.J. Cha, D. Kong, Y. Cui, Ultra-Low Carrier Concentration and Surface-Dominant Transport in Antimony-Doped Bi_2Se_3 Topological Insulator Nanoribbons, Nat. Commun. *3* (2012) 1–7.

[43] D. Kong, Y. Chen, J.J. Cha, Q. Zhang, J.G. Analytis, K. Lai, Z. Liu, S.S. Hong, K. J. Koski, S.K. Mo, et al., Ambipolar Field Effect in the Ternary Topological Insulator $(Bi_xSb_{1-x})_2Te_3$ by Composition Tuning, Nat. Nanotechnol. *6* (2011) 705–709.

[44] H. Steinberg, D.R. Gardner, Y.S. Lee, P. Jarillo-Herrero, Surface State Transport and Ambipolar Electric Field Effect in Bi_2Se_3 Nanodevices, Nano Lett. *10* (2010) 5032–5036.

[45] R. Sondors, K. Niherysh, J. Andzane, X. Palermo, T. Bauch, F. Lombardi, D. Erts, Low-Vacuum Catalyst-Free Physical Vapor Deposition and Magnetotransport Properties of Ultrathin Bi_2Se_3 Nanoribbons, Nanomaterials *13* (2023) 2484.

[46] G. Kunakova, L. Galletti, S. Charpentier, J. Andzane, D. Erts, F. Léonard, C. D. Spataru, T. Bauch, F. Lombardi, Bulk-Free Topological Insulator Bi_2Se_3 Nanoribbons with Magnetotransport Signatures of Dirac Surface States, Nanoscale *10* (2018) 19595–19602.

[47] Z. Ju, Y. Hou, A. Bernard, V. Taufour, D. Yu, S.M. Kauzlarich, Ambipolar Topological Insulator and High Carrier Mobility in Solution Grown Ultrathin Nanoplates of Sb-Doped Bi_2Se_3, ACS Appl. Electron Mater. *1* (2019) 1917–1923.

[48] J. Lee, J. Park, J.H. Lee, J.S. Kim, H.J. Lee, Gate-Tuned Differentiation of Surface-Conducting States in $Bi_{1.5}Sb_{0.5}Te_{1.7}Se_{1.3}$ Topological-Insulator Thin Crystals, Phys. Rev. B Condens Matter Mater. Phys. *86* (2012) 245321.

[49] Y. Yan, X. Zhou, H. Jin, C.Z. Li, X. Ke, G. Van Tendeloo, K. Liu, D. Yu, M. Dressel, Z. M. Liao, Surface-Facet-Dependent Phonon Deformation Potential in Individual Strained Topological Insulator Bi_2Se_3 Nanoribbons, ACS Nano *9* (2015) 10244–10251.

[50] K.A. Niherysh, J. Andzane, M.M. Mikhalik, S.M. Zavadsky, P.L. Dobrokhotov, F. Lombardi, S.L. Prischepa, I.V. Komissarov, D. Erts, Correlation Analysis of Vibration Modes in Physical Vapour Deposited Bi_2Se_3 Thin Films Probed by the Raman Mapping Technique, Nanoscale Adv. *3* (2021) 6395–6402.

[51] H. Aramberri, M.C. Muñoz, Strain effects in topological insulators: topological order and the emergence of switchable topological interface states in Sb_2Te_3/Bi_2Te_3 heterojunctions, Phys. Rev. B *95* (2017) 205422.

[52] J. Liu, Y. Xu, J. Wu, B.L. Gu, S.B. Zhang, W. Duan, Manipulating Topological Phase Transition by Strain, Acta Cryst. *70* (2014) 118–122.

[53] C. Schindler, C. Wiegand, J. Sichau, L. Tiemann, K. Nielsch, R. Zierold, R.H. Blick, Strain-induced dirac state shift in topological insulator Bi_2Se_3 nanowires, Appl. Phys. Lett. *111* (2017).

[54] S.H. Park, J. Chae, K.S. Jeong, T.H. Kim, H. Choi, M.H. Cho, I. Hwang, M.H. Bae, C. Kang, Reversible fermi level tuning of a Sb_2Te_3 topological insulator by structural deformation, Nano Lett. *15* (2015) 3820–3826.

[55] E. Tang, L. Fu, Strain-Induced Partially Flat Band, Helical Snake States and Interface Superconductivity in Topological Crystalline Insulators, Nat. Phys. *10* (2014) 964–969.

[56] C. Lin, M. Ochi, R. Noguchi, K. Kuroda, M. Sakoda, A. Nomura, M. Tsubota, P. Zhang, C. Bareille, K. Kurokawa, et al., Visualization of the strain-induced topological phase transition in a quasi-one-dimensional superconductor $TaSe_3$, Nat. Mater. *20* (2021) 1093–1099.

[57] M. Shafiei, F. Fazileh, F.M. Peeters, M.V. Milošević, High Chern Number in Strained Thin Films of Dilute Magnetic Topological Insulators, Phys. Rev. B *107* (2023) 195119.

[58] X. Luo, M.B. Sullivan, S.Y. Quek, First-Principles Investigations of the Atomic, Electronic, and Thermoelectric Properties of Equilibrium and Strained Bi_2Se_3 and Bi_2Te_3 Including van Der Waals Interactions, Phys. Rev. B Condens Matter Mater. Phys. *86* (2012) 184111.

[59] S. He, B. Jiang, C. Wang, C. Chen, H. Duan, S. Jin, H. Ye, L. Lu, K. Du, High Reversible Strain in Nanotwinned Metals, ACS Appl. Mater. Interfaces *13* (2021) 46088–46096.

[60] H. Liu, J. Zhou, Plasticity in Nanotwinned Polycrystalline Ni Nanowires under Uniaxial Compression, Mater. Lett. *163* (2016) 179–182.

[61] X. Zhang, X. Li, H. Gao, Size and Strain Rate Effects in Tensile Strength of Penta-Twinned Ag Nanowires, Acta Mech. *33* (2017) 792–800.

[62] Y. Yue, Q. Zhang, X. Zhang, Z. Yang, P. Yin, L. Guo, In Situ Observation of Twin Boundary Sliding in Single Crystalline Cu Nanowires, Small *13* (2017) 1604296.

[63] W. Xu, W.K. Kim, Molecular Dynamics Simulation of the Uniaxial Tensile Test of Silicon Nanowires Using the MEAM Potential, Mech. Mater. *137* (2019) 103140.

[64] L. Liu, Q. Deng, M. Su, M. An, R. Wang, Strain rate and temperature effects on tensile behavior of Ti/Al multilayered nanowire: a molecular dynamics study, Superlattices Micro *135* (2019) 106272.

[65] G. Cheng, S. Yin, T.H. Chang, G. Richter, H. Gao, Y. Zhu, Anomalous tensile detwinning in twinned nanowires, Phys. Rev. Lett. *119* (2017) 256101.

[66] R. Sondors, G. Kunakova, L. Jasulaneca, J. Andzane, E. Kauranens, M. Bechelany, D. Erts, High-Yield Growth and Tunable Morphology of Bi_2Se_3 Nanoribbons Synthesized on Thermally Dewetted Au, Nanomaterials *11* (2021) 2020.

[67] L. Jasulaneca, A.I. Livshits, R. Meija, J. Kosmaca, R. Sondors, M.M. Ramma, D. Jevdokimovs, J. Prikulis, D. Erts, Fabrication and characterization of double- and single-clamped CuO nanowire based nanoelectromechanical switches, Nanomaterials *11* (2021) 117.

[68] M. Brahlek, N. Koirala, N. Bansal, S. Oh, Transport properties of topological insulators: band bending, bulk metal-to-insulator transition, and weak anti-localization, Solid State Commun. *215–216* (2015) 54–62.

[69] J. Hajdu, Shubnikov–De. Haas Eff.: Introd. Theory *27* (1991) 997–1030.

[70] G. Kunakova, R. Meija, J. Andzane, U. Malinovskis, G. Petersons, M. Baitimirova, M. Bechelany, T. Bauch, F. Lombardi, D. Erts, Surface structure promoted high-yield growth and magnetotransport properties of Bi_2Se_3 nanoribbons, Sci. Rep. *9* (2019) 1–10.

[71] L. Fang, Y. Jia, D.J. Miller, M.L. Latimer, Z.L. Xiao, U. Welp, G.W. Crabtree, W. K. Kwok, Catalyst-free growth of millimeter-long topological insulator Bi_2Se_3 nanoribbons and the observation of the π-Berry phase, Nano Lett. *12* (2012) 6164–6169.

[72] L. Veyrat, F. Iacovella, J. Dufouleur, C. Nowka, H. Funke, M. Yang, W. Escoffier, M. Goiran, B. Eichler, O.G. Schmidt, et al., Band bending inversion in Bi_2Se_3 nanostructures, Nano Lett. *15* (2015) 7503–7507.

[73] Z. Ren, A.A. Taskin, S. Sasaki, K. Segawa, Y. Ando, Large bulk resistivity and surface quantum oscillations in the topological insulator Bi_2Te_2Se, Phys. Rev. B Condens Matter Phys. *82* (2010) 241306.

[74] G. Kunakova, T. Bauch, X. Palermo, M. Salvato, J. Andzane, D. Erts, F. Lombardi, High-mobility ambipolar magnetotransport in topological insulator Bi_2Se_3 nanoribbons, Phys. Rev. Appl. *16* (2021) 024038.

[75] J. Zhou, X. Yang, B. Wang, W. Xiao, Springback prediction of 7075 aluminum alloy V-shaped parts in cold and hot stamping, Int. J. Adv. Manuf. Technol. *119* (2022) 203–216.

[76] J. Ma, T. Welo, Analytical springback assessment in flexible stretch bending of complex shapes, Int J. Mach. Tools Manuf. *160* (2021) 103653.

[77] R. Roldán, A. Castellanos-Gomez, E. Cappelluti, F. Guinea, Strain engineering in semiconducting two-dimensional crystals, J. Phys.: Condens. Matter *27* (2015) 313201.

[78] S.M. Sze, VLSI Technol. (1983) 654.

[79] J.J. Licari, D.W. Swanson, Test and inspection methods, Adhes. Technol. Electron. Appl. (2011) 345–377.

[80] G. Binnig, N. Garcia, H. Rohrer, J.M. Soler, F. Flores, Electron-metal-surface interaction potential with vacuum tunneling: observation of the image force, Phys. Rev. B *30* (1984) 4816.

[81] D. Erts, A. Lõhmus, R. Lõhmus, H. Olin, A.V. Pokropivny, L. Ryen, K. Svensson, Force interactions and adhesion of gold contacts using a combined atomic force microscope and transmission electron microscope, Appl. Surf. Sci. *188* (2002) 460–466.

[82] W. Liu, X. Peng, C. Tang, L. Sun, K. Zhang, J. Zhong, Anisotropic interactions and strain-induced topological phase transition in Sb_2Se_3 and Bi_2Se_3, Phys. Rev. B Condens Matter Phys. *84* (2011) 245105.

[83] The Engineering ToolBox (2004). Beams - Fixed at Both Ends - Continuous and Point Loads. [Online] Available online: ⟨https://www.engineeringtoolbox.com/beams-fixed-both-ends-support-loads-deflection-d_809.html⟩ (accessed on 21 October 2023).

[84] J. Andzane, G. Kunakova, S. Charpentier, V. Hrkac, L. Kienle, M. Baitimirova, T. Bauch, F. Lombardi, D. Erts, Catalyst-free vapour–solid technique for deposition of Bi_2Te_3 and Bi_2Se_3 nanowires/nanobelts with topological insulator properties. Nanoscale *7* (2015) 15935–15944.

[85] E.K. Iordanishvili, M.B. Nabiev, K.O. Olimov, Y.I. Ravich, Study of the Strain-Resistance Properties of Massive Samples of Bi_2Te_3-Sb_2Te_3 and Bi_2Te_3-Bi_2Se_3, J. Eng. Phys. *56* (1989) 77–79.
[86] S.D.A. Hannot, D.J. Rixen, V. Rochus, Rounding the corners in an electromechanical FEM model, Proc. Second Int. Conf. Comput. Methods Couple Probl. Sci. Eng. (2007) 507–510.
[87] H. Hussein, P. Le Moal, G. Bourbon, Y. Haddab, P. Lutz, Modeling and stress analysis of a pre-shaped curved beam: influence of high modes of buckling, Int. J. Appl. Mech. (2015) 1550055.

Kiryl Niherysh: received the B.S. and M.S. Engineering degrees in Micro-and Nanoelectronics from the Belarusian State University of Informatics and Radioelectronics, Minsk, Belarus, in 2017 and 2018, respectively. He is currently pursuing the Ph.D. degree in Physics from the University of Latvia, Riga, Latvia. Currently he is a researcher at the Institute of Chemical Physics of the University of Latvia. His research interests include nanofabrication of electronic devices, low temperature transport measurements, and synthesis and characterization of nanostructures.

Liga Jasulaneca: received the B.S. and M.S. degrees in Natural Sciences in Physics from the University of Latvia in Riga, Latvia in 2012 and 2015, respectively. Currently, she is actively pursuing the Ph.D. degree in Physics at the same institution. Since 2016, she has been a researcher in the nanotechnology group at the Institute of Chemical Physics, University of Latvia. Her current research focus spans nanoelectromechanical systems, low-dimensional materials and low temperature transport measurements.

Elza Dzene: received the B.S. degree in Chemistry from the University of Latvia, Riga, Latvia in 2022. She is currently pursuing the M.S. degree in Chemistry at the same institution. She is a research assistant in the Institute of Chemical Physics of the University of Latvia. Her current research interests include the low-dimensional materials growth and their structural characterization.

Floriana Lombardi: received the Ph.D. in Physics in 1996 from the University of Napoli, Italy. Her Ph.D. thesis was dedicated to high critical temperature superconductor Josephson devices. From 1996–1998 she was a Postdoctoral Associate at Chalmers University of Technology, Sweden. From 1998–2001 she was a Postdoctoral Associate at the University of Napoli, Italy. From 2002–2006 she was an Assistant Professor, at Chalmers University of Technology. From 2007–2009 she worked as an Associate Professor at Chalmers University of Technology. From 2009 she has been a professor in Condensed Matter physics at Chalmers University of Technology, Department of Microtechnology and Nanoscience MC2. Since 2023, she has been a Full Professor at Quantum Device Physics. Her main research activities focus on superconducting nanostructures, Coulomb blockade devices, and electron transport in topological insulators.

Donats Erts: received the Ph.D. in Chemistry in 1985 (Candidate of Sciences in Chemistry, 1992 equated to Dr. chem.) from the Institute of Inorganic Chemistry, Academy of Latvian SSR. His thesis was dedicated to lyoluminescence of irradiated alkali crystals. From 1985 to the present, he has been a Senior, Leading Researcher at the Faculty of Chemistry, Department of Chemical Physics of Condensed Matter (now the Institute of Chemical Physics) at the University of Latvia. From 1992–2009, he was a part-time visiting researcher at Chalmers University of Technology, Sweden, Cork University College and CRANN, Ireland. Since 2002, he has been Acting Director, Director of the Institute of Chemical Physics at the University of Latvia. From 2013 he has an Associate Professor and since 2021 – Professor at the Department of Chemistry of the University of Latvia. From 2016 he has been a Full Member of Latvian Academy of Sciences. His main research interests are related to the synthesis of nanostructured materials, the investigation of their properties and potential applications.

Paper VIII

Coulomb blockade and chaotic electron motion in a topological insulator quantum dot

Xavier Palermo,[†] Kiryl Niherysh,[†,‡] Ananthu P. Surendran,[†] Yuchen Ji,[§]
Xufeng Kou,[§] Thilo Bauch,[†] and Floriana Lombardi*,[†]

†*Quantum Device Physics Laboratory, Department of Microtechnology and Nanoscience,*
Chalmers University of Technology, SE-41296 Göteborg, Sweden
‡*Institute of Chemical Physics, University of Latvia, Raina Blvd. 19, LV-1586 Riga, Latvia*
§*ShanghaiTech University, Shanghai, China*

E-mail: floriana.lombardi@chalmers.se

Abstract

Creating quantum dots in 3D topological insulators (3D TI) could allow to fabricate novel devices such as terahertz lasers and single electron charge pumps. However existing realizations of 3D TI-based quantum dots are scarce, and all of them rely on as-grown nanostructures at the expense of scalability. This article presents an easy and scalable method to pattern single electron transistors with various geometries from high-quality $(Bi_{1-x}Sb_x)_2Te_3$ thin films. These consist in a nanoribbon in which a central island is delimited by two nano-constrictions acting as tunnel barriers. The presence of multiple sets of Coulomb blockade features in the transport of the device reveals that quantum dots form in the central island as well as in the two constrictions. In the magneto-transport of the tunneling state, we observe conductance fluctuations indicating that the electron motion inside the island is chaotic. The fabrication of such devices opens as a first step towards the realization of practical devices based on TI quantum dots.

Introduction

Three-dimensional topological insulators (3D TIs) are a class of materials that exhibit an insulating bulk as well as conducting and topologically protected surface states.[1] These surface states have a Dirac dispersion, which makes them effectively massless and insensitive to localization or confinement by electrostatic gating because of Klein tunneling.

This makes the fabrication of mesoscopic structures that exploit confinement effects such as quantum dots quite challenging. Nonetheless, these nanostructures are interesting platforms to study emergent transport phenomena like the spin-orbital Kondo effect,[2] and hold promises for novel applications such as room-temperature terahertz lasers[3] and single electron charge pumps for metrology.[4] Despite this potential, only two such realizations have been reported in the literature.[5,6]

The present work follows the proposal by Saxena *et al.*[4] to realize 3DTI quantum dots using constrictions in a 3DTI nanowire, as sketched in Figure 1. In nanowires with perimeters comparable to or smaller than the phase coherence length l_ϕ, Dirac electrons circulating at the surface accumulate a Berry phase of π after one full round around the edge. This leads to destructive self-interference, creating a gap at the Dirac point that is inversely proportional to the radius of the wire.[7] This gap suppresses Klein tunneling and renders the TI electrons massive, thus sensitive to confinement potentials. As a consequence, two constrictions in series in a 3DTI nanowire create a potential well that can act as a quantum dot, as represented in the figure.

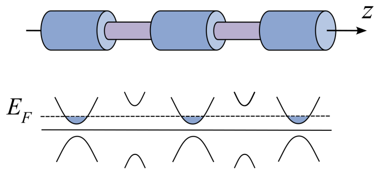

Figure 1: Sketch of the TI nanowire quantum dot model (top) and corresponding band structure in each section of the device (bottom).

In the following, we demonstrate the fabrication of such a device using in $(\mathrm{Bi}_{1-x}\mathrm{Sb}_x)_2\mathrm{Te}_3$ thin films patterned by electron beam lithography. Our method improves upon existing realizations by its better scalability and flexibility in the control of the device geometry by avoiding the use of as-grown nanostructures like flakes or nano-ribbons. Transport measurements at low temperatures confirm the formation of a quantum dot within the central island, alongside additional dots in the barriers. Lastly, under a perpendicular magnetic field, magneto-conductance oscillations exclusively observed in the Coulomb blockade regime suggest chaotic electron motion within the dot.

Results and discussion

Thin films of the topological insulator $(\mathrm{Bi}_{1-x}\mathrm{Sb}_x)_2\mathrm{Te}_3$ (BST) were grown by MBE on sapphire substrates. These are 13 unit cells thick, which corresponds to 12.3 nm as measured by atomic force microscopy. Prior to the fabrication, we also measured the sheet resistance of the film $R_\square = 4$ kΩ per square area, its sheet carrier density $n_{2D} = 5.3 \times 10^{12}$ cm^{-2} with n-type carriers, and its carrier mobility $\mu \approx 200 - 250$ cm$^2\,(\mathrm{V\,s})^{-1}$ (see Methods and Supporting Information). We then proceeded with the fabrication of the devices. Electrodes were first patterned on the film by standard electron beam lithography (EBL), evaporation of 50 nm gold layer, and lift-off. Then, single-electron transistors (SET) were carved in the films by another EBL and argon ion milling, using the resist as an etching mask. An SEM image of the device discussed in this article is presented in Figure 2a. It consists in a 150 nm wide by 1.3 µm long nano-ribbon in which two constrictions of 170 nm in length by 22 nm in width were made. These serve as tunnel barriers to define a central island of 100 nm in length, where a quantum dot should form. A plunger gate is also patterned in the film during the same step, in order to tune the charge state inside the dot (coming from the bottom of the image).

In absence of coaxial magnetic fields, we estimate the gap opened in the constrictions[4] to be of the order of $2\hbar v_F l/R \approx$ 20-25 meV, with $v_F \approx 4\times10^5$ m s^{-1} is the Fermi velocity in BST[8]

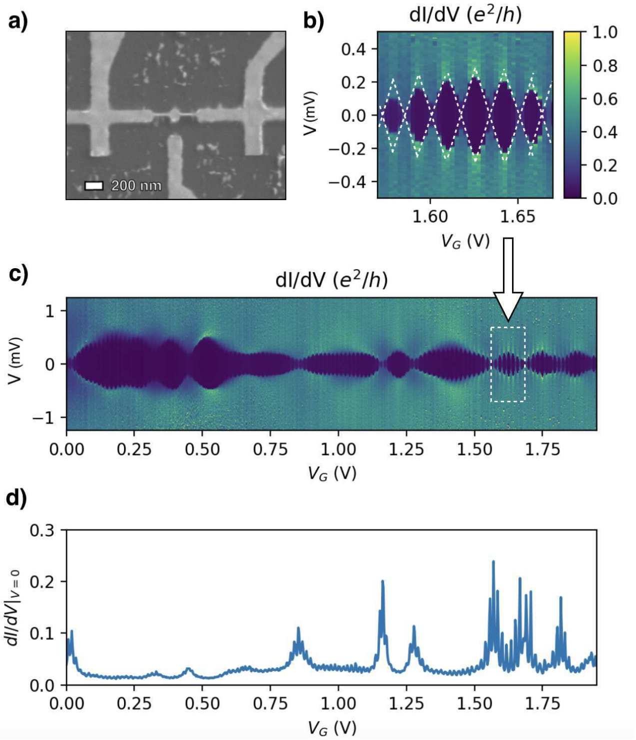

Figure 2: a)SEM image of the dot device, with the side gate contact and leads. b) Small-scale differential conductance map of the same device at 20 mK, showing Coulomb diamonds. Dotted white lines indicate the slopes used for estimating the capacitance of the barriers in the text. c) Same conductance map on a larger gate and voltage scale, the dotted square indicates the diagram region shown in b). The color scale is shared for both plots. d) Zero-bias conductance curve from the same data set as c)

and $l = 1/2$ is the angular momentum of the lowest-lying subband. Here, the equivalent radius R is chosen so that $2\pi R$ equates the perimeter of the constriction. Comparatively, the gap in the nanowire and dot should be of the order of 6 mV, but likely smaller or null since the perimeter exceeds the phase coherence length $l_\phi \approx 60$ nm as estimated in the plain film from magneto-transport (see Supplementary material). These values are in line with those for which confinement is expected to occur.[4]

We then measured the electron transport properties of the devices in a dilution fridge with a base temperature of 20 mK. Figure 2b presents a color plot of the differential conductance dI/dV of the device pictured in panel a, plotted against the 4-points source-drain voltage V and the applied gate voltage V_G. It exhibits small diamond-like regions near zero-bias in which the conductance of the device is strongly attenuated. These have a regular size $\Delta V_G = 15.2$ mV in gate voltage, but their width in source-drain voltage varies smoothly from diamond to diamond. Outside of these, the conductance background is mostly constant in this range and has a value around one half of the quantum of conductance $G_0 = e^2/h$, where e and h are respectively the electron charge and the Planck constant.

These diamond features are typical manifestation of Coulomb blockade, which indicates charging effects occurring in a region of the device that behaves as a quantum dot.[9] The size of the dot can be estimated from the diamond periodicity in gate voltage as follows. We first calculate the gate capacitance from the diamond periodicity as $C_G = e/\Delta V_G =$11 aF. Then, we approximate the dot to an isolated disk of radius R, for which the capacitance is given by $C_G = 8\epsilon_0\epsilon_r R$, where ϵ_0 is the permittivity of vacuum and $\epsilon_r \approx 5.5$ is the relative permittivity of the gate dielectric. The latter value is taken as the average permittivity of vacuum ($\epsilon_r = 1$) and the sapphire substrate ($\epsilon_r \approx 10$). This yields a radius of $R = 27$ nm, which is consistent with a dot being formed in the central region. The value is likely underestimated though, as the formula does not take into account the screening effects of the leads nearby, that also contribute to the measured value.[10] The tunnel capacitance of the barriers C_T can also be obtained from the slopes of the diamond using $C_T = C_G(\mid dV_G/dV \mid + \frac{1}{2})$, where dV_G/dV is the slope of the diamond boundaries (white lines in Figure 2b[11]). This yields $C_T \approx 310$ aF for both constrictions, as the patterns are symmetrical around $V = 0$. Lastly, we calculate the charging energy of the dot to be $E_c = e^2/2C_\Sigma = 0.13$ meV, where $C_\Sigma = 2C_T + C_G = 631$ aF is the total capacitance of the island.

As mentioned earlier, the width of the diamonds along source-drain voltage is modulated by the gate voltage, which becomes more visible when scanning over a wider range of gate voltages, as shown in the map presented in Figure 2c. The measurement reveals that the diamond width varies in a smooth but aperiodic manner that is reminiscent of a beating pattern. Figure 2d displays the corresponding zero-bias conductance curve, revealing a sequence of broad peaks with uneven spacing. These peaks coincide with the intervals between the dark patches, where the conductance becomes comparable to that of the constant background. Notably, the overall pattern is modulated by the small 15 mV Coulomb oscillation originating from the central island dot. The regularity of the latter Coulomb oscillations in gate voltage is also indicative that the dot behaves more akin to a single-electron transistor, where the spacing between energy levels inside the dot is negligible compared to the charging energy $e^2/2C_\Sigma$.

Regarding the larger features, similar beating patterns have been reported for narrow and disordered nanowires, in which additional quantum dots can form due to inhomogeneities[6,12,13] This means that additional dots are formed within the constrictions. It is also supported by the rather large peak spacing in gate voltage, about 150-250 mV, that corresponds to a dot of a few nanometers in size using the same formula as for the island capacitance. In such a system, the current can only flow if the conductance of all the dots is finite, in other words that the Coulomb peaks of all the individual dots overlap. Consequently, the position of the Coulomb peaks observed in the zero-bias conductance of the series becomes stochastic.[14] Lastly, the periodicity of the Coulomb oscillation from the central island being much shorter than the width of the other broader peaks means it modulates the whole pattern but does not change nor prevent other broader peaks from being visible. In 3D TI materials, the formation of such dots is usually prevented by Klein tunneling. However, as explained in the introduction, it is suppressed in the constrictions by the opening of the gap. This also makes the Dirac electrons sensitive to confinement by charge puddles or defects, and eventually leads to the formation of extra dots.

Coulomb blockade in mesoscopic objects can originate from several mechanisms, some of which are sensitive to magnetic fields such as mesoscopic Coulomb blockade .[15] Thus, to further investigate the formation of the dots, we applied a magnetic field B perpendicular to the sample plane and looked at its effect on the diamond structures.

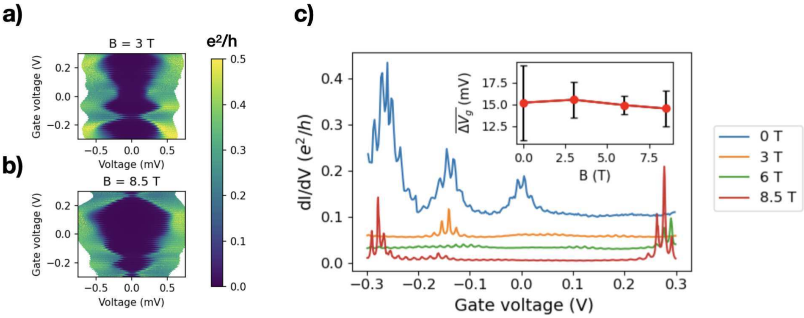

Figure 3: a,b : Small conductance maps for a perpendicular field of respectively 3 T and 8.5 T. c) Zero-bias conductance of the device for several values of the out-of-plane magnetic field. The curves are offset from lowest to highest field for clarity. The inset shows the mean peak spacing for the island dot (15 mV oscillation), as a function of magnetic field. Error bars represent one standard deviation.

We measured smaller conductance maps for several values of the field, two of which are shown in the panels a) and b) of Figure 3. In these, we see that the larger patterns change significantly in shape and periodicity upon applying the field. The zero-bias traces of these maps, plotted in panel c), reveal that the amplitude of individual peaks is affected by the field in a random fashion.

The series arrangement of the dots makes it difficult to disentangle such effects. One possible explanation could be orbital or Zeeman shifts,[16] that lead to significant changes in the pattern by changing the overlaps of Coulomb peaks from each of the dots in the constrictions. Another possibility is the barrier dots are formed by an interference effect such as mesoscopic Coulomb blockade,[15] which can occur if one of the tunnel barriers that delimit the dot is transparent. In this case, the field attenuates the amplitude of the conductance peaks in a similar way to weak-(anti)localization.

In contrast, the Coulomb oscillations related to the central dot remain visible at all fields.

The spacing between the peaks seems to remain regular, and its mean value $\overline{\Delta V_G}$ does not change significantly with magnetic field, as shown in the inset of panel c). This further confirms that the central dot behaves like a single-electron transistor.

We also investigated the evolution of the zero-bias conductance at $V_G = 0$ upon sweeping the magnetic field, which is presented in Figure 4a for several values of the temperature. For these parameters, the conductance is almost equal to that at $V \gg e/C_\Sigma$, meaning that the three dots are simultaneously in the tunneling state. At 20 mK, we observe a broad zero-field peak that seems to reduce upon increasing the temperature, as well as conductance fluctuations for $|B| \geq 2$ T. These are not exactly periodic, but reproducible for consecutive magnetic field sweeps, and weakly affected by increasing the temperature from 20 mK to 400 mK. The patterns do change if the charge inside the dot is changed either by the gate voltage or by the electrostatic background, though. Lastly, all these features vanish as the source-drain voltage is increased further above e/C_Σ, meaning that they are related to the Coulomb blockade, and not to eventual magneto-resistance or conductance fluctuations in the plain TI nanowire. On top of these, one can observe a small weak-antilocalization peak in the range where $\mid B \mid < 250$ mT , that is also observed in the plain film before patterning.

A possible cause for these is universal conductance fluctuations (UCF) inside the dot, in a similar fashion to what has been observed in gate-defined dots in 2D electron gases[17] and graphene billiards.[18] As sketched in Figure 4c), when an electron enters a dot, it can scatter elastically at the boundaries or on impurities multiple times before exiting, which results in a chaotic motion. If there is an out-of-plane magnetic field, a magnetic flux is threaded through the area A enclosed by these scattering paths, along which the electron acquires a finite Aharonov-Bohm phase. this leads to an oscillation of the conductance with a periodicity $\Delta B = \phi_0/A$, where $\phi_0 = h/e$ is the flux quantum. All of these paths contribute to the conductance with a different periodicity, the sum of which leads to aperiodic but reproducible fluctuations with the magnetic field. Although these patterns are random, their features are well described by the statistical theory of quantum dots.[19]

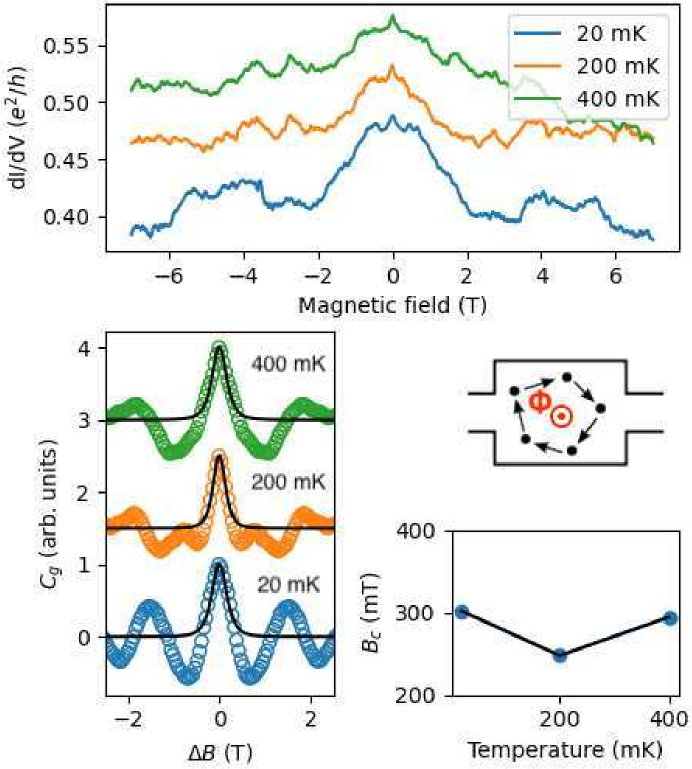

Figure 4: a) Magneto-conductance of the device at $V_G = 0$ and $T = 20$ mK, showing universal conductance fluctuations superimposed on a decreasing magneto-conductance background. b) Auto-correlation function (ACF) of the oscillations at $B \geq 2$ T, and fit of the central lobe to a squared lorentzian. c) Sketch of a chaotic billiard, in which electrons are scattered against edges and impurities and can enclose a finite area. d) Characteristic field B_c extracted from fitting the central lobe of the ACF, which is not significantly affected by temperature. The curves in panels a) and b) are offset by respectively 0.05 and 1.5 for clarity.

Firstly, the broad U-shaped conductance enhancement below $\mid B \mid \leq 2$ T was also observed in the case of chaotic billiards due to an effect similar to weak-(anti)localization[20] . Secondly, above 2 T, the fluctuation pattern can be characterised by its auto-correlation pattern (ACF), denoted C_G, which gives the correlation between the conductance at B and that at $B + \Delta B$.

In the Coulomb blockade regime (closed dot), it takes the form of a squared Lorentzian:[21] $C_G(\Delta B) \propto (1 + (\Delta B/B_c)^2)^{-2}$, where ΔB is the field shift and B_c is the correlation field inside the dot. The normalized curves obtained from the data at $B \geq 2T$ are presented in Figure 4b. We note that the frequencies below 0.25 cycles per Tesla were filtered out to remove the slope from the magneto-resistance background. Fitting the central lobe of C_G yields a characteristic field $B_c = 325$ mT, that corresponds to a flux of $1.2\phi_0$ through the nominal dot area. This value is significantly larger than the typical $0.3\phi_0$ observed for a chaotic billiard, and could indicate that either the electron-electron interactions inside the dot go beyond the charging effects,[22] or that the actual dot size is smaller than the dimensions of the island, which is also suggested by the smaller effective dot radius estimated earlier from the gate capacitance.

Another explanation could be the formation of Darwin-Fock states inside the island or constriction dots if the confinement potential takes the form of an harmonic oscillator.[23] These energy levels shift and cross upon increasing the out-of-plane magnetic field, which leads to changes in the ground state of the dot, and results in fluctuations of the position of the Coulomb peaks.

To summarize, we demonstrated the fabrication of a functional TI-based single electron transistor using a top-down electron beam lithography approach. Coulomb diamonds measured at 20 mK indicate the formation of a quantum dot inside the central island as intended. However, the suppression of Klein tunneling that allows the formation of this dot also leads to trapping of the Dirac electrons by imperfections in the constrictions, which forms additional quantum dots. This is an intrinsic limitation of the approach, and could eventually be mitigated by patterning constrictions as short as possible to still observe Coulomb blockade. Moreover, fluctuations in the magneto-conductance of the device in the tunneling regime can qualitatively be explained by the chaotic motion of electrons inside the dot. While these findings mark a promising initial step towards TI-based single-electron sources, it is crucial to address the aforementioned challenges before the successful realization of such a device.

Experimental

Device fabrication

The sample fabrication consists in two steps of electron beam lithography. Electrical contacts were first patterned on the plain films by EBL, evaporation of $Ti_{3\ \mathrm{nm}}/Au_{50\ \mathrm{nm}}$, and lift-off. A 30 s low power argon ion milling was done before the deposition to ensure good electrical contact. The second EBL step is used to define an etching mask in approximately 130 nm of resist (Allresist AR-P6200) for both the leads, dots, and gate contacts. The pattern is then transferred into the film by argon ion milling. During that step, the sample was cooled with liquid nitrogen to minimize heat damage. Lastly, the etching mask was removed in warm acetone with ultrasounds.

Transport measurements

The sheet resistance and Hall effect of the plain film were measured in a Quantum Design Physical Property Measurement System (PPMS) at 2 K in the Van der Pauw configuration. The data is provided in the Supporting Information. The transport in the single electron transistor was measured in an Oxford Triton dilution fridge at a base temperature of 22 mK. The sample was biased by applying an AC voltage of 1 Hz to a 1 MΩ bias resistor in series with the device, and measuring the voltage and current along with a National Instruments DAQ and Stanford Instruments voltage pre-amplifiers. The conductance is then obtained by numerical differentiation.

Calculation of the autocorrelation measurements

After isolating the $\mid B \mid \geq 2$ T portion of the curve, a Butterworth high-pass filter with a cutoff $f_c = 0.25$ cycles per Tesla to remove the background. The mean value is then removed before calculating the auto-correlation of the signal.

Estimated dot parameters

Table 1: Capacitance values, charging energy, and estimated dot sizes for the different dots found in the device.

	G/G_0	ΔV_G	C_G	C_T	C_Σ	E_c	R
Central dot	0.5	15 mV	11 aF	310 aF	620 aF	0.13 meV	26 nm
Barrier dots	1.75	21 mV	7.5 aF	82 aF	170 aF	0.94 meV	21 nm

Extra information when writing JACS Communications

Acknowledgement

Supporting Information Available

The following files are available free of charge.

- Filename: brief description
- Filename: brief description

References

(1) Hasan, M. Z.; Kane, C. L. *Colloquium* : Topological Insulators. *Reviews of Modern Physics* **2010**, *82*, 3045–3067.

(2) Xin, X.; Zhou, D. Kondo Effect in a Topological Insulator Quantum Dot. *Physical Review B* **2015**, *91*, 165120.

(3) Rider, M. S.; Giannini, V. Proposal for THz Lasing from a Topological Quantum Dot. *Nanophotonics* **2021**, *10*, 3497–3506.

(4) Saxena, R.; Grosfeld, E.; E De Graaf, S.; Lindstrom, T.; Lombardi, F.; Deb, O.; Ginossar, E. Electronic Confinement of Surface States in a Topological Insulator Nanowire. *Physical Review B* **2022**, *106*, 035407.

(5) Cho, S.; Kim, D.; Syers, P.; Butch, N. P.; Paglione, J.; Fuhrer, M. S. Topological Insulator Quantum Dot with Tunable Barriers. *Nano Letters* **2012**, *12*, 469–472.

(6) Jing, Y.; Huang, S.; Wu, J.; Meng, M.; Li, X.; Zhou, Y.; Peng, H.; Xu, H. A Single-Electron Transistor Made of a 3D Topological Insulator Nanoplate. *Advanced Materials* **2019**, *31*, 1903686.

(7) Bardarson, J. H.; Moore, J. E. Quantum Interference and Aharonov–Bohm Oscillations in Topological Insulators. *Reports on Progress in Physics* **2013**, *76*, 056501.

(8) Zhang, J.; Chang, C.-Z.; Zhang, Z.; Wen, J.; Feng, X.; Li, K.; Liu, M.; He, K.; Wang, L.; Chen, X.; Xue, Q.-K.; Ma, X.; Wang, Y. Band Structure Engineering in (Bi1-xSbx)2Te3 Ternary Topological Insulators. *Nature Communications* **2011**, *2*, 574.

(9) Grabert, H., Devoret, M. H., Eds. *Single Charge Tunneling*; NATO ASI Series; Springer US: Boston, MA, 1992; Vol. 294.

(10) Gelmont, B.; Shur, M.; Mattauch, R. Disk and Stripe Capacitances. *Solid-State Electronics* **1995**, *38*, 731–734.

(11) Ref. 9, Chap. 6.

(12) Dröscher, S.; Knowles, H.; Meir, Y.; Ensslin, K.; Ihn, T. Coulomb Gap in Graphene Nanoribbons. *Physical Review B* **2011**, *84*, 073405.

(13) Staring, A. A. M.; Van Houten, H.; Beenakker, C. W. J.; Foxon, C. T. Coulomb-Blockade Oscillations in Disordered Quantum Wires. *Physical Review B* **1992**, *45*, 9222–9236.

(14) Ruzin, I. M.; Chandrasekhar, V.; Levin, E. I.; Glazman, L. I. Stochastic Coulomb Blockade in a Double-Dot System. *Physical Review B* **1992**, *45*, 13469–13478.

(15) Cronenwett, S. M.; Maurer, S. M.; Patel, S. R.; Marcus, C. M.; Duruöz, C. I.; Harris, J. S. Mesoscopic Coulomb Blockade in One-Channel Quantum Dots. *Physical Review Letters* **1998**, *81*, 5904–5907.

(16) Güttinger, J.; Frey, T.; Stampfer, C.; Ihn, T.; Ensslin, K. Spin States in Graphene Quantum Dots. *Physical Review Letters* **2010**, *105*, 116801.

(17) Marcus, C.; Westervelt, R.; Hopkins, P.; Gossard, A. Conductance Fluctuations in a Quantum Dot in the Tunneling Regime: Crossover from Aperiodic to Regular Behavior. *Surface Science* **1994**, *305*, 480–489.

(18) Ponomarenko, L. A.; Schedin, F.; Katsnelson, M. I.; Yang, R.; Hill, E. W.; Novoselov, K. S.; Geim, A. K. Chaotic Dirac Billiard in Graphene Quantum Dots. *Science* **2008**, *320*, 356–358.

(19) Alhassid, Y. The Statistical Theory of Quantum Dots. *Reviews of Modern Physics* **2000**, *72*, 895–968.

(20) Chang, K.; Lou, W.-K. Helical Quantum States in HgTe Quantum Dots with Inverted Band Structures. *Physical Review Letters* **2011**, *106*, 206802.

(21) Ref. 19, Sec.V.

(22) Ref. 19, Sec.VI.

(23) Kouwenhoven, L. P.; Austing, D. G.; Tarucha, S. Few-Electron Quantum Dots. *Reports on Progress in Physics* **2001**, *64*, 701–736.

The author, Kiryl Niherysh, has completed the PhD program at the Institute of Chemical Physics (University of Latvia) and the Department of Microtechnology and Nanoscience MC2 (Chalmers University of Technology, Sweden).

This thesis includes the results of systematic research in the field of topological insulators (TIs), which belong to a new class of quantum matter. The thesis covers the whole technological process starting from the synthesis of TI nanomaterials, their structural characterisation, nanofabrication of devices based on them, and finishing with low-temperature transport measurements of obtained devices.

The technological developments in this thesis prepare the ground for TI-based single-electron charge pumping, as well as for other nanoelectronic devices, such as electro-mechanical switches operating in low temperatures, quantum computing, thermoelectric and space applications, sensing, spintronics and so on.

The author hopes the results of this thesis will become a stepping stone toward new inventions.

ISBN 978-9934-36-272-9

9 789934 362729 >